TECHNISCHE UNIVERSITÄT DRESDEN

Observation of Electroweak Same-Charge $W^{\pm}W^{\pm}jj$ Production at $\sqrt{s} = 13$ TeV with the ATLAS Detector at the LHC

Dissertation
zur Erlangung des akademischen Grades
Doctor rerum naturalium
(Dr. rer. nat.)

vorglegt der
Fakultät für Physik
der Technischen Universität Dresden

von
M.Sc. Franziska Iltzsche (geb. Speiser)
geboren am 19. Juni 1990 in Lübben

Dresden, Mai 2019

Eingereicht am 7. Mai 2019
Verteidigt am 27. September 2019

1. Gutachter: Prof. Dr. Michael Kobel (Technische Universität Dresden)
2. Gutachter: apl. Prof. Dr. Monica Dunford (Universität Heidelberg)

Abstract

The Standard Model of particle physics provides a gauge invariant description of the electroweak and strong interactions between elementary particles. Particle masses are generated through spontaneous breaking of the $SU(2)_L \times U(1)_Y$ gauge symmetry, which also results in an additional boson, the Higgs-boson.

In the Higgs-less Standard Model, the scattering of longitudinally polarized $W^{\pm}$-bosons violates unitarity at energies of approximately 1 TeV. For energies beyond that threshold, the WW production rate would exceed the collision rate, which is unphysical. Contributions of the Higgs-boson are expected to unitarize the vector boson scattering (VBS) cross section. Thus, VBS measurements provide a powerful means to investigate Standard Model predictions and the electroweak symmetry breaking mechanism. Across all VBS channels, electroweak same-charge $W^{\pm}W^{\pm}$ production promises the highest ratio of signal to irreducible backgrounds. All diagrams that, at leading order, involve purely electroweak couplings, α_{ew}, and are of the order $\mathcal{O}(\alpha_{\text{ew}}^6)$ are considered as electroweak production. Due to the small production cross sections, high center-of mass energies and luminosities are necessary to observe VBS processes; these measurements have only become accessible at the LHC.

At the LHC, electroweak $W^{\pm}W^{\pm}$ production can be studied in proton-proton collisions at a center-of-mass energy of 13 TeV. This thesis is based on 36.1 fb^{-1} of data recorded in 2015 and 2016 by the ATLAS detector. VBS events show a special topology with two final state quarks with large rapidity and two centrally decaying gauge bosons. In this analysis, fully leptonic production is considered, where the $W^{\pm}$-bosons decay into lepton-neutrino pairs. The quarks appear as particle jets in the detector. Neutrinos escape the detector without interaction, however the reconstruction of the total transverse neutrino momentum is possible using momentum conservation. The selected final state consists of at least two jets, high missing transverse momentum due to the neutrinos, and two same-charge electrons or muons. Leptonically decaying τ-leptons are not included.

Signal event candidates are selected in a VBS-like phase space requiring a high invariant mass m_{jj} of the leading and subleading jets and a large angular separation between them. A profile likelihood method is implemented to measure the electroweak $W^{\pm}W^{\pm}$ fiducial cross section and determine the statistical significance of the observed data with respect to the background-only expectation using the differential m_{jj} distribution. The highest background contributions originate in $W^{\pm}Z$ production as well as events with mis-reconstructed or mis-identified leptons caused by detector inefficiencies.

A total of 122 signal candidate events are observed, where 118 events are expected. The highest signal-to-background ratio is reached in the high-m_{jj} region above 1500 GeV. Electroweak, leptonic $W^{\pm}W^{\pm}$ production is significantly observed with a significance of 6.7 σ. An expected significance of 4.6 σ is derived. The measured fiducial cross section amounts to $(2.94 \pm {}^{0.62}_{0.56})$ fb. At leading order, the SHERPA generator predicts a fiducial cross section of $(2.01 \pm {}^{0.34}_{0.24})$ fb. The measured and predicted cross sections agree within their uncertainties.

Kurzdarstellung

Das Standardmodell der Teilchenphysik dient der eichinvarianten Beschreibung starker und elektroschwacher Wechselwirkungen zwischen Elementarteilchen. Teilchenmassen werden durch die spontane Brechung der $SU(2)_L \times U(1)_Y$ Eichsymmetrie eingeführt, aus der auch ein zusätzliches Boson, das Higgs-Boson, hervorgeht.

Im Standardmodell ohne Higgs-Boson verletzt die Streuung longitudinal polarisierter $W^{\pm}$-Bosonen die Unitaritätsgrenze bei Energien von etwa 1 TeV. Bei höheren Energien übersteigt die Rate der WW-Produktion die Kollisionsrate, was unphysikalisch ist. Jedoch erhält der Wirkungsquerschnitt für Vektorbosonstreuung (VBS) durch das Higgs-Boson zusätzliche Beiträge und wird dadurch unitarisiert. Daher sind VBS-Messungen besonders geeignet, um die Vorhersagen des Standardmodells sowie den Mechanismus der elektroschwachen Symmetriebrechung zu untersuchen. Von allen VBS-Kanälen hat die elektroschwache Produktion gleichgeladener $W^{\pm}$-Bosonen dabei das beste Verhältnis von Signal zu irreduziblem Untergrund. Dabei bezeichnet elektroschache Produktion all jene Diagramme, welche in erster Ordnung Störungstheorie ausschließlich elektroschwache Kopplungen, α_{ew}, beinhalten und von der Ordnung $\mathcal{O}(\alpha_{\mathrm{ew}}^6)$ sind. Aufgrund des niedrigen Produktionswirkungsquerschnittes sind sowohl hohe Schwerpunktsenergien als auch große Datenmengen notwendig, um VBS-Prozesse nachzuweisen. Messungen dieser Art sind erst am LHC möglich geworden.

Am LHC kann die $W^{\pm}W^{\pm}$ Produktion in Proton-Proton Kollisionen bei einer Schwerpunktsenergie von 13 TeV untersucht werden. Diese Arbeit beruht auf einer Datenmenge von 36,1 fb^{-1}, die 2015 und 2016 mit dem ATLAS Detektor aufgezeichnet wurde. VBS-Ereignisse zeichnen sich durch eine spezielle Topologie aus, bei der zwei vorwärts gestreute Quarks in Kombination mit zwei zentral im Detektor zerfallenden Eichbosonen erwartet werden. In dieser Analyse wird der vollleptonische Zerfall der $W^{\pm}$-Bosonen in Lepton-Neutrino-Paare betrachtet. Obwohl die Neutrinos den Detektor ohne Wechselwirkung verlassen, ist die Rekonstruktion des Gesamtimpulses aller erzeugten Neutrinos durch Anwendung der Impulserhaltung in der Ebene transversal zur Strahlachse möglich. Der Endzustand enthält mindestens zwei Quarks, die im Detektor als Jets erscheinen, einen hohen Anteil fehlenden Transversalimpulses durch die Neutrinos, sowie zwei gleichgeladene Elektronen oder Myonen. Leptonisch zerfallende τ-Leptonen werden nicht betrachtet.

Durch das Fordern zweier Jets mit hoher invarianter Masse m_{jj}, sowie großem Rapiditätsabstand werden mögliche Signalereignisse in einem VBS-ähnlichen Phasenraum selektiert. Zur statistischen Auswertung der Messung wurde ein Likelihood-Quotienten-Test implementiert, der auf der differentiellen m_{jj}-Verteilung beruht. Die größten Beiträge zum Untergrund stammen von $W^{\pm}Z$ Ereignissen und Ereignissen, bei denen Leptonen aufgrund von Detektorunzulänglichkeiten missrekonstruiert oder missidentifiziert wurden.

In der Signalregion wurden insgesamt 122 Ereignisse beobachtet, während 118 Ereignisse erwartet wurden. Das höchste Verhältnis von Signal- zu Untergrunderwartung wurde in Ereignissen mit hohem m_{jj} über 1500 GeV gemessen. Für die elektroschwache $W^{\pm}W^{\pm}$ Produktion konnte eine gemessene und erwartete Signifikanz von 6,7 σ beziehungsweise 4,6 σ ermittelt werden. Im Selektionsphasenraum wurde ein Wirkungsquerschnitt von $\left(2,94\ \pm\ ^{0,62}_{0,56}\right)$ fb gemessen, der innerhalb der Unsicherheiten mit der theoretischen Vorhersage des SHERPA Monte-Carlo Programms in erster Ordnung Störungstheorie von $\left(2,01\ \pm\ ^{0,34}_{0,24}\right)$ fb übereinstimmt.

Contents

1 Introduction

The quest to gain a deeper understanding of the building blocks of nature has fascinated scholars and scientists for centuries. Beginning with the concept of the atom, conceived by Democritus [1] approximately 400 BC, atomic theories underwent many changes. After the discovery of the electron in 1897, Thomson proposed the first atom model with substructure [2]. Interpreting scattering experiments of α- and β-rays with thin metal foils [3], Rutherford proposed the existence of a heavy atom nucleus in 1911 [4]. This was the beginning of a long success story of collision experiments, which have proven to be well suited for investigating the substructure of matter. In these experiments, a beam of decay products from radioactive decays or otherwise accelerated particles is collided with a target, which itself can be a particle beam as well. If the four-momentum transfer from the beam particles to the target is large enough, the structure of the target material can be dissolved and the constituents can, in many cases, be directly observed. As increasingly high energies were reached with advancement in technology, a deeper understanding of sub-atomic particles could be gained.

As a result of many experiments, the Standard Model of particle physics has been constructed, describing the interactions between all known elementary particles. Apart from apparent shortcomings, like the missing candidate for dark matter and other, more technical weaknesses [5, 6] its predictions are generally in very good agreement with measurements [7]. With the discovery of the Higgs boson [8, 9], the riddle of the origin of particle masses is closer to solving as the observed Higgs boson is compatible with the theory of electroweak symmetry breaking embedded in the Standard Model. In this theory, the particle masses are generated by the interactions with the Higgs boson.

Gauge boson scattering in general, and the scattering of longitudinally polarized $W^{\pm}$-bosons in particular is sensitive the the electroweak symmetry breaking mechanism. In the Higgs-less Standard Model, the scattering of longitudinally polarized $W^{\pm}$-bosons is predicted to violate unitarity at an energy scale of approximately 1 TeV. This unphysical prediction is corrected by the introduction of the Higgs boson. Contributions from WWH vertices to the scattering amplitude reunitarizes the cross section.

However, it is yet unknown whether the discovered particle fully unitarizes the vector boson scattering cross section. Measurements of the cross section for $H \to W^{\pm}W^{\mp}$ production are in good agreement with the Standard Model prediction [10]. If the coupling of the Higgs-boson to $W^{\pm}$-bosons differs from the Standard Model expectation, the growth of the scattering cross section is dampened but additional contributions are necessary to unitarize it completely. These contributions would appear as additional resonances in vector boson scattering (VBS). Therefore, the measurement of VBS processes provides a complementary probe of electroweak symmetry breaking.

In this thesis, the electroweak scattering of same-charge $W^{\pm}$-bosons, denoted as $W^{\pm}W^{\pm}jj$-EW, which is at leading order of the order α_{ew}^{6} is studied. The selected final state is characterized by at least two forward jets, as well as two central, leptonically decaying $W^{\pm}$-bosons. An integrated luminosity of $36.1\,\mathrm{fb}^{-1}$ proton-proton collision data recorded with the ATLAS detector in 2015 and 2016 is used. A multi-bin profile likelihood fit of the invariant mass distribution of the leading and subleading jets is performed to estimate the statistical significance of $W^{\pm}W^{\pm}jj$-EW production and measure the respective fiducial cross section. The work presented here is very similar to the analysis presented by the ATLAS collaboration in Reference [11].

2 Theoretical Foundation and Tools

2.1 Elementary Particles and Their Interactions

The current Standard Model (SM) provides a gauge-invariant description of the interactions between all known elementary particles. It was developed over the second half of the last century, and the means to the discovery of some of the by now well established particles, like vector bosons [12–15] and the third-generation quarks [16, 17]. Generally, it describes two types of particles, fermions and bosons, as well as three of the four interactions between them [18]. Only gravity is not yet integrated. The particles and interactions comprised in the SM shall be briefly summarized in the following.

2.1.1 The Standard Model of Particle Physics

The SM models the propagation and interaction of elementary particles, which are the the building bocks of nature. These are called fermions, i. e. particles that follow the Fermi-Dirac statistics, having a half-integer spin quantum number. They can be subdivided into leptons and quarks, based on the assigned charges.

Fermions interact via the exchange of bosons; particles following Bose-Einstein statistics with an integer spin quantum number. The mediators for the three forces are spin-one bosons. Gluons mediate the strong interaction and are described by the theory of Quantum Chromodynamics (QCD). The photon mediates the electromagnetic interaction, described by Quantum Electrodynamics (QED) and vector bosons mediate the weak interaction. However, Salam, Glashow and Weinberg showed that unification of electromagnetic and weak interaction is possible, yielding the electroweak (EW) theory [19–21] and $SU(2)_L \times U(1)_Y$ symmetry.

Within the electroweak theory, fermions are described as states in the space of the weak isospin charge. Because of parity violation, which was first experimentally observed by Chien-Shiung Wu [22], the parametrization in the weak isospin space differs for left- and right-handed leptons. Left-handed particles are particles with negative chirality, which is equivalent to negative helicity for massless particles, or in the relativistic regime.

Left-handed fermions form doublets and carry a weak isospin charge with an absolute value of 1/2, whereas right-handed fermions form singlets and carry a weak isospin charge of 0. Additionally, all quarks and all down-type leptons, i. e. leptons with negative isospin, carry an electric charge $Q \neq 0$.

Gluons only couple to particles carrying the color charge, which is why they are only coupling to quarks. An overview of the particles comprised in the Standard Model as well as their masses and charges is given in Table 2.1.

It has been observed in meson decays that the coupling of the $W^{\pm}$-boson to K and π mesons is different, which seems to contradict quark universality. Cabibbo introduced a mixing angle [23], representing the fact that the $W^{\pm}$-boson does not couple directly to the mass eigenstate of the d-quark, but instead to a weak eigentstate d', which is a superposition of

$$d' = d \cos\theta_C + s \sin\theta_C,$$

where θ_C is the mixing angle between d and s mass eigenstates. This mixing is generalized for three quark generations [24] and written in terms of the Cabibbo-Kaboayashi-Maskawa (CKM) matrix

$$|q'_n\rangle \;=\; \sum_{m=1}^{3} V^{\text{CKM}}_{n,m}\;|q_m\rangle.$$

The down-type mass eigentstates are denoted as $|q_m\rangle$, while $|q'_n\rangle$ represent the flavor eigentstates. It can be seen that the CKM matrix as four free parameters, which are three mixing angles, and one $\mathcal{CP}$ violating phase factor. $\mathcal{CP}$ violation has been experimentally confirmed in decays of K- [25] and B- mesons [26].

In analogy to quark mixing, the concept of neutrino mixing has been introduced [27]. A mixing matrix, called Pontecorvo–Maki–Nakagawa–Sakata (PMNS) matrix, is defined as [28]

$$|\nu'_l\rangle \;=\; \sum_{i=1}^{3} U^{\text{PMNS}}_{l,i}\;|\nu_i\rangle,$$

where $|\nu'_l\rangle$ and $|\nu_i\rangle$ denote the neutrino flavor and mass eigenstates, respectively. Later, flavor oscillations in solar and atmospheric neutrinos have been observed [29, 30]. Commonly, the average masses of the weak eigenstates are then defined as:

$$m(\nu'_l) \;=\; \sum_{i=1}^{3} |U^{\text{PMNS}}_{l,i}|^2\; m(\nu_i).$$

All kinematic and interaction properties of the particles comprised in the Standard Model can be described in the Lagrangian formalism. The Standard Model Lagrangian is given as a superposition of the bosonic and fermionic consituents

$$\mathcal{L}_{SM} \;=\; \mathcal{L}_{boson} \;+\; \mathcal{L}_{lepton} \;+\; \mathcal{L}_{quark}. \tag{2.1}$$

The Lagrangian $\mathcal{L}_{boson}$ describes the kinematics and interaction of gauge bosons

$$\mathcal{L}_{boson} \;=\; \underbrace{-\frac{1}{4}B_{\mu\nu}B^{\mu\nu} \;-\; \frac{1}{4}tr\,(W_{\mu\nu}W^{\mu\nu})}_{\text{Electroweak Theory}} \;\underbrace{-\; \frac{1}{4}tr\,(G_{\mu\nu}G^{\mu\nu})}_{\text{QCD}}, \tag{2.2}$$

using the respective field strength tensors as well as the weak and strong couplings g_W and g_s, with

$$B_{\mu\nu} \;=\; \partial_\mu B_\nu \;-\; \partial_\nu B_\mu, \tag{2.3}$$

$$W^a_{\mu\nu} \;=\; \partial_\mu W^a_\nu \;-\; \partial_\nu W^a_\mu \;+\; g_W \varepsilon^{abc} W^b_\mu W^c_\nu, \tag{2.4}$$

$$G^a_{\mu\nu} \;=\; \partial_\mu G^a_\nu \;-\; \partial_\nu G^a_\mu \;+\; g_s f^{abc} G^b_\mu G^c_\nu. \tag{2.5}$$

Here ε^{abc} denotes the Levi-Civita symbol and f^{abc} represents the structure constants of the $SU(3)_C$ gauge group. The fields B_μ, W_μ and G_μ describe the gauge bosons. During electroweak unification, B_μ and W_μ mix and thus the observable weak bosons $W^\pm$, Z^0 and the photon are created.

As mentioned above, fermions are assembled into left-handed doublets, and right-handed singlets. Below, lepton and quark doublets will be denoted as L and Q_L, respectively. The expressions u_R, d_R, and e_R represent singlets of up- and down-type quarks, as well as down-type leptons. Right-handed, up-type leptons, i. e. neutrinos, are neglected since they do not couple to gauge bosons. Leptons are described by the Lagrangian

$$\mathcal{L}_{lepton} \;=\; \bar{L} i\gamma^\mu \mathrm{D}_\mu L \;+\; \bar{e}_R i\gamma^\mu \mathrm{D}_\mu e_R \;+\; h.\,c., \tag{2.6}$$

where $h.\,c.$ is the hermitian conjugate of the expression and the covariant derivative of the leptonic fields is defined as

$$\mathrm{D}_\mu \;=\; \partial_\mu \;-\; ig_W \frac{\tau_a}{2} W^a_\mu \;-\; ig_Y Y B_\mu. \tag{2.7}$$

			Mass			Charges		
						Q	I_W^3	Color
Leptons	1st Gen	ν_e	<2 eV			0	$+\frac{1}{2}$	-
		e	510.998 946 1 ± 0.000 003 1 keV			-1	$-\frac{1}{2}$	-
	2nd Gen	ν_μ	<2 eV			0	$+\frac{1}{2}$	-
		μ	105.658 374 5 ± 0.000 002 4 MeV			-1	$-\frac{1}{2}$	-
	3rd Gen	ν_τ	<2 eV			0	$+\frac{1}{2}$	-
		τ	1776.86	± 0.12	MeV	-1	$-\frac{1}{2}$	-
Quarks	1st Gen	u	2.2	± 0.45	MeV	$\frac{2}{3}$	$+\frac{1}{2}$	✓
		d	4.7	± 0.4	MeV	$-\frac{1}{3}$	$-\frac{1}{2}$	✓
	2nd Gen	c	1.275	± 0.035	GeV	$\frac{2}{3}$	$+\frac{1}{2}$	✓
		s	95	± 6	MeV	$-\frac{1}{3}$	$-\frac{1}{2}$	✓
	3rd Gen	t	173.0	± 0.4	GeV	$\frac{2}{3}$	$+\frac{1}{2}$	✓
		b	4.18	± 0.04	GeV	$-\frac{1}{3}$	$-\frac{1}{2}$	✓
Bosons		γ	$<1 \cdot 10^{-18}$ eV			0	0	-
		$W^\pm$	80.379	± 0.012	GeV	±1	±1	-
		Z^0	91.1876	± 0.0021	GeV	0	0	-
		g	0			0	0	✓

Table 2.1: Overview of particles in the Standard Model. Masses and charges are taken from Ref. [31]. Heaviside-Lorentz units are used, where $\hbar = c = 1$ is set. Under these conventions, the energy, mass and momentum of a particle all have the unit eV.

The matrices τ_a are the Pauli matrices and generators of the $SU(2)_L$ symmetry group. For quarks, the Lagrangian is nearly identical to the leptonic case

$$\mathcal{L}_{quark} \;=\; \bar{Q}_L i\gamma^\mu \mathrm{D}_\mu Q_L \;+\; \bar{d}_R i\gamma^\mu \mathrm{D}_\mu d_R \;+\; \bar{u}_R i\gamma^\mu \mathrm{D}_\mu u_R \;+\; h.\ c., \tag{2.8}$$

except that the quark-gluon interaction has to be included in the covariant derivative:

$$\mathrm{D}_\mu \;=\; \partial_\mu \;-\; ig_W \frac{\tau_a}{2} W_\mu^a \;-\; ig_Y Y B_\mu \;-\; ig_s \frac{\lambda_a}{2} G_\mu^a.$$

Here λ_a denote the Gell-Mann matrices. The generators T_a of the $SU(3)_C$ group can be written as $T_a = \lambda_a/2$.

2.1.2 Electroweak Symmetry Breaking

The pure Standard Model as summarized above describes massless particle, since mass terms like the one for the gauge field B_μ of the $U(1)_Y$ symmetry group,

$$\frac{1}{2} M_B^2 B_\mu B^\mu,$$

are not invariant under the gauge transformation $B_\mu \to B_\mu - \frac{1}{g_Y}\partial_\mu \beta(x)$, with an arbitrary local phase $\beta(x)$.

A further point of friction is the Standard Model prediction of the electroweak scattering cross section for $W^\pm$-bosons. The Standard Model Lagrangian given in Eq. (2.2) contains two different kind of vertices of gauge boson self interaction. From the $SU(2)_L$ field strength tensor, Eq. (2.4), follows the prediction of triple and quartic vertices. The matrix element for this process depends on the polarization states of the in- and outgoing W-bosons, which can be transversely and longitudinally polarized. The transverse polarization states are independent of the $W^{\pm}$-boson momentum, but the longitudinal polarization vector, evaluated in the WW rest frame, is equal to

$$\varepsilon^{\mu}_{\mathrm{L}} \;=\; (|\vec{p}|/M_W,\ 0,\ 0,\ E/M_W)^{\mathrm{T}}\,,$$

and is directly proportional to the boson momentum. As the polarization vector also enters the matrix element [32] the scattering cross section violates unitarity at energies of 1 TeV to 2 TeV.

However, both problems can be solved by breaking $SU(2)_{\mathrm{L}} \times U(1)_{\mathrm{Y}}$ gauge symmetry, leaving only the $U(1)_Q$ symmetry unbroken. In the Standard Model, this is realized by introducing a scalar, isodoublet field ϕ, and extending the Standard Model Lagrangian described in Eq. (2.1) by the potential $\mathcal{L}_{\phi}$. With the a priori free parameters μ and λ, $\mathcal{L}_{\phi}$ is written as

$$\mathcal{L}_{\phi} \;=\; (D_{\mu}\phi)^{\dagger}(D_{\mu}\phi) \;+\; \mu^2\phi^{\dagger}\phi \;+\; \lambda(\phi^{\dagger}\phi)^2.$$

The shape of the potential is defined by the sign of the μ parameter. For positive μ, the potential has one global minimum and $\mathcal{L}_{\phi}$ remains gauge invariant. If the sign of μ becomes negative, however, two local minima arise. Thus $SU(2)_{\mathrm{L}} \times U(1)_{\mathrm{Y}}$ gauge invariance is broken. The covariant derivative of ϕ, $D_{\mu}\phi$, defined in the usual way as written in Eq. (2.7), generates mass terms for the gauge bosons, which become non-zero if the μ parameter is negative.

Expanding ϕ around its local minimum introduces an excitation that can be interpreted as a spin-zero particle, commonly called the Higgs-boson H. The additional VVH vertices enter the in calculation of the matrix element for longitudinal WW scattering and cancel the divergences.

In 2012, a particle with a mass of approximately 125 GeV was discovered at the LHC [8, 9]. Up to now, many properties of this particle have been measured, and no significant deviations from the predictions for a Standard Model Higgs are observed [10].

The recovery of unitarity is illustrated in Figure 2.1 [32]. The scattering cross sections for longitudinally polarized opposite-sign $W^{\pm}$-bosons are shown, taking into account different interaction vertices. The lines (a) and (b) show the cross section involving only triple and quartic gauge vertices, respectively, as a function of the invariant mass of the WW system $\sqrt{s}$. In these cases, the cross section is proportional to s^3, i. e. to E^6.

When a combination of triple and quartic vertices is considered in the calculation of the matrix element, the energy dependence becomes quadratic (line (a)+(b)). Only when taking into account diagrams involving the Standard Model Higgs boson, the cross section falls with $s^{-1} \sim E^{-1/2}$ (line (c)), and is reunitarized.

2.1.3 Anomalous Quartic Gauge Couplings

Even though there is no current experimental hint to particles or interactions beyond the Standard Model (BSM), there are some fundamental observations that cannot be explained by the Standard Model. For instance, the Standard Model is symmetric in the the production of matter and anti-matter, however a baryon asymmetry is observed in the universe [33]. Up to now, there is no satisfying explanation for this phenomenon. Another example is the existence of dark energy and matter [34] in the universe, which remains unexplained as well.

There is a multitude of BSM theories [35] attempting to reconcile predictions with the observations mentioned above, where the Standard Model is only part of a more complex theory like Supersymmetry [36] or Composite Higgs models [37, 38]. As an alternative to testing specific theories, an effective Lagrangian or field theory can be used to parameterize possible new physics in a model-independent way.

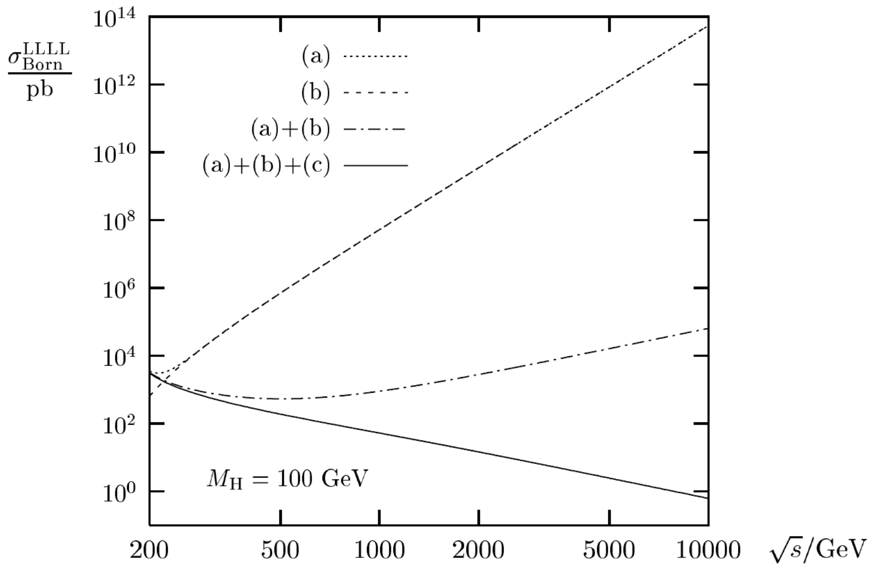

Figure 2.1: Cross sections for longtitudinal opposite-sign $W^{\pm}$-boson scattering resulting form subsets of tree-level diagrams: (a) diagrams involving only triple gauge couplings, (b) diagram including only quartic gauge coupling, and (c) diagrams involving the Standard Model Higgs boson. $\sqrt{s}$ describes the invariant mass in the WW rest frame. Taken from Ref. [32].

In these approaches, the Standard Model Lagrangian is extended with gauge-invariant terms to describe the low-energy effects of heavier, not yet kinematically accessible new contributions. Anomalous couplings to already known vertices parametrize the strength of the BSM contribution, and are valid up to the point where the new physics becomes dominant. In the case of vector boson scattering, anomalous triple (aTGC) and quartic (aQGC) couplings can be defined

The formulation of anomalous triple gauge couplings via an effective Lagragian and dimension-six operators in an effective field theory is described in [39]. Limits on aTGC have been set in the past [40–42], however it is not expected that the $W^{\pm}W^{\pm}$ final state provides additional insight.

Anomalous quartic gauge couplings can be described using the Electroweak Chiral Lagragian [43–45], which is gauge invariant under $SU(2)_L \times U(1)_Y$ transformations and contains all CP-invariant operators up to dimension four. The operators acting on quartic gauge vertices are

$$\alpha_4 \mathcal{L}_4 = \alpha_4 \mathrm{Tr}(V_\mu V_\nu)^2,$$
$$\alpha_5 \mathcal{L}_5 = \alpha_5 \mathrm{Tr}(V_\mu V^\mu)^2,$$

where V_μ is defined as $V_\mu = (D_\mu \Sigma)\Sigma^\dagger$. Σ is a matrix valued field and parameterizes the longitudinal degrees of freedom of the massive electroweak gauge bosons [43]:

$$\Sigma(x) = \exp\left(\frac{i}{v}\sum_{a=1}^{3}\pi^a \tau^a\right),$$

where π^a are the fields of the Goldstone-bosons. This representation has been used in the ATLAS 8 TeV analysis to set limits on aQGC.

A second way to parametrize new interactions between already known particles, introduced by heavier bosons, is via the effective field theory approach [46]. The new interactions appear as higher order operators in addition to the SM Lagragian:

$$\mathcal{L}_{\mathrm{EFT}} = \mathcal{L}_{\mathrm{SM}} + \sum_{d>4}\sum_{i} \frac{\tilde{f}_i}{\Lambda^{d-4}} \mathcal{O}_i,$$

where $\mathcal{O}_i$ are operators of dimension d with coefficients $\tilde{f}_i$. The contributions from these operators are suppressed by the scale of the new physics they describe, Λ. In contrast to the chiral Lagrangian mentioned above, the higher order operators are invariant under SM symmetries. Operators affecting only quartic gauge couplings are of dimension eight, and can be divided into three classes.

Operators of class S are those containing only derivatives of Higgs field ϕ:

$$\begin{aligned} f_{S,0}\ \mathcal{O}_{S,0} &= f_{S,0}\ \left[(D_\mu\phi)^\dagger D_\nu\phi\right] \times \left[(D^\mu\phi)^\dagger D^\nu\phi\right], \\ f_{S,1}\ \mathcal{O}_{S,1} &= f_{S,1}\ \left[(D_\mu\phi)^\dagger D^\mu\phi\right] \times \left[(D_\nu\phi)^\dagger D^\nu\phi\right], \end{aligned}$$

where $f_{S,0}$ and $f_{S,1}$ are the corresponding coefficients. Additionally, there are eight operators of class M, $\mathcal{O}_{M,i}$ consisting of $D_\mu\phi$ and two field strength tensors; as well as ten operators of class T, $\mathcal{O}_{T,j}$ containing only field strength tensors [46]. In CMS $W^\pm W^\pm jj$-EW analyses, limits are to set on the $f_{S,M,T}$ parameters.

The operators $\mathcal{O}_{S,0}$ and $\mathcal{O}_{S,1}$ are the only operators acting solely on vertices with four vector bosons. Converting limits on $(f_{S,0},\ f_{S,1})$ into the $(\alpha_4,\ \alpha_5)$ plane is not easily possible. Nevertheless, relations can be found for specific vertices [46]. For the $WWWW$ vertex for instance, the conversion can be written as

$$\alpha_4 = \frac{f_{S,0}}{\Lambda^4}\frac{v^4}{8}, \tag{2.9}$$

$$\alpha_4 + 2\alpha_5 = \frac{f_{S,1}}{\Lambda^4}\frac{v^4}{8}. \tag{2.10}$$

2.2 Statistical Data Analysis

When trying to measure a new process, it is necessary to quantify the compatibility of the expectation predicted by the full theory including the new process (i. e. signal + background expectation) and the theory without the new process (i. e. background only hypothesis). In order to do that, the p-value, i. e. the probability for a statistical fluctuation of the background-only (i. e. null) hypothesis to be at least as extreme as the signal + background expectation is measured. From the p-value, the expected significance of the measurement is derived. This is done by determining the quantile that this p-value corresponds to in a standard Gaussian distribution. If the significance is larger than five standard deviations ($5\,\sigma$), the background-only hypothesis is rejected. The concept of significance and p-value shall be explained in a simple example.

2.2.1 Exemplary Calculation of Statistical Significance

In order to provide an insight into the procedure of evaluating the statistical significance of an observation, a simple example is used. Consider the exponential decay of radioactive isotopes. When N_0 isotopes are initially activated, the number of remaining isotopes N for times t after the activation is given by the exponential decay law

$$N(t) \ = \ N_0 \cdot e^{-\frac{t}{\tau}}, \tag{2.11}$$

where τ denotes the mean lifetime of the isotopes. The mean lifetime characterizes the time when the number of remaining isotopes is equal to N_0/e. The time-dependent number of remaining isotopes given an initial number of 100 000 isotopes with a mean lifetime of four years is shown in Figure 2.2.

For measurement duration Δt which are much smaller than the mean lifetime, the decay rate $\dot{N}(t)$ is approximately constant throughout Δt. Under this assumption, the decay constant λ, which is defined as $\frac{1}{\tau}$, is a measure of the mean decay probability of a single isotope per time interval. For a measurement duration of $\Delta t = 84$ minutes, the decay probability for a single isotope is $\frac{\Delta t}{\tau} \sim 4 \cdot 10^{-3}$ %, which means, that $100\,000 \ \cdot \ 4 \cdot 10^{-5} = 4$ isotopes are expected to decay in the window $[0, \ \Delta t]$, directly after activation.

If $\Delta t \ll \tau$, such that the number of decaying isotopes is small in comparison to the number of remaining isotopes, the probability $\mathrm{Pois}(N|\nu)$ of observing N decays, when ν decays are expected is given by the Poisson distribution

$$\forall \ N, \nu \in \mathbb{N}: \ \mathrm{Pois}(N|\nu) \ = \ \frac{\nu^N}{N!} \, e^{-\nu}. \tag{2.12}$$

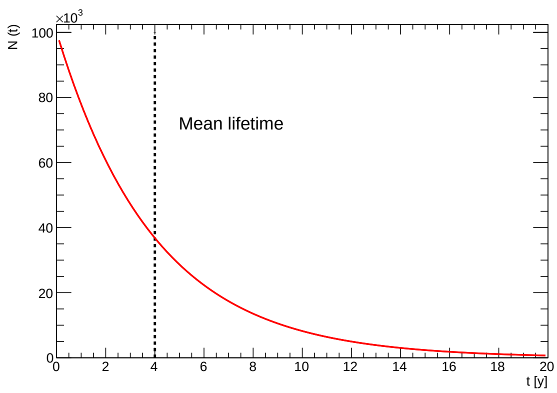

Figure 2.2: Number of remaining isotopes, assuming $N_0 = 100\,000$ radioactive isotopes with a mean lifetime of four years.

It can be shown that the expectation value and variance of this distribution are given by ν [47]. The conditions for the validity of the Poisson distribution are met in the above example. Figure 2.3 shows the Poisson distribution for an expectation value of four, as given in the example. During the measurement, N_{obs} events are observed. In Figure 2.3, N_{obs} corresponds to six events. The probability of a measurement of N_{obs} events needs to be evaluated, given the theory with an expectation value of ν events. Based on the Poisson distribution, the probability for observing a measurement at least as extreme as N_{obs} is given by the p-value[1]

$$p_{\text{obs}} = p(N_{\text{obs}}) = \sum_{N \geq N_{\text{obs}}}^{\infty} \text{Pois}(N|\nu). \tag{2.13}$$

In Figure 2.3, the p-value is represented by the light red area. The median $\tilde{N}$ of the Poisson distribution is defined as [48]

$$\tilde{N} = \inf \{z \in \mathbb{R} \text{ such that } p\text{-value } p(z) \geq 0.5\}\,. \tag{2.14}$$

It is interesting to note, that for a Poisson distribution, the median $\tilde{N}$ differs from the expectation value ν. When $\nu = 4$ for instance, $p(\nu) \sim 0.63 > 0.5$, while the median is $\tilde{N} = 3$ with $p(\tilde{N}) = 0.43$. This can be explained by remembering the definition of the expectation value ν, which is given as

$$\nu = \sum_{N} P(N) \cdot N, \tag{2.15}$$

where N runs over all allowed values and $P(N)$ describes the probability of that value. Note, that this applies to any probability density distribution[2]. For this Poisson distribution it is known from the p-value that 63 % of all values are larger than or equal to ν. However, it is also known, that the probability of these values converges to 0 as N goes to infinity. In the left tail of the distribution, the smallest allowed value is 0, which has a finite probability (approximately 1.8 % for $\nu = 4$). Therefore, the weighted sum of all possible values is larger than the median, which goes along with an asymmetry of the distribution.

Based on the observed p-value p_{obs} determined for a measurement, the statistical significance can be calculated as the quantile of a standard Gaussian distribution which corresponds to the same

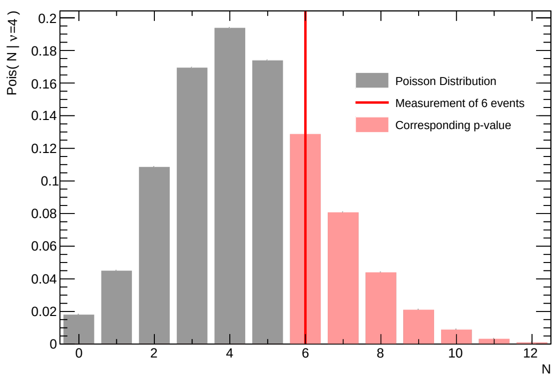

Figure 2.3: Poisson distribution for an expectation value of $\nu = 4$. The red line represents a measurement of six events. The p-value corresponding to that measurement is represented by the integral over the light red bars.

[1] For observations $N_{\text{obs}} < \nu$, the p-value is calculated from the sum over $N \in [0, N_{\text{obs}}]$.

[2] In case of a continuous probability density function, the summation will be replaced by an integration over the parameter space of N.

p-value. In general, a Gaussian probability $\mathrm{G}(x|\mu,\sigma^2)$ is given by

$$\mathrm{G}(x|\mu,\sigma^2) = \frac{1}{\sqrt{2\pi\sigma^2}} \exp\left(-\frac{(x-\mu)^2}{2\sigma^2}\right), \tag{2.16}$$

where μ is the mean and σ defines the standard deviation of the resulting distribution. A standard Gaussian is defined by setting $\mu = 0$ and $\sigma = 1$. The definition of the p-value for a Gaussian distribution is analogous to Eq. (2.13). In Table 2.2, the p-values corresponding to a selected set of quantiles of a normalized Gaussian distribution are shown. The statistical significance Z of a measurement of N_{obs} events with respect to the background-only hypothesis is the quantile of a standard Gaussian distribution, where the p-value is the same as the p-value p_{obs} determined for the measurement[1]

$$Z \text{ such that } p(Z) = \int_Z^\infty \mathrm{G}(Z|\mu=0,\sigma^2=1) = p_{\mathrm{obs}}. \tag{2.17}$$

This procedure is visualized in Figure 2.4. Assuming a measured p-value of $p = 2.28\cdot 10^{-2}$, the corresponding significance is $Z = 2$. The advantage of quoting results in terms of significance rather than p-values is mainly in the fact that significances (that are < 10 in most use cases) are much easier dealt with than p-values, which can become very small (see Table 2.2).

Following the above example of decays of activated isotopes with an expectation value of four events, different outcomes N_{obs} are considered. The p-values and significances for values of N_{obs} between four and 20 are shown in Figure 2.5.

A measurement of 12 events, where only four are expected, has a p-value of $9.15\cdot 10^{-4}$. This means that the probability for observing at least 12 events is 0.0915 %. This corresponds to a significance of 3.12 σ. The smaller the p-value, the lower the probability that the observation corresponds to the null hypothesis (in the example the theory predicting an expectation value of four events). In particle physics, two levels of significance are defined. If the significance is at least equal to 3 σ, the measurement is classified as an evidence. This means that there are hints for the null hypothesis not to describe the measurement correctly. If the significance surpasses 5 σ, the measurement is classified as observation, which means that the null hypothesis has been rejected. In the example, 5.03 σ are reached when 18 events are observed ($p_{\mathrm{obs}} = 2.48\cdot 10^{-7}$). In other words, a measurement of at least 18 events is necessary to reject the hypothesis $\nu = 4$. However, this observation does not contain concrete information about the true value of ν. It has to be evaluated if the difference to the null hypothesis is due to a mis-modeling of the underlying process of if an additional contribution, i. e. a new signal has been observed.

In Figure 2.6(a), the significance of an observation of 18 events is calculated for different expectation values ν. Expectation values between 11 and 27 agree with the observation within 2 σ. Further measurements would be necessary to reduce the number of possible underlying theories.

Quantile	p-value
0	$5.00\cdot 10^{-1}$
1	$1.59\cdot 10^{-1}$
2	$2.28\cdot 10^{-2}$
3	$1.35\cdot 10^{-3}$
4	$3.17\cdot 10^{-5}$
5	$2.87\cdot 10^{-7}$
6	$9.87\cdot 10^{-10}$

Table 2.2: Comparison of one-sided quantiles of a standard Gaussian distribution and the corresponding p-values.

[1] If the p-value is calculated from the interval $[0, N_{\mathrm{obs}}]$, the significance is analogously calculated from the interval $(-\infty, Z]$.

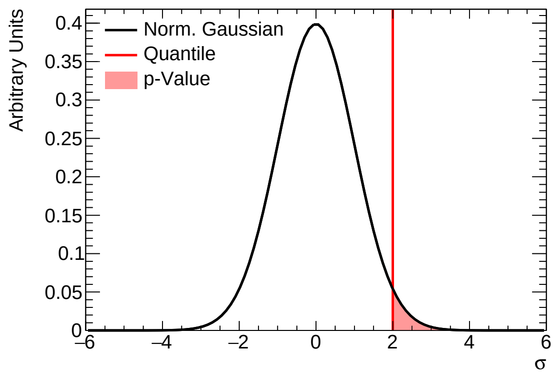

Figure 2.4: Schematic view of calculation of statistical significance. For a given p-value (here: $p = 2.28 \cdot 10^{-2}$), the quantile of a normalized Gaussian distribution corresponding to the same p-value is calculated (here: $Z = 2$).

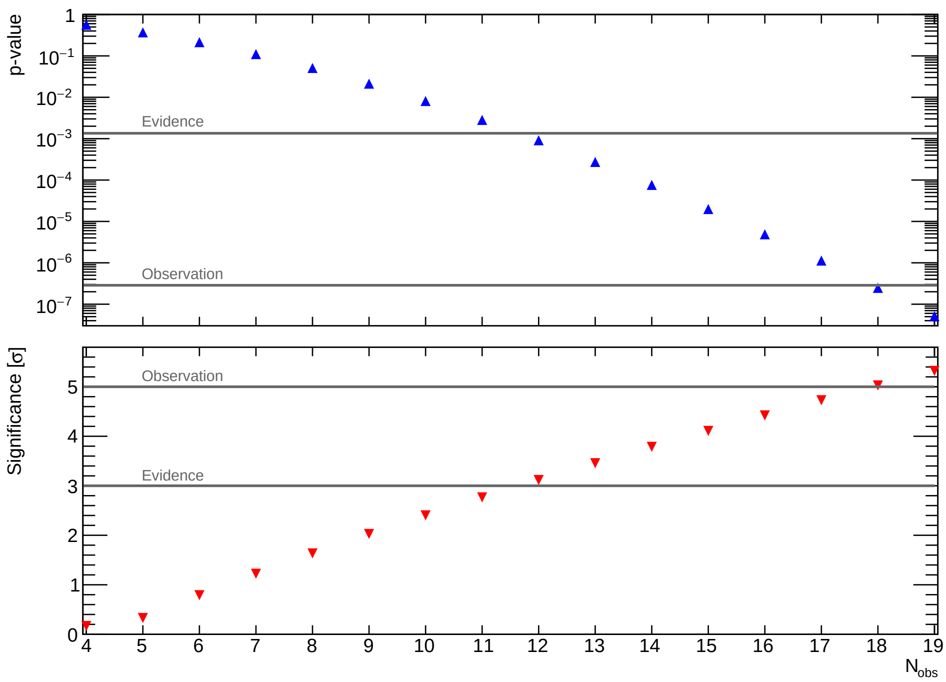

Figure 2.5: p-value (top) and significance (bottom) calculated for different measured number of events N_{obs}, where a Poisson distribution with an expectation value of $\nu = 4$ is taken as background-only hypothesis.

Instead of looking directly at the significance, it is instructive to also consider the Poisson probabilities for different values of ν. When $N_{\mathrm{obs}} = 18$, the value of ν that will give the highest probability P_{max} is $\nu_{\mathrm{max}} = 18$. In a case where ν_{max} should be determined numerically, it would be technically easier to transform this problem into a minimization rather than a maximization task. So instead of $\mathrm{Pois}\,(N_{\mathrm{obs}}|\nu)$, the following expression

$$
\begin{aligned}
-\Delta \ln\left(\mathrm{Pois}\,(N_{\mathrm{obs}}|\nu)\right) &= -\ln\left[\frac{\mathrm{Pois}\,(N_{\mathrm{obs}}|\nu)}{\mathrm{Pois}\,(N_{\mathrm{obs}}|\nu_{\mathrm{max}})}\right], \\
&= -\left[\ln(\mathrm{Pois}\,(N_{\mathrm{obs}}|\nu)) - \ln(\mathrm{Pois}\,(N_{\mathrm{obs}}|\nu_{\mathrm{max}}))\right], \qquad (2.18)
\end{aligned}
$$

is considered. This form takes the difference to the best estimate of the expectation value, ν_{max}, into account, and has the advantage of having a minimum at 0 for ν_{max}. In Figure 2.6(b), the dependence of $-\Delta \ln\left(\mathrm{Pois}\,(N_{\mathrm{obs}}|\nu)\right)$ on ν is shown, which is approximately quadratic. It is also possible to determine the statistical significance with which the current observation deviates from a given theory based on the value $-\Delta \ln\left(\mathrm{Pois}\,(N_{\mathrm{obs}}|\nu)\right)$ corresponding to the tested theory. Details of this relationship will be discussed in the following section. For now it is just noted, that the relation between the significance and $-\Delta \ln\left(\mathrm{Pois}\,(N_{\mathrm{obs}}|\nu)\right)$ can be written as

$$
-\Delta \ln\left(\mathrm{Pois}\,(N_{\mathrm{obs}}|\nu)\right) = \frac{1}{2} Z^2. \qquad (2.19)
$$

There are some conditions to the validity of this equation, which are further discussed in Section 2.2.2. In both diagrams in Figure 2.6, the 1 σ and 2 σ boundaries are indicated by horizontal lines. It can be seen that the same limits on ν can be inferred from the significance (a) as well as the difference to the best estimate (b).

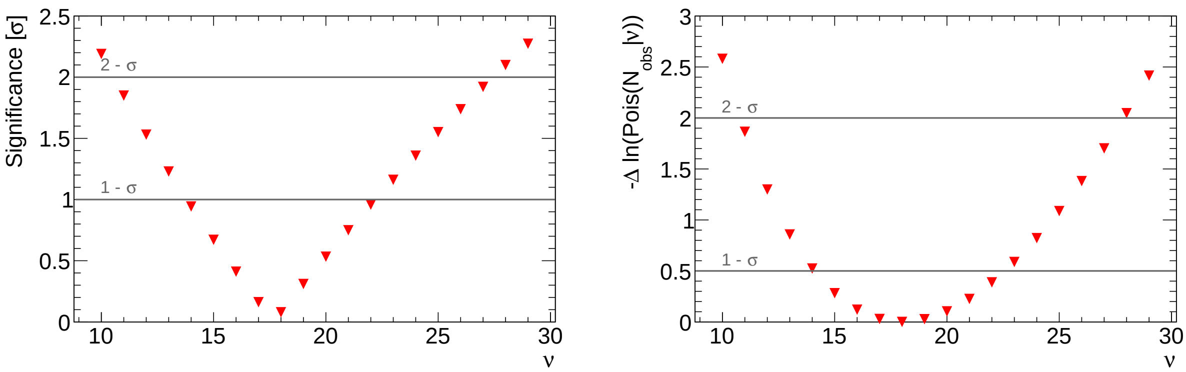

(a) Significance (b) Difference to best estimate

Figure 2.6: Significance (a) and $\frac{1}{2}Z^2$-deviation from the best estimate (b) for an observation of $N_{\mathrm{obs}} = 18$ events for different expectation values ν.

2.2.2 Maximum Likelihood Method

This section provides a brief introduction into statistics and the maximum likelihood method. For details, please refer to References [47] and [49]. The outcome of a physical measurement can be treated as a random variable $x \in \Omega$ where Ω is the sample space of the measurement, i. e. the set of all possible experimental outcomes. x is distributed according to a function $f(x)$ which is generally unknown. The probability for observing x in an interval $[x_1, x_2] \subseteq \Omega$ is then given by $\int_{x_1}^{x_2} f(x')\mathrm{d}x'$. Especially, $f(x)$ is constraint by the boundary condition, that the probability of measuring any value in Ω is 1

$$\int_\Omega f(x')dx' \;=\; 1.$$

Functions describing the distribution of random variables are called probability density functions (p.d.f.) [49]. The expectation or mean value μ of the random variable x is calculated using the p.d.f. $f(x)$ as

$$E[x] \;=\; \mu \;=\; \int_\Omega x \cdot f(x)\ \mathrm{d}x. \tag{2.20}$$

The spread of the distribution is characterized by its variance σ^2 given by

$$V[x] \;=\; \sigma^2 \;=\; \int_\Omega (x-\mu)^2 f(x)\ \mathrm{d}x, \tag{2.21}$$

$$\;=\; E[(x-\mu)^2],$$

$$\;=\; E[x^2] \;-\; \mu^2. \tag{2.22}$$

The square root of the variance is called standard deviation σ. The same definitions can be applied to calculate the expectation value or variance of any normalized function $g(x)$ by replacing x is $g(x)$. [47]

This situation can be generalized to a set of n random variables $\mathbf{X} = \{x_1, x_2, \ldots x_n\}$. For simplicity it is assumed that all x_i follow the same p.d.f. $f(x_i)$. The total p.d.f. for the set is then given by the product of all individual density functions

$$F(\mathbf{X}) \;=\; \prod_{i=1}^{n} f(x_i). \tag{2.23}$$

The density functions $f(x_i)$ are a priori unknown. To determine the properties of f, a set of m parameters $\boldsymbol{\theta} = \{\theta_1, \theta_2, \ldots \theta_m\}$ can be introduced. These parameters can be constrained from measurements of $\mathbf{X}$ and subsequently be used to infer the structure of f. Therefore, $f(x_i)$ will become $f(x_i|\boldsymbol{\theta})$, where x_i is the random variable and $\boldsymbol{\theta}$ are non-fixed parameters.

Once the measurement has been performed, the random variables $\mathbf{X}$ are replaced by the actual observed, and therefore fixed, values $\mathbf{X^0}$. The total probability density function $F(\mathbf{X^0}|\boldsymbol{\theta})$ is then no longer called a p.d.f. but likelihood $L(\mathbf{X^0}|\boldsymbol{\theta})$, since $\mathbf{X^0}$ is not a variable anymore. In some cases, there are external constraints C on the parameters $\boldsymbol{\theta}$ which will also be included in the likelihood:

$$L(\mathbf{X^0}|\boldsymbol{\theta}) \sim F(\mathbf{X^0}|\boldsymbol{\theta}) \cdot C(\boldsymbol{\theta}). \tag{2.24}$$

Depending on the functional form of L, the likelihood is not necessarily normalized to unity. This, however, does not impact the constraining power it has on $\boldsymbol{\theta}$. In order to determine the true value of $\boldsymbol{\theta}$, one defines a function $\hat{\boldsymbol{\theta}}(\boldsymbol{X}^0)$ of the observed values $\boldsymbol{X}^0$, which yields an estimate of $\boldsymbol{\theta}$. Such functions are called estimators. In general, the $\hat{\boldsymbol{\theta}}(\boldsymbol{X}^0)$ are determined using optimization algorithms. Analogous to the expectation value of a random variable in Eq. (2.20) the expectation value of an estimator is defined as

$$E[\hat{\boldsymbol{\theta}}] \;=\; \int_\Omega \hat{\boldsymbol{\theta}}(x) f(x|\boldsymbol{\theta})\ \mathrm{d}x, \tag{2.25}$$

$$\;=\; \int_{\Omega_{\hat{\theta}}} \hat{\boldsymbol{\theta}}(x) q(\hat{\boldsymbol{\theta}}|\boldsymbol{\theta})\ \mathrm{d}\hat{\boldsymbol{\theta}}. \tag{2.26}$$

Eq. (2.26) is an alternative way of describing the expectation value, where $q(\hat{\boldsymbol{\theta}}|\boldsymbol{\theta})$ is the p.d.f. of $\hat{\boldsymbol{\theta}}$ given a true value $\boldsymbol{\theta}$, and $\Omega_{\hat{\theta}}$ is the sample space of $\hat{\boldsymbol{\theta}}$. The variance $V[\hat{\boldsymbol{\theta}}]$ can be written as

$$V[\hat{\boldsymbol{\theta}}] \;=\; \widehat{\sigma^2_{\hat{\boldsymbol{\theta}}}} \;=\; \int_{\Omega_{\hat{\theta}}} \left(\hat{\boldsymbol{\theta}} - E[\hat{\boldsymbol{\theta}}]\right)^2 q(\hat{\boldsymbol{\theta}}|\boldsymbol{\theta})\, \mathrm{d}\hat{\boldsymbol{\theta}}. \tag{2.27}$$

Two important properties of an estimator are its consistency and bias. An estimator is called consistent, if the best estimate based on N measurements $\hat{\boldsymbol{\theta}}_N$ converges to the true value $\boldsymbol{\theta}$ as N goes to infinity in the sense of probability [49]

$$\forall \varepsilon > 0: \lim_{N\to\infty} P\left(|\hat{\boldsymbol{\theta}}_N - \boldsymbol{\theta}| \;>\; \varepsilon\right) \;=\; 0, \tag{2.28}$$

where $P\left(|\hat{\boldsymbol{\theta}}_N - \boldsymbol{\theta}| \;>\; \varepsilon\right)$ is defined as the probability that $|\hat{\boldsymbol{\theta}}_N - \boldsymbol{\theta}|$ is larger than ε. The bias b of an estimator is defined as the difference of the expectation value and the true value of $\boldsymbol{\theta}$,

$$b(\hat{\boldsymbol{\theta}}) \;=\; E[\hat{\boldsymbol{\theta}}] - \boldsymbol{\theta} \;=\; E[\hat{\boldsymbol{\theta}} - \boldsymbol{\theta}]. \tag{2.29}$$

Going back to the likelihood function of $L(\mathbf{X^0}|\boldsymbol{\theta})$, one is interested in the set of parameters $\hat{\boldsymbol{\theta}}$ that is maximizing the likelihood for observing $\mathbf{X^0}$. For numerical reasons, the optimization is performed on $-\ln L(\mathbf{X^0}|\boldsymbol{\theta})$ rather than $L(\mathbf{X^0}|\boldsymbol{\theta})$, thus becoming a minimization problem (cf. Eq. (2.18)).

Assuming that the likelihood $L(x|\mu)$ with a single parameter μ and measurement x is given by a Gaussian distribution (see Eq. (2.16)), the logarithm of the likelihood is a quadratic function of the form:

$$-\ln L(x|\mu) \;=\; -\ln\left(\frac{1}{\sqrt{2\pi\sigma^2}}\right) \;+\; \frac{(x-\mu)^2}{2\sigma^2},$$

where the origin can be shifted, such that the minimum is reached at $-\ln L = 0$ by subtracting the first, constant term. Here it is straight forward to determine the mapping of $-\ln L$ and the statistical significance with which the observation x would deviate from the true value μ

$$\begin{array}{lll} 1\ \sigma: & x = \mu \pm \sigma & \Rightarrow \quad -\ln L = 0.5 \\ 2\ \sigma: & x = \mu \pm 2\sigma & \Rightarrow \quad -\ln L = 2 \end{array}$$

Therefore, in case of a Gaussian likelihood function the uncertainty on the parameter μ and thereby also the significance can be read directly off the likelihood function.

If the likelihood is not Gaussian, the likelihood profile[1] is not exactly quadratic, but can be approximated by a Taylor expansion with respect to the parameter θ_i that the uncertainty should be evaluated for,

$$\ln L(\boldsymbol{X}^0|\theta_i) \;=\; \ln L(\boldsymbol{X}^0|\hat{\boldsymbol{\theta}}) \;+\; \left[\frac{\partial \ln L}{\partial \theta_i}\right]_{\theta_i=\hat{\theta}_i} \Delta\theta_i \;+\; \frac{1}{2!}\left[\frac{\partial^2 \ln L}{\partial \theta_i^2}\right]_{\theta_i=\hat{\theta}_i} (\Delta\theta_i)^2 \;+\; \mathcal{O}\left((\Delta\theta_i)^3\right), \tag{2.30}$$

where $\Delta\theta_i \;=\; \theta_i - \hat{\theta}_i$. The first summand is the constant, maximized likelihood value, denoted as $\ln L_{\max} = \ln L(\boldsymbol{X}^0|\hat{\boldsymbol{\theta}})$. In the second summand, the first derivative of the likelihood function vanishes per construction, since the likelihood is evaluated at its maximum. In order to determine the second derivative, the Rao-Cramér-Frechet (RCF) inequality can be applied. Using the bias $b(\hat{\theta}_i)$ for parameter θ_i defined in Eq. (2.29), the lower bound on its variance $V[\hat{\theta}_i]$ can be written as [47]

$$V[\hat{\theta}_i] \;=\; \widehat{\sigma^2_{\hat{\theta}_i}} \;\geq\; \frac{\left[1 - \dfrac{\mathrm{d}b(\hat{\theta}_i)}{\mathrm{d}\theta_i}\right]^2}{-E\left[\dfrac{\partial^2 \ln L(\boldsymbol{X}^0|\boldsymbol{\theta})}{\partial \theta_i^2}\right]}. \tag{2.31}$$

[1]A likelihood profile is a scan of the likelihood function $L(\boldsymbol{X}^0|\boldsymbol{\theta})$ for one parameter θ_i while fixing all other parameters to some value. Remember that the values of $\boldsymbol{X}^0$ are fixed by the measurement.

This relation is valid under the conditions that

a) the sample space Ω of $\boldsymbol{X}$ is independent of the parameters $\boldsymbol{\theta}$, and

b) the differentiation $\partial/\partial\theta_i$ and the integration over $\mathrm{d}x_1\,\mathrm{d}x_2\ldots\,\mathrm{d}x_n$, which is necessary for the calculation of the expectation value in the denominator, commute.

In case of equality the estimator $\hat{\theta}_i$ is said to be efficient. The equality holds for instance when the p.d.f. $q(\hat{\theta}|\theta)$ and $q(\hat{\boldsymbol{\theta}}|\boldsymbol{\theta})$ follow a Gaussian or χ^2 distribution, respectively for the multidimensional case of $\boldsymbol{\theta}$. Details are given in Reference [47].

The expectation value in Eq. (2.31) is calculated using an integration over $\mathrm{d}x_1\,\mathrm{d}x_2\ldots\,\mathrm{d}x_n$. Using condition b) and the knowledge that $L(\boldsymbol{X}^0|\boldsymbol{\theta})$ is no longer dependent on $\boldsymbol{X}$, the expectation value and can be rewritten as:

$$\begin{aligned}
-E\left[\frac{\partial^2 \ln L(\boldsymbol{X}^0|\boldsymbol{\theta})}{\partial\theta_i^2}\right] &= -\int \frac{\partial^2 \ln L(\boldsymbol{X}^0|\boldsymbol{\theta})}{\partial\theta_i^2}\,F(\boldsymbol{X})\,\mathrm{d}x_1\,\mathrm{d}x_2\ldots\,\mathrm{d}x_n \\
&\overset{\text{b)}}{=} -\frac{\partial^2 \ln L(\boldsymbol{X}^0|\boldsymbol{\theta})}{\partial\theta_i^2}\,\underbrace{\int F(\boldsymbol{X})\,\mathrm{d}x_1\,\mathrm{d}x_2\ldots\,\mathrm{d}x_n}_{=1} \\
&= -\frac{\partial^2 \ln L(\boldsymbol{X}^0|\boldsymbol{\theta})}{\partial\theta_i^2}. \qquad (2.32)
\end{aligned}$$

By substituting the expectation value in the definition of the R.C.F. bound (2.31) using (2.32) and assuming $\hat{\theta}_i$ to be an unbiased estimator, the second derivative in the Taylor expansion of the likelihood can be estimated using:

$$\frac{\partial^2 \ln L(\boldsymbol{X}^0|\boldsymbol{\theta})}{\partial\theta_i^2} \geq \frac{1}{-\widehat{\sigma^2_{\hat{\theta}_i}}}. \qquad (2.33)$$

Inserting this expression in Eq. (2.30), and assuming $\boldsymbol{\theta}$ to be χ^2 distributed yields:

$$\ln L(\boldsymbol{X}^0|\theta_i) = \ln L_{\max} - \frac{1}{2}\frac{(\theta_i - \hat{\theta}_i)^2}{\widehat{\sigma^2_{\hat{\theta}_i}}}.$$

Now the likelihood value at $\hat{\theta}_i + Z\cdot\widehat{\sigma_{\hat{\theta}_i}}$, i. e. by shifting θ_i by Z standard deviations from its optimal value, is given as:

$$\begin{aligned}
\ln L(\boldsymbol{X}^0|\hat{\theta}_i + Z\cdot\widehat{\sigma_{\hat{\theta}_i}}) &= \ln L_{\max} - \frac{Z^2}{2}, \\
\Rightarrow Z &= \sqrt{-2\cdot\left(\ln L(\boldsymbol{X}^0|\hat{\theta}_i + Z\widehat{\sigma_{\hat{\theta}_i}}) - \ln L_{\max}\right)}, \\
Z &= \sqrt{-2\cdot\Delta\ln L}. \qquad (2.34)
\end{aligned}$$

This formula is valid when the likelihood profile is approximately quadratic, i. e. when higher order terms in the Taylor expansion are negligible. This is the case when the likelihood follows either Gaussian or χ^2 distribution. However, in the example in Section 2.2.1, this expression was used as well, even though the likelihood function was a Poissonian and the likelihood profile over ν non-parabolic (see Fig. 2.6(b)). Good agreement between the graphical method using Eq. (2.34) and the method based on p-values was found.

The treatment of non-parabolic likelihood is discussed in [47] Chapter 9.3.2. It is stated that for any non-parabolic likelihood function $\ln L$ it is possible to find a transformation function T such that $T(\ln L)$ is quadratic and (2.34) applies. Since maximum likelihood estimates are invariant, all conclusions obtained for $T(\ln L)$ also hold for $\ln L$.

2.2.3 The Likelihood Template and Asimov Dataset

The appropriate choice of the likelihood function is highly dependent on the intended use case. In the case of particle interactions or decays, usually a Poissonian distribution $\text{Pois}\,(N|\nu)$ (see Eq. (2.12)) is assumed. In the current case, the total number of expected events ν is the sum of the number of signal ν_{S} and background events ν_{B}, where ν_{B} is well known. The number of signal events, however, is variable such that it can be adapted to the measurement. The total number of events with variable signal contribution can be parametrized using the signal strength or parameter of interest μ

$$\nu \;=\; \mu \cdot \nu_{\text{S}} \;+\; \nu_{\text{B}}. \tag{2.35}$$

By varying the signal strength parameter μ, the expectation value of the Poissonian is shifted, generating different underlying hypotheses. Setting μ to zero corresponds to a model, where no signal events are expected, i. e. the background-only theory. In this work, $\mu = 1$ corresponds to the standard model prediction of $W^{\pm}W^{\pm}$ scattering of the order $\mathcal{O}(\alpha_{\text{ew}}^6)$, i. e. the nominal theory. In physics measurements, μ is generally constrained to positive values, since an additional signal is not expected to have a decreasing effect on the expected number of events.

However, Eq. (2.35) only provides a very simplistic description of the expectation value. A more realistic formulation is used in the `HistFactory` package [50], which is used to for the statistical analysis in the course of this thesis. The expectation value in `HistFactory` also accounts for cases, where not only a single number of events is measured, but the measurement is divided into sub-measurements according to:

- Different analysis channels e. g. based on lepton charge or flavor, or different kinematic regions, and
- Several bins in a variable providing high separation power between signal and background events.

Assuming that there is a histogram σ_{csb} containing the nominal prediction for a specific process s differentially as a function of the chosen variable, the expected number of events per channel c and bin b is then written as [50]

$$\nu_{cb}(\phi_p, \alpha_p, \gamma_{cb}) = \gamma_{cb} \sum_{s \in \text{samples}} \eta_{cs}(\boldsymbol{\alpha}) \left[\phi_{cs}(\boldsymbol{\alpha}) \cdot \lambda \cdot \sigma_{csb}(\boldsymbol{\alpha})\right], \tag{2.36}$$

where s and p count all processes taken into account in the analysis as well as all parameters, respectively. In the simplest case there would be only the signal and background histograms, though it is often necessary to provide separated input for different background processes. $\boldsymbol{\alpha} = \{\alpha_1, \dots \alpha_m\}$ is the set of nuisance parameters, which parametrize the effect of external sources of uncertainty on the measurement. This can e. g. be the calibration of detector components or the identification efficiency for some particle. A complete set of sources of systematic uncertainties taken into account in this analysis is given in Section 8.

Equation 2.36 states that the expected number of events per channel c and bin b can be obtained by weighting the prediction given in the input histogram σ_{csb} by a given luminosity nuisance parameter λ and the product ϕ_{cs} of normalization factors $\phi_{cs,p}$ that might be given per channel and sample s:

$$\phi_{cs}(\boldsymbol{\alpha}) \;=\; \prod_p \phi_{cs,p}(\alpha_p).$$

These normalization factors $\phi_{cs,p}$ may depend on nuisance parameters α_p. In this generalized notation, the parameter of interest μ (see Eq. (2.35)) is part of the set $\{\phi_{cs,p}\}$ given for the signal process. Additionally, systematic uncertainties affecting the differential distribution of events are considered. Therefore, the input histogram σ_{csb} may depend on additional nuisance parameters $\boldsymbol{\alpha}$ as well. Finally, normalization uncertainties $\eta_{cs}(\boldsymbol{\alpha})$ and bin-by-bin scale factors γ_{cb} are included. The latter are used to parametrize systematic uncertainties due to statistical fluctuations in simulated data. It is a matter of definition, that it is necessary to distinguish between normalization parameters and normalization uncertainties. They differ by their probability density function. Parameters are distributed according to a box distribution, such that all values in a given interval are equally probable. Normalization uncertainties are constraint by a non-uniform, usually Gaussian density functions.

All nuisance parameters $\boldsymbol{\alpha}$ are constrained by auxiliary measurements, and are defined based on a Gaussian density function. The auxiliary measurement can for instance determine the normalization of a specific background process in a control region. Bin-by-bin scale factors γ_{cb} on the other hand follow a Poissonian density. These are calculated using the Beeston-Barlow method of estimating statistical uncertainties in simulated data. The original approach proposed in Reference [51] involves one nuisance parameter per sample in each bin and channel, and was shown to be unstable in some cases, as well as very computationally expensive [52]. Therefore, a simplified version is implemented in the `HistFactory` package. Here, only one nuisance parameter is applied per channel and bin, modeling the relative statistical uncertainty on the sum of all contributions in that bin.

The binned likelihood function is given as the product of the total Poissonian probability combining all channels and bins and all constraining p.d.f. for nuisance parameters,

$$L(\mu|\boldsymbol{\theta}) = \prod_{c\in\text{channels}} \prod_{b\in\text{bins}} \text{Pois}(n_{cb}|\nu_{cb}(\mu,\phi_p,\alpha_p,\gamma_{cb})) \cdot \text{G}(\mathcal{L}_0|\lambda,\Delta_{\mathcal{L}}) \cdot \prod_{p\in\mathbb{S}+\boldsymbol{\Gamma}} f_p(a_p|\alpha_p). \tag{2.37}$$

The parameters entering here are summarized in Table 2.3. The measured and expected number of events in bin b per channel c are denoted as n_{cb}, and $\nu_{cb}(\mu,\phi_p,\alpha_p,\gamma_{cb})$, respectively. The definition of $\nu_{cb}(\mu,\phi_p,\alpha_p,\gamma_{cb})$ is given in Eq. (2.36). The function f_p refers to the p.d.f. for an auxiliary measurement. In most cases f_p takes a Gaussian form. α_p denote nuisance parameters with external constraints, constrained by an auxiliary measurements a_p with p.d.f. f_p. The set of all α_p and γ_{cb} are represented by $\mathbb{S}$, and $\boldsymbol{\Gamma}$, respectively. The ATLAS luminosity and its uncertainty are denoted as $\mathcal{L}_0$, and $\Delta_{\mathcal{L}}$. The nuisance parameter λ is associated to the luminosity measurement. Finally, $\boldsymbol{\theta}$ represents the set of all nuisance parameters $\{\boldsymbol{\alpha},\phi_{cs},\eta_{cs},\gamma_{cb},\lambda\}$. Details on the implementation can be found in the `HistFactory` package [50].

Parameter	Definition
n_{cb}	Measured number of events in bin b and channel c
$\nu_{cb}(\mu)$	Expected number of events in bin b and channel c
f_p	p.d.f. of an auxiliary measurement
a_p	Auxiliary measurements to constrain nuisance parameters
α_p	Nuisance parameters with external constraints
γ_{cb}	Bin-by-bin scale factors used for systematic uncertainties associated to background precision (shared for all samples in the same channel and bin),
$\mathbb{S},\boldsymbol{\Gamma}$	Sets α_p, and γ_{cb}
$\mathcal{L}_0$, $\Delta_{\mathcal{L}}$	ATLAS luminosity and uncertainty
λ	Luminosity nuisance parameter
$\boldsymbol{\theta}$	Set of all nuisance parameters $\{\boldsymbol{\alpha},\phi_{cs},\eta_{cs},\gamma_{cb},\lambda\}$

Table 2.3: Definition of parameters entering the likelihood function in Eq. (2.37).

After constructing the likelihood function Eq. (2.37), the significance can e. g. be calculated using Eq. (2.34). In practice, the statistical significance needs to be calculated for two separate datasets, one of them being the set of observed data. In the following, this value is referred to as *observed* *significance*. On the other hand, it is also interesting to calculate the *expected significance* for a simulated dataset, that corresponds to the theoretical prediction for the signal and background processes. The optimization of the event selection and the fitting procedure are usually blinded, i. e. performed without observed data in order to avoid optimizing on statistical fluctuations in the observed data set [53]. The expected significance is particularly important, as it is used as a figure of merit in these optimizations.

For calculating the expected significance, an Asimov data set [54] is used. The Asimov data set A is defined such that in each bin b and channel c, the measured number of events n^A_{cb} equals the expected number $\nu_{cb}(\mu)$. To calculate the expected significance, an Asimov data set generated for $\mu = 1$, i. e. corresponding to the Standard model signal prediction is generated.

2.2.4 Discovery Test Statistic

Any function of a random variable x, is called a statistic. A statistic used in hypothesis testing is called test statistic. Therefore, also the likelihood given in Eq. (2.37) is a test statistic. To determine the agreement of measured data and background-only hypothesis, the profile likelihood ratio is used

$$\lambda(\mu) \; = \; \frac{L(\mu, \hat{\hat{\boldsymbol{\theta}}})}{L(\hat{\mu}, \hat{\boldsymbol{\theta}})}, \tag{2.38}$$

where $\hat{\mu}$ and $\hat{\boldsymbol{\theta}}$ are best estimators for the parameter of interest μ and all nuisance parameters $\boldsymbol{\theta}$, and $\hat{\hat{\boldsymbol{\theta}}}$ is the conditional best estimator for a given value of μ. Consequently, $L(\mu, \hat{\hat{\boldsymbol{\theta}}})$ is the maximum likelihood value at a given μ, and $L(\hat{\mu}, \hat{\theta})$ is likelihood value at the optimum. The agreement with the null hypothesis can then be evaluated by setting μ to zero, i. e. using the test statistic

$$q \; = \; \lambda(0). \tag{2.39}$$

Equation (2.38), however, does not yet represent physical boundaries, such as negative values of μ. Therefore, for the discovery of an additional signal, the test statistic [54]

$$q_0 \; = \; \begin{cases} -2 \ln \lambda(0) & \text{if} \;\; \hat{\mu} \; \geq \; 0, \\ 0 & \text{if} \;\; \hat{\mu} \; < \; 0, \end{cases} \tag{2.40}$$

is defined. The p.d.f. $f(q_0|\mu')$ of the test statistic q_0 given a true value of $\mu = \mu'$ is generally unknown[1]. Yet, in the asymptotic case, i. e. in the limit of an infinite number of measurements, it can be shown (cf. [47] Chapter 10.5) that test statistics of the form of Eq. (2.39) follow a χ^2 distribution. In the special case of the test statistic q_0, an additional delta function is introduced, caused by all values, where $\hat{\mu}$ would have been negative [54]

$$f(q_0|\mu' = 0) \; \sim \; \frac{1}{2}\delta(q_0) + \frac{1}{2}\frac{1}{\sqrt{2\pi}}\frac{1}{\sqrt{q_0}}e^{-q_0/2}. \tag{2.41}$$

When calculating the integral $\int f(q_0|\mu' = 0)\, \mathrm{d}q_0$, it is seen clearly, that one half of all possible q_0 where pulled to zero to avoid unphysical, negative signal strengths.

The p.d.f. given in Eq. (2.40) is used to calculate the statistical significance, applying the procedure described in Section 2.2.1. If q_0 indeed follows a χ^2 distribution, the significances calculated using the p-value and the graphical method (see Section 2.2.2) are identical. If p.d.f. of q_0 has some other shape, the graphical method still yields the correct result, but will differ from the asymptotic p-value. In that case, the underlying p.d.f. of q_0 has to be determined by generating a set of pseudo experiments.

[1] It can, however, be determined to some degree using Monte-Carlo techniques.

3 Experiment

The following sections will give a short overview of the experimental setup, featuring the particle accelerator LHC and the ATLAS detector. Additionally, details on the observed and simulated data used throughout this thesis will be given.

3.1 The LHC

The Large Hadron Collider (LHC) is a particle collider able to accelerate protons as well as heavy ions. It is located at the European Organization for Nuclear Research (CERN) near Geneva in the tunnel that formerly accommodated the Large Electron-Positron Collider (LEP). The proton or heavy-ion beams are collided at four interaction points. At each interaction point a detector is installed. Of the four detectors, two are designed to analyze heavy ion collisions. The remaining two, ATLAS and CMS (Compact Muon Solenoid) are general purpose detectors. The LHC has a design luminosity of $20 \cdot 10^{33}\,\mathrm{cm}^{-2}\mathrm{s}^{-1}$, aiming collide bunches of up to 10^{11} protons at a center-of-mass energy of 14 TeV with a bunch spacing of 25 ns.

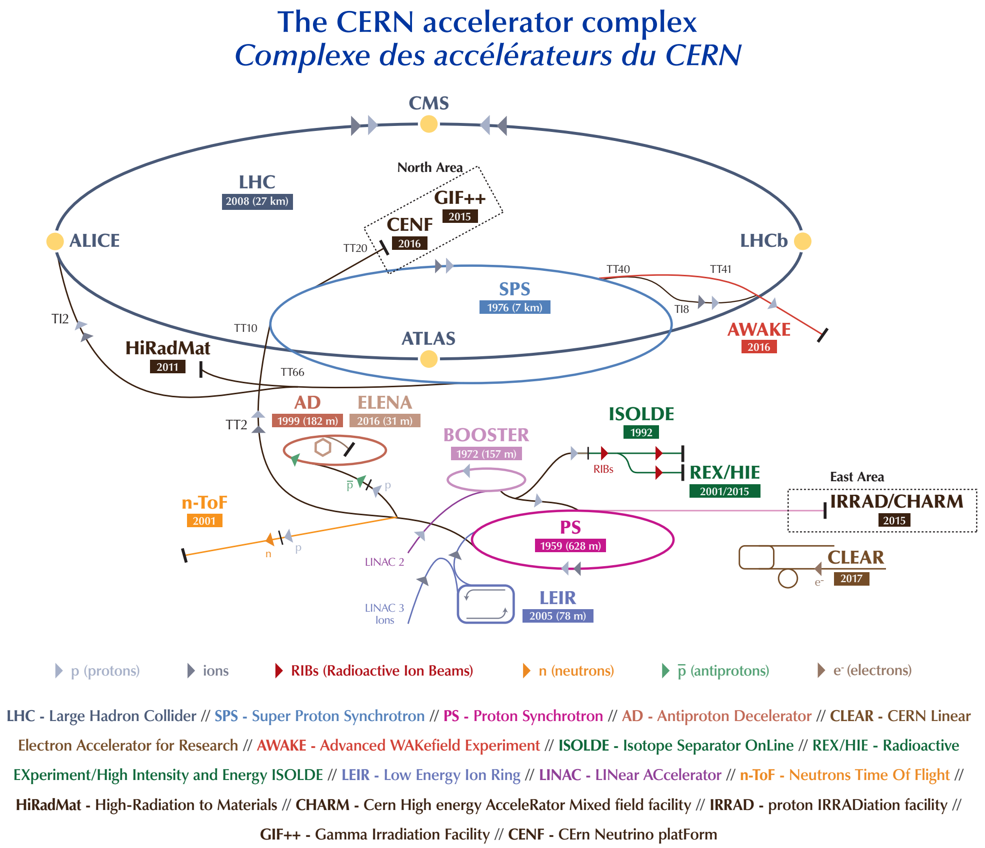

Figure 3.1: The LHC is the final ring (dark blue line) in a complex chain of particle accelerators. The smaller machines are used in a chain to pre-accelerate particles and provide beams to a set of smaller experiments. Figure taken from Ref. [55].

These energies are not reached solely by the LHC, but heavy ions and protons are pre-accelerated in a series of other machines. This process is visualized in Figure 3.1 [55]. Initiating in a bottle of hydrogen gas, the proton beam is generated by ionizing the hydrogen atoms and accelerating the protons with Linac 2 (purple) to an energy of 50 MeV. It is then consecutively injected into the Booster (lilac), Proton Synchrotron (PS, magenta) and Super Proton Synchrotron (SPS, light blue), where it reaches energies of 1.4 GeV, 25 GeV and 450 GeV, respectively. From the SPS, the proton beams are inserted into the LHC (dark blue), where they are accelerated to their final energies [56].

First beams were circulated in September 2008, but the machine suffered a malfunction, during which several magnets were damaged. In November 2009, the repairs were finished and beams were circulating again; followed by fist collisions in December 2009. In 2010 and 2011, the beams were accelerated to an energy of 3.5 TeV, which was increased to 4 TeV in 2012. In February 2013 the machine entered a first long shutdown (Long shutdown 1), to allow for technical updates to the pre-accelerators, the LHC and also the detectors [57]. In 2015, the LHC started to deliver physics data again. The beam energy was increased to 6.5 TeV, yielding a center-of-mass energy of 13 TeV. In order to test the updated components, the instantaneous luminosity was increased but slowly. The peak values amounted to $5.0 \cdot 10^{33}\,\mathrm{cm}^{-2}\mathrm{s}^{-1}$ and $13.8 \cdot 10^{33}\,\mathrm{cm}^{-2}\mathrm{s}^{-1}$ in 2015 and 2016 respectively. This also had an effect on the number of interactions per bunch crossing. The average was 13.7 (2015) and 24.9 (2016) interactions per bunch crossing. This thesis is based on proton-proton collison data from 2015 and 2016 recorded by the ATLAS detector. In total, $3.2\,\mathrm{fb}^{-1}$ and $35.6\,\mathrm{fb}^{-1}$ of data was recorded in 2015 and 2016, respectively, which results in combined a dataset of $36.1\,\mathrm{fb}^{-1}$ to be used in physics analyses [58].

3.2 The ATLAS Detector

The ATLAS detector is situated at interaction point 1 of the LHC. It has a cylindrical shape and is therefore described by a right-handed, cylindrical coordinate system, originating in the nominal interaction point. The x-axis points towards the center of the LHC, while the y-axis points upwards and the z axis is meeting the beamline tangentially. The angular coordinates ϕ and θ are measured as the angles in the $x - y$ plane and $y - z$ plane, respectively. As θ is not invariant under Lorentz transformation, in most cases the pseudo-rapidity η is used instead. For massless particles, the pseudo-rapidity can be derived from the rapidity Y

$$Y \;=\; \frac{1}{2}\ln\left(\frac{E+p_z}{E-p_z}\right),$$

where E is the energy and p_z the longitudinal momentum. For massless particles or in the relativistic limit $p \approx E \gg m$, Y converges to η and takes the form

$$Y \;\xrightarrow[\beta\to 1]{m\to 0}\; \eta \;=\; -\ln\left(\tan\frac{\theta}{2}\right).$$

The angular separation $\Delta R_{k,l}$ between a pair of measured objects k and l is calculated as

$$\Delta R_{k,l} \;=\; \sqrt{(\Delta\phi_{k,l})^2 \;+\; (\Delta\eta_{k,l})^2},$$

where $\Delta\phi_{k,l}$ and $\Delta\eta_{k,l}$ are the distances between k and l in azimuth and rapidity plane, respectively.

In order to provide optimal detection efficiency for the various kinds of particles and bound states that can be produced in proton-proton collisions, particle detectors are typically build in a layered structure. Each layer is adjusted to the kind of particle it is aimed to detect and measure. Following this general concept, the ATLAS detector is composed of four main elements:

Inner Detector: providing position and momentum measurement of charged particles, the

Electromagnetic calorimeter: measuring energy deposition of electrons and photons, the

Hadronic calorimeter: measuring energy deposition of hadronic particles, and the

Muon spectrometer: providing position and momentum measurement of muons.

In the following sections, the main technical characteristics of these components will be discussed. For a detailed description see [59] and [60]. A schematic view of the ATLAS detector is shown in Figure 3.2.

3.2.1 Inner Detector

The Inner Detector (ID) is the innermost part of the ATLAS detector, and is aimed to provide high-resolution position and transverse momentum measurement of charged particles with transverse momenta down to a threshold of 0.5 GeV. It has a length of 3.5 m, and a radius of 1.1 m. It is immersed in the central solenoid, which generates an axial magnetic field of approximately 2 T. The ID is built of independent tracking detectors, which are arranged in separate layers. Each tracking detector consists of a barrel and two end-cap regions. The barrel region of the ATLAS inner detector is shown schematically in Figure 3.3. The ID is divided into the

Pixel detector: The pixel detector originally consisted of 3 layers of semiconductor sensors. These are arranged on concentric cylinders around the beam axis and on disks perpendicular to the beam axis in the barrel and end-cap region, respectively. In the barrel and end-cap regions, it provides a resolution of 10 µm in $R - \phi$ plain and 115 µm along the z and R axis, respectively, while covering a pseudo-rapidity range of $|\eta| \leq 2.5$. Due to radiation damage, the pixel detector is suffering from a loss of hits. In order to mitigate this effect, as well as to improve track reconstruction and identification of jets originating from b-quarks, an additional pixel layer (Insertable B-Layer - IBL) was inserted closer to the beam line during Long shutdown 1 [59].

Silicon microstrip tracker: Like the pixel detector, the silicon microstrip tracker (SCT) is composed of semiconductor sensors, and covers the same η range. The resolution amounts to 17 µm in $R - \phi$ plain (barrel and end-cap) and 580 µm along the z (barrel) and R (end-cap) axis.

Transition radiation tracker: The transition radiation tracker (TRT) consists of drift tubes which are oriented parallel to the beam axis in the barrel region and arranged radially, in wheels in the end-caps. The drift tubes are equipped with a gold-plated tungsten wire anode, and filled with an active gas. An electron passing these tubes will create transition radiation which can then be detected. Thus, the TRT can provide electron identification, separating them from charged pions, for a pseudo-rapidity range of $|\eta| \leq 2.0$. In the beginning of Run 1, a Xe-based gas mixture was used. However, in the 2012 data taking period several leaks developed in gas pipes, some of which were inaccessible and could therefore not be repaired. As a consequence, some parts of the TRT are now filled with a less costly Ar-based gas mixture, which introduced a loss of sensitivity. Nevertheless, improvements in the reconstruction software mitigated this effect [61].

3.2.2 Calorimeters

The ATLAS calorimeters are designed to contain all electromagnetic and hadronic radiation inside the calorimeter volume. This is especially important for an accurate measurement of missing transverse energy due to neutrinos and as not to impact the functionality of the muon spectrometer. The electromagnetic calorimeter has a thickness of more than 22 and 24 radiation lengths[1] in the barrel

[1] A radiation length is the distance needed for an electron to loose all but $1/e$ of its initial energy.

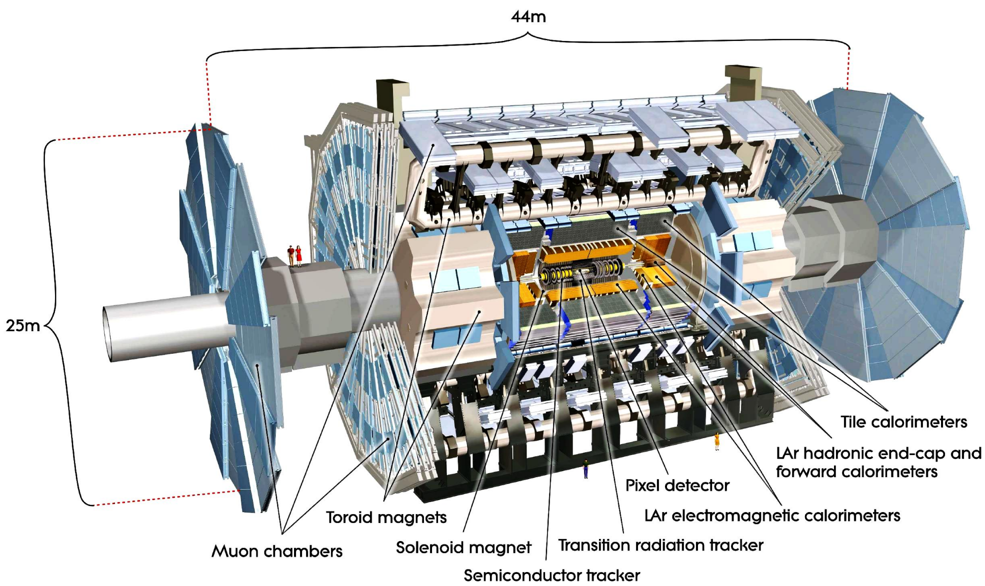

Figure 3.2: Cut-away view of the ATLAS-detector. Figure taken from Ref. [60].

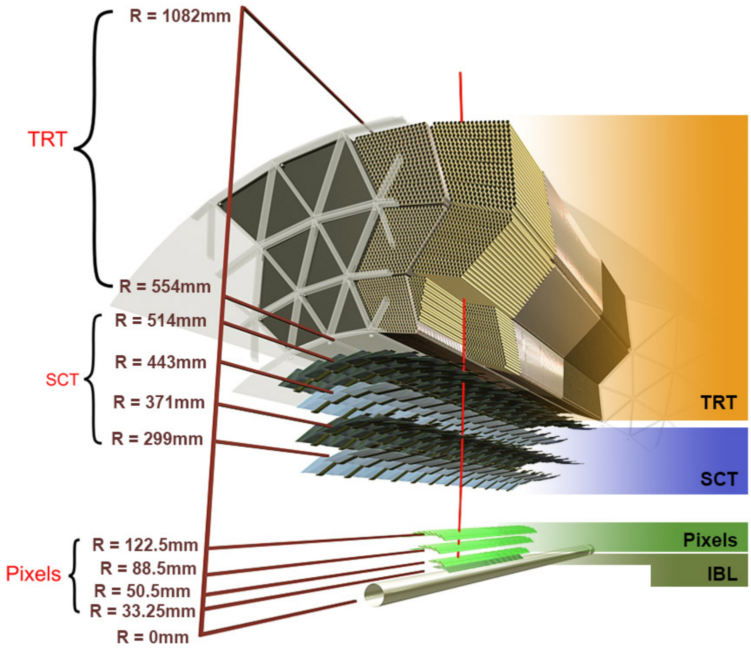

Figure 3.3: Cut-away view of the ATLAS Inner Detector. Figure taken from Ref. [62].

and end-caps, respectively. The total thickness of the hadronic calorimeter at $\eta = 0$ is approximately 11 interaction length[1], of which 9.7 interaction lengths are active material. In Figure 3.4, an overview of the ATLAS calorimeters, consisting of barrel, end-cap and forward regions is shown. The barrel and end-cap regions are separated into two calorimeters (electromagnetic and hadronic calorimeter) while the forward regions are covered by combined calorimeters. The η coverage of all calorimeters is summarized in Table 3.1.

Electromagnetic calorimeter: The electromagnetic calorimeter is designed to provide high-granularity measurement of electron and photon showers. In order to achieve complete coverage in ϕ, the absorbers and electrodes in the barrel and end-caps (EMEC) are built in an accordion-like structure. Absorbers are made of lead plates, which are reinforced by stainless-steel sheets on both sides. The electrodes are placed between two absorbers, with a drift gap of 2.1 mm in the barrel region. Each electrode consists of three copper sheets, separated by polyimide layers. The two outer sheets are at high-voltage potential (2000 V), while the signal is read from the inner layer via capacitive coupling. All copper sheets are segmented in η. The space between the absorbers is filled with liquid argon as active material, which is intrinsically radiation resistant.

The overall dimensions of the barrel calorimeter are 6.4 m in length, with inner and outer diameters of 2.8 m and 4 m, respectively. The barrel calorimeter is segmented in three layers and equipped with a pre-sampling layer in front of the actual calorimeter. The pre-sampler is used to correct for energy loss due to material in front of the calorimeter. Each end-cap is composed of an inner and an outer wheel. Each wheel is 63 cm thick, and has an inner and outer radius of 0.3 m and 2.1 m. The junction between both wheels is located at $|\eta| = 2.5$ and is 3 mm wide. It is mostly filled with low-density material, such that the impact on the energy is small. Due to the junction of the barrel and end-caps, the uncertainty on energy measurements in that region ($1.37 < |\eta| < 1.52$) is comparably large. Therefore, this region is usually excluded in analyses.

Hadronic calorimeter: The hadronic calorimeter is divided into the barrel, extended barrel, and end-cap regions, the η coverage is reported in Table 3.1. The hadronic end-cap calorimeters (HEC) are designed to overlap with the barrel and forward calorimeters, to reduce the drop of material density in the transition region.

The hadronic barrel and extended barrel, called Tile calorimeter, cover the rapidity region up to $|\eta| < 1.7$. Positioned directly behind the electromagnetic barrel, it has inner and outer radii of 2.28 m and 4.25 m, respectively. This corresponds to a total thickness of 9.7 interaction length at $\eta = 0$. The Tile calorimeter is segmented in three layers and consists of scintillator material interleaved with steel plate absorbers. Wavelength shifting fibers are connecting the scintillators with two photomultiplier tubes per module. The fibers are grouped such as to build three-dimensional calorimeter cells with a granularity of $\Delta\eta \times \Delta\phi = 0.1(0.2) \times 0.1$ in the first and second (third) layer.

In the HEC, liquid argon and copper are used as active and passive material. Instead of the accordion structure, a flat-plate design with a 8.5 mm liquid argon gap is chosen. Three electrodes divide the gaps into four drift zones. The lateral segmentation is determined by the middle, read-out electrode. For $|\eta| < 2.5$, each calorimeter cell has a size of $\Delta\eta \times \Delta\phi = 0.1 \times 0.1$. In the forward region, the cell size is increased to 0.2×0.2. The end-caps are housed in the same cryostats as the EMEC and forward calorimeters. Each end-cap consists of two separate wheels, which in turn are segmented in two layers. End-cap modules are wedge-shaped, with an inner and outer radius of 0.475 m and 2.03 m, respectively.

[1]An interaction length is the mean free path of a particle before inelastic scattering occurs.

Forward calorimeter: The forward calorimeter (FCal) completes the ATLAS calorimeter setup. The FCal front faces are located approximately 4.7 m from the nominal interaction point. In pseudo-rapidity, it extends from $|\eta| > 3.1$ to $|\eta| < 4.9$. The FCal consists of three modules per end-cap, reaching a total depth of about 10 interaction lengths. The first module is optimized for measuring electromagnetic showers with copper as absorber material. The second and third module are designed as hadronic calorimeters, equipped with tungsten absorbers. Tubes are drilled into the absorbers, oriented parallel to the beam axis. These are filled with liquid argon as active material and an electrode rod. This makes for comparably small LAr gaps with respect to the electromagnetic barrel. The design was chosen to reduce ion build-up due to the high particle flux. Behind the third FCal module, a shielding plug is installed to minimize punch-through into the muon system.

Detector Regions	Calorimeters	
	Electromagnetic	Hadronic
Barrel	$|\eta| < 1.475$	$|\eta| < 1.0$ $0.8 < |\eta| < 1.7$ (extended barrel)
End-cap	$1.374 < |\eta| < 2.5$ (outer wheel) $2.5 < |\eta| < 3.2$ (inner wheel)	$1.5 < |\eta| < 3.2$
Forward	$3.1 < |\eta| < 4.9$	

Table 3.1: Summary of pseudo-rapidity coverage of ATLAS calorimeters in different detector regions.

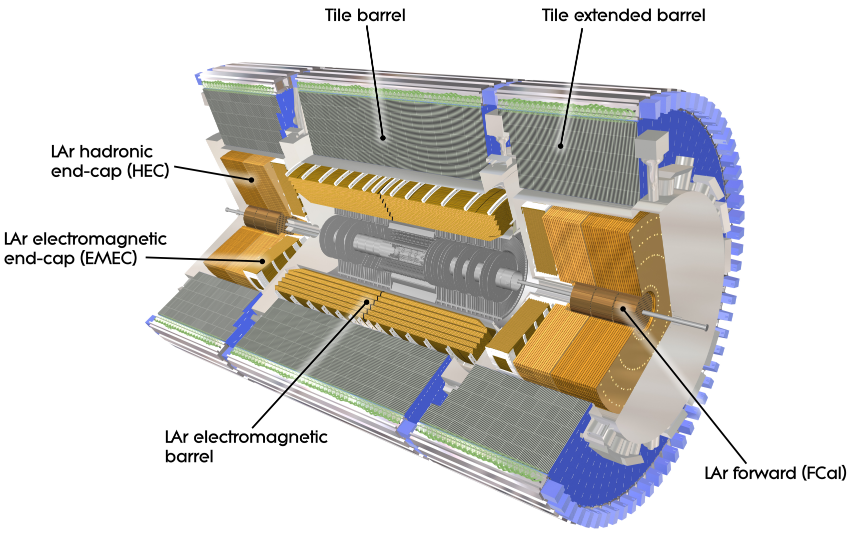

Figure 3.4: Cut-away view of the ATLAS calorimeters. Figure taken from Ref. [60].

3.2.3 Muon spectrometer

The muon spectrometer is the outermost part of the ATLAS detector, designed to provide muon identification and momentum measurement. The magnetic field necessary for the latter is generated by a barrel and two end-cap toroids, covering pseudo-rapidity regions of $|\eta| < 1.4$ and $1.6 < |\eta| < 2.7$, respectively. The magnetic field in the transition region from $1.4 < |\eta| < 1.6$ is a superposition of the barrel and end-cap fields. The generated field is predominantly orthogonal to the muon trajectories.

In the barrel region three layers of precision tracking chambers are installed parallel to the beam axis at radii of 5 m, 7.5 m and 10 m. The end-cap regions are covered by four wheels located at an absolute distance along the z axis of 7.4 m, 10.8 m, 14 m and 21.5 m from the interaction point. The pseudo-rapidity range up to $|\eta| = 2.0$ is equipped with Monitored Drift Tube chambers (MDT). In the region within $2.0 < |\eta| < 2.7$, Cathode Strip Chambers (CSC) are used, since these have a finer granularity and are better suited to cope with the higher particle flux.

In order to provide a stand-alone muon measurement, i. e. a measurement based on information gathered solely by the muon spectrometer without relying on the Inner Detector, trigger chambers are install up to $|\eta| = 2.4$. These chambers also offer a complementary measurement of the muon coordinates orthogonal to those determined by MDTs and CSCs. In the barrel region ($|\eta| < 1.05$), Resistive Plate Chambers (RPC) are used whereas the end caps covering the range $1.05 < |\eta| < 2.4$ are furnished with Thin Gap Chambers (TGC). This setup allows for momentum resolution in a stand-alone measurement of 10 % for 1 TeV tracks.

3.2.4 Trigger System

During Run 1 of the LHC, the bunch spacing was continuously decreased from 150 ns to 50 ns. In Run 2, the bunch spacing was set to the nominal value of 25 ns, corresponding to a frequency of 40 MHz. Due to this decrease, in combination with an increased instantaneous luminosity, the data rate increased by a factor of approximately five from Run 1 to Run 2. However, the final data rate cannot exceed 1 kHz due to data-storage constraints. In order to meet the new requirements, the trigger system was upgraded during Long shutdown 1. The initial ATLAS trigger system is described in Reference [60], while upgrades are discussed in Reference [63].

In a first step, the hard-ware based Level 1 (L1) trigger reduces the data rate from 40 MHz to roughly 100 kHz. For each event, it builds regions of interest (RoIs) with low-granularity calorimeter and muon chamber information. Upgrades to L1 involved replacing part of the hardware to reduce the false trigger rate, and raising the output rate from 75 kHz to 100 kHz. Furthermore, an additional sub-trigger (L1Topo) is introduced, which combines topological information from calorimeter and muon L1 triggers. This allows the calculation of event quantities such as invariant masses or angular separations. The final L1 trigger decision is made by the central trigger processor (CTP).

For all events passing L1, the information concerning the RoIs is forwarded to the high level trigger (HLT). The HLT provides a software-based decision, using the full granularity of detector information. The data rate is again reduced to a final value of approximately 1 kHz. The most notable upgrades with respect to Run 1 are the merging of the Level 2 and the Event Filter triggers into a single code base and computing cluster. This reduces overhead and allows for a more dynamic assignment of resources. The software itself has also been optimized for better agreement with the off-line selection algorithms. This significantly reduces the object scale factors (see Chapter 5) for some particles.

3.3 Simulated Data

Generally, simulated results corresponding to a specific theory are used for one of two objectives. On the one hand, well described processes are used to understand observations. This can for instance mean to derive information about possibly new contributions to measured data during a statistical analysis, or the improvement of analysis techniques by providing ground truth data to machine learning or other multivariate selection algorithms. On the other hand, measurements can be used to correct or tune the underlying model to match observed results. In particle physics, both goals are pursued. The process of generating simulated data can be roughly separated into two steps. For a given process, at first all the final state particles are generated. Subsequently, the detector response to these generated particles has to be inferred.

The simulation of proton-proton collision events is a challenging task, due to the high accuracy needed for data-simulation comparisons, and the wide energy range involved. The concept of factorization of a process into different regimes of momentum transfer has become indispensable. A detailed review of the various challenges in event generation is given in References [64] and [65].

A schematic view of the steps involved in the calculation of a simulated event is shown in Figure 3.5. In most cases, the starting point is the calculation of the matrix element in the desired phase space. This corresponds to the red parts in Figure 3.5. The matrix elements (ME) for the hard scattering can be calculated up to a fixed order in perturbation theory. Based on the parton density distribution of the proton, and the particle content of the desired final state, a probability density function for the momenta of all particles after the hard scattering is calculated. This p.d.f. is used to generate randomized values of the momenta for all outgoing particles in the event.

Quarks and gluons generated in the ME radiate gluons, which results in showers that would be observed as jets in the detector. These parton showers can be modeled in QCD. A parton shower program is used to model QCD bremsstrahlung for all incoming and outgoing[1] partons. In Figure 3.5, this is represented by blue lines.

At the point where the momentum transfer becomes low, and reaches the hadronization scale typically at energies at the order of a few GeV, the formation of hadrons takes place. Due to the large value of α_s in this regime, hadronization is non-perturbative. Hadronization models are built, and tuned to coincide with measurements (green areas). Hadron decays are then modeled using effective theories, called fragmentation models, which is indicated in dark green. Additionally, QED bremsstrahlung needs to be modeled (yellow).

Apart from the hard scattering that is viewed as the main event, many low-momentum transfer interactions can happen in the same proton-proton collision. These lead to diffractive scattering, or the production of particles with low transverse momenta. These processes are summarized under the term *underlying event*, and are described by tunable models as well. In Figure 3.5, all calculations related to the underlying event are drawn in purple. The underlying event is to be distinguished from *pile-up*, which are additional interactions in other proton-proton collisions in the same or neighboring bunch crossings. The effect of pile-up is generated separately and overlaid with the hard scattering events after detector simulation [66].

As the parton shower is designed to model soft collinear radiation, it does not provide a good description of the harder tails of jet momentum distributions, as well as of multi-jet processes. This problem can be solved by introducing an adequate merging of the hard emissions calculated at matrix element level, and the parton shower. The transition between both schemes happens at the merging scale Λ_MS. For physics predictions, like e. g. total cross sections, to be reasonably independent of the specific choice of Λ_MS, matrix element divergences for soft collinear emissions have to be absorbed. This is achieved by re-weighting the matrix element with Sudakov form factors [67]. Different implementations of this method exist. The CKKW-L [68, 69] merging is implemented,

[1] with respect to the already calculated matrix element

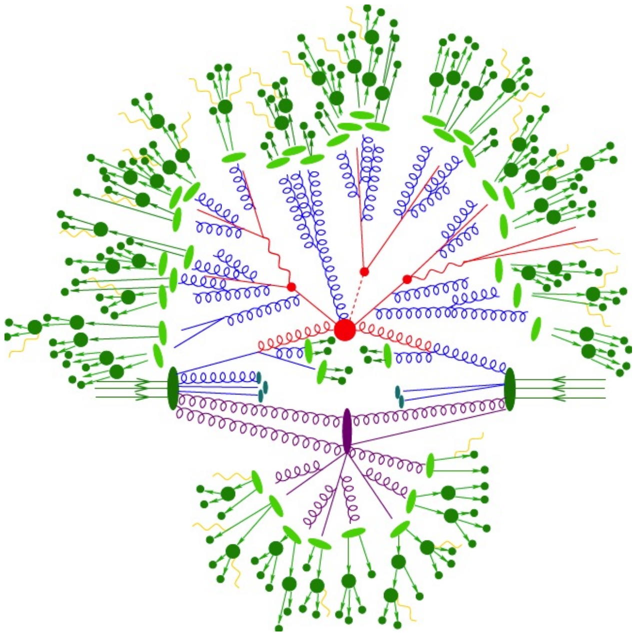

Figure 3.5: Schematic view of a $t\bar{t}H$ event as produced by an event generator. After the calculation of the matrix element (red), initial and final state parton showers model QCD bremsstrahlung (blue). Hadrons are build during hadronization (light green) and their decays are simulated (dark green). Initial- and final-state photon radiation is shown in yellow. Additional parton interactions in the non-perturbative regime are described by hadronization models, as well (purple). Figure taken from Ref. [65].

amongst others, in SHERPA [65]. Other generators, like MADGRAPH5_aMC@NLO [70] use MLM merging [71].

Additionally to ME merging, it is possible to include calculations of additional hard emissions at higher orders in the matrix element. Subsequently, parton showering is applied to all generated partons. As the parton shower also includes higher order emissions, all emissions already explicitly contained in the ME have to be subtracted to avoid double counting. This procedure is called matching [72].

Several programs exist to generate proton-proton collision events. In this thesis, samples generated with SHERPA, MADGRAPH5_aMC@NLO (MG_aMC), and POWHEGBOX [72–75] are used. PYTHIA 8 [76] and HERWIG 7 [77, 78] programs are used for parton showering of MADGRAPH5_aMC@NLO and POWHEGBOX samples.

Simulated events where the parton shower and hadronization steps are applied are said to be on *particle level*. To also include detector effects, these events are are run through the ATLAS detector simulation [79]. The simulation is based on the GEANT4 simulation toolkit [80], and calculates the expected detector response for each particle. Additionally, detector feed-back due to pile-up and noise is added to each event. This results in events on *reconstruction level*. Particle and reconstruction level are sometimes referred to as truth and detector level, respectively.

The data structure of simulated events is identical to the structure of measured events, such that the same offline reconstruction chain can be applied to both groups of data. A HLT trigger decision is calculated for generated events after detector simulation. However, it is not possible to exactly recreate the detector response. Therefore, efficiency correction factors have to be applied to simulated data in order to account for different reconstruction and identification results on measurements and simulation. Furthermore, some effects like the mis-reconstruction of electronic charges or mis-identification of leptons, which heavily rely on detector information are not modeled with high accuracy. Thus, in many analyses, backgrounds arising from those effects are estimated using data-driven techniques.

4 Same-sign $W^{\pm}W^{\pm}$ Scattering

As discussed in Section 2.1.2, the scattering amplitude of longitudinally polarized vector bosons is unitarized by the introduction of additional vertices. Measuring the scattering cross section is therefore a powerful way to probe electroweak symmetry breaking and the Standard Model Higgs mechanism.

A set of possible Feynman diagrams for vector boson scattering is shown in Figure 4.1 (a) to (c). The scattering can happen either directly via a quartic vertex (a) or via t/u- and s-channel diagrams (b, c). However, s-channel diagrams with electrically neutral resonances (c) are only possible for opposite-charge final states. Additionally to these resonant VBS diagrams, other resonant and non-resonant diagrams are possible within the same final state. Examples are shown in Figure 4.1 (d) and (e), respectively. All diagrams depicted in Figure 4.1, are of the order α_{ew}^{6} in the electroweak coupling α_{ew}, at leading order. Diagrams of this type are called electroweak (EW) production in the following. The two final state jets are part of a characteristic VBS detector signature. They usually have a high invariant mass, and are scattered into the forward regions of the ATLAS detector, i. e. have a large angular separation.

In addition to purely electroweak diagrams, the same final state can be generated by diagrams including QCD vertices, referred to as QCD production hereafter. At leading order, these diagrams are of the order of $\alpha_{\mathrm{ew}}^{4}\alpha_{\mathrm{s}}^{2}$. Examples for this group of diagrams are shown in Figure 4.2. Processes of this kind contribute the irreducible background in VBS analyses, as they have the same detector signature as the signal process and can only be partially separated by kinematical requirements. As diagrams of $\mathcal{O}(\alpha_{\mathrm{ew}}^{6})$ and $\mathcal{O}(\alpha_{\mathrm{ew}}^{4}\alpha_{\mathrm{s}}^{2})$ have the same initial and final state, an interference of the order $\mathcal{O}(\alpha_{\mathrm{ew}}^{5}\alpha_{\mathrm{s}})$ occurs, and is further discussed in Section 4.3.

In Table 4.1, electroweak production cross sections, σ_{EW}, are listed for ZZ, $W^{\pm}Z$, $W^{\pm}W^{\pm}$ and $W^{\pm}W^{\mp}$ VBS channels. In order to estimate the sensitivity to vector boson scattering, the ratio of the electroweak to QCD-induced production cross section, $\sigma_{\mathrm{EW}}/\sigma_{\mathrm{QCD}}$, is calculated as well [81]. Same-sign $W^{\pm}$-boson scattering is the most promising channel for observing VBS, as it has the highest $\sigma_{\mathrm{EW}}/\sigma_{\mathrm{QCD}}$ ratio. At leading order, it is not possible to generate a final state with two same-sign leptons when there is one or more gluons in the initial state. These contributions only enter at $\mathcal{O}(\alpha_{\mathrm{ew}}^{4}\alpha_{\mathrm{s}}^{3})$. An example diagram is shown in Figure 4.2 (c). The missing gluon contributions at leading order are reflected in the very high $\sigma_{\mathrm{EW}}/\sigma_{\mathrm{QCD}}$ ratio.

The cross sections for ZZ and $W^{\pm}Z$ scattering are small in comparison to $W^{\pm}W^{\pm}$ production, due to the involved Z-bosons. These channels become important with increasing recorded luminosity. ZZ and $W^{\pm}Z$ channels tend be have a better overall signal to background ratio, as it is possible to veto other processes with much higher cross sections. Thus, background processes like Z production or di-leptonic $t\bar{t}$ decays can be rejected, due to the high number of leptons and well reconstructable final states. In the past, semi-leptonic $W^{\pm}Z/WW$ and fully leptonic $W^{\pm}Z$ VBS have been investigated [42, 82, 83] by the ATLAS collaboration. In the 13 TeV $W^{\pm}Z$ VBS analysis by the ATLAS collaboration, the electroweak $W^{\pm}Zjj$ production was observed with a significance of 5.3 σ [83]. CMS measured the electroweak $ZZjj$ production with an observed significance of 2.7 σ at 13 TeV center-of-mass energy [84].

Even though it has the highest production cross section, opposite-sign $W^{\pm}W^{\mp}$ scattering is the most challenging channel, as its detector signature is very similar to leptonic Z-boson and $t\bar{t}$ decays. However, it is the only channel where a neutral resonance can appear in the s-channel diagram

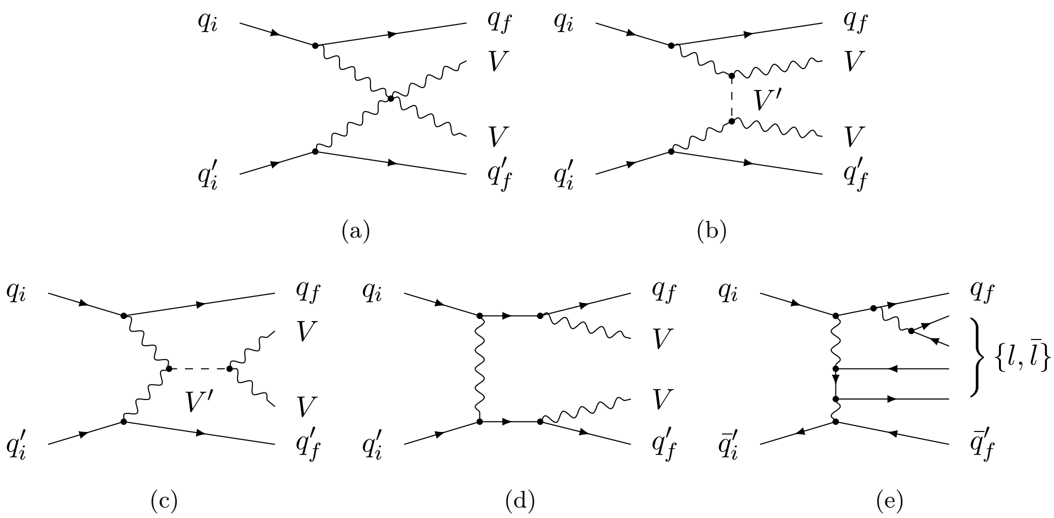

Figure 4.1: Diagrams contributing to vector boson scattering at the order of α_{ew}^6. Incoming quarks (q_i, q_i') radiate bosons V', which can be any of $(Z, \gamma^*, H, W^\pm)$. The bosons scatter either directly (a) or via t/u- (b) or s-channel (c) diagrams. Various non-VBS diagrams, like (d) and (e), also exist. The final states are defined to only include vector bosons, or their decay products.

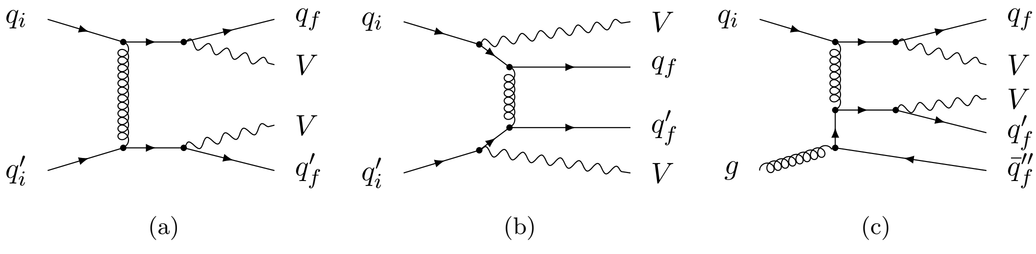

Figure 4.2: Diagrams contribution to vector boson scattering at the order of $\alpha_{\mathrm{ew}}^4\alpha_{\mathrm{s}}^2$ (a, b) and α_{s}^3 (c). At leading order, i. e. $\mathcal{O}(\alpha_{\mathrm{ew}}^4\alpha_{\mathrm{s}}^2)$, no gluons appear in the initial state for a same-sign final state.

and has been used in resonance searches as presented in Reference [85]. Moreover, analyses of exclusive $pp \to pp\gamma\gamma \to ppW^\pm W^\mp$ VBS have been published by CMS and ATLAS [86, 87], reporting an observed significance of 3.4 σ and 3.0 σ, respectively. Nevertheless, studies have shown, that much more data and evolved analysis strategies are needed to measure electroweak $W^\pm W^\mp jj$ production [88].

Process	Final State	σ_{EW}[fb] 8 TeV	σ_{EW}[fb] 13 TeV	$\sigma_{\text{EW}}/\sigma_{\text{QCD}}$ 8 TeV	$\sigma_{\text{EW}}/\sigma_{\text{QCD}}$ 13 TeV
ZZ	$lll'l'jj$	0.027	0.098	1.13	0.98
$W^\pm Z$	$lll'\nu jj$	0.571	2.34	0.51	0.53
$W^\pm W^\pm$	$ll'\nu\nu' jj$	1.13	3.97	10.27	11.47
$W^\pm W^\mp, ZZ$	$ll'\nu\nu' jj$	3.64	12.3	0.66	0.56

Table 4.1: Overview of electroweak production cross sections for different VBS final states at center-of-mass energies of 8 TeV and 13 TeV generated with SHERPA. Additionally, the cross section ratio of electroweak to QCD-induced production is given. Cross sections are calculated on parton level, in a fiducial volume defined by selecting charged leptons with $p_{\text{T}} > 25$ GeV, and $|\eta| \leq 2.5$. All charged lepton pairs are required to have an invariant mass larger than $m_{\ell\ell} > 20$ GeV, with angular angular separations larger than $\Delta R_{l,l} > 0.3$. Jets are reconstructed using the anti-k_{T} algorithm with a radius parameter of $\Delta R = 0.4$. They need to satisfy $p_{\text{T}} > 30$ GeV, $|\eta| \leq 4.5$ and need to be separated from charged leptons by at least $\Delta R_{lj} > 0.3$. A VBS-like topology is ensured by requiring $m_{jj} > 500$ GeV, and $|\Delta Y_{jj}| > 2.4$. Based on Ref. [81].

4.1 Previous Studies on $W^\pm W^\pm$ Scattering

Several analyses investigating electroweak $W^\pm W^\pm$ scattering have been performed in the past. The analysis presented in this thesis is based to a large extent on the 8 TeV analysis [89] by the ATLAS collaboration, which was also used to provide a cross-check for the implementation of the statistical analysis (see Section 9.1.1). It is summarized in the following. Furthermore, the CMS collaboration published analysis results for center-of-mass energies of 8 TeV [90] and 13 TeV [91]. Results of the latter are shortly summarized below.

4.1.1 Summary of 8 TeV ATLAS Analysis

The 8 TeV ATLAS analysis [89] is conducted in three charge-inclusive lepton flavor channels, ee, $\mu\mu$, and $e\mu/\mu e$. Different signal regions are defined for measuring the inclusive electroweak and QCD-induced $W^\pm W^\pm$ cross section, and the purely electroweak production, as well as setting limits on anomalous couplings. All background contributions except for events containing mis-identified leptons (non-prompt) and electrons with mis-reconstructed charge (charge mis-ID) are taken from simulation. In general, the methodology for estimating the non-prompt and charge mis-ID background in a data-driven way is similar to the current procedures described in Section 6.2.

The inclusive signal region is defined by selecting events with exactly two same-charge leptons with tight lepton identification criteria. A looser lepton definition is used for rejecting additional leptons. The invariant lepton mass $m_{\ell\ell}$ is required to be greater than 20 GeV. To reduce background from charge mis-ID, events with $m_{\ell\ell}$ close to the Z-resonance are rejected in the ee channel, using $|m_Z - m_{\ell\ell}| > 10$ GeV. A minimum missing transverse energy of $E_{\text{T}}^{\text{miss}} > 40$ GeV is required. Furthermore, only events with at least two tagging jets with an invariant mass $m_{jj} > 500$ GeV are accepted. Events containing b-jets are vetoed to reduce contributions from $t\bar{t}$ decays.

An additional selection criterion on the rapidity gap between the tagging jets $|\Delta Y_{jj}| > 2.4$ is used to define the VBS signal region. To set limits on aQGC, the transverse mass of the $W^\pm W^\pm$-system, $m_{WW,\text{T}}$, is required to be at least 400 GeV.

The signal prediction is generated at leading order using the Sherpa event generator [65]. The cross section is scaled to next-to-leading order in Qcd based PowhegBox predictions [72–75] with Pythia 8 [76] parton showering. Theory uncertainties on the signal prediction are evaluated using scale and parton distribution function variations, as well as a generator comparison to Vfbnlo [92–94]. The interference between electroweak and Qcd diagrams is found to be 6.5 % in the Vbs region and included in the signal definition.

As they are needed for the cross-check of the statistical framework presented in Section 9.1.1, event yields and systematic uncertainties in the Vbs signal region are summarized in Tables 4.2 and 4.3. Relative systematic uncertainties are given for each source with respect to the total background and signal estimate, respectively. In particular, the relative theoretical uncertainties on the $t\bar{t}V$, $ZZjj$ Ew and Qcd and $W\gamma$ backgrounds are estimated to be 30 %, 19 %, and 17 %, respectively.

Using the event yields in the Vbs signal region, a one-bin profile likelihood fit is used to calculate the statistical significance of $W^{\pm}W^{\pm}jj$-Ew production and measure the fiducial cross section. An expected and observed significance of 2.3 σ and 3.6 σ is derived, respectively, thereby finding the first evidence for Vbs across all lepton flavor channels.

The measured fiducial $W^{\pm}W^{\pm}jj$-Ew cross section of $\sigma^{\text{fid}}_{\text{meas}} = (1.5 \pm 0.5\ (\text{stat}) \pm 0.2\ (\text{syst}))$ fb, is found to be in agreement with the value predicted by the Standard Model[1], $\sigma^{\text{fid}}_{\text{theo}} = (0.95 \pm 0.06)$ fb. The slight deviation between expectation and observation is due to an excess in data with respect to the total prediction.

This effect can also be seen in the expected and observed limits on anomalous quartic couplings. K-matrix unitarization [95] is applied, before calculating the limits. These are set by fitting the number of events in the aQgc signal region, and found to be

$$\begin{aligned} &\text{expected:} \quad \alpha_4 \in [-0.06, 0.07], \quad \text{and} \quad \alpha_5 \in [-0.10, 0.11], \\ &\text{observed:} \quad \alpha_4 \in [-0.14, 0.15], \quad \text{and} \quad \alpha_5 \in [-0.22, 0.22]. \end{aligned}$$

4.1.2 Summary of 13 TeV CMS Analysis

In this analysis [91], events in the signal region are split into six lepton charge and flavor channels, e^+e^+, $e^+\mu^+/\mu^+e^+$, $\mu^+\mu^+$ and charge conjugates. The event selection is very similar to the Atlas selection described in the previous section. An additional requirement on the Zeppenfeld variable z^*_ℓ [96] of the leptons is made. For each lepton ℓ_i, $z^*_{\ell,i}$ is defined using its pseudo rapidity $\eta_{\ell,i}$ and the pseudo rapidities of the tagging jets $\eta_{j(1,2)}$ as [96]

$$z^*_{\ell,i} = \frac{\left|\eta_{\ell,i} - \frac{\eta_{j1} + \eta_{j2}}{2}\right|}{|\Delta\eta_{jj}|}.$$

	ee	$e\mu/\mu e$	$\mu\mu$	Total
$W^{\pm}W^{\pm}jj$-Ew	2.34 ± 0.23	6.3 ± 0.6	3.77 ± 0.35	12.4 ± 1.1
$W^{\pm}W^{\pm}jj$-Qcd	0.26 ± 0.06	0.67 ± 0.14	0.43 ± 0.09	1.36 ± 0.27
Prompt	2.2 ± 0.5	4.2 ± 1.0	1.9 ± 0.5	8.2 ± 1.9
Charge Mis-ID	1.39 ± 0.27	0.64 ± 0.24	$\pm$	2.0 ± 0.5
$W\gamma$	0.7 ± 0.4	1.3 ± 0.7	$\pm$	2.0 ± 1.0
Non-Prompt	0.50 ± 0.26	1.5 ± 0.6	0.34 ± 0.19	2.3 ± 0.7
Total predicted	7.4 ± 1.0	14.5 ± 1.9	6.4 ± 0.7	28.3 ± 3.4
Data	6	18	10	34

Table 4.2: Event yields in the Vbs signal region. Taken from Ref. [89].

[1] The predicted cross section is determined using the generator configuration as discussed above.

Uncertainty Source	Background [%]			Signal [%]		
	ee	$e\mu/\mu e$	$\mu\mu$	ee	$e\mu/\mu e$	$\mu\mu$
$W^{\pm}W^{\pm}jj$-Ew				6	6	6
WZ-Ew	5	5	8			
WZ-Qcd	0.9	1.5	2.6			
Simulation Precision	9	6	8	5	2.7	4
Luminosity	1.7	2.1	2.4	2.8	2.8	2.8
Trigger efficiency	0.1	0.2	0.4	0.1	0.3	0.5
Leptons-related	1.7	1.1	1.1	1.9	1.0	0.7
Jet-related	13	20	20	5	5	5
$E_{\mathrm{T}}^{\mathrm{miss}}$ reconstruction	2.9	3.2	1.4	1.1	1.1	1.1
b-tagging	0.8	0.9	0.7	0.6	0.6	0.6
non-prompt	4	7	7			
charge mis-ID	6	4				
$W\gamma$	3.1	2.6				
Total	18	20	21	10	9	9

Table 4.3: Summary of relative systematic uncertainties in the ee, $e\mu/\mu e$ and $\mu\mu$ channels in the Vbs signal region, calculated with respect to the total background and signal yields. The first three lines refer to the theory uncertainty on the predicted cross section of the respective processes. Numbers taken from Ref. [89].

It is sensitive to the rapidity gap between the two tagging jets, and the fact that the leptons from $W^{\pm}$-decays are expected to be central. Only events are accepted where the maximum Zeppenfeld variable, $\max(z^*_{\ell,1}, z^*_{\ell,2})$, of both leptons is smaller than 0.75. In the ee channels, the invariant mass of the electrons is required to fulfill $|m_Z - m_{\ell\ell}| > 15\,\text{GeV}$.

The interference between $W^{\pm}W^{\pm}jj$-Ew and $W^{\pm}W^{\pm}jj$-Qcd is treated as a systematic uncertainty and estimated to be 4.5 %. A $W^{\pm}Z$ control region is defined to measure the normalization of this background.

The statistical significance is evaluated in a simultaneous profile likelihood fit of the $m_{\ell\ell}$ and m_{jj} distributions in the signal region, and the m_{jj} distribution in the $W^{\pm}Z$ control region. An expected and observed significance of 5.5 σ and 5.7 σ is reached. Therefore, this analysis states the first observation of $W^{\pm}W^{\pm}jj$-Ew production.

The cross section calculation for $W^{\pm}W^{\pm}jj$-Ew production is based on a leading order fiducial cross section generated using the MadGraph5_aMC@NLO [70] generator with Pythia 8 parton showering. The predicted cross section is $\sigma^{\text{fid}}_{\text{theo}} = (4.25 \pm 0.27)$ fb. Theory uncertainties include contributions from parton distribution and scale variations. The measurement results in a fiducial cross section of $\sigma^{\text{fid}}_{\text{meas}} = (3.83 \pm 0.66\ (\text{stat})\ \pm 0.35\ (\text{syst}))$ fb.

Limits on anomalous couplings are set using the profile likelihood fit of the ununitarized $m_{\ell\ell}$ distributions in the signal and $W^{\pm}Z$ control regions. Dimension-eight operators are used to parametrize anomalous couplings. The parameters relevant for the quartic vertex are limited to

$$\begin{aligned} \text{expected:} \quad & f_{\text{S0}}/\Lambda^4 \in [-7.0, 7.2], \quad \text{and} \quad f_{\text{S1}}/\Lambda^4 \in [-19.9, 20.2], \\ \text{observed:} \quad & f_{\text{S0}}/\Lambda^4 \in [-7.7, 7.7], \quad \text{and} \quad f_{\text{S1}}/\Lambda^4 \in [-21.6, 21.8]. \end{aligned}$$

Even after converting these limits into $\alpha_{4,5}$, as given in Eq. (2.9) and (2.10), the results are not directly comparable to Atlas limits, as different unitarization schemes are applied in both analyses.

4.2 Theory Predictions

In this thesis, the $W^{\pm}W^{\pm}jj$-Ew production cross section is measured in a fiducial region defined in Table 4.4. Exactly two same-sign leptons are required, where lepton refers to electrons or muons not originating in τ-lepton decays. These are dressed with photons lying inside a cone of $\Delta R_{l,\gamma} < 0.1$ along the lepton axis, i. e. the momentum of these photons is added to the lepton momentum. In order to stay as close to the signal region definition (see Table 7.2) as possible, both leptons are required to have a transverse momentum larger than 27 GeV, lie inside $|\eta| = 2.5$ and have an invariant mass exceeding 20 GeV. Jets are reconstructed using anti-k_{T} clustering with a radius parameter of $\Delta R = 0.4$. Only events containing at least two particle jets within $|\eta| = 4.5$ are accepted. The leading and subleading jet transverse momenta must be greater than 65 GeV and 35 GeV, respectively. A rapidity gap between these tagging jets of at least 2.0, as well as an invariant mass larger than 500 GeV are required. Furthermore, the selection is restricted to events with high missing transverse momentum by enforcing the sum of the two leading neutrino momenta, $\sum p_{\mathrm{T}}^{\nu}$, to surpass 30 GeV. For a motivation of these requirements see Section 7.1. In order to reproduce the object isolation requirements given in Table 5.1 as well as the overlap removal (Olr) described in Section 5.5, all leptons and jets must be separated by at least $\Delta R = 0.3$.

Object	Criterion	Value
Electrons/	N_{lep}	$= 2$
Muons	p_{T}	> 27 GeV
	$\|\eta\|$	< 2.5
	same-charge	
	$m_{\ell\ell}$	> 20 GeV
Neutrinos	$\sum p_{\mathrm{T}}^{\nu}$	> 30 GeV
Jets	N_{jet}	≥ 2
	$p_{\mathrm{T}}^{1(2)}$	> 65 (35) GeV
	$\|\eta\|$	< 4.5
	$\|\Delta Y_{jj}\|$	> 2.0
	m_{jj}	> 500 GeV
Olr	$\Delta R_{l,l}$	> 0.3
	$\Delta R_{l,j}$	> 0.3

Table 4.4: Summary of selection requirements defining the fiducial phase space used for measuring the $W^{\pm}W^{\pm}jj$-Ew cross section [97].

The Sherpa program configured with the Nnpdf3.0Nnlo set of proton parton distribution functions (Pdf) [98] is used to generate the nominal signal sample. Detailed comparisons of the predictions of MadGraph5_aMC@NLO (MG_aMC) and PowhegBox generators with Pythia 8 (Py8) [76] parton shower are presented in Reference [99], which is extending the work presented in Reference [100]. A generally good agreement between MG_aMC+Py8 and PowhegBox+Py8 is found. The differences of both generators compared to Sherpa can become large. There is a known problem [101] in the way color flow between incoming and outgoing partons is treated within Sherpa. This problem is known to cause a lower total cross section and a slightly steeper m_{jj} spectrum.

Sherpa is used to generate the nominal signal sample, as it models up to three jets in the matrix element, while the MG_aMC+Py8 includes simply Lo predictions. Additionally, an inaccurate modeling of the third jet in MG_aMC in combination with the Pythia 8 shower is reported in Reference [99]. Furthermore, tri-boson contributions are not included in the PowhegBox+Py8 sample. An exemplary Feynmen diagram for resonant tri-boson production is shown in Figure 6.4

(a). It is shown that these contributions have a comparably small impact at leading order in the fiducial region [100]. However, a larger impact up to 20 % is observed at NLO QCD. Furthermore, the POWHEGBOX+PY8 sample is generated with a fixed scale set to the mass of the $W^{\pm}$-boson. The impact of this scale choice is studied [97]. It can be seen that a fixed scale at m_W can lead to an overestimation of the hard tail in the m_{jj} distribution. Therefore, SHERPA rather than POWHEGBOX is used as the nominal event generator.

The simulated events are generated in the total phase space, and the definition of which is listed in Table 4.5. The predicted cross section $\sigma^{\text{fid}}_{\text{theo}}$ in the fiducial region is calculated from the total cross section $\sigma^{\text{tot}}_{\text{theo}}$ as

$$\sigma^{\text{fid}}_{\text{theo}} = \sigma^{\text{tot}}_{\text{theo}} \cdot \mathcal{A}, \text{ with} \tag{4.1}$$

$$\mathcal{A} = \frac{N_{\text{fid}}}{N_{\text{tot}}}. \tag{4.2}$$

Here, the fiducial acceptance $\mathcal{A}$ is calculated as the ratio of the number of events in the total and fiducial phase spaces, denoted as N_{tot} and N_{fid}, respectively. The total and fiducial cross sections, as wells as acceptance factors are reported in Reference [97]. The total cross section generated by SHERPA is (40.81 ± 0.05) fb. An acceptance of $(4.93 \pm 0.02) \cdot 10^{-2}$ is calculated, yielding a fiducial cross section of (2.01 ± 0.02) fb. All given uncertainties are purely statistical.

4.2.1 Signal Theory Uncertainties

The procedure to derive theory uncertainties is detailed in Reference [97], and summarized in Section 8.2. Uncertainties related to the choice of the strong coupling α_{s}, the values of the renormalization and factorization scales μ_R and μ_F, the set of parton distribution functions (PDF), as well as the parton showering are calculated. These sources of uncertainties are treated as separate, a priori uncorrelated nuisance parameters in the statistical analysis. All uncertainties are evaluated in bins of m_{jj}, as this distribution is used in the profile likelihood fit. The total theoretical uncertainty on the fiducial cross section is calculated as the squared sum of the individual components.

The α_{s}, scale and PDF uncertainties are available on reconstruction level, while parton shower uncertainties on the signal prediction are calculated on particle level. Therefore, the varied m_{jj} distribution derived by varying the parton shower scheme is folded to reconstruction level using the method described in Section 4.5.

The treatment of signal theory uncertainties in the statistical analysis and cross section measurement is non-trivial, and it is worth to consider the impact theory uncertainties have on the predicted number of signal events on particle and reconstruction level. These are denoted as $\mathcal{N}^{\text{fid}}_{\text{sig}}$ and $N^{\text{SR}}_{\text{sig}}$, respectively. On particle level, $\mathcal{N}^{\text{fid}}_{\text{sig}}$ can be calculated from the luminosity $\mathcal{L}$, and the total predicted cross section $\sigma^{\text{tot}}_{\text{theo}}$ as

$$\mathcal{N}^{\text{fid}}_{\text{sig}} = \mathcal{L} \cdot \sigma^{\text{tot}}_{\text{theo}} \cdot \mathcal{A}, \tag{4.3}$$

Object	Criterion	Value
Electrons	m_{ee}	> 0.1 GeV
Electrons Muons, Taus	p_{T}	> 5 GeV
Jets	N_{jet}	$= 2$
	p_{T}	>15 GeV
	E_{T}	> 0

Table 4.5: Definition of the total phase space used in the generation of simulated events. Jets are reconstructed using the anti-k_{T} algorithm with a radius parameters of $\Delta R \leq 0.4$.

where $\mathcal{A}$ is the acceptance as defined in Equation (4.2). Similarly, when regarding a differential distribution on particle level, the number of events $\mathcal{N}^{\text{fid}}_{\text{sig},i}$ in bin i can be calculated using the acceptance $\mathcal{A}_i$ in the respective bin. The number of events in a reconstruction-level bin j can than be calculated from the differential distribution on particle level as

$$N^{\text{SR}}_{\text{sig},j} = \sum_i \mathcal{C}_{ji} \cdot \mathcal{N}^{\text{fid}}_{\text{sig},i}. \tag{4.4}$$

Here, $\mathcal{C}_{ji}$ is the total efficiency correction factor introduced during the folding, described in Section 4.5. Equation (4.4) is a simplified version of Equation (4.11).

Each variation of theory uncertainties, represented by nuisance parameters $\boldsymbol{\theta}_{\text{theo}}$, results in a variation of the total acceptance $\mathcal{A}(\boldsymbol{\theta}_{\text{theo}})$, but also the differential acceptance $\mathcal{A}_i(\boldsymbol{\theta}_{\text{theo}})$, as well as the efficiency correction $\mathcal{C}_{ji}(\boldsymbol{\theta}_{\text{theo}})$. As $\mathcal{C}_{ji}(\boldsymbol{\theta}_{\text{theo}})$ is purely related to the reconstruction level event yield, these effects cannot be assigned to particle level qualities like the predicted fiducial cross section. However, the effect of theory uncertainties on the acceptance has to be splitted and appropriately assigned to particle and reconstruction level.

Variations of $\mathcal{A}$ result in varied predicted fiducial cross section, while variations of $\mathcal{A}_i$ can cause shape differences in the differential cross section. In order to separate the normalization effects from the shape effects, $\mathcal{A}_i(\boldsymbol{\theta}_{\text{theo}})$ is normalized with $\mathcal{A}(\boldsymbol{\theta}_{\text{theo}})$. Thus, Equation (4.3) is used to substitute $\mathcal{N}^{\text{fid}}_{\text{sig},i}$ in Equation (4.4), and a neutral factor of $1 = \frac{\mathcal{A}}{\mathcal{A}}$ [97] is introduced. The predicted number of signal events in reconstruction-level bin j can then be written as

$$N^{\text{SR}}_{\text{sig},j}(\boldsymbol{\theta}_{\text{theo}}) = \mathcal{A} \cdot \mathcal{L} \cdot \sum_i \mathcal{C}_{ji}(\boldsymbol{\theta}_{\text{theo}}) \cdot \sigma^{\text{tot}}_{\text{theo}} \cdot \frac{\mathcal{A}_i}{\mathcal{A}}(\boldsymbol{\theta}_{\text{theo}}). \tag{4.5}$$

Hence, only the shape effect of $\frac{\mathcal{A}_i}{\mathcal{A}}$ and the full effect of $\mathcal{C}_{ji}$ are considered on reconstruction level; while the total effect of the normalization is assigned to the fiducial cross section [97]

$$\sigma^{\text{fid}}_{\text{theo}}(\boldsymbol{\theta}_{\text{theo}}) = \sigma^{\text{tot}}_{\text{theo}} \cdot \mathcal{A}(\boldsymbol{\theta}_{\text{theo}}).$$

The final uncertainties included in the statistical analysis range between 1 % and 10 %, where the largest variations are due to the parton shower uncertainty. A detailed overview of the effects of signal theory nuisance parameters is given in Section 8.2.

4.3 Interference between EW and QCD Diagrams

As $\mathcal{O}(\alpha^6_{\text{ew}})$ and $\mathcal{O}(\alpha^4_{\text{ew}}\alpha^2_{\text{s}})$ diagrams have the same initial and final state, there is an interference between both types, which is of order $\mathcal{O}(\alpha^5_{\text{ew}}\alpha_{\text{s}})$. The contributions of the respective diagrams to the total cross section are evaluated in Reference [100]. The corresponding m_{jj} and $|\Delta Y_{jj}|$ distributions are shown in Figure 4.3. The peak in the Ew m_{jj} distribution at around 80 GeV is caused by tri-boson diagrams where the tagging jets are actually $W^\pm$-boson decay products.

It can be seen, that the interference has a comparably small effect, especially in the Vbs-like region with $|\Delta Y_{jj}| > 2$ and $m_{jj} > 500$ GeV. It is therefore not included as a separate contribution into the statistical analysis, but treated as systematic uncertainty on the signal m_{jj} distribution.

The procedure applied to determine the shape of this systematic uncertainty is described in detail in Reference [102]. The interference, as well as Ew and Qcd contributions are generated separately using the MG_aMC+Py8 generator in the fiducial phase space defined for this analysis. The definition of the fiducial volume is listed in Table 4.4. Relative contributions to the total cross section are comparable to the fractions reported in Reference [100]. The relative interference contribution amounts to approximately 6 %.

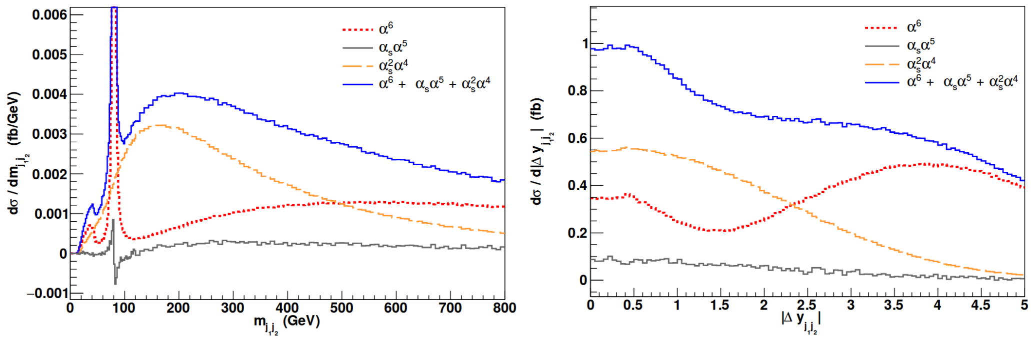

(a) m_{jj} (b) $|\Delta Y_{jj}|$

Figure 4.3: m_{jj} (a) and $|\Delta Y_{jj}|$ (b) distributions for Ew (red, dotted), Qcd (orange, dashed) and interference (black, solid) contributions to the process $pp \to \mu^+\nu e^+\nu jj$. Additionally, the sum of all contributions (blue) is shown. Figures taken from Ref. [100].

The interference and Ew m_{jj} distributions generated with MG_aMC+Py8 are folded to reconstruction level as discussed in Section 4.5. In order to mitigate possible shape differences in the predictions from MG_aMC+Py8 and Sherpa, which is used for the modeling of the nominal signal in this analysis, the relative difference between the interference and the MG_aMC+Py8 $W^\pm W^\pm jj$-Ew prediction is calculated in bins of m_{jj}. This relative uncertainty is then applied to the Sherpa signal m_{jj} distribution. However, as no uncertainty on the overall effect of the interference is available, the varied m_{jj} distributions of the Sherpa signal sample are normalized to the fiducial cross section on particle level. The final variations therefore include shape as well as residual normalization effects. As the interference is expected to be independent on lepton flavor or charge, the same uncertainty is applied in all lepton channels. The impact of the variation on the profile likelihood fit is further discussed in Section 8.2.

4.4 Next-to-leading Order EW Corrections

Full next-to-leading order corrections of the orders $\mathcal{O}(\alpha_{\text{ew}}^6\alpha_{\text{s}})$, $\mathcal{O}(\alpha_{\text{ew}}^5\alpha_{\text{s}}^2)$, and $\mathcal{O}(\alpha_{\text{ew}}^4\alpha_{\text{s}}^3)$, as well as $\mathcal{O}(\alpha_{\text{ew}}^7)$ to the $W^\pm W^\pm jj$-Ew process are calculated in Reference [103]. It has been shown that the $\mathcal{O}(\alpha_{\text{ew}}^7)$ corrections are dominating. Therefore, only these will be taken into account in this analysis.

To estimate the effect of the next-to-leading order corrections on the signal distribution in this analysis, the authors of Reference [103] provided $\mathcal{O}(\alpha_{\text{ew}}^7)$ corrections at particle level in a phase space which is, except for a lower jet momentum constraint of 30 GeV and the missing requirement on the invariant mass of leading and subleading jet, identical with the fiducial region of this analysis, as listed in Table 4.4.

The leading (Lo) and next-to-leading order (Nlo) differential cross sections $\mathrm{d}\sigma^{\text{fid}}_{\text{Lo,Nlo}}/\,\mathrm{d}m_{jj}$ on particle level are provided in 325 bins with a width of 40 GeV in a range from $m_{jj} = 0$ GeV up to $m_{jj} = 13\,000$ GeV. The binning of both distributions is adapted to the chosen binning for the profile likelihood fit (see Section 9.1.4), and the distributions are folded to reconstruction level as discussed in Section 4.5. The differential Lo and Nlo cross sections over m_{jj} on reconstruction level are shown in Figure 4.4. In the lower panel, the ratio between both distributions, i. e. the Nlo Ew corrections are shown. Rather than applying the relative corrections as a bin-wise k-factor, they are included as systematic uncertainties on the signal distribution. This more conservative approach is chosen as Ew corrections are not yet available in Monte Carlo event generators, and the systematic uncertainties on the corrections are unknown.

The procedure to include Ew corrections as systematics in the fit is similar to the treatment of the interference discussed above. The relative corrections to the leading order distribution are calculated, and applied to the SHERPA signal sample on particle level. The variation is normalized to the nominal fiducial cross section and symmetrized; such that the full shape effect is considered as uncertainty in the fit. The distributions are then folded to reconstruction level, which introduces a small normalization effect. The final systematic uncertainty applied to the signal sample is further discussed in Section 8.2.

The normalization effect of the EW corrections, i. e. the NLO k-factor is calculated as

$$k = \frac{\sigma^{\text{fid}}_{\text{NLO}}}{\sigma^{\text{fid}}_{\text{LO}}} = 0.842. \tag{4.6}$$

NLO EW corrections include, amongst other corrections, the real emissions of a photon. In addition, the SHERPA parton shower includes resummed QED radiation of final state particles. Therefore a double counting of the first photon emission from the parton shower and the NLO EW correction coming from real photon emission is introduced. The effect of this has been studied in Reference [97] by generating a $W^{\pm}W^{\pm}jj$-EW sample with the same settings as the nominal signal sample, but excluding final state QED radiation in the parton shower. The difference between the nominal and the modified sample was found to be within the statistical uncertainties, and the double counting is therefore neglected.

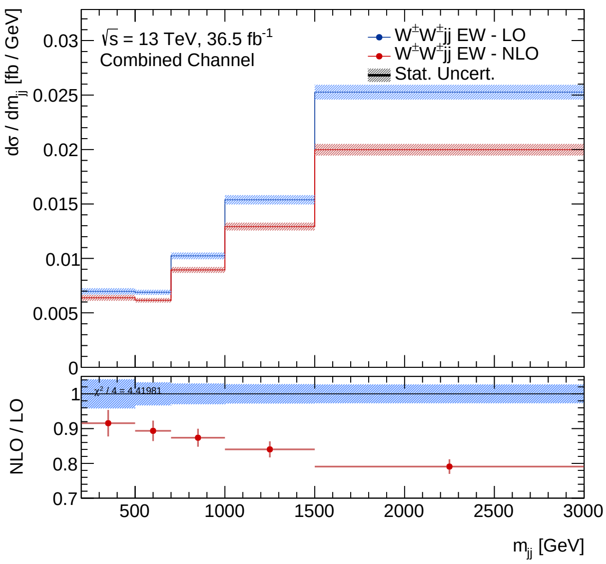

Figure 4.4: Comparison NLO (red) and LO (blue) differential cross sections for $W^{\pm}W^{\pm}jj$-EW production, folded to reconstruction level. Statistical uncertainties are also shown. The lower panel contains the electroweak corrections to the leading-order cross section.

4.5 Folding From Particle to Reconstruction Level

As discussed above, some theory uncertainties are only available on particle level, i. e. do not include detector effects. This is applicable to $W^{\pm}W^{\pm}jj$-EW next-to-leading order EW corrections, the uncertainty converting the interference between EW and QCD $W^{\pm}W^{\pm}$ diagrams as well as $W^{\pm}W^{\pm}jj$-EW and QCD parton shower systematics. In these cases, a folding procedure is used to add detector effects to the m_{jj} distribution. In the following, the procedure will be summarized. A schematic view of the folding procedure is shown in Figure 4.5. A detailed description is given in Reference [97].

Starting from the set T of all events in the fiducial region, the number of events in bin i of the m_{jj} distribution on particle level is denoted as $N_{T,i}$. In analogy, the set R of events in the signal region on reconstruction level is characterized by the number of events $N_{R,j}$ in bin j. $N_{R,j}$ can be estimated from Bayes' theorem

$$N_{R,j} \;=\; \frac{\sum_i P(R_j|T_i)\cdot N_{T,i}}{\sum_i P(T_i|R_j)}. \tag{4.7}$$

Here $P(R_j|T_i)$ is the probability for an event to migrate from particle level bin i to reconstruction level bin j, given it is present in both sets T and R. $P(R_j|T_i)$ is normalized such that

$$\sum_j P(R_j|T_i) = 1, \tag{4.8}$$

holds for all bins i. This means, that acceptance effects are not included in $P(R_j|T_i)$. In order to account for events that pass the fiducial selection, but fail the signal selection on reconstruction level, an *efficiency correction* is introduced, and used to correct $N_{T,i}$,

$$C_{\text{eff},i} \;=\; \frac{\sum_j N(R_j\cap T_i)}{N_{T,i}}. \tag{4.9}$$

The denominator $\sum_i P(T_i|R_j)$ in Eq. (4.7) corresponds to the conditional probability for an event that is in R to be found in any particle level bin i. This encodes the correction necessary to account for different phase space definitions on particle and reconstruction level, called *fiducial correction* $C_{\text{fid},j}$,

$$C_{\text{fid},j} \;=\; \sum_i P(T_i|R_j) \;=\; \frac{\sum_i N(T_i\cap R_j)}{N_{R,j}}. \tag{4.10}$$

Inserting the efficiency and fiducial corrections into the Bayes' theorem Eq. (4.7), the prescription for calculating the number of events in reconstruction level bin j becomes

$$N_{R,j} \;=\; \frac{1}{C_{\text{fid},j}}\cdot\sum_i P(R_j|T_i)\cdot C_{\text{eff},i}\cdot N_{T,i}. \tag{4.11}$$

The probability $P(R_j|T_i)$ is calculated using particle level and reconstruction level information from the nominal signal sample. A two-dimensional distribution of particle versus reconstruction level invariant tagging jet mass m_{jj} is generated, and normalized such that Eq. (4.8) holds. The resulting response matrix is shown in Figure 4.6(a). Additionally, the efficiency and fiducial corrections are shown in Figure 4.6(b) with their respective statistical uncertainties.

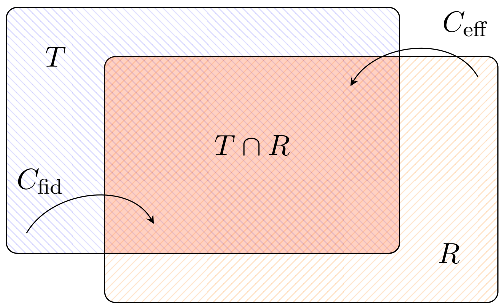

Figure 4.5: Representation of the folding procedure. The set of events in the fiducial region T is corrected by the fiducial correction C_{fid}. Additionally, events on reconstruction level are corrected using the efficiency correction C_{eff}. These corrections are necessary due to different selection efficiencies in the fiducial and signal regions. Figure adapted from Ref. [104].

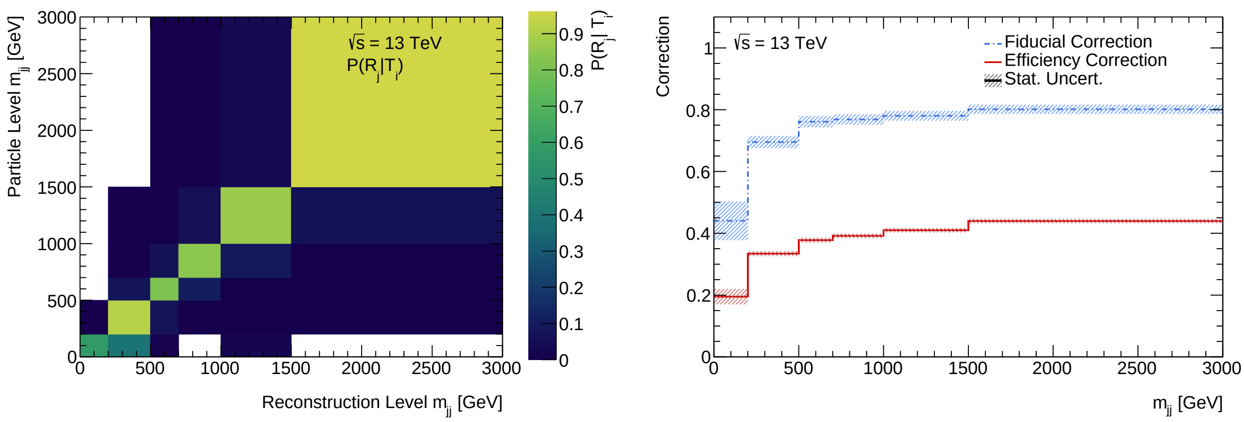

(a) $P(R_j|T_i)$ (b) Correction Factors

Figure 4.6: Response matrix $P(R_j|T_i)$ (a) as well as efficiency (solid, red) and fiducial correction (dashed, blue) used in the folding procedure. Figure adapted from Ref. [97].

5 Object Reconstruction and Selection

The selection criteria applied on reconstructed objects, such as electrons, muons and jets, are a crucial part of the analysis, as these have a major impact on the final sensitivity. The following chapter summarizes the object selection, More detail can be taken from Reference [105].

ATLAS combined performance (CP) groups provide reconstruction and identification tools for final state particles in proton-proton collisions. These were used in this analysis to select the vertices, electrons, muons, missing transverse energy, jets. Furthermore it is necessary to identify jets originating in b-quarks, called b-jets. A summary of the selection requirements applied to these is given in Table 5.1, which is based on Reference [105].

Electrons	Baseline	Analysis Level	Anti-ID
$\|\eta\|$	< 2.47	ee channel:	< 1.37
		other channels:	< 2.47 and $\|\eta\| \notin [1.37, 1.52]$
p_{T}	> 6 GeV	> 27 GeV	> 20 GeV
ID	`Loose+BLayer`	`Tight`	`Medium` and `!Tight`*
Isolation	–	`Gradient`	`!Gradient`*
`Author`	–	$= 1$	–
$\|z_0 \sin\theta\|$	< 0.5 mm	✓	✓
$\|d_0/\sigma_{d_0}\|$	< 5	✓	✓
Muons			
$\|\eta\|$	< 2.7	< 2.5	
p_{T}	> 6 GeV	> 27 GeV	> 15 GeV
Quality	`Loose`	`Medium`	`Medium`
Isolation	–	`Gradient`	`!Gradient`*
$\|z_0 \sin\theta\|$	< 0.5 mm	✓	✓
$\|d_0/\sigma_{d_0}\|$	< 10	< 3	≥ 3 *
Jets			
p_{T}	> 25 GeV, $\|\eta\| < 2.4$	$p_{\mathrm{T}}^{j1(2)} > 65(35)$ GeV	–
	> 30 GeV, $\|\eta\| < 4.5$		
$\|\eta\|$	< 4.5	✓	–
b-tag eff.	–	85 %	–
JVT	–	if $p_{\mathrm{T}}^{j} \in (25\text{ GeV}, 60\text{ GeV})$	–

Table 5.1: Summary of object selection criteria at various points in the analysis. Requirements marked with * are connected by a logical `OR`; in order for an object to pass the anti-ID selection level, only one of these requirements has to be passed. Baseline-level objects are used for overlap removal. The final analysis is done with analysis-level objects. Anti-ID-level objects are used to estimate the non-prompt background contribution. Information taken from Reference [105].

5.1 Vertex Requirements and Pile-Up Reweighting

As mentioned in Section 3.1 the average number of interactions per bunch crossing was 13.7 and 24.9 during data taking in 2015 and 2016, respectively [58]. It is therefore necessary to define which of the interaction vertices in an event is considered the primary vertex. The reconstruction of all other objects in an event is then performed with respect to that vertex. The primary vertex is chosen as the vertex having the highest squared sum of transverse momentum of associated tracks, where at least two tracks are required [106].

Objects from other vertices affect the measurement of objects associated to the primary vertex. Remnants of other vertices are called pile-up. The amount of pile-up in an event is measured using the number of interactions per bunch crossing, denoted as μ. In observed data, μ is calculated using the instantaneous luminosity per bunch L_{bunch}, the proton-proton inelastic scattering cross section σ_{inel}, and the LHC revolution frequency f_r [58]

$$\mu = \frac{L_{\text{bunch}} \cdot \sigma_{\text{inel}}}{f_r}. \tag{5.1}$$

Monte-Carlo simulation also includes these pile-up contributions, and integer values of μ are assumed. The assumed or measured value of μ does not necessarily agree with the average number of reconstructed vertices per event $\langle N_{\text{vtx}} \rangle$. It is observed that the slope of the $\langle N_{\text{vtx}} \rangle$ vs. μ distribution differs between observed and simulated data.

A pile-up profile is calculated as the binned, differential distribution of the integrated luminosity L and sum of all generator weights N over μ, for observed and simulated data, respectively. The observed pile-up profile during 2015 and 2016 data taking is shown in Figure 5.1. As can be seen, and is expected, the pile-up profile varies with different beam and detector conditions. Therefore, simulated events are also separated in groups with similar conditions, called MC run-numbers. Nevertheless, the simulated pile-up profile does not match the observed one exactly and has to be corrected accordingly.

A procedure called pile-up reweighting is used to correct both, the $\langle N_{\text{vtx}} \rangle$ vs. μ distribution as well as the pile-up profile. It is described in Reference [107]. At first, the slope of the $\langle N_{\text{vtx}} \rangle$ vs. μ distribution is corrected. To achieve this, the μ value in data is scaled by a factor of 1.0/1.09 [108]. The scale factor is applied to observed rather than simulated data, since μ values in simulated data are always integers, and therefore scaling by a real number is not defined.

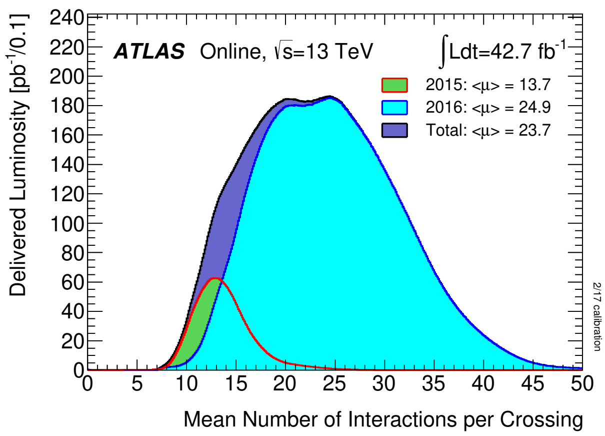

Figure 5.1: Measured pile-up profile for complete 2015 and 2016 dataset, taken from Ref. [58].

The pile-up weight w_{pu} is calculated on an event-to-event basis, depending on the corresponding μ bin i and MC run-number A from

$$w_{pu} = \frac{L_{A,i}}{L} \left(\frac{N_{A,i}}{N} \right)^{-1}, \tag{5.2}$$

where $L_{A,i}$ and $N_{A,i}$ refer to the integrated luminosity and summed generator weight for events with MC run-number A in pile-up bin i. As a result, the pile-up profile of simulated data is weighted to match the observed one. Events in observed data with a μ_{data} value not reproduced in simulated data are called unrepresented data. These events are reassigned to the μ_{MC} bin that is represented in simulated data and closest to the actual value of μ_{data} in data. Thus, simulated events in that bin will receive a higher pile-up weight.

5.2 Treatment of Leptons

Three different selection levels are defined for leptons in the analysis. Events entering the signal region and control regions used in the statistical evaluation are selected using leptons on *analysis level*, while the estimation of non-prompt background is based on *anti-ID* leptons. The loosest set of requirements that are shared between the analysis-level and anti-ID selections is used to define a *baseline level*. Objects on baseline level are used for overlap removal, as outlined in Section 5.5 and for vetoing leptons, as described in Section 7.1. Additionally to the selection requirements described below, on all levels at least one lepton has to match a triggered object, to ensure that one of the signal leptons fired the trigger. A summary of all selection levels is given in Table 5.1.

5.2.1 Lepton Isolation

Lepton candidates are reconstructed using calorimeter, tracking, and in case of muons, spectrometer information. Subsequently, identification algorithms are applied to select prompt leptons and the isolation of each lepton candidate is required. The isolation of objects in the detector can be calculated either using energy deposition in the calorimeter or tracks in the Inner Detector. In both methods, the amount of energy found in the region surrounding the lepton is taken as a measure for the lepton isolation; the higher the close-by energy deposits, the less likely it is for the lepton to be well isolated.

Calorimeter isolation is based on the lepton's topological calorimeter cluster, which consists of all calorimeter cells with energy responses higher than a pre-defined threshold. The barycenter of the lepton cluster is used to define the lepton axis. The energy of all clusters in a cone with a radius of $\Delta R = 0.2$ around the lepton axis is summed. The actual lepton energy has to be subtracted, and a leakage correction (correct for lepton energy that leaked into the isolation cone) as well as correction for pile-up energy deposition has to be applied. A more detailed description is given in Reference [109].

A second method, called *track isolation*, used to measure the isolation of a lepton candidate consists of summing up the transverse momenta of all tracks that lie in a cone around the lepton, and subtracting the lepton transverse momentum. For muons, the transverse momentum is taken as the momentum of the muon track. This procedure is not applicable to electrons, as these have a higher probability to create bremsstrahlung which can in turn convert and create secondary electrons. Therefore, the prompt electron transverse momentum is determined by dressing the primary electron track with the transverse momenta of all tracks that can be extrapolated into a cone of $\Delta R = 0.1$ around the electron calorimeter cluster.
The cone radius that is used to collect all surrounding tracks is dependent on the lepton track momentum:

$$\Delta R = \min \left(\frac{10\,\text{GeV}}{p_{\text{T}}[\text{GeV}]},\ \Delta R_{\text{max}} \right).$$

The maximum cone radius is given as ΔR_{max} which is taken as 0.2 for electrons and 0.3 for muons. A more detailed description can be found in Reference [109].

A set of different isolation working points are defined. The `Gradient` working point which is used for analysis-level electrons and muons in this analysis is optimized to have a high background rejection at low p_{T} while providing a high signal efficiency for high p_{T} tracks. The isolation efficiency ε_{iso} is therefore dependent on the lepton p_{T}, and given as $\varepsilon_{\text{iso}} = (0.1143 \cdot p_{\text{T}}[\text{GeV}] + 92.14)$ % [110].

5.2.2 Track Impact Parameters

In order to reject non-prompt leptons originating in secondary vertices or leptons from pile-up events, track impact parameters are calculated for each lepton candidate with respect to the primary vertex.

The distance of a track to the primary vertex is evaluated in the transverse and longitudinal direction. First, the track's *point of closest approach* (pca) to the z-axis is determined in the transverse $(x-y)$ plane, spanned by the unit vectors $\vec{e}_x$ and $\vec{e}_y$. The transverse impact parameter d_0 is defined as the distance of the pca to the z-axis in the transverse plane, as shown in Figure 5.2(a). The z-coordinate of the pca is called longitudinal impact parameter, z_0. The projection of the track on the $z-r$ plane is shown in Figure 5.2(b). The vector $\vec{r}$ is a linear combination of $\vec{e}_x$ and $\vec{e}_y$, perpendicular to the z-axis. As can be seen in Figure 5.2(b), z_0 is not necessarily transverse to the tangential track direction in pca. Therefore, requirements on the longitudinal distance to the primary vertex are generally set on $|z_0 \ \sin(\theta)|$, i. e. the component transverse to the track.

5.2.3 Electron Calibration

Electrons are calibrated in order to correct for energy lost in passive material in front of the electromagnetic calorimeter, leakage out of the reconstructed electromagnetic cluster and energy deposited beyond the electromagnetic calorimeter. The calibration procedure applied is explained in Reference [112]. As it is very similar to the one used in Run 1, more details can be found in Reference [113]. A brief summary of the process is given in the following. A flowchart visualizing the process is shown in Figure 5.3.

The procedure is applied in measured and simulated data. In simulated data (step 1), a boosted decision tree is trained [1] in order to provide an accurate estimate of the true electron or photon energy from measured quantities, using truth information. This is done in bins of E_{T} and η and separately for electrons, as well as converted and unconverted photons.

The electromagnetic calorimeter is segmented longitudinally in multiple layers. The first and second calorimeter layers are inter-calibrated (step 2). This is necessary in order to adjust the energy response for observed data to the simulation. Using $Z \to \mu\mu$ decays, the most probable value of the deposited particle energy $\langle E_{1/2} \rangle$ is calculated for the first and second layer, in observed and simulated data. This procedure is applied in bins of η. The resulting scale factor, $\alpha_{1/2}$, is calculated as

$$\alpha_{1/2} = \frac{\langle E_{1/2} \rangle^{\text{data}}}{\langle E_{1/2} \rangle^{\text{MC}}}.$$

In the barrel, $\langle E_{1/2} \rangle^{\text{data}}$ is on average 3 % lower than $\langle E_{1/2} \rangle^{\text{MC}}$, where as in the endcap the mean value of $\alpha_{1/2}$ is approximately 1. The values of $\alpha_{1/2}$ were determined in Run 1 and are reused in Run 2.

In step 3, the calibration trained in step 1 is applied to reconstructed cluster energies from measured and simulated data.

[1] Amongst others, the total shower energy, as well as the ratio of energy deposited in 1$^{\text{st}}$ to 2$^{\text{nd}}$ calorimeter layer E_1/E_2, and the pseudo rapidity of the cluster barycenter are used as input variables in the training of MC-based calibration procedure.

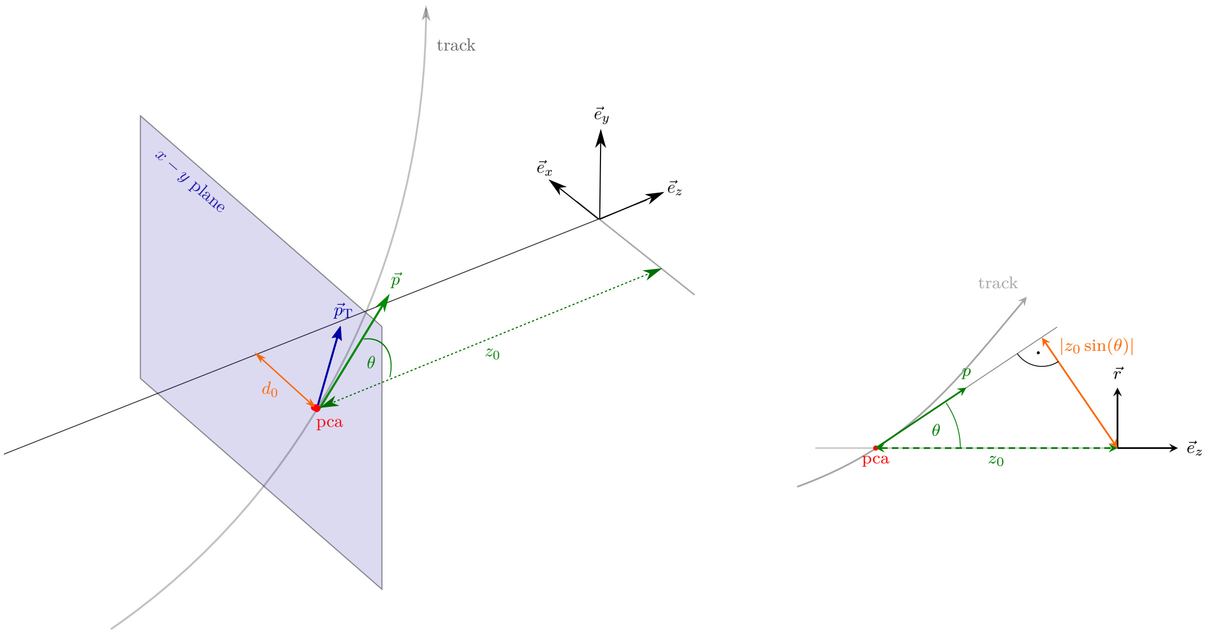

(a) Three-dimensional visualization of impact parameters (b) Projection onto $z-r$ plane

Figure 5.2: Illustration of the transverse (a) and longitudinal (b) impact parameters. The unit vectors $\vec{e}_x$, $\vec{e}_y$, $\vec{e}_z$ form the basis of the Cartesian coordinate system, as described in Section 3.2. The point of closest approach of the track to the z-axis (beam line) is labeled pca. The track momentum $\vec{p}$ in the pca is shown in green. The transverse momentum $\vec{p}_\mathrm{T}$ is the projection of $\vec{p}$ onto the $x-y$ plane. The impact parameters used in the analysis, d_0 and $|z_0\ \sin(\theta)|$, are highlighted in orange. Figure adapted from Ref. [111].

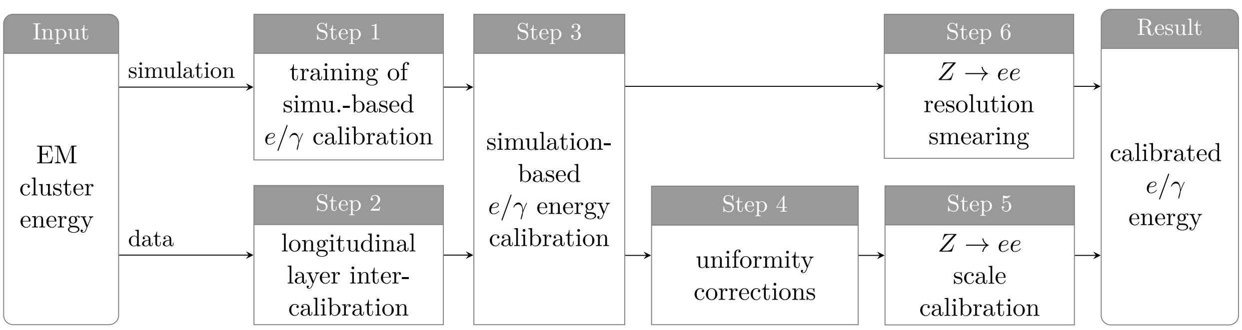

Figure 5.3: Illustration of calibration procedure applied to electrons, adapted from Ref. [113].

A set of corrections is applied to data (step 4), to mitigate the effect of variations not included in detector simulation. Thus, corrections need to be applied to account for calorimeter cells having a high-voltage value lower than the nominal value because of short circuits. In these sectors, the energy response differs from the nominal one. Clusters in the affected regions are corrected to restore uniformity of the response over ϕ. In the object selection, electron candidates are removed, if their cluster includes a bad cell. Additionally, the high-voltage values in the pre-sampler had to be lowered from the nominal value of 2000 V throughout Run 1 in order to counteract increasing noise due to higher instantaneous luminosity. It is currently run at a high-voltage value of 1200 V. The pre-sampler energy response has therefore to be reweighted to the nominal expectation. Furthermore, energy loss between barrel calorimeter modules needs to be considered. Due to gravity, the gaps between barrel modules have increased since the construction of the ATLAS detector. The calorimeter response has to be corrected accordingly. At last, the response of the electromagnetic calorimeter, although it is shown to be gain-independent in general, is observed to to vary with the selected gain[1] in small η regions. The response in these areas is appropriately corrected.

Then, the overall energy response in measured data is calibrated to the simulated response using $Z \to ee$ events, based on the position of the Z-peak. The deviation of the energy response in measured data from the simulated value is quantified as

$$E_i^{\text{data}} \;=\; E_i^{\text{MC}}\,(1+\alpha_i), \tag{5.3}$$

per η bin i. Considering only first-order terms and assuming that the angle between the electrons produced in the Z decay is known, this equation can be translated to invariant masses m_{ij} as follows

$$m_{ij}^{\text{data}} \;=\; m_{ij}^{\text{MC}}\,(1+\alpha_{ij}), \tag{5.4}$$

where i and j denote the η bins of the electron pair used to calculate the invariant mass. The scale factor α_{ij} can be approximated by $(\alpha_i + \alpha_j)/2$. The true value of the invariant mass is assumed to be m_{ij}^{MC}. The likelihood of the measured value of m_{ij}^{data} to be in agreement with the true value depends on the parameters α_i and α_j, and is denoted as $L_{ij}(m_{ij}^{\text{data}}|\alpha_i,\alpha_j)$. $L_{ij}(m_{ij}^{\text{data}}|\alpha_i,\alpha_j)$ is defined as convolution of a Breit-Wigner function and a Gaussian. The Breit-Wigner distribution models the shape of the resonance, while the Gaussian is used to describe the energy uncertainty due to imperfect detector resolution. The parameters α_i and α_j can be determined using a maximum-likelihood procedure (step 5). The likelihood $L_{ij}(m_{ij}^{\text{data,k}}|\alpha_i,\alpha_j)$ is evaluated for each event k and combined into a total likelihood. The resulting set of α_i is shown in Figure 5.4 (a).

The relative energy resolution, i. e. the width of the Z-peak in simulation is corrected (step 6) to match the measured resolution using

$$\left(\frac{\sigma(E)}{E}\right)_i^{\text{data}} \;=\; \left(\frac{\sigma(E)}{E}\right)_i^{\text{MC}} \oplus c_i', \tag{5.5}$$

where the operator $\oplus$ represents the quadratic summation of the respective quantities. The width of the measured and simulated distributions $\sigma(E)^{\text{data,MC}}$ are determined simultaneously with the $\alpha_{i,j}$ parameters in the likelihood fit. The constant smearing term c_i' is then calculated per η bin i according to Eq. (5.5). The derived set of c_i' values are shown in Figure 5.4 (b).

Systematic uncertainties include contributions from the uncertainty of the pre-sampler calibration, uniformity corrections (step 4), mis-modeling of the IBL material distribution in simulation, event selection of $Z \to ee$ events used for the data-driven calibration procedure as well as methodology and closure of this procedure (step 5), and from pile-up and calorimeter temperature variations between 2015 and 2016 data taking.

[1] Signal can be read as low, medium or high gain.

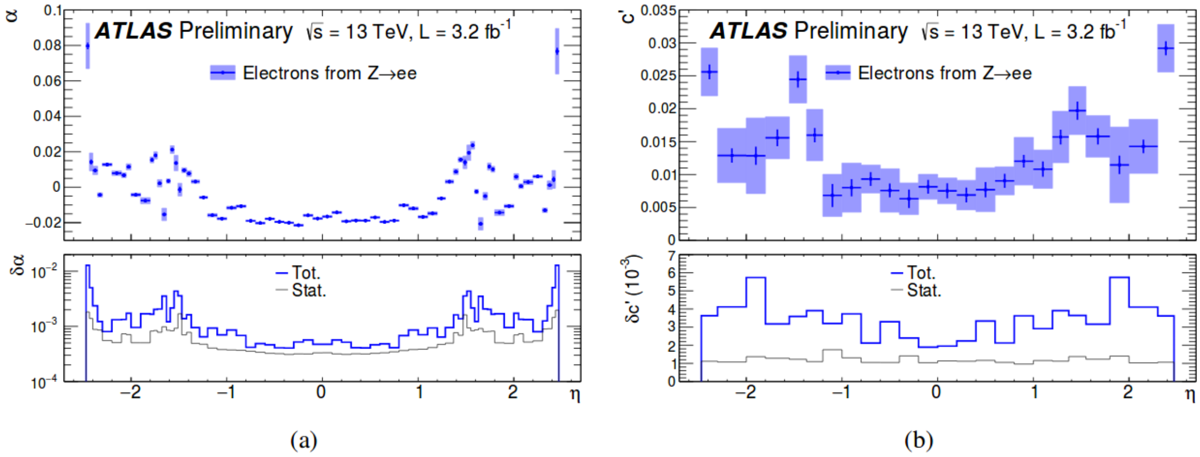

Figure 5.4: Energy scale factor α (a) and constant term c' used for smearing the energy resolution in simulation (b) are presented as a function of pseudo-rapidity η. In the top plots, the total uncertainty is shown (blue), while in the bottom plots, the statistical uncertainties are also given (gray). Figure taken from Ref. [112].

5.2.4 Electron Reconstruction and Selection

Electron as well as photon reconstruction is seeded in a cluster in the electromagnetic calorimeter. The cluster is then matched to tracks in the Inner Detector, and classified as electron candidate (`Author` $= 1$), photon candidate (`Author` $= 4$) or both (`Author` $= 16$). Only electrons which are classified as `Author` $= 1$ are accepted at analysis level [114].

Electron candidates are calibrated as discussed in Section 5.2.3. Baseline electrons are required to have a transverse momentum of at least 6 GeV, while the transverse momentum of anti-ID- and analysis-level electrons is required to be at least 20 GeV and 27 GeV, respectively. The geometric acceptance is constrained by detector layout. Reconstruction of central electrons depends on tracking information, therefore only object $|\eta| < 2.47$ are accepted[1]. Since baseline objects are used for overlap removal (see Section 5.5), electrons in the transition region between the tracker barrel and end-caps with $|\eta| \in [1.37, 1.52]$ are included. These objects are, however, rejected at analysis and anti-ID level. Additionally, on both levels, the geometric acceptance of the ee channel is reduced to barrel tracks with $|\eta| < 1.37$, as the charge mis-ID rate notably increases for end-cap tracks. All electrons have to meet impact parameter requirements of $|z_0 \sin\theta| < 0.5$ mm and $|d_0/\sigma_{d_0}| < 5$.

In order to select prompt electrons, an identification algorithm is applied to electron candidates. The identification algorithm is based on a set of variables sensitive to the shape of the electromagnetic shower, the Inner Detector track quality and the accuracy with which a track can be matched to an electromagnetic cluster. These variables are combined in a likelihood template. Details on the variables and the identification procedure are given in Reference [114]. Three different identification working points, `Loose`, `Medium` and `Tight` are defined. The electron reconstruction and identification efficiencies in $Z \to ee$ events are shown in Figure 5.5 for all working points. Baseline electrons are required to pass the `Loose` working point and have at least one IBL hit. On analysis level, electrons are required to satisfy the `Tight` selection and `Gradient` isolation (see Section 5.2.1). This criterion is inverted for anti-ID electrons, which are required to pass the `Medium` identification but fail either `Tight` identification or `Gradient` isolation.

[1]Forward electrons, which lie beyond $|\eta| = 2.47$ are not used in this analysis. Their reconstruction and calibration is purely based on calorimeter information, which introduces comparably large systematic uncertainties. These cannot be compensated by the gain in statistical power.

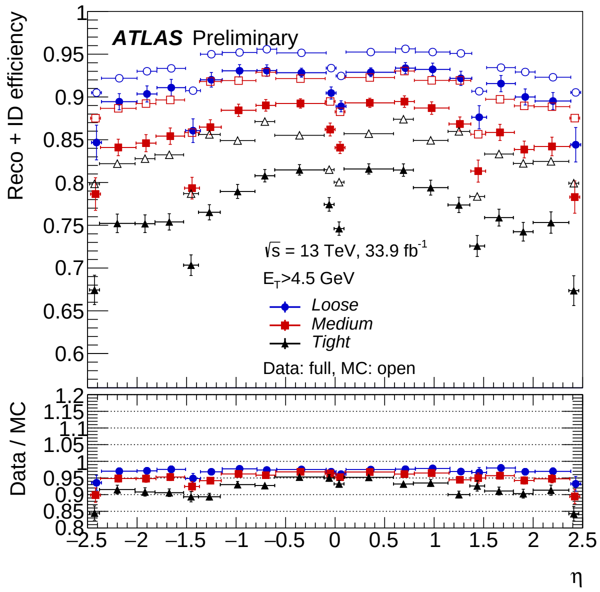

Figure 5.5: Electron reconstruction and identification efficiencies in observed (full) and simulated (open) $Z \to ee$ events as a function of pseudo-rapidity, for electrons with $E_{\mathrm{T}} > 4.5\,\mathrm{GeV}$ and different identification working points. The total statistical and systematic uncertainty is given. Figure taken from Ref. [115].

5.2.5 Muon Calibration

As described in the Section 5.2.6, the momentum of combined muons is measured separately in the Inner Detector and the muon spectrometer (MS). The measured quantities are denoted as $p_{\mathrm{T}}^{\mathrm{ID}}$ and $p_{\mathrm{T}}^{\mathrm{MS}}$, respectively. In the calibration procedure, the transverse momenta $p_{\mathrm{T}}^{\mathrm{ID}}$ and $p_{\mathrm{T}}^{\mathrm{MS}}$ of muons in simulated events are corrected separately. The method is explained in Reference [116] and is shortly summarized hereafter.

Scale corrections $s^{\mathrm{ID,MS}}$ and resolution smearing parameters $\Delta r^{\mathrm{ID,MS}}$ are applied to $p_{\mathrm{T}}^{\mathrm{ID,MS}}$ in bins of pseudo-rapidity η and azimuth ϕ. The bins are chosen in a way to create regions of similar detector performance and equipment. For the MS, two sets of scale corrections are derived. s_0^{MS} accounts for the energy loss of a muon while proceeding from the primary vertex to the MS. It is assumed that no energy is lost between the primary vertex and the Inner Detector, and s_0^{ID} is therefore set to zero. The inaccuracy in the modeling of the magnetic field and the detector (Inner Detector or MS) dimensions perpendicular to it are represented in $s_1^{\mathrm{ID,MS}}$. The scaled transverse momentum $p_{\mathrm{T}}^{\mathrm{scaled}}$ is then written as

$$p_{\mathrm{T}}^{\mathrm{scaled,ID}} = p_{\mathrm{T}}^{\mathrm{ID}}\,(1 + s_1^{\mathrm{ID}}), \tag{5.6}$$
$$p_{\mathrm{T}}^{\mathrm{scaled,MS}} = p_{\mathrm{T}}^{\mathrm{MS}}\,(1 + s_1^{\mathrm{MS}}) + s_0^{\mathrm{MS}}. \tag{5.7}$$

The scaled momentum is subsequently smeared to match the resolution in data. This is achieved using two smearing parameters, $\Delta r_1^{\mathrm{ID,MS}}$ and $\Delta r_2^{\mathrm{ID,MS}}$. These are used to correct for multiple scattering and unsimulated magnetic field inhomogeneities as well as resolution effects caused by the spatial resolution and residual mis-alignment of the detectors. The corrected momentum is given as

$$p_{\mathrm{T}}^{\mathrm{Cor,Det}} = \frac{p_{\mathrm{T}}^{\mathrm{scaled,Det}}}{1 + g_1\,\Delta r_1^{\mathrm{Det}} + g_2\,\Delta r_2^{\mathrm{Det}}\,p_{\mathrm{T}}^{\mathrm{Det}}}, \tag{5.8}$$

where Det either refers to the Inner Detector or MS and $g_{1,2}$ are random numbers following a standard Gaussian distribution.

Scale and resolution parameters are determined in simulated $J/\Psi \to \mu\mu$ and $Z \to \mu\mu$ events, selecting events with an invariant mass near the respective resonance[1]. A template fit of the resonance is performed in each (η, ϕ) bin. The resulting parameters $s_1^{\mathrm{ID,MS}}$ and $\Delta r_1^{\mathrm{ID,MS}}$ are of the order of 10^{-3}. The values of Δr_2^{ID} and Δr_2^{MS} range from $(0.05 \pm 0.01$ to $0.34 \pm 0.08)\,\mathrm{TeV}^{-1}$ and $(0.080 \pm 0.006$ to $0.162 \pm 0.007)\,\mathrm{TeV}^{-1}$, respectively. s_0^{MS} varies between $(-26 \pm 7)\,\mathrm{MeV}$ and $(-3 \pm 12)\,\mathrm{MeV}$.

The final combined corrected momentum $p_{\mathrm{T}}^{\mathrm{Cor,comb}}$ is calculated as the weighted sum of $p_{\mathrm{T}}^{\mathrm{Cor,ID}}$ and $p_{\mathrm{T}}^{\mathrm{Cor,MS}}$. The weights remain unchanged with respect to the weights used to calculated the initial, uncorrected $p_{\mathrm{T}}^{\mathrm{comb}}$.

Systematic uncertainties assigned to the calibration results take into account uncertainties from the definition of the invariant mass window for $Z \to \mu\mu$ events, the parametrization of the background in the fit of J/Ψ events, and variations in the fit strategy for determining the scale factors. Systematic uncertainties for Δr_2^{MS} are taken from separate alignment studies performed during dedicated runs.

5.2.6 Muon Reconstruction and Selection

In general, muons traverse the ATLAS detector, creating a track in the Inner Detector, depositing a small part of their energy in the calorimeters and are finally measured precisely in the MS. Muon reconstruction is seeded in the MS. Muon tracks are built by combining hits in different parts and layers of the MS. Based on that track, different muon objects can be reconstructed. Details on muon reconstruction are given in Reference [116].

Combined (CB) muons are reconstructed, by matching a MS track to an inner detector track. The combined transverse momentum is taken as a weighted sum of the Inner Detector and MS track momenta. In the case of *extrapolated* (ME) muons, the MS track is not matched to an Inner Detector track, but extrapolated to the nominal interaction point. These muons are included in the baseline definition, as they enlarge the geometric acceptance to $|\eta| = 2.7$, and are used in the overlap removal procedure. The region of $|\eta| < 0.1$, the MS is only partially instrumented as cabeling and service access is needed for the Inner Detector and calorimeters. In this region, *segment-tagged* (ST) and *calorimeter-tagged* (CT) muons are also used. ST muons are reconstructed if the extrapolated Inner Detector track matches at least one track segment in the MS. A muon is reconstructed as CT muon if the extrapolated Inner Detector track can be matched to an energy deposit in the calorimeters that is consistent with a minimum-ionizing particle. ST and CT muons are included on baseline level, as they are useful in the overlap removal. On analysis and anti-ID level, combined muons up to $|\eta| = 2.5$ are used. Impact parameters are required to pass $|z_0 \sin\theta| < 0.5\,\mathrm{mm}$ (all levels) and $|d_0/\sigma_{d_0}| < 10$ (3) on baseline and analysis level, respectively.

Muons are calibrated as described in Section 5.2.5, and are required to have a transverse momentum of at least 6 GeV and 27 GeV at baseline and analysis/anti-ID level, respectively.

Muon identification is optimized to reduce contributions from background like pion and kaon decays. The charge and momentum measurement significance in Inner Detector and MS, the fit quality of the combined muon track and the difference in the Inner Detector and MS momentum measurements are used as identification variables. Further information on the identification can be found in Reference [116]. Four muon reconstruction quality working points are provided, `Loose`, `Medium`, `Tight` and `High-`p_{T}. The `Loose` working point is identical to the `Medium` one for CB and ME muons, however, CT and ST muons are included in the region of $|\eta| < 0.1$. In this analysis, `Loose` muons are selected on baseline level. Analysis-level and anti-ID muons are to pass `Medium` quality requirements. Reconstruction efficiencies for `Loose` and `Medium` muons are shown in Figure 5.6.
`Gradient` isolation is required on analysis level in order to suppress muons from heavy meson decays. Anti-ID muons are required to either fail `Gradient` isolation or have a transverse impact parameter significance of $|d_0/\sigma_{d_0}| \geq 3$.

[1] In $J/\Psi \to \mu\mu$ ($Z \to \mu\mu$) events with an invariant mass from 2.65 GeV to 3.6 GeV (76 GeV to 106 GeV) are selected.

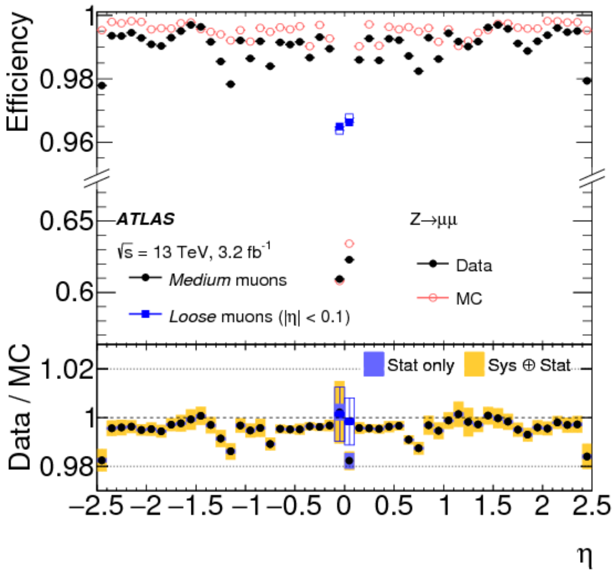

Figure 5.6: Muon reconstruction efficiency for the `Loose` and `Medium` working points as a function of pseudo-rapidity η. Efficiencies are measured in $Z \to \mu\mu$ events for muons with $p_{\mathrm{T}} > 10\,\mathrm{GeV}$. In the ratio plot, the statistical and total uncertainties are given. Figure taken from [116].

5.3 Treatment of Jets

The jet reconstruction starts with the collection of topological clusters of calorimeter cells. The necessary signal-to-noise ratio is defined taking into account pile-up contributions as explained below. Topological clusters exceeding a transverse momentum of 7 GeV are reconstructed as anti-k_{T} jets [117] with a radius parameter of $R = 0.4$ [118]. In the course of this section, a short description of the treatment of pile-up, the jet energy scale and resolution correction as well as the identification of b-jets is given. Finally, the jet selection applied in this analysis is summarized.

5.3.1 Jet Reconstruction and Pile-Up Rejection

Pile-up, i. e. energy deposits coming from vertices other than the primary vertex in the current (*in-time* pile-up) or other LHC bunch crossing (*out-of-time* pile-up) can impact the energy and momentum measurement of objects from the hard scattering process. As the amount of hadronic activity is generally high, jet reconstruction is particularly susceptible to pile-up.

In order to reduce its impact on jet measurements, subtraction techniques are applied. These are designed to reject energy deposits that cannot be associated to the primary vertex. Moreover, jets originating in pile-up are identified and suppressed using central and forward *jet vertex tagging* (JVT, fJVT) [119, 120]. Regarding pile-up subtraction and JVT, the Run 1 approaches are used by analyses relying purely on 2015 and 2016 data. These are explained in Reference [121], summarized in the following.

Pile-up reduction is already applied during jet clustering. When building topological clusters from calorimeter cells, only cells surpassing a certain signal-to-noise ratio are accepted. The noise introduced by pile-up is estimated from simulation and added to the electronic noise, thus reducing the number of cells included in jet clusters but also impeding the creation of jet clusters seeded in pile-up energy deposits. As mentioned above, anti-k_{T} jets are reconstructed based on these jet clusters.

Pile-up subtraction, i. e. the correction of the reconstructed $p_{\mathrm{T}}^{\mathrm{jet}}$, is the first step in *jet energy scale* (JES) correction. It therefore has high impact on the JES systematic uncertainties. The momentum correction is applied as

$$p_{\mathrm{T}}^{\mathrm{corr}} = p_{\mathrm{T}}^{\mathrm{jet}} - \mathcal{O}^{\mathrm{jet}}, \tag{5.9}$$

where the offset correction $\mathcal{O}^{\mathrm{jet}}$ is calculated as the product of the the pile-up p_{T} density ρ and the jet area A^{jet} [122, 123]. For each event, ρ is estimated from the set of all k_{T} jets [124] with index i as

$$\rho = \mathrm{median}\left\{\frac{p_{\mathrm{T,i}}^{\mathrm{jet}}}{A_i^{\mathrm{jet}}}\right\}. \tag{5.10}$$

After this event-by-event subtraction, a small pile-up dependence persists. In general, this applies to cells with a high signal-to-noise ratio in the center of hard jets, where the clustering algorithm is not susceptible to additional energy deposits from pile-up. Furthermore, jets in the forward regions with $|\eta| > 2.5$ are less pile-up robust, as the coarser calorimeter segmentation increases the probability to include pile-up contributions. This is partially remedied by subtracting a residual correction $\langle \mathcal{O}^{\mathrm{jet}}(\langle\mu\rangle, N_{\mathrm{vtx},\eta})\rangle$, which is taken from simulation and averaged over all events. Based on Eq. (5.9), the final pile-up corrected jet momentum is then given by

$$p_{\mathrm{T}}^{\mathrm{corr}} = p_{\mathrm{T}}^{\mathrm{jet}} - \rho \times A^{\mathrm{jet}} - \langle \mathcal{O}^{\mathrm{jet}}(\langle\mu\rangle, N_{\mathrm{vtx},\eta})\rangle. \tag{5.11}$$

Following the soft pile-up correction discussed above, pile-up jets can still be reconstructed as a consequence of an actual hard pile-up process or the superposition of several soft contributions. Two separate tools are used to identify pile-up jets in the central and forward region. In the central region, which is covered by the Inner Detector, the identification relies on a multivariate combination of several, pile-up sensitive tracking variables. The *jet vertex fraction* (JVF) is calculated per jet, using the transverse track momenta of tracks k belonging to the specific jet. For each jet, the scalar sum of all track momenta $\Sigma p_{\mathrm{T}}^{\mathrm{trk}}$ associated to the primary vertex V_0 is calculated as $\sum_k p_{\mathrm{T}}^{\mathrm{trk},k}(V_0)$. Further, the scalar sum of all track momenta associated to additional (pile-up) vertices $p_{\mathrm{T}}^{\mathrm{PU}}$ is given by $\sum_{n\geq 1}\sum_l p_{\mathrm{T}}^{\mathrm{trk},l}(V_n)$, where n and l are counting all reconstructed vertices and tracks, respectively. The JVF is then defined as [119]

$$\mathrm{JVF} = \frac{\Sigma p_{\mathrm{T}}^{\mathrm{trk}}}{\Sigma p_{\mathrm{T}}^{\mathrm{trk}} + p_{\mathrm{T}}^{\mathrm{PU}}}. \tag{5.12}$$

However, $p_{\mathrm{T}}^{\mathrm{PU}}$ increases proportionally with the number of reconstructed vertices per event, which is growing with increasing luminosity. Therefore, a correction term is introduced by normalizing $p_{\mathrm{T}}^{\mathrm{PU}}$ with a constant c and the number of pile-up tracks per event $N_{\mathrm{trk}}^{\mathrm{PU}}$. The corrected JVF, denoted as corrJVF is then written as

$$\mathrm{corrJVF} = \frac{\Sigma p_{\mathrm{T}}^{\mathrm{trk}}}{\Sigma p_{\mathrm{T}}^{\mathrm{trk}} + \frac{p_{\mathrm{T}}^{\mathrm{PU}}}{c\, N_{\mathrm{trk}}^{\mathrm{PU}}}}. \tag{5.13}$$

Another variable used for JVT is the ratio of $\Sigma p_{\mathrm{T}}^{\mathrm{trk}}$ and the fully calibrated jet momentum $p_{\mathrm{T}}^{\mathrm{jet}}$, called $R_{p_{\mathrm{T}}}$.

There is a high separation power between real and pile-up jets in the two-dimensional $(R_{p_{\mathrm{T}}}, \mathrm{corrJVF})$ plane. This is exploited by calculating a two-dimensional likelihood for a jet to originate in the primary vertex, based on a k-nearest neighbor algorithm [125]. The resulting JVT score ranges from 0 for pile-up like jets to 1 for hard-scatter-like jet[1]. The JVT selection efficiency is approximately 92 % for hard-scattering jets with $p_{\mathrm{T}}^{\mathrm{jet}} > 20\,\mathrm{GeV}$ at the recommended working point. The efficiency distribution as function of $p_{\mathrm{T}}^{\mathrm{jet}}$ is shown in Figure 5.7(a).

The central JVT procedure is not applicable in the forward region due to the lack of tracking information. Instead, the fJVT exploits transverse momentum conservation, under the assumption that the production cross section of high-p_{T} neutrinos is small compared to the multi-jet cross section. The total transverse momentum of tracks and jets in the central region associated to vertices

[1] A value of -1 is assigned to central jets without any tracking information.

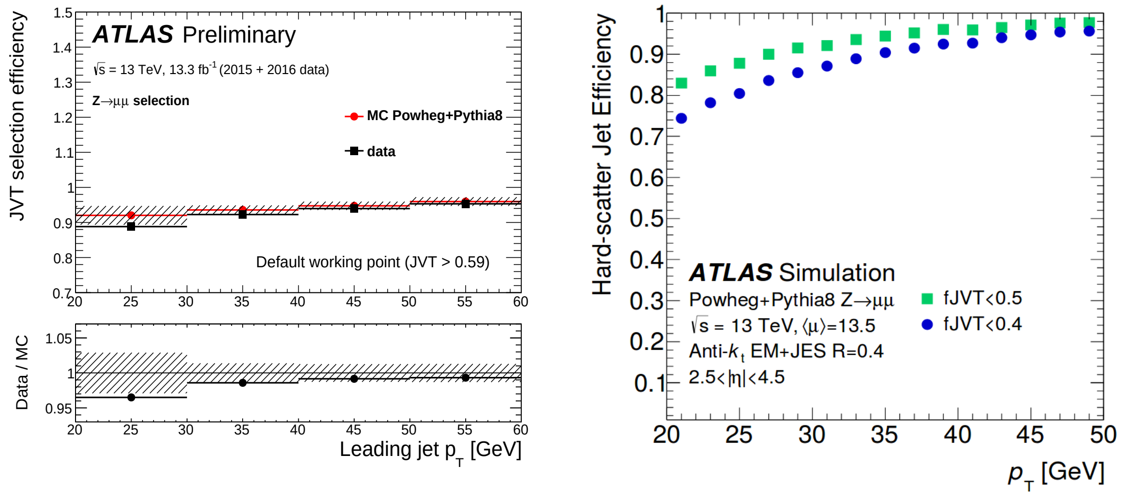

(a) JVT Efficiency (b) fJVT Efficiency

Figure 5.7: (a) JVT selection efficiency of jets originating in the primary vertex, measured in $Z \to \mu\mu + j$ events for the recommended working point [126] and (b) fJVT selection efficiency of jets originating in the primary vertex, measured in $Z +$ jets events. The recommended working point of fJVT < 0.5 is used in the analysis [120].

other than the primary vertex is calculated. Consequently, the missing transverse momentum $\langle p_{\mathrm{T,i}}^{\mathrm{miss}} \rangle$ is calculated per vertex V_i as

$$\langle \vec{p}_{\mathrm{T,i}}^{\,\mathrm{miss}} \rangle \;=\; -\frac{1}{2}\left(k \cdot \sum_{\substack{\text{tracks}\\ \in\, V_i}} \vec{p}_{\mathrm{T}}^{\,\mathrm{trk}} \;+\; \sum_{\substack{\text{jets}\\ \in\, V_i}} \vec{p}_{\mathrm{T}}^{\,\mathrm{jet}} \right), \tag{5.14}$$

where the constant k is compensating the momenta from neutral particles, which are included in the total transverse jet, but not the track momentum. For each forward jet with transverse momentum $\vec{p}_{\mathrm{T}}^{\,\mathrm{fw-jet}}$, the fJVT$_i$ score can be calculated per vertex i, and its final fJVT score is defined as the maximum over all vertices:

$$\text{fJVT(fw-jet)} \;=\; \max\left(\text{fJVT}_i\,(\text{fw-jet})\right) \;=\; \max\left(\frac{\langle \vec{p}_{\mathrm{T,i}}^{\,\mathrm{miss}} \rangle \cdot \vec{p}_{\mathrm{T}}^{\,\mathrm{fw-jet}}}{\left| \vec{p}_{\mathrm{T}}^{\,\mathrm{fw-jet}} \right|^2} \right). \tag{5.15}$$

The selection efficiency for hard-scattering jets from the primary vertex is shown in Figure 5.7(b). The recommended working point of fJVT < 0.5 is used in this analysis.

5.3.2 Jet Calibration

The four-momentum of uncalibrated, reconstructed jets is given at the electromagnetic scale, and with respect to the center of the detector. At first, its direction is corrected to point to the primary vertex, leaving the energy unchanged [118]. Then, the event-by-event and residual pile-up correction are applied as discussed above. The complete calibration approach including systematic uncertainties is given in Reference [118] and will be outlined below.

The *absolute jet energy scale* (JES) *calibration* is derived from simulation, following the Run 1 approach [127, 128]. It is calculated in bins of η and used to correct the reconstructed four-momentum to the energy scale at particle level. This leaves the JES response $\mathcal{R}$ almost independent on the jet transverse momentum and pseudo-rapidity. $\mathcal{R}$ is defined as

$$\mathcal{R} \;=\; \frac{E^{\mathrm{reco}}}{E^{\mathrm{truth}}}, \tag{5.16}$$

where E^{reco} denotes the reconstructed, pile-up corrected jet energy, and E^{truth} represents the jet energy on truth level.

After the absolute calibration, the JES response is still dependent on the jet shower shape. The shower shape is influenced by the particle and flavor content. Leakage out of the hadronic calorimeter can occur for high-p_{T} jets. In this case, the shower would extend into the muon spectrometer (MS), which is often referred to as *punch-through*. The *global sequential calibration* consists of independent four-momentum corrections applied to a set of shower shape observables. The corrections are derived in bins of jet p_{T} and E for observables referring to calorimeter or track properties and the MS, respectively.

The final step in JES calibration is the *in-situ calibration*, applied to remove residual difference in the JES responses of measured and simulated data. These can, amongst others, be caused by imperfections in the simulation of pile-up, hadronization and the detector material distribution. The in-situ calibration is derived by comparing jets to well-measured reference objects. The in-situ energy response $\mathcal{R}_{\text{in-situ}}$ is defined in observed data and simulation as averaged ratio of jet p_{T} over reference object p_{T}. Four different inter-calibration schemes are defined in order to generate a large kinematic and geometric coverage. The corresponding in-situ responses are measured by comparing 1. forward jets ($0.8 < |\eta| < 4.5$) to central jets ($|\eta| < 0.8$), and central jets to 2. Z-boson, 3. photon (both within $|\eta| < 0.8$), and 4. multi-jet systems ($|\eta| < 0.8$). For each inter-calibration scheme j, the response is measured in observed data and simulation, and denoted as $\mathcal{R}_{\text{in-situ}}^{\text{data,j}}$ and $\mathcal{R}_{\text{in-situ}}^{\text{MC,j}}$, respectively. The ratio $c_j = \mathcal{R}_{\text{in-situ}}^{\text{data,j}} / \mathcal{R}_{\text{in-situ}}^{\text{MC,j}}$ is calculated per inter-calibration scheme and statistically combined to a final value c. After inverting c, the calibration is applied to observed data, and ranging between 4 % and 2 % for low- and high-p_{T} jets, respectively.

Systematic uncertainties are related to pile-up correction, flavor composition, punch-through jets, and all inter-calibration schemes. An additional uncertainty is assigned to the effect of varying the jet energy resolution (JER) on the calibration results. The JER is defined as the width of the jet response distribution as given in Eq. (5.16). JER values in simulation are smeared, and all calibration results are re-derived. The difference to the nominal result is taken as a systematic uncertainty [129].

5.3.3 Identification of b-Jets

The identification of b-jets, i. e. jets stemming from b-quarks is crucial for reducing the background from $t\bar{t}$ decays and hadronically decaying $W^{\pm}$-bosons. The algorithm used in this analysis is explained in Reference [130]. The identification relies on decay properties of hadrons containing b-quarks. In contrast to jets from light quarks like u, d and s, heavy jets are more likely to be collimated, with high p_{T} and a reconstructable secondary vertex. The secondary vertex marks the point where the b-hadron decayed into a $W^{\pm}$-boson and lighter quarks. In case the $W^{\pm}$-boson decays leptonically, it may be possible to reconstruct the lepton outside of, but close to the jet. Thus, muons produced in b-hadron decays have a large contribution to the non-prompt background in this analysis.

Various methods have been used in the past to identify b-jets. These were based on the transverse and longitudinal impact parameter distributions (IP2D, IP3D), trying to reconstruct the secondary vertex (SV) or reconstructing the heavy quark trajectory between the primary and secondary vertex (`JetFitter`). An overview of these algorithms is given in Reference [130].

The current algorithm combines the output of IP2D, IP3D, SV and `JetFitter` as well as the jet pseudo-rapidity and transverse momentum using a boosted decision tree (BDT). During the training, b-jets from $t\bar{t}$ decays are considered as signal. The background is taken as a mixture of c- and light-flavor jets. A set of three different BDTs are provided by the CP group, where the c-jet fraction in the background composition is varied between 15 % and 0 %. Increasing the c-jet fraction has a positive effect on the separation power between c- and b-jets, at the expense of a reduced light-flavor jet rejection. The recommended BDT has a c- to light-flavor jet ratio of 7 : 93, which yields the best balance of high light-flavor and c-quark rejection.

In Figure 5.8, the rejection rate for light-flavor and c-jets over the b-jet identification efficiency is shown. In this analysis, b-jets are identified with an efficiency of 85 %, corresponding to a rejection factor[1] of 33 and 3.1 for light-flavor and c-jets, respectively. In the analysis selection, events are vetoed if they contain an identified b-jet. Several b-tagging working points have been tested, and the relatively loose working point of 85 % is chosen to ensure a precise estimate of the non-prompt background [131].

5.3.4 Jet Selection

The allowed geometrical region for jets covers the whole detector volume up to $|\eta| = 4.5$. Central jets inside $|\eta| = 2.4$ are accepted down to a transverse momentum of $p_{\mathrm{T}} = 25\,\mathrm{GeV}$. To reduce pile-up jets, the lower p_{T} requirement is raised to 30 GeV for forward jets above $|\eta| = 2.4$. Jets passing these selection criteria are defined as baseline jets, used for overlap removal. On analysis-level, a minimum transverse momentum of 65 GeV and 35 GeV is required for the leading and subleading jet, respectively. Furthermore, the JVT and fJVT selection is applied to jets with transverse momentum between 25 GeV and 60 GeV as explained in Section 5.3.1.

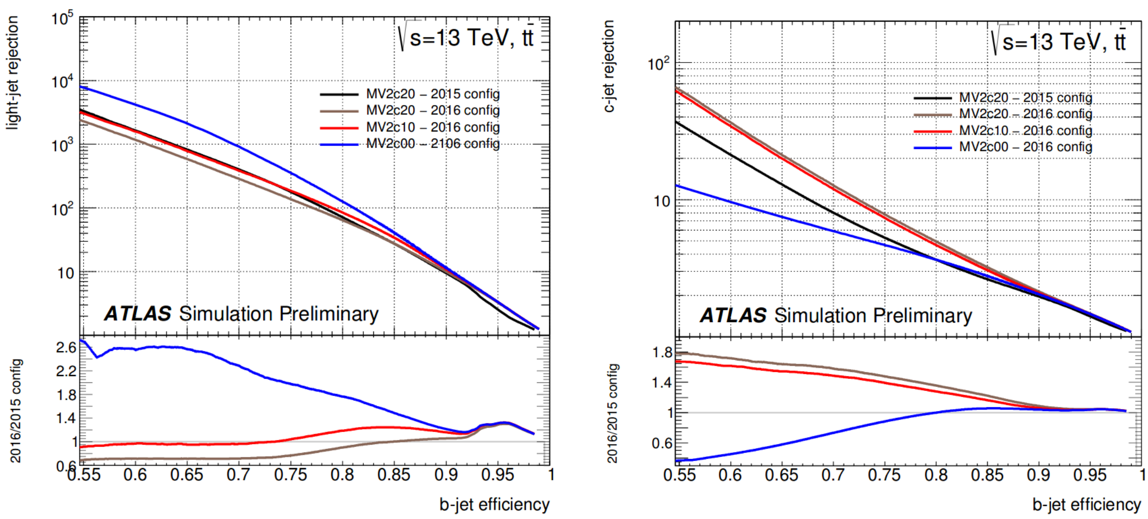

(a) light-flavor jet rejection

(b) c-jet rejection

Figure 5.8: Rejection versus b-jet identification efficiency for light-flavor (a) and c-jets (b) as a comparison between different BDT training options, measured in $t\bar{t}$ events. MV2c20 (2015 config) refers the to 2015 version of a BDT with a c-jet fraction of 20 % included in the background estimate. In addition to other improvements, background composition in the 2016 configuration was changed to include 0 %, 7 % and 15 % of c-jets, named MV2c00, MV2c10 and MV2c20 respectively. Figure taken from Ref. [130].

[1]The rejection factor is calculated as the ratio of the number of rejected over falsely accepted background objects

5.4 Missing Transverse Momentum Reconstruction

The reconstruction procedure and its performance is discussed in Reference [132], and summarized below. In general, the missing transverse energy and momentum, $E_{\mathrm{T}}^{\mathrm{miss}}$ and $\vec{E}_{\mathrm{T}}^{\mathrm{miss}}$, consists of two components. One refers to to the *hard objects* in the scattering process (i. e. all objects needed in the analysis) and the *soft-event* (which are charged tracks associated to the primary vertex, but not to any aforementioned analysis object).

Some particles produced in hard scattering processes can leave the detector without depositing any energy. This is true for Standard Model neutrinos, but also for other proposed, more exotic particles. The presence of these particles in an event can only be registered by summing all measured transverse momenta. As the beam is highly collimated in (x, y) direction before the collision, momentum conservation dictates that the sum of all momenta in the transverse plane has to be zero. Therefore, if the vectorial sum is not zero, another, invisible particle has to have carried the remaining momentum out of the detector in the opposite direction of the remaining transverse momentum. This missing transverse momentum $\vec{E}_{\mathrm{T}}^{\mathrm{miss}}$ is defined as

$$\vec{E}_{\mathrm{T}}^{\mathrm{miss}} = - \sum_{i \in \{\text{hard objects}\}} \vec{p}_{\mathrm{T,i}} - \sum_{j \in \{\text{soft objects}\}} \vec{p}_{\mathrm{T,j}}, \tag{5.17}$$

from which the missing transverse energy $E_{\mathrm{T}}^{\mathrm{miss}}$ can be calculated as the absolute value

$$E_{\mathrm{T}}^{\mathrm{miss}} = |\vec{E}_{\mathrm{T}}^{\mathrm{miss}}| = \sqrt{(E_x^{\mathrm{miss}})^2 + \left(E_y^{\mathrm{miss}}\right)^2}. \tag{5.18}$$

The azimuthal angle ϕ^{miss} associated to the missing transverse momentum can be calculated as

$$\phi^{\mathrm{miss}} = \arctan\left(\frac{E_x^{\mathrm{miss}}}{E_y^{\mathrm{miss}}}\right). \tag{5.19}$$

As all detector components are included in the calculation of $\vec{E}_{\mathrm{T}}^{\mathrm{miss}}$, resolution effect have an important role in the process. It is observed that $\vec{E}_{\mathrm{T}}^{\mathrm{miss}}$ is finite, even in simulated processes where $E_{\mathrm{T}}^{\mathrm{miss}}$ is expected to be zero. Therefore, the scalar sum of transverse momenta, ΣE_{T}, in the event is calculated as an additional quantity, and used to judge the activity in the event. It is given as

$$\Sigma E_{\mathrm{T}} = \sum_{i \in \{\text{hard objects}\}} p_{\mathrm{T,i}} + \sum_{j \in \{\text{soft objects}\}} p_{\mathrm{T,j}}. \tag{5.20}$$

Which types of objects are considered as *hard object* in Eq. (5.17) and (5.20) is dependent on analysis requirements. In this analysis, all objects reconstructed as electrons, jets or muons are included in the $E_{\mathrm{T}}^{\mathrm{miss}}$ calculation.

In order to avoid double-counting of energy deposits, the *signal ambiguity resolution* algorithm assures, that all objects contributing to $E_{\mathrm{T}}^{\mathrm{miss}}$ and ΣE_{T} are reconstructed from mutually exclusive detector signals. This is done by assigning a priority to each type of object, and adding the respective objects to the $E_{\mathrm{T}}^{\mathrm{miss}}$ calculation accordingly. In general, electrons are treated with highest priority, followed by photons, hadronically decaying tau-leptons, and jets. In case a lower ranked object contains detector signals already contained in an accepted object with higher priority, the lower ranked object is rejected. Remaining energy deposits not associated to any accepted hard object are added to the soft contribution. Muons are added last, and in case of isolated muons, no overlap with any other object is expected. In case of non-isolated muons, a muon-jet overlap removal is performed. As the $E_{\mathrm{T}}^{\mathrm{miss}}$ calculation depends on the calibration of all objects, only calibrated electrons, muons and jets passing the baseline selection criteria are used in the $E_{\mathrm{T}}^{\mathrm{miss}}$ calculation.

Taking into account the step-wise procedure of adding hard objects mentioned above, Eq. (5.17) can be written more explicitly, for the simplified case of this analysis, as

$$\vec{E}_{\mathrm{T}}^{\mathrm{miss}} = \underbrace{- \sum_{\substack{\text{selected}\\\text{electrons}}} \vec{p}_{\mathrm{T}}^{\,e} - \sum_{\substack{\text{accepted}\\\text{muons}}} \vec{p}_{\mathrm{T}}^{\,\mu} - \sum_{\substack{\text{accepted}\\\text{jets}}} \vec{p}_{\mathrm{T}}^{\,\mathrm{jet}}}_{\text{hard term}} - \underbrace{\sum_{\substack{\text{unused}\\\text{tracks}}} \vec{p}_{\mathrm{T}}^{\,\mathrm{track}}}_{\text{soft term}}, \tag{5.21}$$

$$= - \vec{p}_{\mathrm{T}}^{\,\mathrm{hard}} - \vec{p}_{\mathrm{T}}^{\,\mathrm{soft}}. \tag{5.22}$$

It is also possible to include contributions from neutral particles in the soft term by considering calorimeter clusters without associated Inner Detector tracks. This, however, introduces a pile-up dependence resulting in a decreasing resolution with increasing number of reconstructed vertices in the event [132]. Hence, the recommended track-based soft term is used in this analysis.

Systematic scale and resolution uncertainties on the $E_{\mathrm{T}}^{\mathrm{miss}}$ reconstruction are derived. As the systematic uncertainties on the hard objects are included separately in the analysis, only the the scale and resolution uncertainties on the soft component have to be evaluated. The soft component $\vec{p}_{\mathrm{T}}^{\,\mathrm{soft}}$ can be written as the sum of the components parallel and perpendicular to the hard component

$$\vec{p}_{\mathrm{T}}^{\,\mathrm{soft}} = \vec{p}_{\mathrm{T},\parallel}^{\,\mathrm{soft}} + \vec{p}_{\mathrm{T},\perp}^{\,\mathrm{soft}}. \tag{5.23}$$

The absolute values of $\vec{p}_{\mathrm{T},\parallel}^{\,\mathrm{soft}}$ and $\vec{p}_{\mathrm{T},\perp}^{\,\mathrm{soft}}$ are denoted as $\mathcal{P}_{\parallel}$ and $\mathcal{P}_{\perp}$, respectively. In order to estimate the systematic uncertainties, $\vec{p}_{\mathrm{T}}^{\,\mathrm{soft}}$ is treated as a function of $\vec{p}_{\mathrm{T}}^{\,\mathrm{hard}}$. The average value $\langle \mathcal{P}_{\parallel} \rangle$, as well as the variances $\langle \mathcal{P}_{\parallel} \rangle^2$ and $\langle \mathcal{P}_{\perp} \rangle^2$ are calculated in bins of $\vec{p}_{\mathrm{T}}^{\,\mathrm{hard}}$. The offset between $\langle \mathcal{P}_{\parallel} \rangle$, $\langle \mathcal{P}_{\parallel} \rangle^2$, and $\langle \mathcal{P}_{\perp} \rangle^2$ values measured in different simulated samples and observed data is fitted and taken as systematic uncertainty.

5.5 Overlap Removal

After applying the baseline selection to all objects, it is necessary to check for duplicates as it is possible for one physical object in the event to be reconstructed as two different objects by reconstruction algorithms. The general procedure is defined in Reference [133], details on the specific requirements are given in Reference [134]. Different sets of conditions are defined for the lepton-lepton and lepton-jet overlap removal. According to the recommendations, the lepton-jet overlap removal is applied after the lepton-lepton overlap removal.

Lepton-lepton overlap removal: There are different possibilities for two overlapping leptons. One scenario ist that two electrons overlap when the reconstructed objects have an overlapping EM cluster or share an Inner Detector track. In that case, the higher p_{T} electron is kept.

Electrons and muons overlap when they share an Inner Detector track. This can be caused by muon radiating a high-energy bremsstrahlung photon. In such a case the muon is kept, unless it has not been tagged as a muon in the muon chambers.

Lepton-jet overlap removal: If a jet overlaps with a lepton candidate with $\Delta R_{\ell,j} < 0.2$, the jet is removed, unless it is a heavy-flavor jet. If the $\Delta R_{\ell,j}$ between the lepton and the jets is between 0.2 and 0.4, the lepton is removed.

For muons, it is additionally checked if the muon is associated to the jet as a ghost particle. This procedure is proposed in Reference [123] and compared to the established method of matching a lepton to a jet based on their spatial separation using $\Delta R_{\ell,j}$ in Reference [135]. Whenever a jet contains a ghost-associated muon and has less than three tracks the jet is removed.

The overlap removal procedure for anti-ID leptons is slightly different. In that case, leptons within $0.2 < \Delta R_{\ell,j} < 0.4$ of a jet are kept while the jet is removed. Consequently, the lepton axis, i. e. its p_{T} vector, is slightly tilted with respect to the jet axis. Therefore, an isolation cone which is arranged concentrically around the muon does not capture all of the underlying jet momentum. This can lead to problems in the estimation of the non-prompt background and has to be accounted for.

6 Background Estimation

In the following sections, the estimation of the most important background processes is discussed. In general, background contributions to $W^{\pm}W^{\pm}jj$-EW production can be split into events with exactly two same-charge leptons, more than two true leptons, and events with falsely reconstructed lepton.

The largest background is caused by events with *falsely reconstructed leptons*. These events can contain either two opposite-charge leptons, where the charge of one lepton is mis-reconstructed or they contain only one true lepton, and the second lepton is a falsely reconstructed jet. As the underlying detector effects are not accurately modeled, these background contributions are hard to estimate using simulation. They are therefore evaluated using data-driven techniques, which are discussed in Sections 6.2.1 and 6.2.2 for non-prompt and charge mis-ID backgrounds, respectively. Processes entering the signal region by mis-reconstruction of a photon are not included in the non-prompt estimation and are taken from simulation.

The most important background contributions to events with *more than two true leptons* is caused by $W^{\pm}Z$ and ZZ production in association with two jets, where the bosons decay leptonically. If the additional leptons are forward, i. e. escape the tracker volume, or hadronically decaying τ-leptons, they do not pass the lepton selection criteria. Events with three or four true leptons can thus be accepted in the signal region.

Events with *exactly two same-charge leptons* from $W^{\pm}W^{\pm}jj$-QCD or tri-boson production are irreducible by object selections. These can only be suppressed by choosing a VBS-like phase space, by for instance requiring high invariant mass m_{jj} and a large rapidity difference $|\Delta Y_{jj}|$ of the tagging jets.

6.1 Simulated Backgrounds

Well modeled backgrounds like $W^{\pm}Z$ and $W^{\pm}W^{\pm}jj$-QCD production, as well as comparatively small backgrounds such as $V\gamma$, tri-boson, ZZ, and single-top production are taken from simulation.

The electroweak and strong $W^{\pm}Z$ production is studied in the $W^{\pm}Z$ control region, as described in Section 7.2.1. Feynman diagrams are analogous to the signal diagrams shown in Figure 4.1 and 4.2. The event yields in this region are included in the profile likelihood fit. Thus, the shape of the $W^{\pm}Z$ m_{jj} distribution in the signal region is taken from simulation, while the normalization can be measured using observed data in the $W^{\pm}Z$ control region and included in the measurement of the signal strength. Details on this procedure are given in Section 9.2. Theory uncertainties on the simulation related to the choice of the renormalization and factorization scales, as well as the strong coupling α_{s} are taken into account in addition to modeling uncertainties of the proton PDF and the parton shower. Details on these uncertainties is given in Section 8.2.

In case a photon is mis-reconstructed as an electron, events from $W\gamma$ and $Z\gamma$ production in association with two jets ($V\gamma jj$) can enter the signal region. A subset of possible Feynman diagrams contributing to this background is shown in Figure 6.1. The photon can either be created as part of the hard scattering, or as initial as well as final state radiation. Diagrams including triple vertices, like Figure 6.1 (a) are only possible for $W^{\pm}\gamma$ final states, as the photon does not couple to Z-bosons. Depending on the momentum of the photon created in diagram (b) of Figure 6.1, the interaction is classified as hard scattering or initial state radiation. The modeling of $V\gamma$ production is studied in a dedicated $V\gamma$ control region, as described in Section 7.2.3.

The production cross section for electroweak ZZ production with leptonically decaying Z-bosons is small in comparison to the $W^{\pm}W^{\pm}jj$-Ew cross section [81]. The contribution to the signal region is further suppressed because two leptons have to escape reconstruction. As that background is almost negligible in the signal region (see Table 7.3), no dedicated control region is defined. An uncertainty of 20 % is assigned to the cross section. This value is taken from the uncertainty derived in the 8 TeV Atlas analysis [136], as listed in Section 4.1.1.

Another source of background events is single-top production. Possible Feynman diagrams are shown in Figure 6.2. In all following considerations, the single-top background will be merged with $t\bar{t}$ production in association with a $W^{\pm}$, Z or off-shell photon γ^{*}, and denoted as *top* background. Typical Feynman diagrams for these processes are shown in Figure 6.3.

Irreducible background contributions from $W^{\pm}W^{\pm}jj$-Qcd and tri-boson production are estimated using the Sherpa program. Tri-boson contributions are included in the signal sample. While the tagging jets in $W^{\pm}W^{\pm}jj$-Qcd events are, at leading order, due to partons of the colliding protons (see Figure 4.2), tri-boson contributions can enter the signal region if one of the three $W^{\pm}$-bosons decays hadronically, and thus produces a $\ell^{\pm}\nu\ell^{\mp}\nu jj$ signature. A set of Feynman diagrams is shown in Figure 6.4. The invariant mass of the two jets in a tri-boson event with a hadronically decaying $W^{\pm}$-boson is expected to be close to the $W^{\pm}$-mass. Therefore, tri-boson contributions to the signal region with m_{jj} larger than 500 GeV are kinematically suppressed and very small. As in the case of ZZ production, no separate control region is defined.

6.2 Data-Driven Backgrounds

For background processes that can not be taken from MC simulation with sufficient accuracy, data-driven techniques are used in order to determine the contribution of those backgrounds in the signal and control regions. These techniques will briefly be summarized in the following sections.

6.2.1 Estimation of Non-Prompt Background

In the signal region, the second largest (see Table 7.3) background contribution are non-prompt events, with one real lepton and a jet that has been mis-reconstructed as a lepton. These events mainly originate in $W^{\pm}$+jets, $t\bar{t}$, single-top, and Qcd multi-jet production.

As the contribution from this background highly depends on the detector modeling, it is usually not well described in simulated events. Therefore, a data-driven technique is used to estimate it. The probability for a jet to be mis-reconstructed as a lepton, called non-prompt correction factor f, is measured in a *di-jet region*. In order to estimate the number of non-prompt events in the signal region and low-m_{jj} control region, the non-prompt correction factor is applied to events passing the corresponding event selections, where the acceptance requirements for one of the leptons are relaxed from analysis- to anti-ID-level (see Table 5.1).

The procedure to measure and apply non-prompt correction factors is described in Reference [137] and will be briefly summarized hereafter.

6.2.1.1 Measurement of Non-Prompt Correction Factors

Non-prompt correction factors are measured in a di-jet region. The definition of the di-jet region is summarized in Table 6.1. Events with exactly one analysis- or anti-ID-level lepton are selected. Anti-ID leptons are defined in a way to primarily correspond to real jets which have been mis-reconstructed as leptons, by relaxing the object's identification and more importantly the isolation requirements. It is likely for the lepton axis to point in a slightly different direction than the underlying jet, such that some of the true jet momentum is outside of the lepton calorimeter cluster, and therefore not included in the lepton momentum. Thus, the anti-ID lepton p_{T} is only

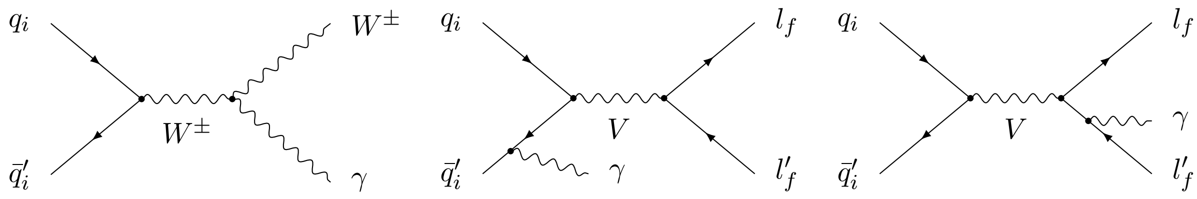

(a) $W^\pm\gamma$ (b) ISR or hard scattering (c) FSR

Figure 6.1: Exemplary Feynman diagrams for $V\gamma$ production with leptonically decaying gauge bosons V. Photons can be created as part of the hard process (a,b) or as initial and final state radiation (ISR, FSR), as shown in (b) and (c), respectively.

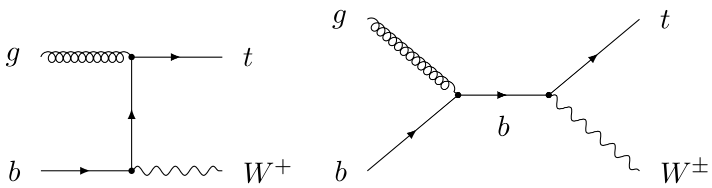

(a) t/u-channel (b) s-channel

Figure 6.2: Feynman diagrams for single-top production. Analogous diagrams exist where all quarks are replaced by their anti-particles.

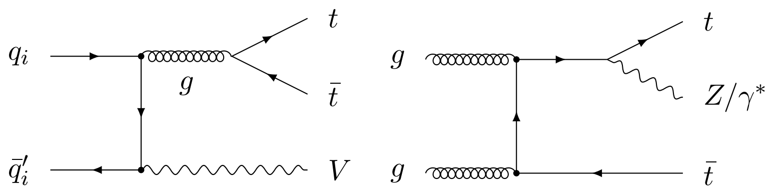

(a) $t\bar{t}V$ (b) $t\bar{t}Z/\gamma^*$

Figure 6.3: Representative Feynman diagrams for $t\bar{t}$ production in association with a gauge boson V, which can be either a W, Z or γ^*.

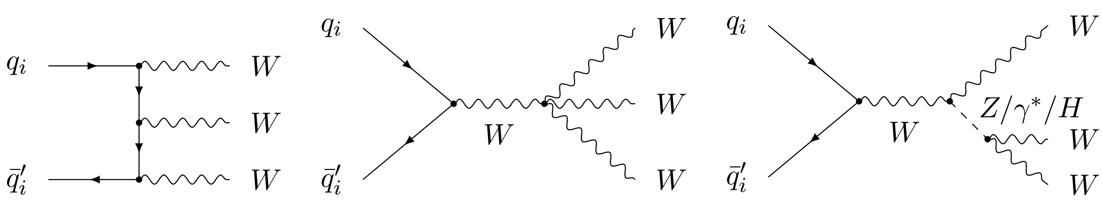

(a) (b) (c)

Figure 6.4: Exemplary Feynman diagrams of resonant tri-boson production, where the initial-state quarks q_i and q'_i can be of different flavor.

part of the full underlying jet transverse momentum. It is desirable to select underlying jets covering the same p_{T} range as prompt leptons in the signal region. Therefore, the p_{T} threshold of anti-ID leptons is lowered from 27 GeV to 15 GeV and 20 GeV for muons and electrons, respectively. The p_{T} requirement for analysis-level leptons in the di-jet region has to be adjusted accordingly. However, for a precise estimate of the non-prompt background, the momentum distribution of the anti-ID lepton should be similar to the underlying jet's momentum distribution. In order to recover most of the underlying jet's momentum, the energy in the isolation cone, $p_{\mathrm{T}}^{\mathrm{cone}}$ around the anti-ID lepton is added to the anti-ID lepton p_{T}. Momentum distributions used for calculating the non-prompt correction factor are shown in Figure 6.5.

Before selecting events specific to di-jet production, a preselection consisting of event and object cleaning steps as well as trigger requirements is applied. The preselection is common to all event selection chains and detailed in Chapter 7, Table 7.1. The nominal trigger chains are adapted to match the lowered lepton p_{T} threshold[1]. Trigger pre-scales are corrected for by assigning an additional event weight. Furthermore, events are required to have at least one jet. All jets have to satisfy baseline selection criteria and pass JVT or fJVT requirements. Since a large fraction of non-prompt leptons come from heavy-flavor decays, the leading jet is required to be tagged as a b-jet. The lepton and tagging jet are required to be back-to-back with $|\Delta\phi_{l,j}| > 2.8$. Events from $W^{\pm}$+jet production are suppressed by requesting that the scalar sum of the transverse mass of the lepton $m_{\mathrm{T},l}$ and the missing transverse energy $E_{\mathrm{T}}^{\mathrm{miss}}$ is smaller than 50 GeV. The event selection defining the di-jet region is summarized in Table 6.1.

In the di-jet region, the non-prompt correction factor is calculated from the number of analysis- and anti-ID-level leptons, under the assumption that analysis-level leptons are always true leptons and anti-ID leptons are always mis-reconstructed jets. Contributions from prompt backgrounds with real anti-ID leptons, like $W^{\pm}Z$, ZZ, Vjets, $t\bar{t}$, and single-top are subtracted. The non-prompt correction factor is measured separately for electrons and muons. For muons, it is calculated in bins i of lepton transverse momentum, and defined as

$$f_{\mu,i} \;=\; \frac{N_{\text{ana, } i(p_{\mathrm{T}})}}{N_{\text{anti-ID, } i(p_{\mathrm{T}}+p_{\mathrm{T}}^{\mathrm{cone}})}}, \tag{6.1}$$

where $N_{\text{anti-ID, } i(p_{\mathrm{T}}+p_{\mathrm{T}}^{\mathrm{cone}})}$ and $N_{\text{ana, } i(p_{\mathrm{T}})}$ denote the number of anti-ID- and analysis-level leptons, respectively. For analysis-level leptons, the distributions is binned according to the pure transverse momentum p_{T}, while the corrected lepton momentum $p_{\mathrm{T}} + p_{\mathrm{T}}^{\mathrm{cone}}$ is used for anti-ID leptons. For electrons, a two-dimensional non-prompt correction factor is measured in two lepton $|\eta|$ bins ($|\eta| < 1.37$ and $1.37 < |\eta| < 2.5$) as a function of the pure and corrected transverse momentum for analysis- and anti-ID-level electrons, respectively. Electron non-prompt correction factors $f_{e,i}$ are defined analogous to Eq. (6.1), where i is counting all $(|\eta|, p_{\mathrm{T}} + p_{\mathrm{T}}^{\mathrm{cone}})$ bins. In Figure 6.6, a comparison of muon and electron non-prompt correction factors is shown. The largest non-prompt correction factor is measured for end-cap electrons.

6.2.1.2 Systematic Uncertainties

Systematic uncertainties on non-prompt correction factors come from different aspects of the measurement procedure. Effects related to the di-jet event selection, prompt lepton subtraction, the jet flavor composition and some residual dependence on the underlying jet p_{T} are taken into account. All uncertainties are estimated in the same binning used to calculate the non-prompt correction factors. In Table 6.2, an overview of the relative statistical and systematic uncertainties in the non-prompt correction factors for central and end-cap electrons, as well as muons is given. For each source of uncertainty, the minimal and maximal value over all $p_{\mathrm{T}} + p_{\mathrm{T}}^{\mathrm{cone}}$ bins are given.

[1]Trigger chains for electrons: `HLT_e12_lhvloose_nod0_L1EM10VH` and `HLT_e40_lhvloose_nod0`
Trigger chains for muons: `HLT_mu14` and `HLT_mu50`. All triggers, except for `HLT_mu50` are pre-scaled.

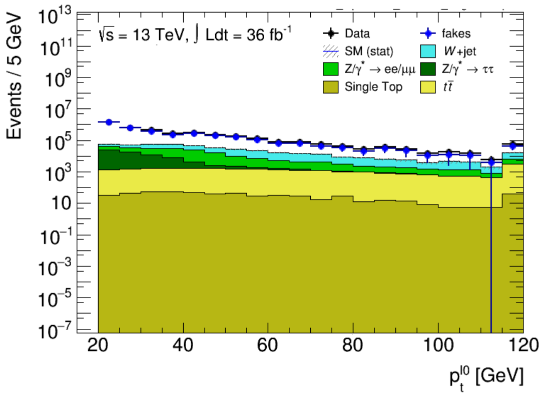

(a) Analysis-Level Electron, p_{T}

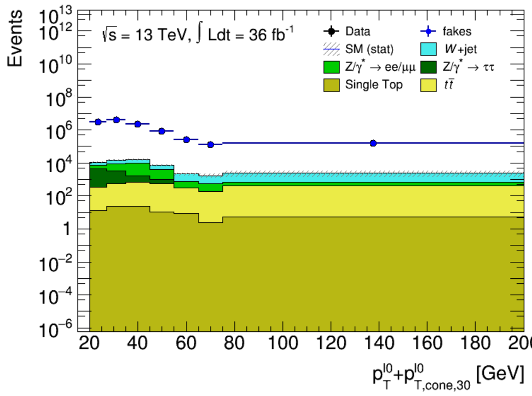

(b) Anti-ID-Level Electron, $p_{\mathrm{T}} + p_{\mathrm{T}}^{\mathrm{cone}}$

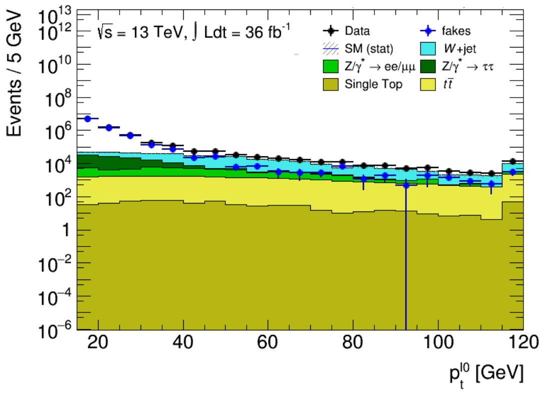

(c) Analysis-Level Muon, p_{T}

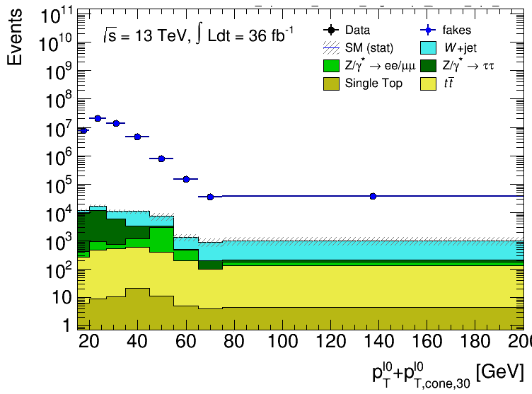

(d) Anti-ID-Level Muon, $p_{\mathrm{T}} + p_{\mathrm{T}}^{\mathrm{cone}}$

Figure 6.5: p_{T} (left) and $p_{\mathrm{T}} + p_{\mathrm{T}}^{\mathrm{cone}}$ (right) distributions in the di-jet region for analysis and anti-ID-level leptons, respectively. The distributions are shown separately for electrons (top) and muons (bottom). Observed data in the di-jet region are represented by black points. Non-Prompt background is estimated by subtracting the prompt simulated background (filled histograms) from observed events, and depicted by blue points. Statistical uncertainties are shown. Figures taken from Ref. [137].

Criterion	Value
Preselection	Table 7.1 with adapted trigger chains
N_{lep}	$= 1$
N_{jet}	≥ 1
$\lvert\Delta\phi_{l,j}\rvert$	> 2.8
$m_{\mathrm{T},l} + E_{\mathrm{T}}^{\mathrm{miss}}$	$< 50\,\mathrm{GeV}$

Table 6.1: Event selection criteria defining the di-jet region, used to derive the non-prompt correction factor.

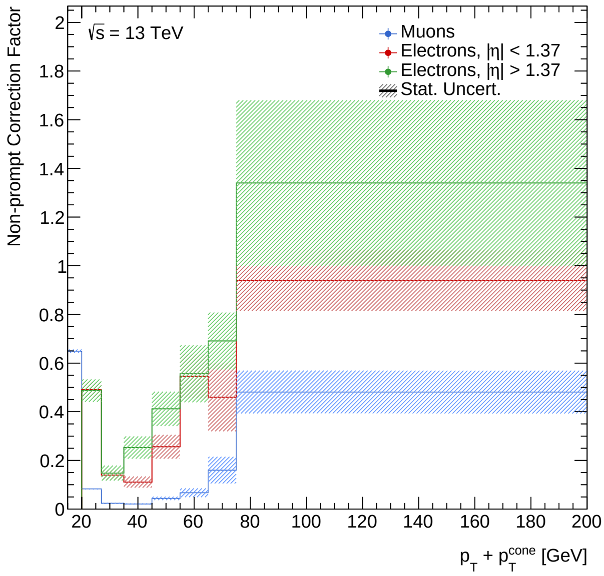

Figure 6.6: Non-prompt correction factors for muons (blue), central (red) and end-cap electrons (green), including statistical uncertainties. Based on Ref. [137].

The impact of the di-jet event selection on the final non-prompt correction factor is evaluated by varying the jet p_{T}, $m_{\mathrm{T},l} + E_{\mathrm{T}}^{\mathrm{miss}}$ and $|\Delta\phi_{l,j}|$ requirements. In most bins, these variations only have a small effect that is of the order of the statistical uncertainty on the nominal non-prompt correction factor.

The modeling of backgrounds used for the prompt lepton subtraction is checked in a separate validation region. The validation region is defined to be relatively pure in $W^{\pm}$+jets production, as this is the dominant background in the di-jet region. This $W^{\pm}$+jets validation region is defined similarly to the di-jet region (see Table 6.1) by requiring a lepton momentum of at least 35 GeV and inverting the $m_{\mathrm{T},l} + E_{\mathrm{T}}^{\mathrm{miss}}$ criterion to $m_{\mathrm{T},l} + E_{\mathrm{T}}^{\mathrm{miss}} > 60\,\mathrm{GeV}$. In this region, observed data and simulation agree within approximately 10 %. The modeling uncertainty is assumed to be similar for all simulated backgrounds. Consequently, the non-prompt correction factors are re-derived where the MC backgrounds are scaled up and down by 10 %.

Since a b-jet is required in the di-jet region, the non-prompt correction factors are mainly modeling heavy flavor jets. Separate studies [105] have shown that, in contrast to the region where the non-prompt correction factors are applied, the di-jet region is dominated by light jets. To estimate the impact of kinematical differences between light and heavy flavor jets, non-prompt correction factors are re-derived without the b-jet requirement. The difference is assigned as systematic uncertainty to the non-prompt correction factor.

Even after correcting the anti-ID lepton p_{T} with $p_{\mathrm{T}}^{\mathrm{cone}}$, the transverse momentum distribution of the underlying jet cannot be exactly reproduced. To estimate the residual dependence on the underlying jet p_{T}, the tag jet p_{T} distribution in the di-jet sample is re-weighted to the true underlying jet p_{T} distribution in the region where the non-prompt correction factors are applied. Non-prompt correction factors are re-calculated after applying this event weight in the di-jet region. The largest contribution to the total systematic uncertainty comes from the jet p_{T} re-weighting and the flavor composition.

Uncertainty		Muons [%]	Electrons [%] $\lvert\eta\rvert < 1.37$	Electrons [%] $\lvert\eta\rvert > 1.37$
Statistical		1.1 - 34.4	6.3 - 30.4	9.4 - 25.4
$m_{\mathrm{T},l} + E_{\mathrm{T}}^{\mathrm{miss}}$	up	< 0.1 - 241.7	0.4 - 42.6	0.8 - 19.8
	down	< 0.1 - 29.4	0.6 - 23.7	1.6 - 34.0
$\lvert\Delta\phi_{l,j}\rvert$	up	< 0.1 - 60.0	0.4 - 22.6	2.4 - 49.1
	down	< 0.1 - 13.4	<0.1 - 18.7	1.6 - 16.0
Prompt subt.	up	< 0.1 - 40.0	0.6 - 5.7	0.6 - 2.2
	down	< 0.1 - 40.0	0.4 - 5.4	0.4 - 2.2
$p_{\mathrm{T}}^{\mathrm{jet}}$		< 0.1 - 3.0	<0.1 - 4.3	< 0.1 - 7.4
Flavor comp.		10.4 - 90.9	7.1 - 189.2	7.8 - 154.5
$p_{\mathrm{T}}^{\mathrm{jet}}$ re-weighting		4.2 - 307.9	2.1 - 77.4	16.2 - 78.0

Table 6.2: Overview of relative statistical and systematic uncertainties (in [%]) on muon and electron non-prompt correction factors. Uncertainties are calculated per $p_{\mathrm{T}} + p_{\mathrm{T}}^{\mathrm{cone}}$ bin. Minimum and maximum values over the whole $p_{\mathrm{T}} + p_{\mathrm{T}}^{\mathrm{cone}}$ range are given in the table. For asymmetric uncertainties, the up and down variations are listed separately. Based on Ref. [105].

6.2.1.3 Application of Non-Prompt Correction Factors

In order to estimate the non-prompt background yield in the signal (SR) and low-m_{jj} control regions (CR), events are selected in the anti-ID signal region and low-m_{jj} control region. These regions are defined by the same event selections are the nominal signal region and low-m_{jj} control region (see Table 7.2, and Section 7.2.2, respectively), except that one of the leptons is required to pass the anti-ID-level rather than the analysis-level object selection.

Events in the anti-ID signal and low-m_{jj} control regions are weighted with the non-prompt correction factor corresponding to the anti-ID lepton's type, $p_{\mathrm{T}} + p_{\mathrm{T}}^{\mathrm{cone}}$, and $\lvert\eta\rvert$ in case of electrons. Uncertainties on the electron and muon non-prompt correction factors listed in Table 6.2 are propagated to the event yields in both regions. For each lepton flavor, the variations are grouped into two nuisance parameters, statistical and systematic. Electron nuisance parameters are applied to the non-prompt estimate in the ee and $e\mu/\mu e$ channels. Analogously, nuisance parameters covering the muon non-prompt correction factor variations are applied in the $e\mu/\mu e$ and $\mu\mu$ channels.

The resulting shape variations are shown in Figure 6.7, in bins from 200 GeV to 3000 GeV. The lowest bin from 200 GeV to 500 GeV corresponds to the low-m_{jj} control region. The signal region consists of bins above 500 GeV. The shown statistical uncertainties correspond to the statistical uncertainties in the anti-ID signal and low-m_{jj} control regions, where the non-prompt correction factors are applied.

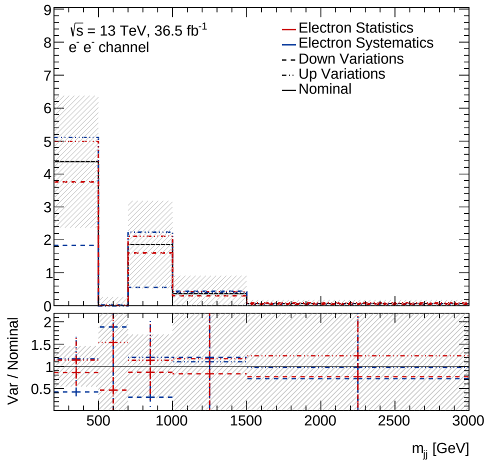

(a) e^-e^- Channel

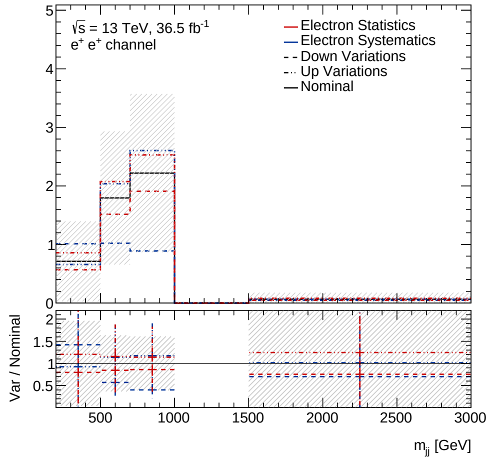

(b) e^+e^+ Channel

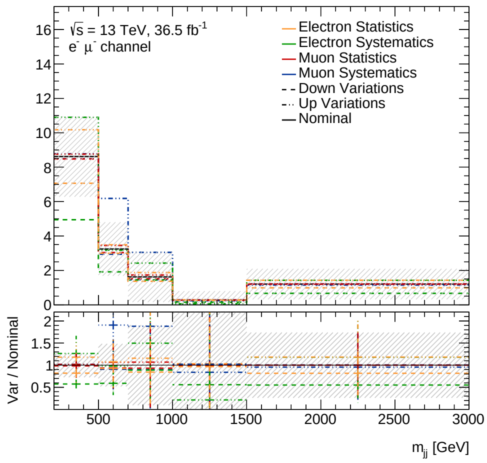

(c) $e^-\mu^-/\mu^-e^-$ Channel

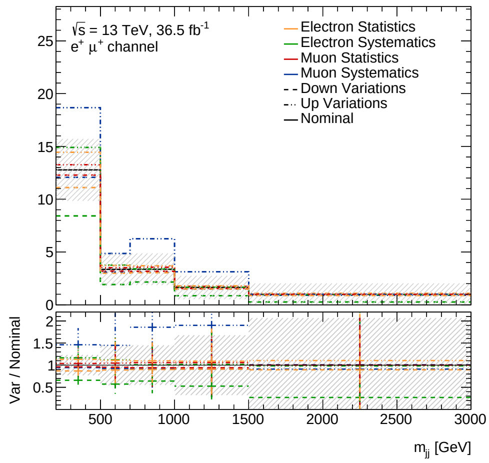

(d) $e^+\mu^+/\mu^+e^+$ Channel

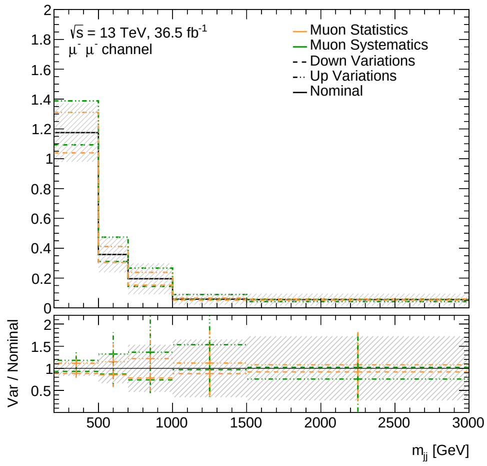

(e) $\mu^-\mu^-$ Channel

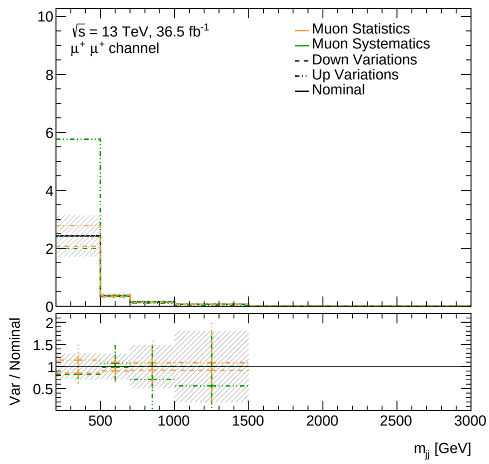

(f) $\mu^+\mu^+$ Channel

Figure 6.7: Non-prompt background estimate for different lepton charge and flavor channels. The shape variations corresponding to electron and muon non-prompt correction factor systematics are shown. The bin from 200 GeV to 500 GeV corresponds to the low-m_{jj} control region.

6.2.2 Estimation of Charge Mis-ID Background

Charge mis-ID background arises due to imperfections in the charge reconstruction of leptons. This can happen for instance when a lepton emits bremsstrahlung and the bremsstrahlung photon decays into an electron-positron pair. It is then possible for the track reconstruction algorithm to wrongly assemble the initial lepton track to the track of a photon decay product with the opposite charge. In that case, the curvature of the track will be opposite to that of the initial particle, leading to the wrong reconstructed charge. This is schematically shown in Figure 6.8.

As the cross section for bremsstrahlung is proportional to $\frac{1}{m^2}$ [138] where m is the mass of the lepton, electrons are much more likely to be affected by it than muons. Additionally, charge mis-ID can occur if the track curvature in the Inner Detector is wrongly estimated. This mainly arises for high-p_{T} leptons, where the tracks are only slightly bent or in situations, where the occupancy of the Atlas Inner Detector is very high. However, this problem impacts electron reconstruction more acutely than muon reconstruction, as the Muon Spectrometer provides an independent measurement of muon track curvatures. As a result of the reduced bremsstrahlung cross-section and higher precision of the charge measurement, the fraction of muons that undergo charge mis-ID is assumed to be negligibly small [139]. Therefore, charge mis-ID rates are derived for electrons only.

Events that can result in charge mis-ID background predominantly originate from $Z \to ee$, Drell-Yan, $t\bar{t}$, and $W^{\pm}W^{\mp}$ processes. Even though the charge mis-ID probability for a single electron is reasonably small, the high production cross-section of the backgrounds in question in combination with the very small signal cross-section makes for a non-negligible contribution to the event count in the signal region. In order to estimate this contribution, a correction factor is applied to observed data passing all signal region requirements (see Table 7.2) with an inverted charge cut. This region is called *opposite-charge signal region* in the following.

In order to determine that correction factor, first the probability, i. e. charge mis-ID rate, for an electron to undergo charge mis-identification is measured in observed and simulated data. The correction factor is then calculated using these rates. This procedure is explained in Reference [131], and is summarized in the following.

6.2.2.1 Deriving Charge Mis-ID Rates

Charge mis-ID rates are derived in three steps. When analyzing observed data, it is impossible to know, whether the charge of a specific electron is correctly reconstructed. Therefore, only the probability that the charge for one out of two leptons is mis-reconstructed is measurable. The probability to measure a same-charge (*sc*) event from a pair of opposite-charge (*oc*) electrons is given by

$$p_{\mathrm{sc}} = (1 - \varepsilon_i)\varepsilon_j + (1 - \varepsilon_j)\varepsilon_i, \tag{6.2}$$

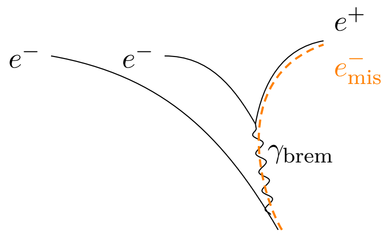

Figure 6.8: Schematic view of a charged electron track in the detector. The electron emits bremsstrahlung γ_{brem}, which creates an electron-positron pair. The track reconstruction algorithm wrongly assembles the initial electron track to the track of the positron (orange dashed line), yielding the wrong reconstructed charge.

where $\varepsilon_{i,j}$ are the probabilities for each of the electrons to undergo charge mis-reconstruction. When considering in interaction, where a number of opposite-charge lepton pairs, ν_{oc} is produced, the expected number of same-charge lepton pairs ν_{sc} due to charge mis-ID is given as $\nu_{\text{sc}} = \nu_{\text{oc}} \cdot p_{\text{sc}}$.

In order to estimate p_{sc} with high statistical accuracy, the region of $75\,\text{GeV} < m_{\ell\ell} < 105\,\text{GeV}$ in invariant electron mass is selected in observed data and dedicated simulated samples of $Z \to ee$ events. This corresponds to the Z-resonance, and is therefore highly populated. ν_{sc} as a function of p_{sc} and thereby $\varepsilon_{i,j}$ is then determined by a maximum-likelihood estimation of the number of observed of same-charge events N_{sc}, assuming a Poisson distribution:

$$\text{Pois}\left(N_{\text{sc}}|\nu_{\text{sc}}\right) \;=\; \text{Pois}\left(N_{\text{sc}}|\varepsilon_{i,j}\right) \;=\; \frac{\nu_{\text{sc}}^{N_{\text{sc}}}}{N_{\text{sc}}!}\,e^{\nu_{\text{sc}}}. \tag{6.3}$$

The optimization is done in five and six bins of electron transverse momentum and pseudo-rapidity, respectively[1].

Once $\varepsilon(p_{\text{T}}, |\eta|)$ are known in data ($\varepsilon_{\text{data}}$) and simulated events ($\varepsilon_{\text{MC}}$), scale factors for correctly and wrongly measured electrons can be calculated. These are denoted as f_{right} and f_{wrong} respectively.

$$f_{\text{wrong}} = \frac{\varepsilon_{\text{data}}}{\varepsilon_{\text{MC}}}, \tag{6.4}$$

$$f_{\text{right}} = \frac{1-\varepsilon_{\text{data}}}{1-\varepsilon_{\text{MC}}}. \tag{6.5}$$

Just as ε, these scale factors are a function of p_{T} and $|\eta|$. The resulting nominal values and systematic uncertainties are shown in Figure 6.9. Scale factors for correctly measured electrons are very close to one, while factors for mis-reconstructed electrons have can an effect up to 40 %. In order to correct the mis-modeling of charge mis-ID in simulated events, simulated $Z \to ee$ events are corrected such that the charge mis-ID rate matches the one observed in data. This is achieved by applying f_{right} and f_{wrong} to the electron objects, depending on the their truth information and reconstructed charge. The precise charge mis-ID rate ε_{WW} for the $W^{\pm}W^{\pm}$ selection is then calculated as

$$\varepsilon_{WW} \;=\; \frac{\text{wrong-charge electrons}}{\text{all prompt electrons}}. \tag{6.6}$$

Here, the number of wrong-charge electrons is determined by the number of simulated $Z \to ee$ events in the nominal signal region, whereas the total number of prompt electrons is taken as the number of $Z \to ee$ events a region identical to the signal region except that no charge requirement is enforced. In this context, well isolated electrons and parent electrons of bremsstrahlung photons are considered as prompt electrons. The complete electron object selection is given in Table 5.1. Charge mis-ID rates ε_{WW} are shown in Figure 6.10 as a function of p_{T} and $|\eta|$. The measured rates are below 10 % for all electrons.

As these rates are to be applied per electron, the total weight f_{tot} for an event with two electrons can be calculated as

$$f_{\text{tot}} \;=\; \frac{(1-\varepsilon_{WW}^{(1)})\varepsilon_{WW}^{(2)} + (1-\varepsilon_{WW}^{(2)})\varepsilon_{WW}^{(1)}}{(1-\varepsilon_{WW}^{(1)})(1-\varepsilon_{WW}^{(2)}) + \varepsilon_{WW}^{(1)}\varepsilon_{WW}^{(2)}}. \tag{6.7}$$

Equation (6.7) yields the probability of observing two same-charge leptons from a pair of opposite-charge leptons. Either the leading ($\varepsilon_{WW}^{(1)}$) or subleading ($\varepsilon_{WW}^{(2)}$) electron's charge is mis-reconstructed. In $e\mu/\mu e$ channels, this expression is simplified, as $\varepsilon_{WW}^{(\mu)}$ is assumed to be 0. The weight is applied to observed data in the opposite-charge signal region, to determine the contribution of same-charge events in the signal region.

[1] p_{T} bins boundaries are 20 GeV, 27 GeV, 60 GeV, 90 GeV, 130 GeV and 1000 GeV.
$|\eta|$ bin boundaries are 0.0, 0.6, 1.1, 1.37, 1.52, 1.7, 2.3 and 2.5 where the region $1.37 < |\eta| \leq 1.52$ is excluded.

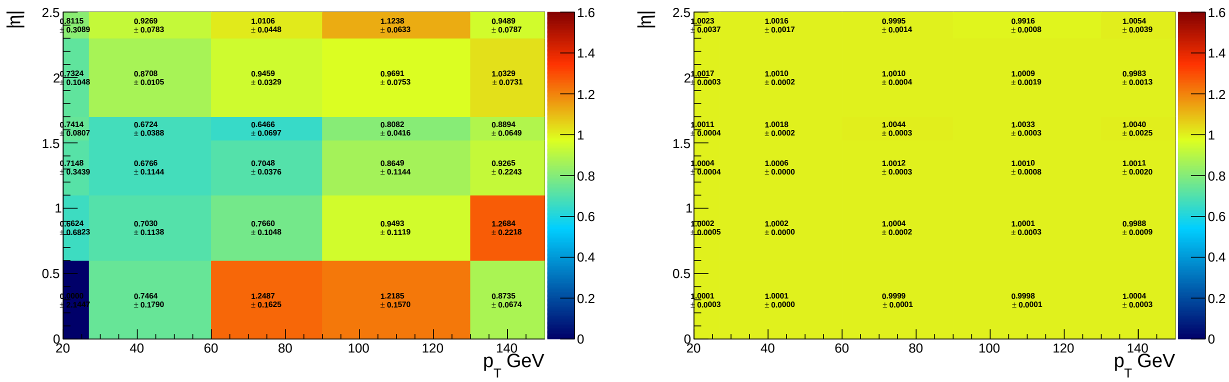

(a) f_{wrong} (b) f_{right}

Figure 6.9: Scale factors to be applied to electrons with wrongly (a) and correctly (b) reconstructed charges. Figures taken from Reference [131].

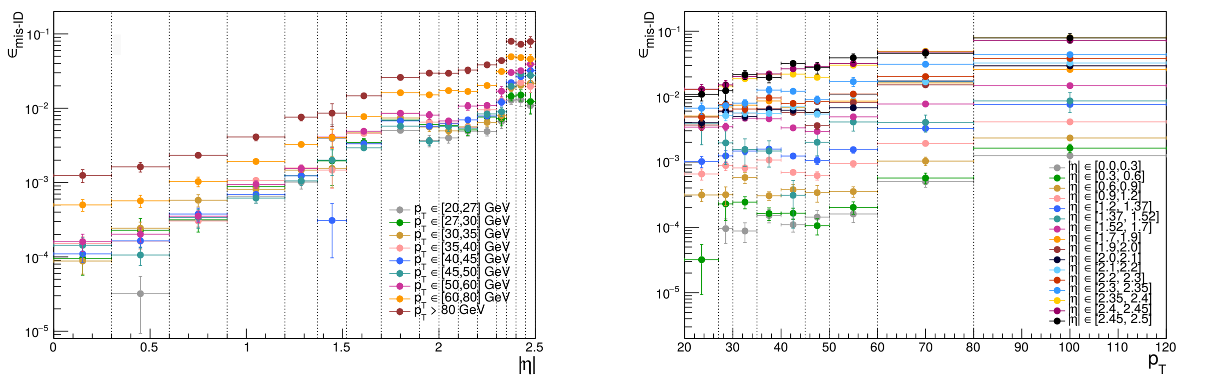

(a) $\varepsilon_{WW}(|\eta|)$ (b) $\varepsilon_{WW}(p_{\mathrm{T}})$

Figure 6.10: Charge mis-identification rates ε_{WW} as a function of the electron $|\eta|$ (a) and p_{T} (b), retrieved on $Z \to ee$ MC after applying the scale factors [131].

6.2.2.2 Energy Correction

On average, electrons which underwent charge mis-ID have a lower transverse momentum than electrons with a correctly reconstructed charge. This is because electrons with a wrongly reconstructed charge have most probably emitted bremsstrahlung along their way through the detector, leading to energy deposition outside of the electromagnetic calorimeter cluster. This effect can be seen in the spectrum of invariant electron mass near the Z-resonance shown in Figure 6.11(a). In this figure, invariant electron masses are compared for opposite- and same-charge data and Drell-Yan simulation, as well as the data-driven charge mis-ID estimate. This comparison is performed in an inclusive region, where no $m_{\ell\ell}$ and jet requirements are enforced.

In can be seen that the Z-peak in same-charge simulation and data is shifted to lower energies with respect to opposite-charge events. In order to account for this energy loss, the original electron transverse momentum $p_{\mathrm{T}}^{\mathrm{orig}}$ in a same-charge event is corrected by a factor of $1/\alpha$ as

$$p_{\mathrm{T}}^{\mathrm{corr}} = \frac{p_{\mathrm{T}}^{\mathrm{orig}}}{\alpha} + \mathrm{d}E. \tag{6.8}$$

The term $\mathrm{d}E$ is used for Gaussian smearing of the original electron momentum to correctly represent the reduced energy resolution due to bremsstrahlung. $\mathrm{d}E$ is determined in pseudo-experiments

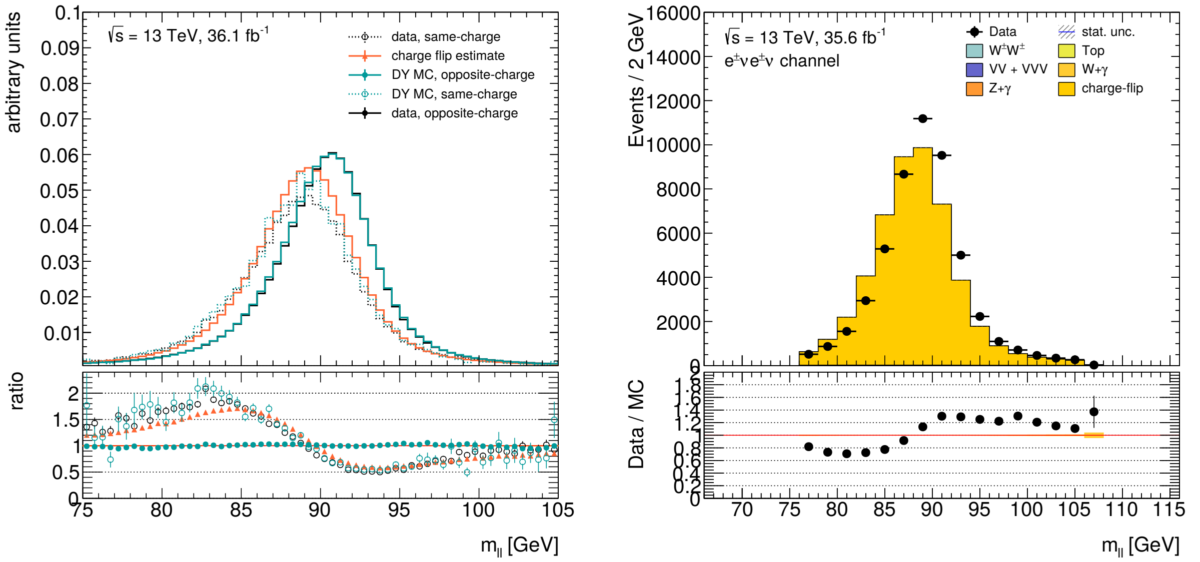

(a) Inlusive in $|\eta|$, no $m_{\ell\ell}$, no jet requirements (b) $|m_Z - m_{\ell\ell}| < 15\,\mathrm{GeV}$, 2 jets with $m_{jj} > 200\,\mathrm{GeV}$

Figure 6.11: Effect of electron energy correction. Figures taken from Reference [131].

using a Gaussian p.d.f. with an expectation value of zero, and a width c. This width and the correction factor α are determined using truth information from $Z \to ee$ simulated data. The correction factor α is based on energy response $p_\mathrm{T}^\mathrm{reco}/p_\mathrm{T}^\mathrm{truth}$, and models the shift of the reconstructed $p_\mathrm{T}^\mathrm{reco}$ and truth level $p_\mathrm{T}^\mathrm{truth}$ distributions for correctly and wrongly reconstructed electrons,

$$\alpha = \frac{E\left[\frac{p_\mathrm{T}^\mathrm{reco}}{p_\mathrm{T}^\mathrm{truth}}\right]^\mathrm{right}}{E\left[\frac{p_\mathrm{T}^\mathrm{reco}}{p_\mathrm{T}^\mathrm{truth}}\right]^\mathrm{wrong}}, \tag{6.9}$$

where $E\left[\frac{p_\mathrm{T}^\mathrm{reco}}{p_\mathrm{T}^\mathrm{truth}}\right]$ is the expectation value of the $\frac{p_\mathrm{T}^\mathrm{reco}}{p_\mathrm{T}^\mathrm{truth}}$ distribution, as defined in Eq. (2.20)[1]. The width of the Gaussian used to smear the original lepton momentum is calculated using the square root of the variance, $\sigma\left(\frac{p_\mathrm{T}^\mathrm{reco}}{p_\mathrm{T}^\mathrm{truth}}\right)$ of this distribution, as defined in Eq. (2.21)[1],

$$c = \sigma\left(\frac{p_\mathrm{T}^\mathrm{reco}}{p_\mathrm{T}^\mathrm{truth}}\right)^\mathrm{wrong} - \sigma\left(\frac{p_\mathrm{T}^\mathrm{reco}}{p_\mathrm{T}^\mathrm{truth}}\right)^\mathrm{right}. \tag{6.10}$$

Both quantities, α and c, are derived differentially in bins of electron $|\eta|$. The resulting distributions for are shown in Figure 6.12. It can be seen that α is very close to, but always larger than one, because the reconstructed momentum is closer to the truth level momentum in the case of correctly reconstructed charges than for wrongly reconstructed charges. Additionally it is observed that the width c is very close to zero.

In Figure 6.11(a) the charge mis-ID estimate including energy correction is shown by the orange line, with an inclusive selection. It can be seen that the energy correction improves the modeling of energy loss. In the inclusive signal region without jet and $m_{\ell\ell}$ requirements, good agreement is observed between charge mis-ID estimate and same-charge data as shown in Figure 6.11(b).

[1] The integral in this definition has to be replaced by a sum over all bins in the p_T histogram.

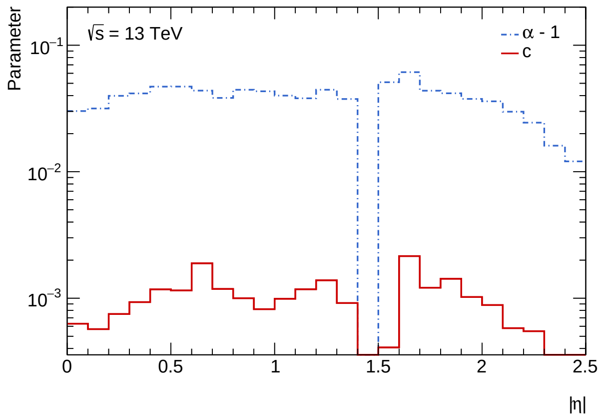

Figure 6.12: Correction factors accounting for differences in the energy reconstruction of electrons with correctly and incorrectly reconstructed charge. Instead of the residual energy scale correction α, $\alpha - 1$ is shown as a dashed blue line. The residual constant term c is shown in red. Figure adapted from [131].

6.2.2.3 Systematic Uncertainties

The charge mis-ID estimate is highly dependent on the value of the scale factors used to weight the charge mis-ID efficiency in simulation to the value measured in data, as well as the energy correction described in the previous section. To account for this, two sources of systematic uncertainties are considered:

Scale factor variations: The systematic uncertainties of the scale factors f_{wrong} and f_{right} are determined following the recommendations [140], details on the procedure are given in Reference [131]. The total systematic uncertainty is calculated as the squared sum of a set of four variations. The following sources of uncertainty are calculated taking into account: 1. a variation of the $m_{\ell\ell}$ window considered in the maximum-likelihood estimate, 2. the effect of background subtraction in the chosen $m_{\ell\ell}$ window, 3. the result of a closure test on simulated data, where scale factors are determined on simulated data using truth information, and 4. the effect of requiring a di-lepton rather than a single-lepton trigger.

Energy correction: The full effect of the energy correction is taken as systematic uncertainty.

Both sources of uncertainty are treated as separate nuisance parameters in the fit, which are a priori uncorrelated. The nominal charge mis-ID estimate as well as the 1-σ variations of the nuisance parameters are shown differentially in Figure 6.13.

6.2.2.4 Charge Mis-ID Estimate in ID-AntiID Region

As explained in Section 6.2.1 the non-prompt background contributions to the signal and low-m_{jj} control regions are determined from the corresponding anti-ID regions using a data-driven technique. Prompt backgrounds, taken from simulation, as well as data-driven charge mis-ID contribution are subtracted. The calculation of the charge mis-ID estimate in the anti-ID signal and low-m_{jj} control region, i. e. on anti-ID electrons is explained in this section. A dedicated charge mis-ID estimate with a loosened object selection is necessary, as the nominal estimate only takes into account analysis-level electrons. This is not exact in the region, where the non-prompt background is calculated, and one of the leptons is required to be an anti-ID lepton.

In order to estimate the charge mis-ID contribution in the anti-ID region, a tag-and-probe method is applied to $Z \to ee$ events in the same-charge and opposite-charge signal region with a loosened object selection for the anti-ID electron. Nominal (analysis-level) and anti-ID-level electron selections are

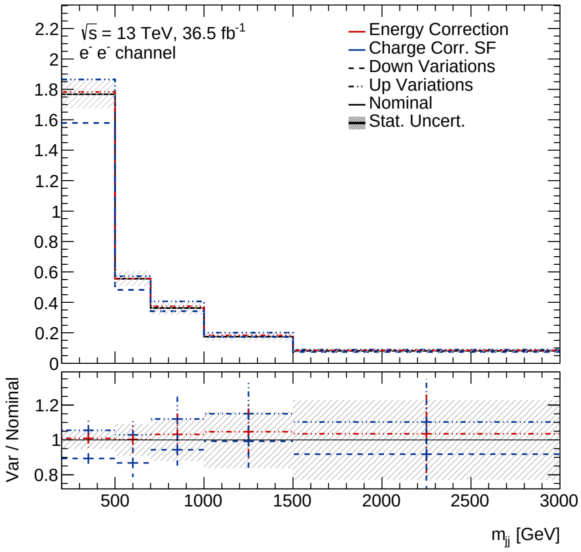

(a) e^-e^- Channel

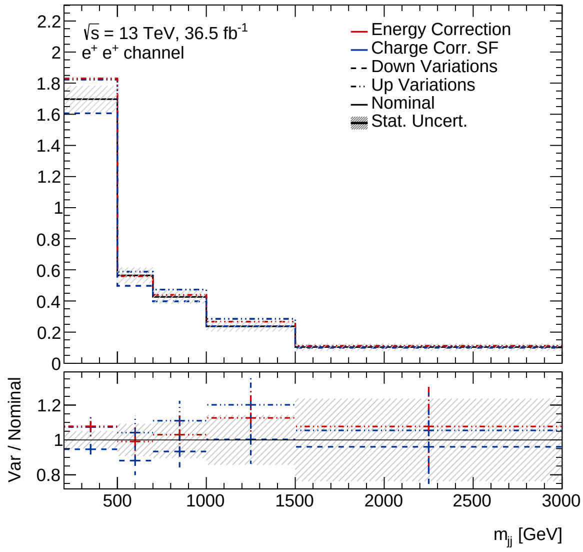

(b) e^+e^+ Channel

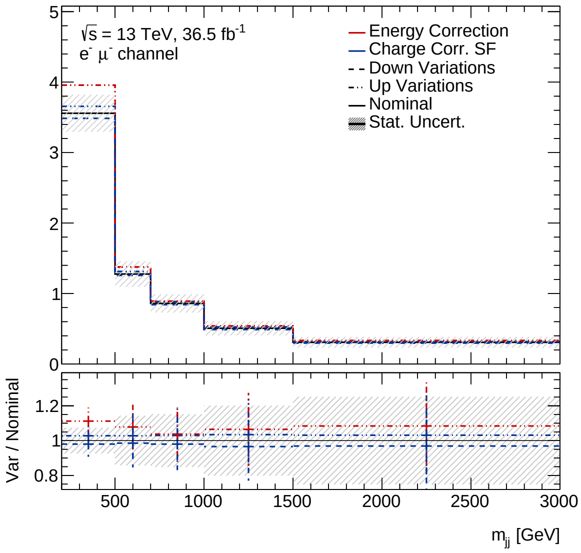

(c) $e^-\mu^-/\mu^-e^-$ Channel

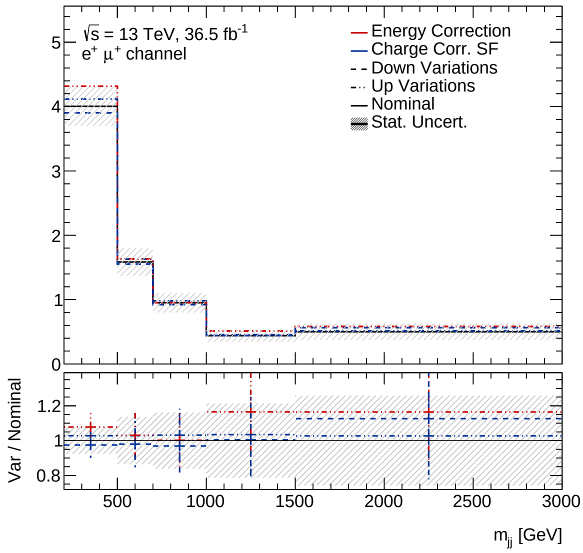

(d) $e^+\mu^+/\mu^+e^+$ Channel

Figure 6.13: Charge mis-ID background estimate in the e^-e^- (a), e^+e^+ (b), $e^-\mu^-/\mu^-e^-$ (c), and $e^+\mu^+/\mu^+e^+$ (d) channels in bins of the invariant mass of the tagging jet, m_{jj}. The lowest bin from 200 GeV to 500 GeV corresponds to the low-m_{jj} control region. The signal region consists of events with $m_{jj} > 500$ GeV.

selected as summarized in Table 5.1. Additionally, a $m_{\ell\ell}$ requirement of $|m_Z - m_{\ell\ell}| < 15\,\text{GeV}$ is applied, to ensure a high purity of $Z \to ee$ events. The analysis-level electron is considered as the tag lepton, while the anti-ID electron is probed.

The charge mis-ID rate is then determined analogous to Equation (6.6), where the number of electrons with mis-identified charge is taken as the number of same-charge probe electrons. This is done under the assumption that the anti-ID probe electron is always the lepton with wrongly reconstructed charge. This assumption is validated by deriving the charge mis-ID rates for simulated events in two separate approaches. At first, the electron with the wrongly reconstructed charge is determined using truth information. The resulting charge mis-ID rates are compared to the rates generated under the assumption that the anti-ID electron has always undergone charge mis-ID (see appendix, Figure A.2).

The final rates for anti-ID electrons are then determined on observed data (see Figure 6.14). As in the nominal procedure discussed above, event weights are calculated according to Equation (6.7) in the opposite-charge region, as defined above. The nominal rate and the anti-ID rate are used for the tag and probe electron, respectively. The purity in prompt leptons of the opposite-charge region is tested by introducing a truth level requirement to reject non-prompt electrons. The effect of this additional requirement is shown to be negligible. Some kinematic distributions with and without truth requirement are shown in the appendix, Figure A.3.

The event weights are applied to data in the opposite-charge anti-ID region, in order to estimate the charge mis-ID estimate in the anti-ID region. This contribution is used in the prompt subtraction of the non-prompt estimate, as explained in Section 6.2.1.

This anti-ID charge mis-ID procedure is controlled in a separate anti-ID validation region. A short summary of this region, as well as kinematic distributions is given in Appendix A.1. The overall event yield for data and the charge mis-ID estimate in the validation region is shown in Table 6.3. A disagreement of 10 % is observed, which is assigned as a systematic uncertainty.

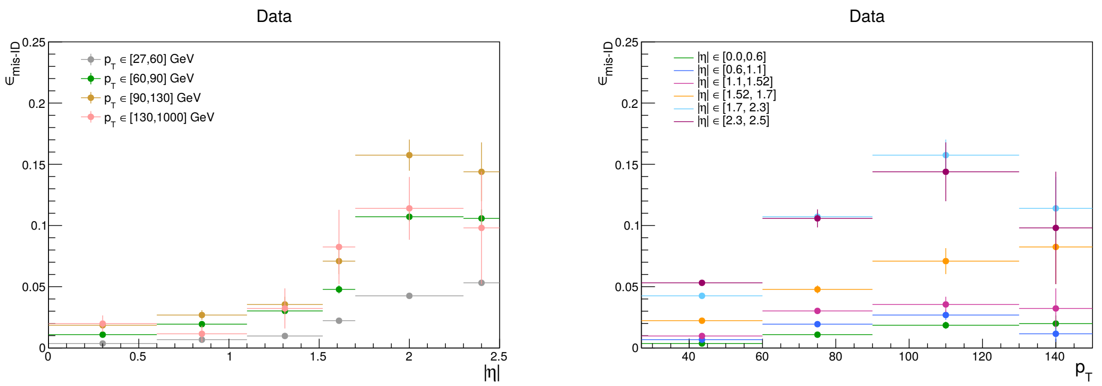

(a) $\varepsilon(|\eta|)$ for anti-ID electrons, data

(b) $\varepsilon(p_{\mathrm{T}})$ for anti-ID electrons, data

Figure 6.14: Charge mis-ID rates for anti-ID electrons retrieved on data $Z \to e^+e^-$ events as a function of $|\eta|$ (a) and p_{T} (b). Figure taken from Reference [131].

	Charge Mis-ID	Other prompt	Data	Data/Predicted
Yield	820.58	5.28	740	0.90

Table 6.3: Event yields for separate charge mis-ID, prompt and data in the ID-AntiID region [131].

7 Event Selection in Signal and Control Regions

The event selection steps used to define the signal as well as a set of two control regions and several validation regions is explained in the course of this chapter. Detailed descriptions are given in Reference [105].

Before splitting events into separate regions, a common preselection is applied. It is summarized in Table 7.1. For observed data, only events are accepted that were recorded during a luminosity block where the detector was fully functional. These blocks are listed in the good run list [141]. Moreover, during the event cleaning step, all events are rejected if they are affected by a problematic calorimeter (LAr or Tile) or SCT cell. Incomplete events are also rejected. During high luminosity runs in 2015 and 2016 data-taking, saturation problems occurred in the inner wheel of the EMEC [142]. Affected events are vetoed.

Electrons and jets are rejected if they fail to pass object quality requirements defined by the respective CP groups [143, 144]. Additionally, only events with at least one reconstructed primary vertex are selected. In all regions, events have to fire at least one single-lepton trigger[1]. A lepton trigger matching is done in most regions, ensuring that either the leading or subleading lepton where triggered upon.

A common characteristic of all event selection chains is the application of efficiency corrections to simulated data. For each selection tool, like identification or isolation algorithms, these factors are derived in the CP groups to account for different selection efficiencies in measured data and simulation. Efficiency correction factors are applied to electrons and muons to correct isolation and identification or quality determination, respectively. An additional scale factor is applied to leptons after matching them to a triggered object. Furthermore, electrons are corrected for different charge mis-ID rates in data and simulation, as described in Section 6.2.2. Analysis level jets are corrected using JVT and fJVT scale factors. In regions where a b-veto is performed, mis-tagging correction factors are applied to all accepted jets. Finally, simulated events are weighted with their corresponding generator and pile-up weight.

Criterion	Comment
Good Run List	Rejecting luminosity blocks where detector was not fully functional [141]
Event Cleaning	Reject events with problematic LAr, Tile or SCT hits, and incomplete events
Object Cleaning	Reject objects not passing object quality requirements
$N_{\mathrm{vtx}} \geq 1$	Select events with at least one reconstructed primary vertex
Triggers	Single-lepton trigger[1]

Table 7.1: Summary of preselection applied to all events.

[1] Trigger chains used for 2015 data: `HLT_e24_lhmedium_L1EM20VH`, `HLT_e60_lhmedium`, `HLT_e120_lhloose` for electrons a and `HLT_mu20_iloose_L1MU15`, `HLT_mu50` for muons.
Trigger chains used for 2016 data for electrons: `HLT_e26_lhtight_nod0_ivarloose`, `HLT_e140_lhloose_nod0`, `HLT_e60_lhmedium_nod0` and for muons: `HLT_mu26_ivarmedium`, `HLT_mu50`.

7.1 Definition of the Signal Region

The selection of the signal region is designed to yield a maximal sensitivity. For some selection requirements, such as $E_{\mathrm{T}}^{\mathrm{miss}}$ and the b-tagging working point, relatively loose values are chosen in order to reduce the impact of statistical fluctuations in the non-prompt background estimate [131]. The final selection requirements are summarized in Table 7.2. Six orthogonal channels defined by lepton flavor and charge e^+e^+, e^-e^-, $e^+\mu^+/\mu^+e^+$, $e^-\mu^-/\mu^-e^-$, $\mu^+\mu^+$, and $\mu^-\mu^-$ are analyzed.

After applying the preselection defined above, events with exactly two same-sign, analysis-level leptons are selected. In addition, events with more than two baseline-level leptons are rejected in order to reduce background from $W^{\pm}Z$ and ZZ processes. The number of analysis- and baseline-level leptons is denoted as $N_{\mathrm{lep}}^{\mathrm{ana}}$ and $N_{\mathrm{lep}}^{\mathrm{veto}}$, respectively. A summary of the corresponding object definitions is given in Table 5.1.

The two accepted signal leptons are required to have an invariant mass $m_{\ell\ell}$ of at least 20 GeV to reduce the modeling uncertainty of low-mass Drell-Yan processes [105]. Events from $Z \to ee$ processes can enter the signal region if the charge of one of the electrons is mis-reconstructed. To suppress the background contribution of such events, events with an invariant mass close the the Z-resonance are rejected in the ee channels using $|m_{ee} - m_Z| \geq 15\,\mathrm{GeV}$. As two neutrinos are produced in the signal process, a missing transverse momentum of $E_{\mathrm{T}}^{\mathrm{miss}} \geq 30\,\mathrm{GeV}$ is required. Thus the impact of charge mis-ID background is further reduced. The $E_{\mathrm{T}}^{\mathrm{miss}}$ cut is the final step in the definition of the *inclusive signal region*.

Events with less than two jets are vetoed to select vector boson (VBS) scattering processes. Jets are sorted according to their transverse momentum. The leading and subleading jets are called *tagging jets*. Another background process with a high production cross section compared to VBS is $t\bar{t}$ production. These events can enter the signal region in two ways. Leptonically decaying t-quarks can be selected as signal leptons through charge mis-ID and the b-quarks can be mis-identified as leptons, as well. The latter option would, however, be classified as non-prompt background. In order to reduce these effects, events containing any b-jets are rejected. To enhance the sensitivity to VBS, an high invariant mass m_{jj} of the tagging jets and a large rapidity gap $|\Delta Y_{jj}|$ between them is required.
Requirements on the leading and subleading jet p_{T}, the subleading lepton p_{T}, $E_{\mathrm{T}}^{\mathrm{miss}}$ and $|\Delta Y_{jj}|$ as well as the b-tagging working point are optimized by emulating the profile likelihood fit [131]. The optimization was done in three bins of m_{jj}[1] and all six channels.

Event yields for the signal and background processes as well as observed data in the signal region are presented in Table 7.3 with statistical uncertainties. Uncertainties for the data-driven charge mis-ID and non-prompt backgrounds correspond to the statistical uncertainties in the opposite-charge and anti-ID signal regions, respectively. Event yields are split into six lepton charge and flavor channels. Additionally, the total yield over all channels is given in the $\ell^{\pm}\ell^{\pm}$ column. A breakdown of uncertainties into statistical, theory and other systematic sources is given in Appendix C.4, Table C.11. The m_{jj} distribution for all processes and observed data in the combined $\ell^{\pm}\ell^{\pm}$ channel is shown in Figure 7.1.

7.2 Control Regions

Control regions are regions orthogonal to the signal region which are also included in the profile likelihood fit. In this analysis, two control regions are used to determine the normalization of $W^{\pm}Z$ background from data and constrain non-prompt systematic uncertainties. These are called $W^{\pm}Z$ and low-m_{jj} control region, respectively. The phase space definitions as well as pre-fit m_{jj} distributions are presented in this section. The fitting strategy for including these two control regions is optimized in Section 9.1.

[1] The m_{jj} bins border where chosen as 200 GeV, 500 GeV and 800 GeV.

Criterion	Value	Comment
Preselection		see Table 7.1
$N_{\text{lep}}^{\text{ana}}$	$= 2$	using analysis-level leptons
$N_{\text{lep}}^{\text{veto}}$	$= 2$	3rd lepton veto using baseline leptons
Charge	same-charge	
$m_{\ell\ell}$	≥ 20 GeV	
$\lvert m_{ee} - m_Z \rvert$	≥ 15 GeV	only in ee channel
$E_{\text{T}}^{\text{miss}}$	≥ 30 GeV	*inclusive signal region*
$N_{\text{jet}}^{\text{ana}}$	≥ 2	using analysis-level jets
$N_{b-\text{jet}}$	$= 0$	b-jet veto
m_{jj}	≥ 500 GeV	
$\lvert \Delta Y_{jj} \rvert$	≥ 2	

Table 7.2: Summary of selection requirements defining the signal region

	e^+e^+	e^-e^-	$e^+\mu^+/\mu^+e^+$	$e^-\mu^-/\mu^-e^-$	$\mu^+\mu^+$	$\mu^-\mu^-$	$\ell^\pm\ell^\pm$
$W^\pm W^\pm$jj EW	$3.80 \pm <0.01$	$1.49 \pm <0.01$	$16.49 \pm <0.01$	$6.45 \pm <0.01$	$9.14 \pm <0.01$	$3.50 \pm <0.01$	$40.88 \pm <0.01$
$W^\pm Z$	1.64 ± 0.15	1.14 ± 0.10	12.08 ± 0.47	7.81 ± 0.40	4.81 ± 0.24	3.19 ± 0.22	30.67 ± 0.72
Non Prompt	4.08 ± 1.75	2.31 ± 1.47	9.35 ± 2.62	6.34 ± 2.38	0.57 ± 0.13	0.67 ± 0.17	23.32 ± 4.23
Charge Mis-ID	1.33 ± 0.08	1.17 ± 0.08	3.48 ± 0.31	2.95 ± 0.26	–	–	8.93 ± 0.42
$W^\pm W^\pm$jj QCD	0.38 ± 0.02	0.16 ± 0.01	3.02 ± 0.06	1.21 ± 0.04	1.80 ± 0.04	0.76 ± 0.03	7.34 ± 0.09
ZZ, tri-boson, top	0.17 ± 0.03	0.14 ± 0.03	0.90 ± 0.08	0.60 ± 0.07	0.36 ± 0.04	0.19 ± 0.03	2.36 ± 0.13
$V\gamma$	0.41 ± 0.17	0.62 ± 0.22	2.65 ± 0.75	0.80 ± 0.26	< 0.01	< 0.01	4.47 ± 0.84
Data 2015/16	10	4	44	28	25	11	122

Table 7.3: Event yields in the signal region with statistical uncertainties. In addition to all six lepton charge and flavor channels, yields in the combined $\ell^\pm\ell^\pm$ channel are shown.

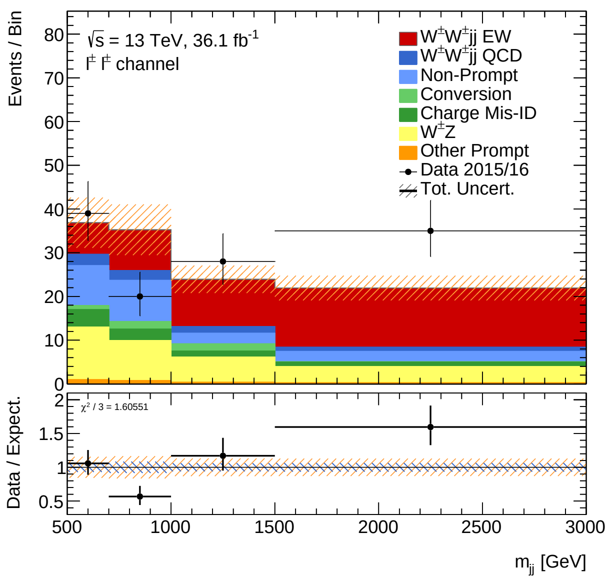

Figure 7.1: Distribution of the invariant mass of the two tagging jets, m_{jj}, in the combined $\ell^\pm\ell^\pm$ channel in the signal region. The uncertainties on the m_{jj} distribution for signal and background processes includes the complete set of statistical and systematic uncertainties. In the ratio plot, the systematic uncertainties (orange) and statistical uncertainties (blue) are shown separately.

7.2.1 $W^{\pm}Z$ Control Region

The $W^{\pm}Z$ control region is used in order to determine the normalization of the electroweak and strong $W^{\pm}Z$ production cross section.

The selection is based on the inclusive signal region, except for the same-charge requirement and the 3rd lepton veto. Since leptonic $W^{\pm}Z$ production results in three leptons, the 3rd lepton veto is replaced by requiring a third analysis-level lepton, with a lower p_{T} of 15 GeV. For reconstructing the Z-boson, two of the three selected leptons must have the opposite charge and same flavor (OCSF pair). The contribution from Z+jets and $V\gamma$ production is reduced by requiring an invariant three-lepton mass $m_{\ell\ell\ell}$ larger than $m_Z + 15$ GeV.

Events with an m_{jj} of at least 200 GeV are accepted. The requirements on the number of jets, and $|\Delta Y_{jj}|$ are identical to the signal region definition. The selection is summarized in Table 7.4.

As the production of $W^{\pm}Z$ events is symmetric in lepton charge and flavors, the complexity of the statistical analysis can be reduced by not splitting this region into lepton channels. In order to verify this assumption, the $W^{\pm}Z$ normalization is measured in the combined and lepton flavor split channels. Results of this study are presented in Section 9.1.2.

Pre-fit m_{jj} distributions in this, and the low-m_{jj} control region are presented in Figure 7.2. To allow for an easier comparison, the $W^{\pm}Z$ yields are scaled with a factor of 0.1. Furthermore, event yields for the signal and background processes are listed in Table 7.5. Purely statistical uncertainties are given. No data-driven background estimates are available in this region. Therefore the charge mis-ID and non-prompt contributions are estimated from $W^{\pm}W^{\pm}$, $t\bar{t}$, and $Z/W^{\pm}$+jets simulation.

Criterion	Value/ Comment
Inclusive SR	see Table 7.2
1 additional lepton	using analysis-level leptons with $p_{\mathrm{T}} > 15$ GeV
OCSF pair	
$m_{\ell\ell\ell}$	$m_Z + 15$ GeV
$N_{\mathrm{jet}}^{\mathrm{ana}}$	≥ 2
$N_{b-\mathrm{jet}}$	$= 0$
m_{jj}	≥ 200 GeV
$\|\Delta Y_{jj}\|$	≥ 2

Table 7.4: Selection requirements used to define the $W^{\pm}Z$ control region [105].

	$\ell^{\pm}\ell^{\pm}\ell^{\mp}$
$W^{\pm}W^{\pm}$jj EW	< 0.01
$W^{\pm}Z$	172.45 ± 1.42
$t\bar{t}$, $Z/W^{\pm}$+jets	6.82 ± 1.73
WW	0.02 ± 0.01
ZZ, tri-boson, top	21.55 ± 0.37
Conversion	2.68 ± 0.60
$W^{\pm}W^{\pm}$jj QCD	–
Data 2015/16	201

Table 7.5: Event yields in the $\ell^{\pm}\ell^{\pm}\ell^{\mp}$ channel of the $W^{\pm}Z$ control region including statistical uncertainties. No data-driven background estimates are available in this region. Therefore the charge mis-ID and non-prompt contributions are estimated from WW, $t\bar{t}$, and $Z/W^{\pm}$+jets simulation.

7.2.2 Low-m_{jj} Control Region

Up to the b-jet veto, the low-m_{jj} control region is defined by the same set of requirements used to the define the signal region, listed in Table 7.2. Orthogonality is ensured by selecting events with 200 GeV $< m_{jj} <$ 500 GeV. As in the signal region, the rapidity gap between the tagging jets is required to be $|\Delta Y_{jj}| > 2$. Analogous to the signal region, events are split into lepton charge and flavor channels.

In Figure 7.2, pre-fit number of events in this control region are shown. The non-prompt background makes up for a large fraction of events. It can therefore be used to constrain the systematic uncertainties attributed to that background. In combination with the $W^\pm Z$ control region, it is also possible to constrain theory uncertainties describing the $W^\pm Z$ production. Detailed event yields including statistical uncertainties for all channels as well as the combined $\ell^\pm\ell^\pm$ channels are listed in Table 7.6.

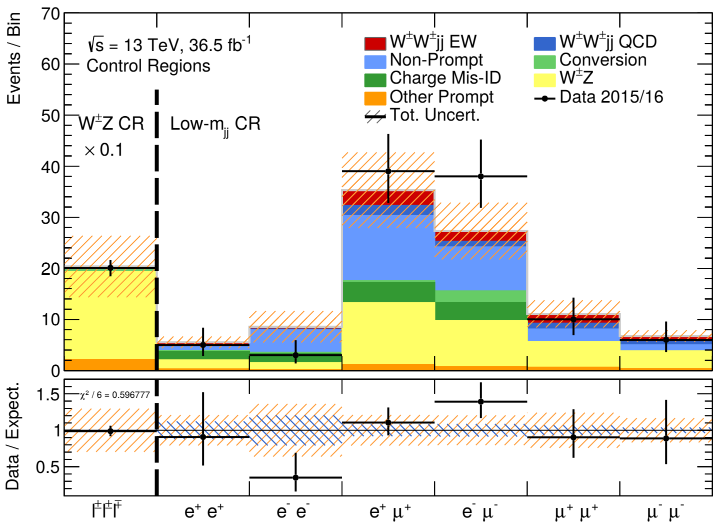

Figure 7.2: Pre-fit number of event in the $W^\pm Z$ control region and the e^+e^+, e^-e^-, $e^+\mu^+/\mu^+e^+$, $e^-\mu^-/\mu^-e^-$, $\mu^+\mu^+$ and $\mu^-\mu^-$ channels in the low m_{jj} control region. In the ratio plot, the systematic uncertainties (orange) and statistical uncertainties (blue) are shown. Event yields in the $W^\pm Z$ control region are scaled by a factor of 0.1. Poisson uncertainties on the observed data are shown.

	e^+e^+	e^-e^-	$e^+\mu^+/\mu^+e^+$	$e^-\mu^-/\mu^-e^-$	$\mu^+\mu^+$	$\mu^-\mu^-$	$\ell^\pm\ell^\pm$
$W^\pm W^\pm$jj EW	0.64 ± <0.01	0.47 ± <0.01	2.97 ± <0.01	1.99 ± <0.01	1.83 ± <0.01	1.11 ± <0.01	9.01 ± <0.01
$W^\pm Z$	1.77 ± 0.18	1.37 ± 0.13	12.07 ± 0.52	9.02 ± 0.46	5.04 ± 0.22	3.46 ± 0.19	32.72 ± 0.78
Non-Prompt	0.71 ± 0.64	4.37 ± 1.77	12.78 ± 2.80	8.62 ± 2.24	2.43 ± 0.71	1.18 ± 0.18	30.08 ± 4.12
Charge Mis-ID	1.70 ± 0.08	1.77 ± 0.09	4.00 ± 0.27	3.56 ± 0.25	–	–	11.03 ± 0.38
$W^\pm W^\pm$jj QCD	0.24 ± 0.02	0.15 ± 0.01	1.99 ± 0.04	1.15 ± 0.03	1.16 ± 0.03	0.64 ± 0.03	5.32 ± 0.07
ZZ, tri-boson, top	0.28 ± 0.04	0.16 ± 0.03	1.20 ± 0.09	0.77 ± 0.08	0.63 ± 0.06	0.37 ± 0.04	3.40 ± 0.15
$V\gamma$	0.18 ± 0.05	0.26 ± 0.15	0.28 ± 0.07	2.20 ± 0.48	–	–	2.93 ± 0.51
Data 2015/16	5	3	39	38	10	6	101

Table 7.6: Event yields in the low-m_{jj} control region with statistical uncertainties.

7.2.3 $V\gamma$ Control Region

The $V\gamma$ control region is used to study the modeling of photon conversion in $V\gamma$ processes. Even though $W^{\pm}\gamma$ production is more important in the signal region, the control region is enriched with simulated $Z\gamma$ events because photon conversion can be more easily studied in this final state. Under the assumption that the photon conversion probability is similar in both processes, the normalization correction is calculated based on $Z\gamma$ production but applied to $W^{\pm}\gamma$ events as well. A potential overlap between Z+jets and $Z\gamma$ samples is removed before calculating the normalization correction.

Based on the preselection (cf. Table 7.1), events with two opposite-charge, analysis-level muons and one analysis-level electron are selected. The lower p_{T} requirement for the leading and subleading muon is adjusted to 27 GeV and 20 GeV, respectively. The region close to the Z-resonance is selected using $75\,\mathrm{GeV} < m_{\ell\ell\ell} < 100\,\mathrm{GeV}$. Events containing neutrinos are rejected by requiring $E_{\mathrm{T}}^{\mathrm{miss}} < 30\,\mathrm{GeV}$. The selection criteria are summarized in Table 7.7.

The $V\gamma$ control region is relatively pure, small contributions from VV and top production are observed. The event yields and distribution of the invariant di-muon mass are shown in Table 7.8 and Figure 7.3, respectively. And overall scale factor $c_{V\gamma}$ was calculated as

$$c_{V\gamma} = \frac{N_{\mathrm{Data}} - N_{\mathrm{Other}}}{N_{Z\gamma} + N_{Z\mathrm{jets}}}. \tag{7.1}$$

The scale factor was found to be 1.77 ± 0.36, including statistical uncertainties. This factor is used to scale $Z\gamma$ and $W\gamma$ m_{jj} distributions when building the fitting template and the Asimov data set in the statistical analysis. The full effect of the normalization is covered with a systematic uncertainty in the profile likelihood fit.

Criterion	Value
Preselection	see Table 7.1
Overlap removal	Z+jets / $Z\gamma$
N_{μ}^{ana} (N_{e}^{ana})	2 (1)
$m_{\ell\ell\ell}$	$75\,\mathrm{GeV} < m_{\ell\ell\ell} < 100\,\mathrm{GeV}$
$E_{\mathrm{T}}^{\mathrm{miss}}$	$< 30\,\mathrm{GeV}$

Table 7.7: Selection requirements defining the $V\gamma$ CR, information taken from Ref. [145].

Process	Event Yield
$Z\gamma$	24.60 ± 3.32
Z+jets	3.02 ± 1.54
Other Backgrounds	8.15 ± 0.60
Data	57

Table 7.8: Event yields in the $V\gamma$ CR, including statistical uncertainties. Taken from Ref. [145].

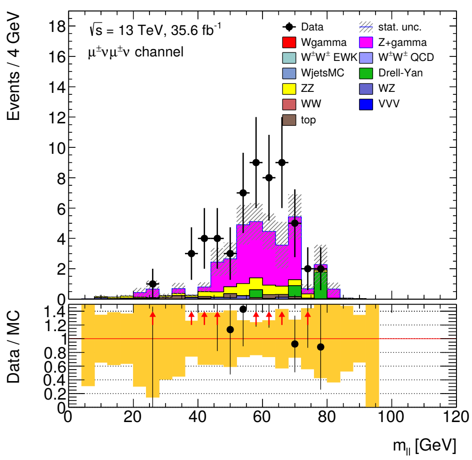

Figure 7.3: Invariant di-muon mass distribution in the $V\gamma$ CR, including statistical uncertainties. Figure taken from Ref. [145].

8 Systematic Uncertainties

In this section, all relevant systematic and theory uncertainties occurring in the analysis are summarized. Theory uncertainties cover the effect variations in the generation of simulated samples have on the total or differential cross section. Systematic uncertainties are associated to the measurement of all analysis objects and cover all inaccuracies that impact the event yields in the fitting regions, and the bins of the fitting distribution. Here, they are split into experimental and data-driven uncertainties, as well as systematics accounting for statistical fluctuations in the background contributions and the uncertainty on the luminosity measurement.

Experimental uncertainties are attributed to all simulated backgrounds and account for detector, reconstruction and identification imperfections. Data-driven uncertainties are derived for the non-prompt and charge mis-ID background estimates by evaluating the impact experimental uncertainties have on the respective data-driven method.

In the statistical analysis, each source of uncertainty is represented by a single nuisance parameter θ, acting on various signal and background contributions. Therefore, correlations between different contributions to the signal and control regions are considered. Even though the same nuisance parameter is applied to different contributions, the impact, i. e. the 1 σ upper and lower uncertainty, is evaluated separately for each background and signal contribution. For experimental, luminosity and theory uncertainties, nuisance parameters have a Gaussian constraint. Details on the integration of nuisance parameters into the likelihood function are given in Section 2.2.3. Background precision nuisance parameters are constrained with a Poissonian density function, and correspond to the γ-parameters in Eq. (2.37).

For systematic and theory nuisance parameters θ, the interval $[\theta - \Delta\theta, \theta + \Delta\theta]$ spans the range of nuisance parameter values corresponding to variations in the associated samples within the previously derived 1 σ uncertainty band. As θ is used to scale the event yield of a contribution according to the calculated uncertainties, the exact numerical values of $-\Delta\theta$ and $\Delta\theta$ may be different for each nuisance parameter, and even for different contributions affected by the same nuisance parameter. Therefore, in the likelihood function Eq. (2.37), uncertainties are represented by the parameter α, which is defined as the pull of θ [146]

$$\alpha = \frac{\theta - \theta'}{\Delta\theta'}. \tag{8.1}$$

Here θ' and $\Delta\theta'$ denote the true value and true 1 σ uncertainty band of the parameter θ. The pull α has the advantage of being defined in the same range for all systematic and theory uncertainties and all contributions. Hereafter, the term nuisance parameter always refers to α rather than θ.

The nominal parameter value of α is zero, which corresponds to the nominal estimate of all affected contributions. Nuisance parameter values of $+1$ and -1 correspond to the 1 σ upper and lower uncertainties, respectively. Hence, the initial uncertainty on a nuisance parameter is ± 1. Before the fit, all nuisance parameters are set to their nominal values, i. e. all nuisance parameters α are constrained by a standard Gaussian probability density. During the fit, nuisance parameters can be pulled from the nominal value, which is associated to a pull of the event yield for the corresponding contributions. The post-fit nuisance parameter value $\hat{\alpha}$ is the best estimator of the true value α', i. e. $\hat{\alpha}$ is the value that maximizes the likelihood for a given dataset. Additionally, the width of the Gaussian p.d.f. may be changed. Hence, the post-fit value of $\Delta\hat{\alpha}$ can be different from 1. Nuisance parameters with $\Delta\hat{\alpha}$ larger and smaller than one are called under- and over-constrained, respectively.

The fitting strategy is discussed in Chapter 9. The profile likelihood fit is performed using the differential distribution of the invariant mass of the leading and subleading jets in the signal region, as well as $W^{\pm}Z$ and low-m_{jj} control region. The signal region is split into four m_{jj} bins. Depending on the uncertainty type, uncertainties are either treated as overall normalization uncertainties or shape uncertainties. Normalization uncertainties have the same effect in all bins of a region. Shape uncertainties, on the other hand, evaluate the impact of systematic uncertainties separately in each bin of the fitting distribution, to account for possible shape effects. In general, shape uncertainties include variations in shape as well as in normalization. As the $W^{\pm}Z$ and low-m_{jj} control regions consist only of one bin in m_{jj}, all uncertainties are effectively treated as pure normalization uncertainties.

In the following, all nuisance parameters entering the profile likelihood fit will be briefly discussed. An complete overview of the relative impact of all nuisance parameters on the signal and background estimates in all different lepton charge and flavor channels and regions is given in Appendix B.3. For some nuisance parameters, like the nuisance parameters accounting for the jet energy scale resolution uncertainty or the parton shower uncertainty, only one variation can be derived. However, the parton density functions of the nuisance parameters in the profile likelihood fit are built for nuisance parameters which have an up and down variation, i. e. parameters that can take positive and negative values. Using only one variation in the fit could potentially result in underestimated uncertainties on these nuisance parameters. Therefore, the effect of systematic uncertainties with only one variation is symmetrized, to yield two-sided nuisance parameters. This treatment is more conservative than the approach used in the analysis presented by the ATLAS collaboration in Reference [11].

8.1 Experimental Uncertainties

As mentioned above, experimental uncertainties are linked to the reconstruction and identification procedure of all objects needed in the analysis. These are mainly electrons, muons, jets and missing transverse energy. Additional experimental uncertainties are assigned to selection steps, like the rejection of b-jets (flavor tagging) and the pile-up reweighting procedure. The reconstruction and identification algorithms are discussed in detail in Chapter 5.

An overview of all considered experimental uncertainties and the corresponding number of nuisance parameters in each category is given in Table 8.1. The corresponding data processing steps are detailed in the references listed in the table. In total, a set of 99 experimental nuisance parameters is used. The complete list of nuisance parameters is given in Appendix B.1. Almost all uncertainties listed in Table 8.1 are treated as shape uncertainties. The only exception is the modeling of $V\gamma$ conversions, which is described by a pure normalization uncertainty. This uncertainty amounts to 43 % and is based on a scale factor derived in the $V\gamma$ control region as discussed in Section 7.2.3.

A set of four nuisance parameters is introduced to parametrize the uncertainty on the non-prompt background. In order to decorrelate the uncertainty on non-prompt electrons and muons, separate statistical and systematic nuisance parameters are used for each lepton flavor. These uncertainties are described in Section 6.2.1.2. Total event yields in all channels in the signal and low-m_{jj} control region are shown in Table 8.2. In addition to the nominal event yields, the impact of the nuisance parameters is given. For the systematic uncertainties, up and down variations are listed separately. Statistical uncertainties in Table 8.2 correspond to the statistical uncertainties in the anti-ID signal and low-m_{jj} control regions[1], where the non-prompt correction factors are applied.

For the charge mis-ID estimate, the effect of the energy correction and the charge mis-ID correction factor are considered as systematic uncertainties, resulting in two nuisance parameters. The method to derive these uncertainties is detailed in Section 6.2.2.3, where comparison plots of the nominal

[1] For a definition of these regions see Section 6.2.1.

Uncertainty Source	N_θ	Description	Reference
Data-Driven	6		
Non-Prompt	4	Nuisance parameters for statistical and systematic variation in e and μ non-prompt estimate	Sec. 6.2.1
Charge Mis-ID	2	Energy correction and charge mis-ID correction scale factor uncertainties	Sec. 6.2.2
Electrons	40		
e/γ Resolution	1	Uncertainty on the smearing of the energy resolution	Sec. 5.2.3
e/γ Scale	5	Nuisance parameters for e/γ calibration procedure	
Electron Identification Eff.	31	Consists of a set of 15 correlated and 16 uncorrelated nuisance parameters	
Electron Other Eff.	3	Parameters for reconstruction, isolation, and trigger efficiencies	
Muons	13		
Muon Calibration	3	Two parameters are accounting for smearing of the Inner Detector and muon spectrometer p_T, one parameter is assigned to the p_T scaling	Eq. (5.8)
Muon Isolation Efficiency	2	Statistical and systematic uncertainty	
Muon Selection Efficiency	6	Statistical and systematic uncertainty on, including low-p_T muons and efficiency correction on the track-to-vertex association	
Muon Trigger Efficiency	2	Statistical and systematic uncertainty	
Jets	18		
Jet In-Situ Calibration	8	A reduced set, to cover uncertainties on the jet in-situ calibration	Sec. 5.3.2
Jet η Intercalibration	3	Uncertainties on non-closure of intercalibration	
Jet Flavor and Topology	5	Uncertainties on jet response and composition for quark or gluon initiated jets, b-jets, as well as punch-through and high-p_T jets	
Jet Energy Resolution	1	Parametrizes the effect a p_T smearing has on the jet calibration	
Jet JVT Efficiency	1	Nuisance parameter for JVT and fJVT selection efficiencies	
Flavor Tagging	13		
Flavor Tagging Efficiency	11	Three parameters for b-tag and c-tag, respectively, and five parameters on light quark tagging	Sec. 5.3.3
Flavor Tagging Extrapolation Eff.	2	Accounting for uncertainties on the extrapolation to high-p_T and c-jets	
Pile-up	5		
Jet Pile-up p_T correction	4	Nuisance parameters are associated to ρ, A^{jet}, $\langle\mu\rangle$ and N_{vtx}	Eq. (5.11)
Pile-up Scale Factor	1	Uncertainty on scale factor applied to data	Sec. 5.1
Other	4		
E_T^{miss} Soft Term	3	Accounting for the scale and resolution uncertainty on the soft contribution	Sec. 5.4
$V\gamma$ Conversion Model	1	Determined in $V\gamma$ control region	Sec. 7.2.3

Table 8.1: Overview of experimental uncertainties. In each uncertainty category, the number of contributing nuisance parameters N_θ is given. Where applicable, a reference to the description of the systematic uncertainties is given.

and varied charge mis-ID distribution are shown in Figure 6.13. A comparison of total event yields is given in Table 8.3. For the energy correction uncertainty, only one variation exists. However, the effect is symmetrized in the statistical analysis.

Furthermore, experimental uncertainties on electrons, muons, jets and $E_{\mathrm{T}}^{\mathrm{miss}}$ are given in Table 8.1. The calibration and reconstruction of these objects is detailed in Sections 5.2, 5.3, and 5.4, respectively. The experimental nuisance parameters showing the highest pulls after the various fits in the statistical analysis are

- $V\gamma$ Conversion Model,
- Jet η Intercalibration Non-Closure,
- Jet Flavor Composition,
- Jet Energy Resolution,
- Jet Pile-up N_{vtx} Offset, p_{T} Term, ρ Topology, and
- Pile-up Reweighting Data Scale Factor.

In Figure 8.1 and 8.2, the impact of these jet and pile-up nuisance parameters on the total simulated prediction is shown in the low-m_{jj} control and signal regions. Data-driven non-prompt and charge mis-ID estimates are not included. The nominal distribution is shown as a solid black line, while colored lines represent the different nuisance parameters. Up and down variations for a specific nuisance parameter are drawn in the same color and different line styles. Moreover, the statistical uncertainty on the nominal prediction is shown.

It can be seen from Figure 8.1 that the jet energy resolution nuisance parameter corresponds to only one variation. In the fit, the effect of this variation is symmetrized. The effect of the jet nuisance parameters is less than 10 % in most bins. The jet energy resolution and flavor composition are the leading uncertainties. As can be seen in Figure 8.2, the data scale factor has the highest impact across the pile-up nuisance parameters.

In the fits to observed data, the muon calibration nuisance parameters related to the muon p_{T} measurement in the Inner Detector and the Muon Spectrometer, as well as the p_{T} scaling are under-constrained. Event yields in the signal region, as well as the low-m_{jj} and $W^{\pm}Z$ control regions are given in Tables 8.4. For each of the afore mentioned nuisance parameters, the yield impact per channel is shown. It can be seen that the effect of these nuisance parameters has the same sign for the up and down variation in most channels. Thus, the nominal yield is not included in the error band spanned by both variations. Therefore, the uncertainties on the nuisance parameters are increased in the fit to also cover the nominal value.

		e^+e^+	e^-e^-	$e^+\mu^+/\mu^+e^+$	$e^-\mu^-/\mu^-e^-$	$\mu^+\mu^+$	$\mu^-\mu^-$
				Signal Region Yields			
Nominal, Statistical Unc.		4.08 ± 1.77	2.31 ± 1.47	9.35 ± 2.62	6.34 ± 2.38	0.57 ± 0.14	0.67 ± 0.17
Muon Systematics	up	–	–	+5.78	+4.27	−0.05	+0.20
	down	–	–	−0.69	−0.46	−0.01	−0.10
Electron Systematics	up	+0.63	+0.40	+0.45	+0.74	–	–
	down	−2.12	−1.23	−4.14	−2.17	–	–
Muon Statistics		–	–	±0.45	±0.32	±0.05	±0.11
Electron Statistics		±0.61	±0.34	±0.95	±0.73	–	–
				Low-m_{jj} Control Region Yields			
Nominal, Statistical Unc.		0.71 ± 0.68	4.37 ± 2.00	12.77 ± 2.93	8.62 ± 2.34	2.43 ± 0.72	1.18 ± 0.20
Muon Systematics	up	–	–	+5.90	+0.16	+3.34	+0.21
	down	–	–	−0.71	−0.13	−0.43	−0.08
Electron Systematics	up	−0.05	+0.73	+2.13	+2.28	–	–
	down	+0.30	−2.54	−4.36	−3.67	–	–
Muon Statistics		–	–	±0.49	±0.14	±0.36	±0.14
Electron Statistics		±0.15	±0.61	±1.67	±1.56	–	–

Table 8.2: Event yields for non-prompt background in the signal region and low-m_{jj} control region, including statistical and systematic uncertainties.

Channel		e^-e^-	e^+e^+	$e^-\mu^-/\mu^-e^-$	$e^+\mu^+/\mu^+e^+$	$\ell\,\ell$
				Signal Region Yields		
Nominal, Statistical Unc.		1.17 ± 0.08	1.33 ± 0.08	2.95 ± 0.26	3.48 ± 0.31	8.93 ± 0.42
Energy Correction		±0.02	±0.05	±0.19	±0.21	±0.47
Charge Corr. SF	up	+0.09	+0.12	+0.09	+0.10	+0.41
	down	−0.10	−0.10	−0.06	0.00	−0.26
				Low-m_{jj} Control Region Yields		
Nominal, Statistical Unc.		1.77 ± 0.09	1.70 ± 0.09	3.56 ± 0.26	4.00 ± 0.30	11.03 ± 0.42
Energy Correction		±0.02	±0.13	±0.40	±0.31	±0.86
Charge Corr. SF	up	+0.10	+0.13	+0.10	+0.11	+0.43
	down	−0.19	−0.09	−0.07	−0.10	−0.45

Table 8.3: Event yields for charge mis-ID background in the signal region and low-m_{jj} control region, including statistical and systematic uncertainties.

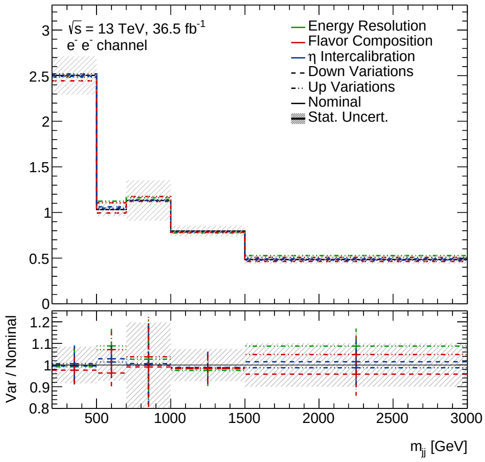

(a) e^-e^-

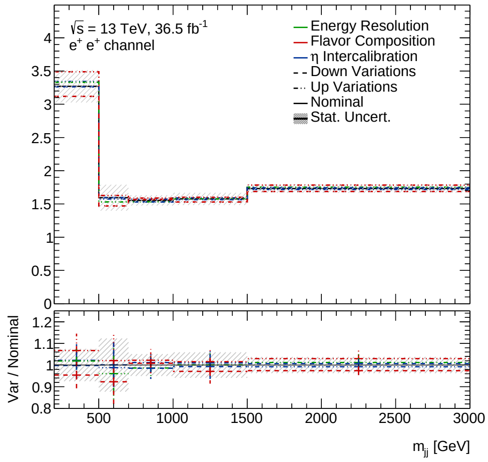

(b) e^+e^+

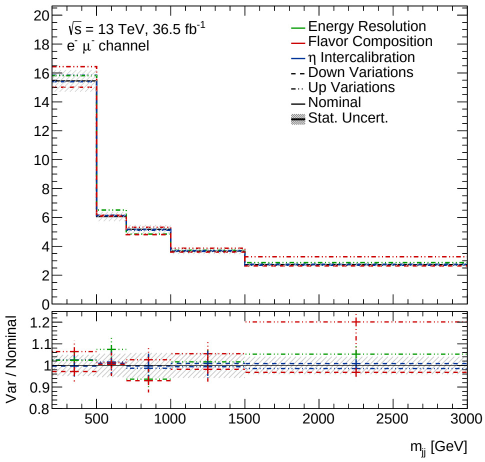

(c) $e^-\mu^-/\mu^-e^-$

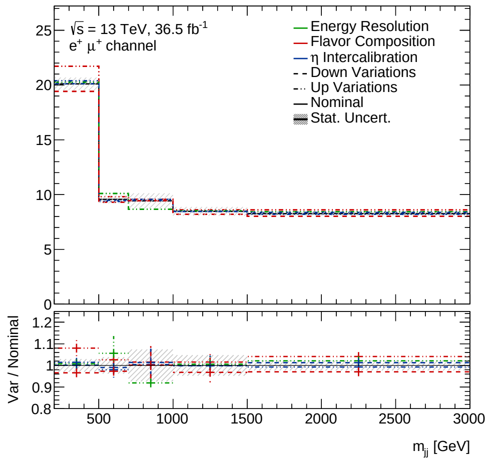

(d) $e^+\mu^+/\mu^+e^+$

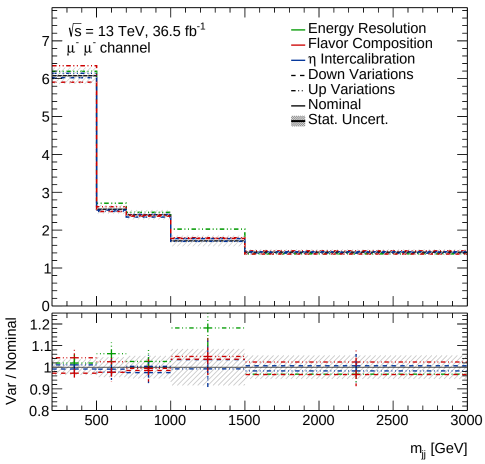

(e) $\mu^-\mu^-$

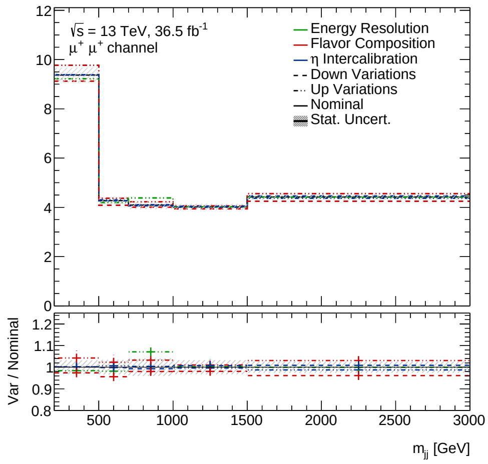

(f) $\mu^+\mu^+$

Figure 8.1: Total simulated prediction for different lepton charge and flavor channels. In each bin, the event yield corresponds to the sum of the ZZ, $V\gamma$, tri-boson, top, $W^\pm Z$, $W^\pm W^\pm jj$-QCD, and $W^\pm W^\pm jj$-EW estimates. The nominal prediction (solid, black), as well as the shape variations of the jet energy resolution (green), flavor composition (red) and η intercalibration (blue) nuisance parameters are shown. Up and down variations are represented by dashed and dotted lines, respectively. Statistical uncertainties on the nominal prediction are depicted by the hatched, gray error band. The bin from 200 GeV to 500 GeV corresponds to the low-m_{jj} control region.

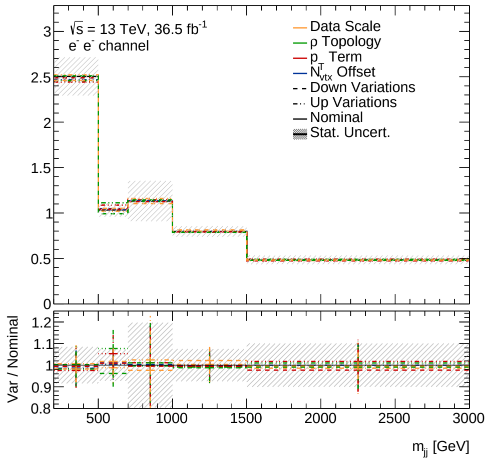

(a) e^-e^-

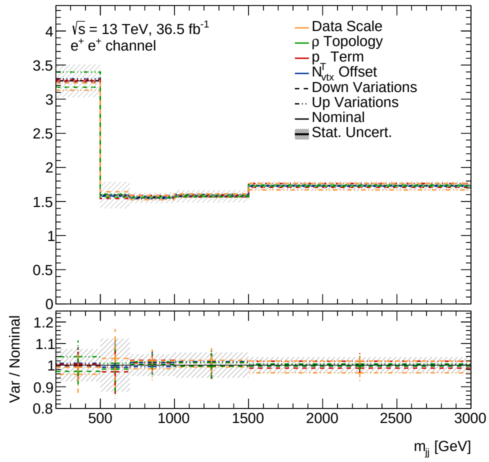

(b) e^+e^+

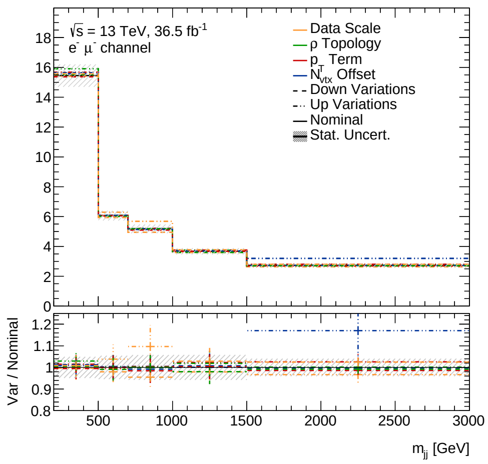

(c) $e^-\mu^-/\mu^-e^-$

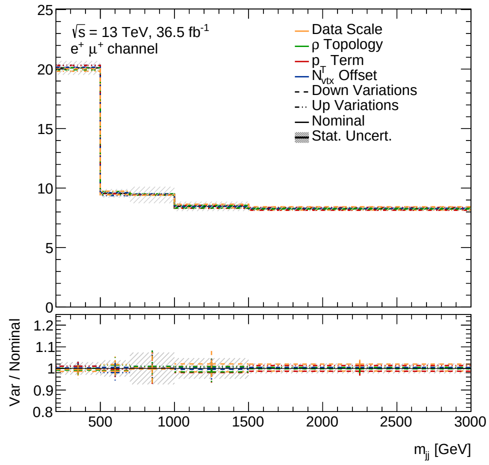

(d) $e^+\mu^+/\mu^+e^+$

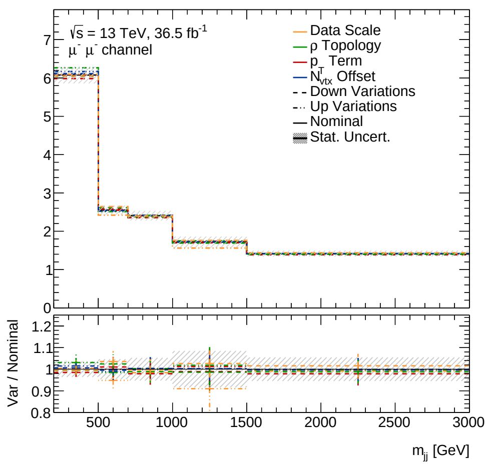

(e) $\mu^-\mu^-$

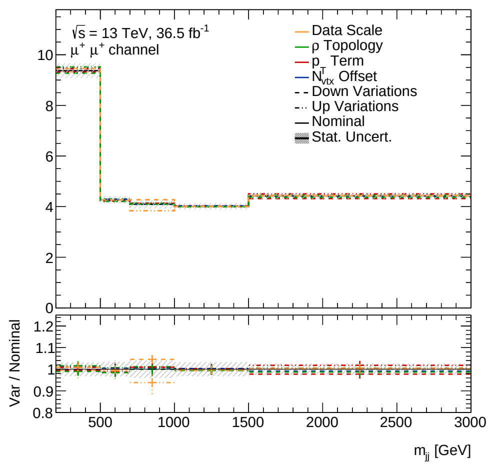

(f) $\mu^+\mu^+$

Figure 8.2: Total simulated prediction for different lepton charge and flavor channels. In each bin, the event yield corresponds to the sum of the ZZ, $V\gamma$, tri-boson, top, $W^{\pm}Z$, $W^{\pm}W^{\pm}jj$-QCD, and $W^{\pm}W^{\pm}jj$-EW estimates. The nominal prediction (solid, black), as well as the shape variations of the pile-up data scale factor (orange), ρ topology (green), p_{T} term (red) and N_{vtx} offset (blue) nuisance parameters are shown. Up and down variations are represented by dashed and dotted lines, respectively. Statistical uncertainties on the nominal prediction are depicted by the hatched, gray error band. The bin from 200 GeV to 500 GeV corresponds to the low-m_{jj} control region.

Channel		$e^+\mu^+/\mu^+e^+$	$e^-\mu^-/\mu^-e^-$	$\mu^+\mu^+$	$\mu^-\mu^-$	$\ell^\pm\ell^\pm\ell^\mp$
		Signal Region				
Nominal, Statistical Unc.		35.72 ± 0.90	17.64 ± 0.50	16.80 ± 0.28	8.09 ± 0.24	
Scale	up	+0.01	−0.05	−0.06	−0.05	
	down	+0.03	−0.04	−0.03	−0.04	
Inner Detector p_T	up	+0.02	−0.05	−0.05	−0.06	
	down	−0.01	−0.04	−0.06	−0.05	
Muon Spectrometer p_T	up	+0.01	< 0.01	−0.06	−0.04	
	down	+0.04	−0.08	−0.07	−0.04	
		Low-m_{jj} Control Region				$W^\pm Z$ Cr
Nominal, Statistical Unc.		20.11 ± 0.58	15.45 ± 0.75	9.37 ± 0.30	6.08 ± 0.22	116.71 ± 1.92
Scale	up	−0.05	+0.16	−0.05	−0.04	−4.61
	down	−0.02	+0.18	−0.05	−0.04	−4.50
Inner Detector p_T	up	−0.02	+0.17	−0.06	−0.04	−4.55
	down	−0.03	+0.16	−0.05	−0.05	−4.66
Muon Spectrometer p_T	up	−0.03	+0.17	−0.05	−0.03	−4.59
	down	−0.03	+0.20	−0.07	−0.04	−4.58

Table 8.4: Event yields for the sum of all simulated signal and background predictions in the signal, as well as low-m_{jj} and $W^\pm Z$ control regions. Only lepton channels involving muons are shown. Statistical and well as systematic uncertainties due to a subset of muon-related systematic uncertainties are shown.

8.2 Theory Uncertainties

Nuisance parameters covering the systematic uncertainty on the generated cross section are assigned to all simulated background and signal contributions. For all simulated backgrounds, except for the $W^\pm Z$ and $W^\pm W^\pm jj$-Qcd production, normalization uncertainties are applied. Uncertainties of 20 % are assigned to the ZZ, $W^\pm\gamma$, and $Z\gamma$ predictions. For tri-boson and top production, an uncertainty of 30 % is assumed. These values are based on the uncertainties reported in the 8 TeV Atlas analysis [89].

In contrast, the theory uncertainties on the signal prediction as well as the $W^\pm W^\pm jj$-Qcd and $W^\pm Z$ backgrounds are calculated as shape uncertainties. Contributions related to the choice of the strong coupling α_s, the values of the renormalization and factorization scales μ_R and μ_F, the set of proton parton distribution functions (Pdf), as well as the parton showering are derived separately.

The impact of a specific choice of the μ_R and μ_F values is evaluated by varying μ_R and μ_F independently up and down by a factor of two. Scenarios where μ_R and μ_F are varied in opposite directions are not included, yielding a total of seven variations. The symmetrized envelope of these variations is taken as final scale uncertainty.

Uncertainties on the Pdf set are evaluated using internal Pdf variations provided within the Nnpdf3.0Nnlo Pdf set. Additionally, the impact of external variations using the Ct14 Nnlo [147] and Mmht2014 [148] Pdf sets are studied. The total Pdf uncertainty is taken as the envelope of all variations. The nominal value of α_s is set to the Z-boson mass. α_s uncertainties are estimated by varying the nominal value and re-weighting the events accordingly. Scale, Pdf and α_s uncertainties are available on reconstruction level.

Parton shower uncertainties for the $W^\pm W^\pm jj$-Ew and $W^\pm W^\pm jj$-Qcd samples are assessed using different shower settings available in Sherpa. The merging scale Λ_{MS}, the hadronization scale as well as the shower recoil scheme are varied. The total uncertainty is taken as the envelope of the individual variations. These variations are only available on particle level; and are folded to reconstruction level using the method described in Section 4.5.

The $W^{\pm}Z$ parton shower uncertainties are estimated on reconstruction level using a PowhegBox sample that has been interfaced to the showering algorithms of Pythia 8 [76] and Herwig 7 [77, 78]. The relative difference between these two samples is applied as a relative uncertainty to the nominal $W^{\pm}Z$ Sherpa sample.

In Tables 8.5 and 8.6, nominal event yields with statistical, as well as systematic uncertainties due to theory variations are shown in the signal and low-m_{jj} control region for the $W^{\pm}W^{\pm}jj$-Qcd and $W^{\pm}Z$ estimate, respectively. Additionally, varied m_{jj} distributions in the signal and low-m_{jj} control regions are shown in Figure 8.3 (a) and (b). For both samples, the scale uncertainty is dominating. The effect of theory uncertainties on the $W^{\pm}Z$ estimate in the $W^{\pm}Z$ control region is listed in Table 8.7. No events from the $W^{\pm}W^{\pm}jj$-Qcd and $W^{\pm}W^{\pm}jj$-Ew samples are accepted in the $W^{\pm}Z$ control region. Therefore, the calculation of theory uncertainties on these samples is not possible in this control region.

Special consideration has to be given to the final theory uncertainties on the signal prediction. Each nuisance parameter affects the overall normalization, as well as the m_{jj} shape of the signal distribution. The normalization effect of these uncertainties on particle level is assigned to the predicted fiducial signal cross section. It is therefore necessary to separate the normalization effect on particle level from shape effects in order to avoid double-counting. As discussed in Section 4.2.1, signal theory uncertainties are normalized on particle level to the nominal fiducial cross section, such that the remaining uncertainties only include shape effects as well as small normalization effects due to different selection efficiencies on particle and reconstruction level. Hence, the theory uncertainties on the signal distribution are smaller than the uncertainties on the $W^{\pm}Z$ and $W^{\pm}W^{\pm}jj$-Qcd estimate.

In addition to the α_{s}, Pdf, scale, and parton shower variations, uncertainties accounting for the interference between $W^{\pm}W^{\pm}jj$-Ew and $W^{\pm}W^{\pm}jj$-Qcd as well as next-to-leading order electroweak corrections are taken into account on the signal sample. These variations are discussed in Sections 4.3 and 4.4, respectively. In Table 8.8, the nominal $W^{\pm}W^{\pm}jj$-Ew event yields including statistical and theory uncertainties are given in the signal and low-m_{jj} control region. In agreement with the observations on the $W^{\pm}Z$ and $W^{\pm}W^{\pm}jj$-Qcd background estimates, the parton shower systematic is the dominant uncertainty.

In Figure 8.4, the nominal and varied signal m_{jj} distributions in the signal and low-m_{jj} control region are shown. The effects of the nuisance parameters range between 1 % and 9 % for different m_{jj} bins. The largest uncertainties are observed in the low-m_{jj} control region and at high-m_{jj} values larger than 1500 GeV. This, as well as the comparably small systematic uncertainties on the central m_{jj} bin from 1000 GeV to 1500 GeV, is a side-effect of the normalization on particle level. The largest shape variation is observed for the Nlo Ew corrections and interference systematics.

Channel		e^+e^+	e^-e^-	$e^+\mu^+/\mu^+e^+$	$e^-\mu^-/\mu^-e^-$	$\mu^+\mu^+$	$\mu^-\mu^-$	$\ell^\pm\ell^\pm$
$W^\pm W^\pm jj$-QCD Yields – Signal Region								
Nominal, Statistical Unc.		0.38 ± 0.02	0.16 ± 0.01	3.02 ± 0.06	1.21 ± 0.04	1.80 ± 0.04	0.76 ± 0.03	7.34 ± 0.09
Scale Variations	up	+0.15	+0.06	+1.15	+0.46	+0.68	+0.29	+2.78
	down	−0.09	−0.04	−0.74	−0.30	−0.44	−0.19	−1.80
PDF	up	+0.01	<0.01	+0.09	+0.04	+0.06	+0.02	+0.23
	down	−0.01	<0.01	−0.08	−0.03	−0.05	−0.02	−0.19
α_S	up	+0.01	<0.01	+0.06	+0.02	+0.04	+0.02	+0.15
	down	−0.01	<0.01	−0.06	−0.03	−0.04	−0.02	−0.15
Parton Shower		+0.05	+0.02	+0.37	+0.15	+0.22	+0.09	+0.90
$W^\pm W^\pm jj$-QCD Yields – Low-m_{jj} Control Region								
Nominal, Statistical Unc.		0.24 ± 0.02	0.15 ± 0.01	1.99 ± 0.05	1.15 ± 0.03	1.16 ± 0.03	0.64 ± 0.03	5.32 ± 0.08
Scale Variations	up	+0.08	+0.05	+0.63	+0.37	+0.37	+0.20	+1.70
	down	−0.05	−0.03	−0.43	−0.25	−0.25	−0.14	−1.14
PDF	up	+0.01	<0.01	+0.06	+0.03	+0.03	+0.02	+0.15
	down	<0.01	<0.01	−0.03	−0.02	−0.02	−0.01	−0.07
α_S	up	<0.01	<0.01	+0.04	+0.02	+0.02	+0.01	+0.11
	down	−0.01	<0.01	−0.04	−0.03	−0.03	−0.01	−0.12
Parton Shower		+0.01	+0.01	+0.07	+0.04	+0.04	+0.02	+0.20

Table 8.5: Nominal event yields and statistical uncertainties for the $W^\pm W^\pm jj$-QCD background in the signal and low-m_{jj} control regions. The effect of theory variations is also given.

Channel		e^+e^+	e^-e^-	$e^+\mu^+/\mu^+e^+$	$e^-\mu^-/\mu^-e^-$	$\mu^+\mu^+$	$\mu^-\mu^-$	$\ell^\pm\ell^\pm$
$W^\pm Z$ Yields – Signal Region								
Nominal, Statistical Unc.		1.87 ± 0.14	1.31 ± 0.10	13.81 ± 0.46	8.93 ± 0.40	5.50 ± 0.24	3.64 ± 0.22	35.06 ± 0.72
Scale Variations	up	+0.52	+0.36	+3.81	+2.46	+1.52	+1.01	+9.68
	down	−0.35	−0.24	−2.55	−1.65	−1.02	−0.67	−6.48
PDF	up	+0.04	+0.03	+0.30	+0.19	+0.12	+0.08	+0.76
	down	−0.03	−0.02	−0.21	−0.14	−0.08	−0.06	−0.53
α_S	up	+0.01	+0.01	+0.07	+0.04	+0.03	+0.02	+0.18
	down	−0.01	−0.01	−0.07	−0.04	−0.03	−0.02	−0.17
Parton Shower		+0.32	+0.23	+2.39	+1.55	+0.95	+0.63	+6.07
$W^\pm Z$ Yields – Low-m_{jj} Control Region								
Nominal, Statistical Unc.		2.02 ± 0.23	1.57 ± 0.14	13.79 ± 0.57	10.31 ± 0.54	5.76 ± 0.27	3.95 ± 0.21	37.40 ± 0.90
Scale Variations	up	+0.56	+0.43	+3.82	+2.86	+1.60	+1.10	+10.36
	down	−0.38	−0.30	−2.63	−1.96	−1.10	−0.75	−7.12
PDF	up	+0.05	+0.04	+0.31	+0.23	+0.13	+0.09	+0.84
	down	−0.02	−0.02	−0.16	−0.12	−0.07	−0.05	−0.43
α_S	up	+0.03	+0.02	+0.18	+0.13	+0.07	+0.05	+0.48
	down	−0.03	−0.02	−0.18	−0.13	−0.07	−0.05	−0.48
Parton Shower		+0.29	+0.23	+1.98	+1.48	+0.83	+0.57	+5.36

Table 8.6: Nominal event yields and statistical uncertainties for the $W^\pm Z$ background in the signal and low-m_{jj} control regions. The effect of theory variations is also given.

Channel		$\ell^\pm\ell^\pm$
Nominal, Statistical Unc.		197.09 ± 1.42
Scale Variations	up	+54.03
	down	−37.13
PDF	up	+3.89
	down	−2.62
α_S	up	+1.35
	down	−1.46
Parton Shower		+49.10

Table 8.7: Nominal event yields and statistical uncertainties for the $W^\pm Z$ background in the $W^\pm Z$ control region. The effect of theory variations is also given.

Channel		e^+e^+	e^-e^-	$e^+\mu^+/\mu^+e^+$	$e^-\mu^-/\mu^-e^-$	$\mu^+\mu^+$	$\mu^-\mu^-$	$\ell^\pm\ell^\pm$
				$W^\pm W^\pm jj$-EW Yields – Signal Region				
Nominal, Statistical Unc.		3.80 ± 0.08	1.49 ± 0.05	16.49 ± 0.17	6.45 ± 0.11	9.14 ± 0.13	3.50 ± 0.07	40.88 ± 0.27
Scale Variations	up	+0.03	+0.01	+0.15	+0.06	+0.08	+0.03	+0.37
	down	−0.03	−0.01	−0.13	−0.05	−0.07	−0.03	−0.33
PDF	up	<0.01	<0.01	+0.01	<0.01	+0.01	<0.01	+0.03
	down	<0.01	<0.01	−0.02	0.01	−0.01	<0.01	−0.05
α_S	up	<0.01	<0.01	−0.01	<0.01	<0.01	<0.01	−0.02
	down	<0.01	<0.01	+0.01	<0.01	+0.01	<0.01	+0.03
Parton Shower		+0.20	+0.08	+0.89	+0.35	+0.49	+0.19	+2.19
EW-QCD Interference	up	−0.03	−0.01	−0.14	−0.06	−0.08	−0.03	−0.35
	down	+0.04	+0.01	+0.16	+0.06	+0.09	+0.03	+0.40
EW Corrections	up	−0.05	−0.02	−0.20	−0.08	−0.11	−0.04	−0.51
	down	+0.05	+0.02	+0.20	+0.08	+0.11	+0.04	+0.51
				$W^\pm W^\pm jj$-EW Yields – Low-m_{jj} Control Region				
Nominal, Statistical Unc.		0.64 ± 0.03	0.47 ± 0.04	2.97 ± 0.07	1.99 ± 0.06	1.82 ± 0.09	1.11 ± 0.04	9.01 ± 0.15
Scale Variations	up	−0.03	−0.02	−0.12	−0.08	−0.08	−0.05	−0.38
	down	+0.02	+0.02	+0.11	+0.07	+0.07	+0.04	+0.33
PDF	up	<0.01	<0.01	−0.01	<0.01	<0.01	<0.01	−0.02
	down	<0.01	<0.01	+0.02	+0.01	+0.01	+0.01	+0.05
α_S	up	<0.01	<0.01	+0.01	<0.01	<0.01	<0.01	+0.02
	down	<0.01	<0.01	−0.01	−0.01	−0.01	<0.01	−0.02
Parton Shower		−0.08	−0.06	−0.36	−0.24	−0.22	−0.13	−1.09
EW-QCD Interference	up	+0.05	+0.03	+0.22	+0.14	+0.13	+0.08	+0.65
	down	−0.05	−0.04	−0.25	−0.16	−0.15	−0.09	−0.74
EW Corrections	up	+0.05	+0.04	+0.23	+0.15	+0.14	+0.09	+0.69
	down	−0.05	−0.04	−0.23	−0.15	−0.14	−0.09	−0.69

Table 8.8: Nominal event yields and statistical uncertainties for the $W^\pm W^\pm jj$-EW signal prediction in the signal and low-m_{jj} control regions. The effect of theory variations is also given.

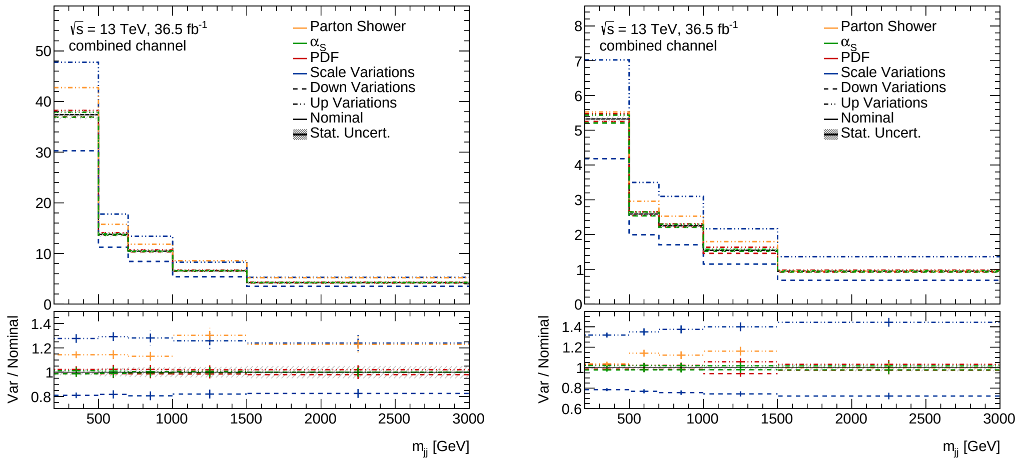

(a) $W^{\pm}Z$ (b) $W^{\pm}W^{\pm}jj$-Qcd

Figure 8.3: m_{jj} distributions of the $W^{\pm}Z$ (a) and $W^{\pm}W^{\pm}jj$-Qcd (b) background contributions in the combined lepton channel in the signal and low-m_{jj} control region. Shape variations corresponding to parton shower (orange), α_s (green), Pdf (red), and scale nuisance parameters (blue) are shown. Up and down variations for a specific nuisance parameter are drawn as dotted and dashed lines, respectively. The bin from 200 GeV to 500 GeV corresponds to the low-m_{jj} control region.

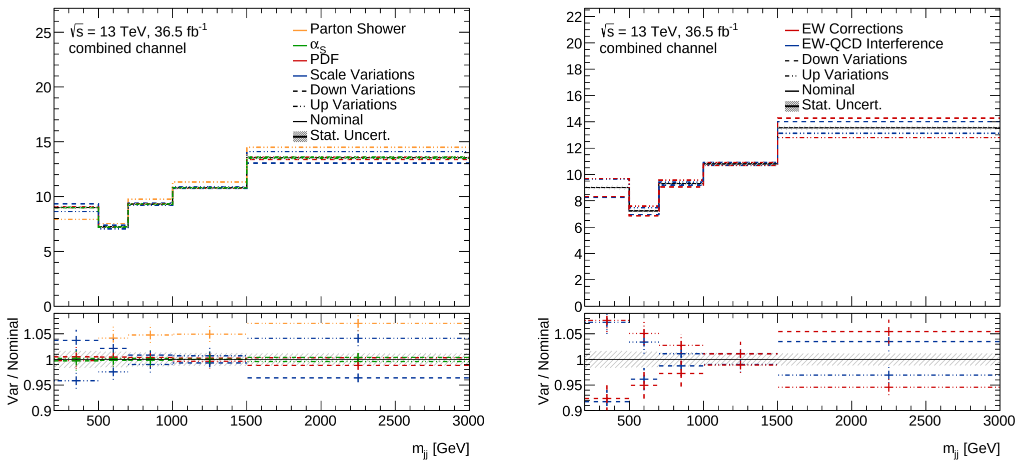

(a) α_s, Pdf, Scale, Parton Shower (b) Ew-Qcd Interference, Ew Nlo Corrections

Figure 8.4: m_{jj} distributions of the $W^{\pm}W^{\pm}jj$-Ew signal prediction and different sources of systematic uncertainties in the combined lepton channel in the signal and low-m_{jj} control region. In (a), shape variations corresponding to parton shower (orange), α_s (green), Pdf (red), and scale nuisance parameters (blue) are shown. Shape uncertainties due to interference between Ew and Qcd production (blue) as well as Ew next-to-leading order corrections (red) are presented in (b). Up and down variations for a specific nuisance parameter are drawn as dotted and dashed lines, respectively. The bin from 200 GeV to 500 GeV corresponds to the low-m_{jj} control region.

8.3 Luminosity Uncertainty

For all simulated contributions where the normalization is not determined from data, i. e. $W^{\pm}W^{\pm}jj$-EW, $W^{\pm}W^{\pm}jj$-QCD, ZZ, $V\gamma$, top, tri-boson, as well as V+jets, $W^{\pm}W^{\mp}$ and $t\bar{t}$ production, an additional nuisance parameter is assigned to the event yield. This nuisance parameter accounts for the normalization uncertainty on the luminosity measurement, and is constrained by a Gaussian density.

The methodology of the luminosity measurement is detailed in Reference [149]. The instantaneous luminosity is determined using the interaction rate per bunch crossing μ, as described in Eq. (5.1). The visible interaction rate μ_{vis} can be measured with dedicated forward detectors like LUCID-2 [150], and is the product of the detector efficiency ε and the total interaction rate μ. The corresponding visible inelastic cross section σ_{vis} is calculated as $\varepsilon \cdot \sigma_{\text{inel}}$, using the cross section for inelastic proton-proton scattering σ_{inel}. If σ_{vis} is known, the instantaneous luminosity per bunch, $\mathcal{L}_b$, is given as

$$\mathcal{L}_b = \frac{\mu_{\text{vis}}\, f_r}{\sigma_{\text{vis}}}, \tag{8.2}$$

where f_r denotes the LHC revolution frequency. As σ_{inel} is a well-known quantity, this means that the detector efficiency ε has to be precisely known in order to calculate $\mathcal{L}_b$.

To determine ε for the LUCID-2 detector, the beam widths $\Sigma_{x,y}$ along the x- and y-axes are measured during van-der-Meer (vdM) scans [151]. Using the number of protons $n_{1,2}$ in the colliding bunches, the bunch luminosity can then be calculated from

$$\mathcal{L}_b = \frac{n_1\, n_2\, f_r}{2\pi\ \Sigma_x \Sigma_y}. \tag{8.3}$$

As van-der-Meer scans are done under low-luminosity beam-conditions, and repeated only in large time intervals, extrapolation uncertainties to high-luminosity situations as well as long-term drift corrections are introduced. In addition, systematic uncertainties for the vdM calibration method and beam-induced backgrounds in the measurement of the instantaneous luminosity are taken into account [149]. The total uncertainty on the integrated luminosity of the combined 2015 and 2016 dataset amounts to 2.1 %.

8.4 Statistical Uncertainties on Simulated Backgrounds

As briefly discussed in Section 2.2.3, the statistical uncertainty on the simulated predictions is described using one nuisance parameter per m_{jj} bin, region and channel [50]. In each bin, the relative total statistical uncertainty is constructed from the statistical uncertainties of all simulated contributions[1].

The caveat in this procedure is the treatment of statistical uncertainties on the signal prediction. Generally, the statistical uncertainty on the signal prediction is lower than the uncertainties on the simulated backgrounds, as a very large number of signal events has been generated. Therefore, the total relative uncertainty on the prediction in each bin is reduced when the signal sample is included in the calculation; an effect that becomes especially important in bins with a high signal-to-background ratio. This can result in an increase of the expected significance, which then depends on the statistical precision of the signal sample. This increase is found to be of the order of a few percent in this analysis. In order to give a conservative significance estimate, which is independent of the signal precision, the signal statistical uncertainty is not included in the fit[2].

[1] In the HISTFACTORY package, samples to use for the calculation of the relative total statistical uncertainty are flagged using the `ActivateStatError` property. Data-driven background estimates are excluded from the calculation by setting `ActivateStatError` to `False`.

[2] The `ActivateStatError` flag is set to `False` for the signal sample as well.

The relative statistical uncertainties on the total simulated background included in the fit are given in Table 8.9. The size of these uncertainties varies between approximately 1 % in the $W^{\pm}Z$ control region to 60 % in the $e^{-}e^{-}$ channel of the signal region. In the signal and low-m_{jj} control region, the uncertainty decreases with increasing number of muons in the event. Additionally, it is observed that the uncertainty in the $\ell^{-}\ell^{-}$ channel is slightly larger than in the corresponding $\ell^{+}\ell^{+}$ channel. As the uncertainty on the non-prompt background is dominating, this can be explained by reconsidering the event yields for the non-prompt backgrounds before the fit. Event yields with total uncertainties are listed Table 9.9, while yields with purely statistical uncertainties are given in Table 8.2. In Appendix C.2, the bin-wise yields in the signal region are reported. It can be seen that the fraction of non-prompt events is lower for channels involving muons, but also the statistical uncertainty on the non-prompt prediction in the muon channels is reduced. This leads to an overall smaller relative statistical uncertainty.

Lower Bin Boundary	Statistical Uncertainty [%]						
[GeV]	$e^{-}e^{-}$	$e^{+}e^{+}$	$e^{-}\mu^{-}/\mu^{-}e^{-}$	$e^{+}\mu^{+}/\mu^{+}e^{+}$	$\mu^{-}\mu^{-}$	$\mu^{+}\mu^{+}$	$\ell^{\pm}\ell^{\pm}\ell^{\mp}$
	Signal Region						
500	±22.81	±33.47	±18.02	±13.97	±8.44	±5.73	
700	±42.52	±40.38	±27.02	±16.17	±10.29	±8.22	
1000	±59.94	±11.40	±21.38	±18.41	±18.43	±8.16	
1500	±52.63	±24.20	±34.45	±30.15	±14.63	±8.06	
	Low-m_{jj} Control Region						$W^{\pm}Z$ CR
200	±21.98	±13.77	±9.30	±8.87	±4.65	±8.08	±1.15

Table 8.9: Bin-wise relative statistical uncertainties on the total simulated background estimate in the signal and low-m_{jj} control regions. For each bin, the lower bin boundary is given. In all regions, the maximal m_{jj} value is set to 3000 GeV. Events with an m_{jj} value larger than that are included in the last bin.

9 Fitting and Cross Section Measurement

The statistical analysis in this thesis is implemented using the `HistFactory` framework [50]. The likelihood template used in the optimization is described in Section 2.2.3. The signal strength parameter μ, which has been introduced in Eq. (2.35), is used to scale the signal expectation to the value providing best agreement with the observed data. Therefore, it can also be written as

$$\mu = \frac{\sigma_{\text{meas}}}{\sigma_{\text{SM}}}, \tag{9.1}$$

where σ_{SM} is the $W^{\pm}W^{\pm}jj$-EW cross section predicted by the SM, and σ_{meas} corresponds to cross section providing the best agreement with the observed data set. Hence, the measured fiducial cross section can be inferred using the measured signal strength.

The signal strength is measured by simultaneously fitting the signal region in combination with the low-m_{jj} and $W^{\pm}Z$ control regions. The signal and low-m_{jj} control regions are separated by lepton charge and flavor into six channels. As the $W^{\pm}Z$ background is not dependent on lepton flavor or charge, events in the $W^{\pm}Z$ control region are not split into channels. The m_{jj} distribution used in the statistical analysis is split in four bins in the signal region. Therefore, a total of 31 different categories are included in the fit[1].

An overview of all process categories included in the different regions in the profile likelihood fit is given in Table 9.1. In the following, background contributions given in figures and tables are grouped according to these categories. The data-driven estimate of charge mis-ID and non-prompt backgrounds is only derived for the signal and low-m_{jj} control regions. Therefore, simulated events for $W^{\pm}/Z$+jets, $t\bar{t}$, $W^{\pm}W^{\mp}$, as well as ZZ production are used in the background estimate of the $W^{\pm}Z$ control region. A summary of the included nuisance parameters is given in Chapter 8.

Category/Process		SR	Low-m_{jj} CR	$W^{\pm}Z$ CR
$W^{\pm}W^{\pm}jj$-EW		✓	✓	✓
$W^{\pm}W^{\pm}jj$-QCD		✓	✓	✓
$W^{\pm}Z$		✓	✓	✓
Other Prompt	Top	✓	✓	✓
	Tri-Boson	✓	✓	✓
	ZZ	✓	✓	✓
Conversion	$V\gamma$	✓	✓	✓
Charge Mis-ID	Data-Driven Charge Mis-ID	✓	✓	
	Z+jets			✓
	$W^{\pm}W^{\mp}$			✓
Non-Prompt	Data-Driven Non-Prompt	✓	✓	
	$t\bar{t}$			✓
	$W^{\pm}$+jets			✓

Table 9.1: Summary of all processes used in the signal and control regions in the statistical analysis.

[1]The $W^{\pm}Z$ control region builds one fitting category, the low-m_{jj} control region consists of six categories. Additionally, there are $4 \cdot 6$ categories in the signal region.

In Section 9.1, pre-conditional studies are described. This includes studies determining the binning and channel splitting in the signal and control regions. As several control regions are used in this analysis, special consideration has to go into the calculation of the expected significance. This is discussed, along with the documentation of expected results in Section 9.2. After finalizing the analysis strategy the signal region is unblinded, and the observed results are documented in Section 9.3. Finally, the expected and observed values of the signal strength are used to calculate the expected and observed fiducial cross sections. This is detailed further in Section 9.4.

9.1 Preparatory Studies

This section summarizes all preparatory studies necessary to determine the optimal configuration of the profile likelihood fit. In Section 9.1.1, the implementation of the statistical analysis is tested, using the event yields previously reported by the ATLAS collaboration. The binning and channel splitting of the $W^{\pm}Z$ control region is discussed in Section 9.1.2. In order to increase the performance of the fit in the studies to determine the optimal binning in the signal region, a pruning of nuisance parameters is used. This procedure is described in Section 9.1.3. The final results are, however, based on the full fit without any nuisance parameter pruning. The binning in the signal region is investigated, as presented in Section 9.1.4.

9.1.1 Cross-Check using Previous ATLAS Results

In order to provide an independent cross-check for the current implementation of the statistical analysis, previous results reported by the ATLAS collaboration [89] are re-interpreted. A summary of these results is given in Section 4.1.1. An expected and observed significance of 2.3 σ and 3.6 σ was announced, respectively.

In analogy to the method used in Reference [89], a one-bin profile likelihood fit is performed. Events are categorized into three lepton flavor channels, namely ee, $e\mu/\mu e$ and $\mu\mu$. The event yields and systematic uncertainties listed in Table 4.2 and 4.3 are used. The background is grouped according to the rows presented in Table 4.2. Therefore the following background categories are included in the fit:

- $W^{\pm}W^{\pm}jj$-QCD,
- Prompt, corresponding to $W^{\pm}Z$, $t\bar{t}V$, and ZZ,
- $W\gamma$,
- Charge Mis-ID, and
- Non-Prompt.

For each row in Table 4.3 and each sample, a nuisance parameter is defined. Nuisance parameters corresponding to detector systematics, i. e. luminosity, trigger, lepton, jet, $E_{\mathrm{T}}^{\mathrm{miss}}$, and b-tagging uncertainties, are correlated between all samples. In Table 4.3, systematic uncertainties for all background samples are given with respect to the total background yield. Therefore, the values have to be re-calculated per sample, such that the nuisance parameters can be configured accordingly.

Neglecting all uncertainties, the purely statistical expected and observed significances amount to 2.9 σ and 4.3 σ, respectively. Including the complete set of uncertainties, expected and observed significances of 2.3 σ and 3.5 σ are calculated. The evolution of the figure of merit depending on the included sources of systematic uncertainty in shown in Table 9.2. The distribution of pulls on nuisance parameters after the fit to observed data is shown in Figure 9.1.

Comparing these results to the values reported for the ATLAS 8 TeV analysis, small differences are observed. However, an exact reproduction of the 8 TeV results is impossible. Some background contributions, like $W^{\pm}Z$, $t\bar{t}V$ and ZZ are merged into a single background "Prompt" category, but were previously treated separately in the fit to account for different theory uncertainties. Additionally, only a summary of all systematic uncertainties for all background contributions is available. In this test it has been assumed, that all detector systematics are equally distributed across background contributions. Due to these approximations, small deviations from the numbers reported in [89] are expected.

9.1.2 Optimizing the WZ Control Region

This section describes the setup to include the $W^{\pm}Z$ control region into the full profile likelihood fit. Rather than taking into account a differential distribution over m_{jj} only the number of events in the $W^{\pm}Z$ CR is considered. One reason for this lies in the invariant mass distribution of the tagging jets, which has different shapes in the control region and signal region.

A comparison of the m_{jj} distribution in the signal and $W^{\pm}Z$ control regions is shown in Figure 9.2. Both m_{jj} distributions are normalized to unit area. It is observed that the m_{jj} spectrum in the signal region is slightly steeper than in the $W^{\pm}Z$ control region. As the $W^{\pm}Z$ control region has a requirement for three leptons (definition see Table 7.4), it is very likely for the tagging jets to come from the partons that radiated the $W^{\pm}$ or Z boson. This yields a very high purity in $W^{\pm}Z$ events. In the signal region however, it is more likely to mis-reconstruct hadronically decaying τ-leptons or leptons outside the tracker acceptance as jets. As these mis-reconstructed jets are expected to have lower transverse momentum, it is anticipated for the m_{jj} distribution in the $W^{\pm}Z$ control region to be harder than in the signal region.

In order to test the assumption that the $W^{\pm}Z$ normalization is independent on lepton flavor, different fit configurations are tested. The $W^{\pm}Z$ prediction in the $W^{\pm}Z$ control region is fitted, i. e. the $W^{\pm}Z$ production is taken as signal while all other simulated processes, including $W^{\pm}W^{\pm}jj$-EW production, are considered as backgrounds. Accordingly, the $W^{\pm}Z$ strength μ_{WZ} measures the $W^{\pm}Z$ normalization. The fit is done once with combining all lepton flavors into one channel, denoted as $\ell^{\pm}\ell^{\pm}\ell^{\mp}$ channel. A second combination is tested, where leptons are split by lepton flavor into $ee\ell$, $\mu\mu\ell$, and $e\mu\ell$ channels. Both fit configurations are run with the Asimov and observed datasets. The complete set of nuisance parameters is taken into account.

The figure of merit in this test is the calculated value of μ_{WZ} and its statistical (Δ_{stat}), theory (Δ_{theo}), and systematic uncertainties (Δ_{sys}). These values are summarized in Table 9.3. It is observed that theory uncertainties are as large as 46 % and 27 % in the up and down variation, respectively. This is due to the $W^{\pm}Z$ theory uncertainties, most notably the shower and scale variation uncertainties. The $W^{\pm}Z$ yields as well as theory uncertainties in the $W^{\pm}Z$ control region are listed in Table 8.6. The impact of the parton shower is approximately 25 %, scale variations uncertainties amount to + 30 % and - 20 %.

No significant difference is observed between the one-channel and three-channel fit results. A slight constraint on the up-variation of systematic uncertainties is observed in the three-channel fit to observed data. However, in the final setup, μ_{WZ} is measured in a combined fit of the $W^{\pm}Z$ and low-m_{jj} control region (see Section 9.2.1), where similar systematic uncertainties are observed. In order to use the simplest configuration, the combined $\ell^{\pm}\ell^{\pm}\ell^{\mp}$ channel is used for the final fit. Nuisance parameter pulls after the fit to observed data in the $\ell^{\pm}\ell^{\pm}\ell^{\mp}$ channel are shown in Figure 9.3. No significant constraint or pull on the nuisance parameters is observed. As only one bin and one channel is fitted, the difference between prediction and observation is completely absorbed into the post-fit value of μ_{WZ}.

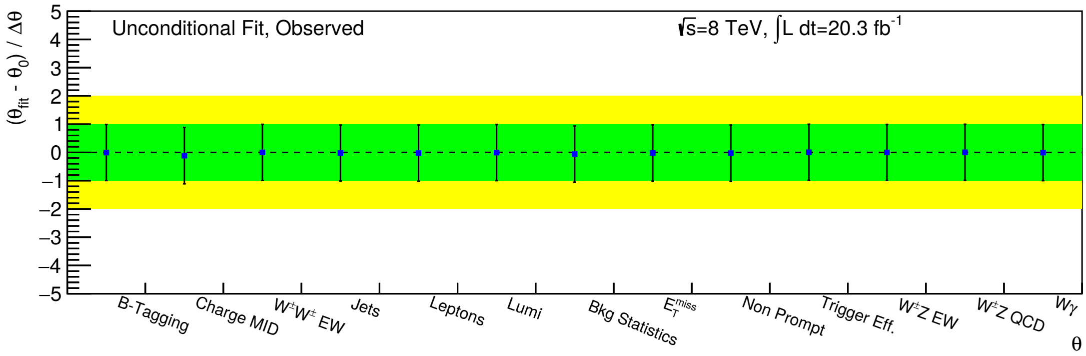

Figure 9.1: Nuisance parameter pulls for parameters with Gaussian constraint after the fit to observed data.

Source	Included Uncertainties				Full Result
Bkg. Statistics	✓	✓	✓	✓	✓
Theory	–	✓	✓	✓	✓
Charge Mis-ID	–	–	✓	✓	✓
Non-Prompt	–	–	–	✓	✓
Detector	–	–	–	–	✓
Expected [σ]	2.9	2.8	2.8	2.7	2.3
Observed [σ]	4.3	4.3	4.2	4.1	3.5

Table 9.2: Evolution of the significance when including different systematic sources. All sources marked with a ✓are included in the fit. Nuisance parameter representing the statistical uncertainty of the simulated samples are always included, but have a negligible effect.

9.1.3 Pruning of Nuisance Parameters

Running the full fit including the signal, low-m_{jj}, and $W^{\pm}Z$ control region is very time-consuming. Therefore a pruning method was implemented to reduce the number of nuisance parameters without affecting the final fit result. This pruning is applied in additional studies, to increase the computing performance. The results presented in Sections 9.2, 9.3, and 9.4 are generated using the complete set of systematic uncertainties.

The pruning is applied to all shape nuisance parameters with Gaussian constraints, i. e. overall normalization uncertainties and background precision bin-by-bin scale factors are not affected. The decision to include a nuisance parameter in the fit is based on the nominal, pre-fit estimate N_i of the affected contribution in a certain bin i, and the pre-fit 1-σ variation S_i. An impact threshold t as well as a percentage of bins p_b, in which the threshold has to be exceeded are tunable parameters. All nuisance parameters in a channel and region that do not exceed

$$\frac{|N_i - S_i|}{N_i} \geq t \tag{9.2}$$

in at least p_b percent of all bins are rejected.

A comparison of the expected significance, as well as the post-fit value and total uncertainty of the signal strength μ_exp is shown in Table 9.4 for different choices of the pruning parameters. Moreover, the time needed to run each fit is given with respect to the computing time needed for the full, unpruned fit. Note that this study is performed with one bin m_{jj} distributions in the control regions, and four bins in the signal region. Therefore, requiring a variation in at least 20 % of the bins in each region corresponds to a variation in at least one bin in the signal region.

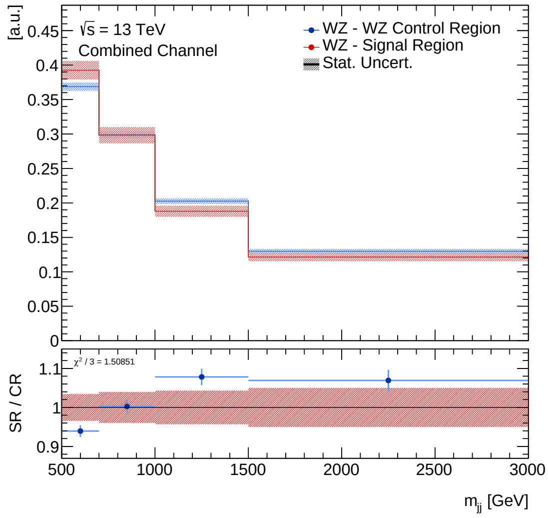

Figure 9.2: Comparison of $W^{\pm}Z$ m_{jj} distributions in the signal region and the $W^{\pm}Z$ control region above $m_{jj} = 500\,\text{GeV}$. The distributions are taken from the combined $\ell^{\pm}\ell^{\pm}\ell^{\mp}$ and $\ell^{\pm}\ell^{\pm}$ channel in the $W^{\pm}Z$ control and signal regions, respectively. Both histograms are normalized to unit area. The shape of the m_{jj} distributions differs between both regions as different production processes are involved, respectively.

Data type	Channel	μ_{WZ}	Δ_{stat}		Δ_{theo}		Δ_{sys}	
Asimov	$\ell^{\pm}\ell^{\pm}\ell^{\mp}$	1.00	+0.08	−0.08	+0.47	−0.27	+0.13	−0.04
	$ee\ell$, $\mu\mu\ell$, $e\mu\ell$	1.00	+0.08	−0.08	+0.47	−0.27	+0.14	−0.03
Observed	$\ell^{\pm}\ell^{\pm}\ell^{\mp}$	0.88	+0.07	−0.07	+0.41	−0.24	+0.12	−0.03
	$ee\ell$, $\mu\mu\ell$, $e\mu\ell$	0.88	+0.07	−0.07	+0.41	−0.24	+0.08	−0.04

Table 9.3: Comparison of μ_{WZ} for different channel combinations used in the fit of the $W^{\pm}Z$ control region. The best fit value of μ_{WZ} is given, as well as the statistical (Δ_{stat}), theory (Δ_{theo}), and other systematic uncertainties (Δ_{sys}).

The purely statistical significance, i. e. the significance derived with purely statistical uncertainties, not including additional nuisance parameters, is 5.01 σ. The smaller the thresholds t and p_{b} are chosen, the more nuisance parameters are included. The significance decreases from the purely statistical significance to the value of the full fit, which is 4.59 σ. It is seen that this decrease is not monotonous. There is for instance a slight increase in significance when changing the settings from ($t = 10$ %, $p_{\text{b}} = 20$ %) to ($t = 1$ %, $p_{\text{b}} = 40$ %). This can be due to correlations between nuisance parameters, which are neglected with tighter pruning settings.

From Table 9.4 it can be seen that even for very tight pruning settings like ($t = 40$ %, $p_{\text{b}} = 20$ %) the expected significance is relatively close to the full significance. A summary of all nuisance parameters used in that fit is given in Table 9.5. Here, nuisance parameters are grouped according to the categories defined in Section 8, Table 8.1.

It is observed that the settings ($t = 0.1$ %, $p_{\text{b}} = 20$ %) and ($t = 0.01$ %, $p_{\text{b}} = 20$ %) yield identical results which deviate from the full significance only in the fourth digit. Therefore, the following studies to optimize the signal region are completed by setting $t = 0.1$ % and $p_{\text{b}} = 20$ %. In this configuration, 92 of a total of 112 shape nuisance parameters are included in the fit. A detailed overview of nuisance parameter usage is shown in Appendix C.1.

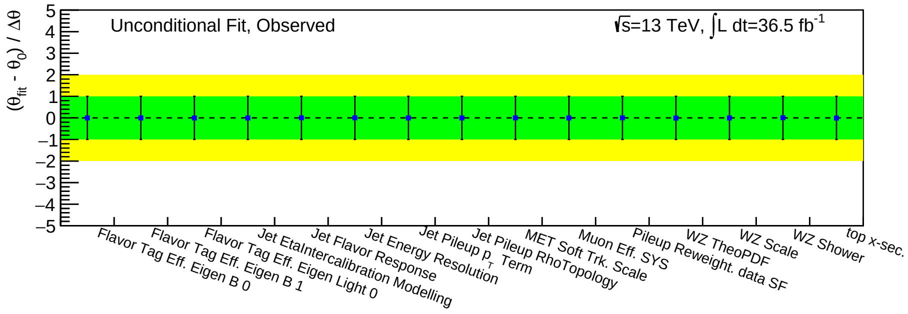

Figure 9.3: Nuisance parameter pulls for parameters with Gaussian constraint after the $W^{\pm}Z$ control region fit to observed data in the $\ell^{\pm}\ell^{\pm}\ell^{\mp}$ channel. Only the 15 nuisance parameters showing the highest pulls or constraints are displayed.

Settings t[%]	p_{b}[%]	Exp. Sig. [σ]	μ_{exp}			Time [%]
40	20	4.636	1.00	+0.27	−0.25	0.6
20	40	4.650	1.00	+0.27	−0.25	0.7
10	20	4.569	1.00	+0.27	−0.25	1.6
1	40	4.586	1.00	+0.29	−0.26	4.6
0.1	20	4.584	1.01	+0.29	−0.27	23.0
0.01	20	4.584	1.01	+0.29	−0.27	31.8
No Pruning		4.588	1.01	+0.28	−0.27	100
Only Statistics		5.014	1.00	+0.25	−0.24	0.5

Table 9.4: Comparison of fit results for different pruning parameters. Additionally, the results of the full fit (No Pruning) and the purely statistical fit (Only Statistics) are given. The post-fit value and total uncertainty on the signal strength μ_{exp} is listed, as well as the expected significance. To illustrate the change in computing intensity, the time needed to run the pruned fit is given relative to the run time of the full fit.

9.1.4 Optimizing the Signal Region

In order to maximize the expected significance, the binning of the m_{jj} distribution in the signal and low-m_{jj} control regions is optimized. The binning is constructed in a way to avoid bins with zero background events, as this would cause problems in the profile likelihood method.

The procedure starts from the input histograms, which have a fine m_{jj} binning with equidistant, 12.5 GeV wide bins. These histograms contain weighted events and cover a range from 200 GeV to 500 GeV and 500 GeV to 3000 GeV in low-m_{jj} control and signal region, respectively. In the signal region, events with m_{jj} larger than 3000 GeV are included in the last bin. In each region, the final binning is generated by merging bins until two criteria are fulfilled:

1. Each bin contains at least a specified number of signal N_{S} and background events N_{B},
2. and the relative statistical uncertainty[1] in each bin is smaller than a certain ΔN_{S}, and ΔN_{B}.

The conditions on N_{B} and ΔN_{B} are evaluated using the sum of all background contributions. It is therefore still possible for small background categories to have some empty bins. In these cases, the statistical error in the respective bins is set to 1.

[1] For simulated contributions, this corresponds to the precision of the simulated prediction. For data-driven charge mis-ID and non-prompt estimates, the statistical uncertainty is calculated from the amount of data available in the regions where the respective correction factors are applied.

Sample	Jets	Pile up	Flavor Tagging	Non-Prompt	Theory
			Signal Region		
$W^\pm Z$	1/18	–	–	–	–
$V\gamma$	3/18	–	–	–	–
ZZ	3/18	–	–	–	–
Non-Prompt	–	–	–	2/4	–
Top	3/18	1/5	2/14	–	–
Triboson	3/18	3/5	–	–	–
$W^\pm W^\pm jj$-QCD	–	–	–	–	1/4
			$W^\pm Z$ Control Region		
$V\gamma$	2/18	–	–	–	–
ZZ	–	1/5	–	–	–
Non-Prompt	–	–	–	1/4	–
			Low-m_{jj} Control Region		
ZZ	1/18	–	–	–	–
$W^\pm W^\pm jj$-EW	–	1/5	–	–	–

Table 9.5: Overview of nuisance parameter groups included in the pruned fit with $t = 40$ % and $p_\mathrm{b} = 20$ %. In total, 19 different nuisance parameters are accepted. Categories where no shape nuisance parameters are accepted for the respective sample/region combination are marked with "–". Nuisance parameters are collected into groups according to the definitions in given in Table 8.1.

The final binning in the signal region is derived by requiring at least two signal events and one background event in each bin, with a statistical uncertainty of $\Delta N_\mathrm{S} = 10$ %, and $\Delta N_\mathrm{B} = 25$ %, respectively. These settings result in four m_{jj} bins.

As discussed in the previous section, a pruning of $t = 0.1$ % and $p_\mathrm{b} = 20$ % is applied to the list of all shape nuisance parameters, before evaluating the significance for this binning. The $W^\pm Z$ and low-m_{jj} control region are included in the fit. The lower bin boundary in both regions is set to 200 GeV. The bin boundaries in the signal region as well as the resulting expected significances for the pruned and purely statistical fit are listed in Table 9.6.

In order to improve readability, the bin boundaries generated by the algorithm are rounded to the nearest hundred; with the exception of the last bin, where the lower boundary is set to 1500 GeV rather 1400 GeV to gain a slightly higher significance. The rounded boundaries as well as the corresponding fit results are given in Table 9.6 as well. The rounding, however, has a negligible effect on the significance. The pre-fit m_{jj} distributions for the combined $\ell^\pm\ell^\pm$ channel in the signal region, using the final binning are shown in Figure 9.4. It can be seen that the signal-to-background ratio increases with m_{jj} in the chosen binning. Tables containing pre-fit event yields per bin for all samples and channels in the signal and control regions are listed in Appendix C.2. It is not beneficial to split the signal region into more than four bins, as even with this binning, there are some empty bins for the smaller backgrounds, such as $V\gamma$, and tri-boson production but also the non-prompt estimate in the $\mu^+\mu^+$ channel.

The impact of a finer binning in the low-m_{jj} control region is tested as well, where the final binning of four bins is used for the signal region. The settings used to derive the signal region binning yield one bin in the control region, which is due to the relatively high requirement on N_S. Therefore, the control region binning is generated using $N_\mathrm{S} = N_\mathrm{B} = 1$ and $\Delta N_{\mathrm{S(B)}} = 10$ % (25 %). The derived binning and the corresponding fit result are given in Table 9.6. Increasing the number of bins in the low-m_{jj} control region only has a small effect on the pruned significance. Additionally, the statistical uncertainty on non-prompt background estimate especially in the ee channels is larger than 50 % already (cf. Table C.7) with a combined bin from 200 GeV to 500 GeV. As this background is one of the main backgrounds in this analysis, only one bin in the low-m_{jj} control region is used for the production of the final results presented in the following sections.

The lower boundary of the low-m_{jj} control region is chosen in a way to reduce the s-channel tri-boson contributions to electroweak $W^{\pm}W^{\pm}$ production. In addition to the already tested value of 200 GeV, a lower bin boundary of 250 GeV is assessed. The result is listed in Table 9.6. It can be seen that this change has no effect on the purely statistical significance, as it is mainly sensitive to the signal to background ratio in the high-m_{jj} bins. Only a minor impact on the pruned significance is observed. In order to not limit the constraining power of the final fit it is chosen to keep as much background statistics as possible. A lower m_{jj} value of 200 GeV is chosen.

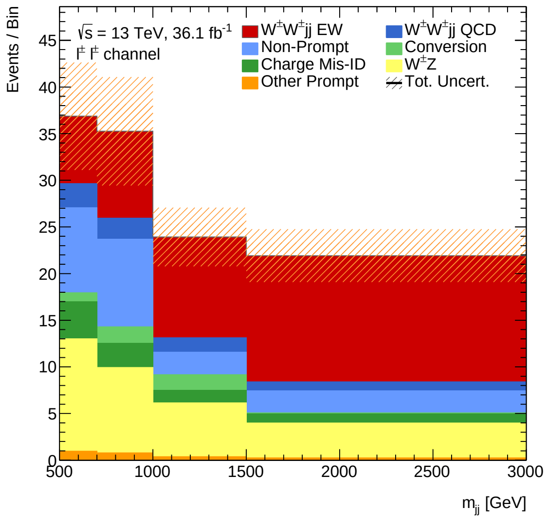

Figure 9.4: Pre-fit m_{jj} distributions in the combined $\ell^{\pm}\ell^{\pm}$ channel in the signal region. Total systematic and statistical uncertainties are shown. Background contributions are grouped into categories as listed in Table 9.1.

Optimized Region	Bin Boundaries					Significance [σ] Pruned	Stat.
SR	500.0	675.0	987.5	1412.5	3000.0	4.57	5.37
	500	700	1000	1500	3000	4.58	5.38
Low-m_{jj} CR	200.0	375.0	500.0			4.60	5.39
	250	500				4.57	5.39

Table 9.6: Overview of fit results using different bin boundaries in the signal and low-m_{jj} control regions. In the signal region optimization, one bin from 200 GeV to 500 GeV is used in the low-m_{jj} control region. When studying the low-m_{jj} CR binning, the final signal region binning is applied. Events with m_{jj} larger than 3000 GeV are included in the last bin.

9.2 Results using Asimov Dataset

In this section, results of the statistical analysis using the Asimov dataset are presented. During measurements of the $W^{\pm}Z$ electroweak production [83], the $W^{\pm}Z$-Ew strength μ_{WZ-EW}, as well as the background normalization for $W^{\pm}Z$-QCD production, μ_{WZ-QCD} are measured. The observed values amount to $1.77^{+0.49}_{-0.43}$ and 0.56 ± 0.16, respectively [83], suggesting that the electroweak and QCD $W^{\pm}Z$ production cross section in the VBS phase space is not well modeled. Consequently, in this analysis a separate measurement of the combined electroweak and QCD $W^{\pm}Z$ cross section is performed in the $W^{\pm}Z$ control region. In this measurement, observed data in both control regions is used. However, the measured $W^{\pm}Z$ strength μ_{WZ} has then to be included in the calculation of the expected results, in order for them to be comparable to observed ones.

9.2.1 Methodology of Expected Significance Extraction

The $W^{\pm}Z$ normalization factor μ_{WZ} is introduced into the fitting template in order to scale the simulated $W^{\pm}Z$ prediction to match the observation. The measurement of μ_{WZ} is mainly dependent on the data observation in the $W^{\pm}Z$ control region. However, the expected significance is usually derived purely based on Asimov data. In order to benefit from the μ_{WZ} measurement in the calculation of the expected results, first a combined fit of the $W^{\pm}Z$ and low-m_{jj} control regions is completed using observed data. In this fit, $W^{\pm}Z$ production is considered as signal and the $W^{\pm}Z$ strength μ_{WZ} is measured. In case the $W^{\pm}Z$ production cross section is not accurately modeled in the simulated background estimate, the measured μ_{WZ} takes a value different from 1.

Subsequently, μ_{WZ} is used as an unconstrained normalization factor in the combined fit of both control regions and the signal region. Before this final fit, μ_{WZ} is set to the value determined in the control region fit, and thus the $W^{\pm}Z$ background in the fitting template as well the construction of the Asimov dataset is scaled with this measured value. Consequently, the background estimate in all regions is affected which impacts the expected significance. Including μ_{WZ} as a non-fixed rather than a constant normalization factor allows for identical fitting procedures in the case of Asimov and observed datasets. However, the observed data in the signal region may also impact the measurement of μ_{WZ}, such that the post-fit value after the fit to observed data can differ from the value after the fit to Asimov data. In any case, for the fit to observed data, the post-fit value is independent of the pre-fit one, as the normalization factor follows a box probability density distribution.

The results of the control region fit to observed data are presented in this section. The main difference with respect to the results presented in Section 9.1.2 is that the low-m_{jj} control region is also included here. Pre- and post-fit event yields in the control regions are shown in Figures 9.5(a) and 9.5(b). Additionally, post-fit event yields and their total uncertainties[1] in both control regions are listed in Table 9.7. It can be seen that the observed number of events exceeds the prediction in the $e^+\mu^+/\mu^+e^+$ and more notably the $e^-\mu^-/\mu^-e^-$ channel of the low-m_{jj} control region. In all other channels as well as the $W^{\pm}Z$ control region the number of observed events is less then expected. However, in all channels but the e^-e^- and $e^-\mu^-/\mu^-e^-$ of the low-m_{jj} control region the discrepancies are covered by the uncertainties on the expectation.

In the post-fit distributions, all channels except for the e^-e^- channel agree within their uncertainties. A $W^{\pm}Z$ strength of

$$\mu_{WZ} \;=\; 0.88\ ^{+0.07}_{-0.07}\ (\text{stat})\ ^{+0.47}_{-0.28}\ (\text{theo})\ ^{+0.08}_{-0.06}\ (\text{sys}) \tag{9.3}$$

is measured. Comparing this result to the μ_{WZ} derived in Section 9.1.2, only minor deviations are observed. The total theory uncertainty is marginally larger than in the fit only including the $W^{\pm}Z$ control region, as the $W^{\pm}W^{\pm}jj$-Ew theory uncertainties have an non-negligible impact in

[1]Event yields with separate statistical, theory and experimental uncertainties before and after the fits to Asimov and observed data are listed in the appendix, Tables C.9 and C.10.

the low-m_{jj} control region. The total systematic uncertainty is slightly reduced w.r.t. the $W^{\pm}Z$ control region fit, as the combined fit has some constraining power on detector nuisance parameters. However, the systematic uncertainties in both fits are not entirely comparable, as no charge mis-ID and non-prompt nuisance parameters are included in the $W^{\pm}Z$ CR fit[1]. An overview of nuisance parameter pulls after the $W^{\pm}Z$ control region fit is shown in Figure 9.3, and can be compared to Figure 9.6. As no significant deviations are observed between the fits with and without the low-m_{jj} control region, the hypothesis that μ_{WZ} is primarily dependent on the $W^{\pm}Z$ control region is confirmed.

Nuisance parameter pulls after the fit to observed and Asimov data are shown in Figure 9.6 (a) and (b), respectively for the 15 most affected parameters. As can be seen, the fit has a large impact on the non-prompt background. The nuisance parameter accounting for systematic uncertainties on the non-prompt correction factor for muons is constrained in both cases. Moreover, nuisance parameters for mis-identified electrons and parameters affecting the $V\gamma$ background are pulled up to improve the agreement in the $e^+\mu^+/\mu^+e^+$ and $e^-\mu^-/\mu^-e^-$ channels. A small pull and constraint is observed for the $W^{\pm}Z$ shower uncertainty. It is also observed that some of the jet and muon nuisance parameters are under-constrained in the fit to observed data. This behavior is not observed in the fit to Asimov data.

	e^+e^+	e^-e^-	$e^+\mu^+/\mu^+e^+$	$e^-\mu^-/\mu^-e^-$	$\mu^+\mu^+$	$\mu^-\mu^-$	$\ell^{\pm}\ell^{\pm}$	$\ell^{\pm}\ell^{\pm}\ell^{\mp}$
Other prompt	0.28 ± 0.09	0.12 ± 0.05	1.22 ± 0.27	0.87 ± 0.22	0.63 ± 0.15	0.37 ± 0.09	3.47 ± 0.67	21.75 ± 4.24
Charge Mis-ID	1.68 ± 0.33	1.30 ± 0.36	4.08 ± 0.52	3.92 ± 0.54	–	–	10.97 ± 1.05	0.02 ± 0.00
Conversion	0.19 ± 0.10	0.21 ± 0.11	0.59 ± 1.28	2.72 ± 1.37	< 0.01	< 0.01	3.71 ± 2.28	2.85 ± 1.68
Non Prompt	0.70 ± 0.23	3.61 ± 1.24	14.36 ± 3.56	10.90 ± 3.03	2.40 ± 1.31	1.17 ± 0.18	33.14 ± 7.17	6.81 ± 0.45
$W^{\pm}W^{\pm}$jj QCD	0.24 ± 0.08	0.11 ± 0.04	2.05 ± 0.61	1.28 ± 0.39	1.17 ± 0.35	0.65 ± 0.19	5.49 ± 1.55	–
$W^{\pm}W^{\pm}$jj EW	0.63 ± 0.14	0.35 ± 0.11	3.03 ± 0.54	2.19 ± 0.40	1.81 ± 0.33	1.12 ± 0.17	9.13 ± 1.32	< 0.01
$W^{\pm}Z$	1.78 ± 0.54	1.35 ± 0.41	11.98 ± 3.41	9.02 ± 2.58	5.01 ± 1.44	3.46 ± 1.01	32.60 ± 9.29	170.30 ± 60.16
Data 2015/16	5	3	39	38	10	6	101	201
Total Expected	5.49 ± 0.92	7.04 ± 1.73	37.32 ± 5.61	30.88 ± 4.69	11.02 ± 2.11	6.76 ± 1.09	98.52 ± 12.81	201.74 ± 60.64

Table 9.7: Post-fit event yields and total uncertainties for the control region fit to observed data in different lepton channels in low-m_{jj} and $W^{\pm}Z$ ($\ell^{\pm}\ell^{\pm}\ell^{\mp}$ channel) control regions. Background contributions are grouped into categories as listed in Table 9.1.

The post-fit value of μ_{WZ} is propagated to the full fit including the signal region, while pulls or constraints on other nuisance parameters are not taken into account. Therefore, the total predicted event yield in the control regions after the CR fit is expected to differ slightly from the pre-fit Asimov data yields for the full fit. This effect can be verified by comparing Table 9.7 to Tables 9.9 and 9.10. However, the observed discrepancy is small. After the control region fit, the total expectation in the $W^{\pm}Z$ control region amounts to 201.74 events, where the Asimov dataset including the measured μ_{WZ} predicts 203.52 events. The deviation is due to a larger $W^{\pm}Z$ estimate before the full fit, as the negative pull on the $W^{\pm}Z$ theory uncertainties is not propagated. Similarly, the total post-fit yield in the low-m_{jj} control region is 98.52 events, which is approximately four events higher than the pre-fit Asimov yield. Most of the difference is caused by a positive pull on non-prompt nuisance parameters, resulting in an increase of three events in the non-prompt background during the control region fit.

[1] These nuisance parameters are not included as there is no data-driven estimate of the charge mis-ID and non-prompt backgrounds in the $W^{\pm}Z$ control region.

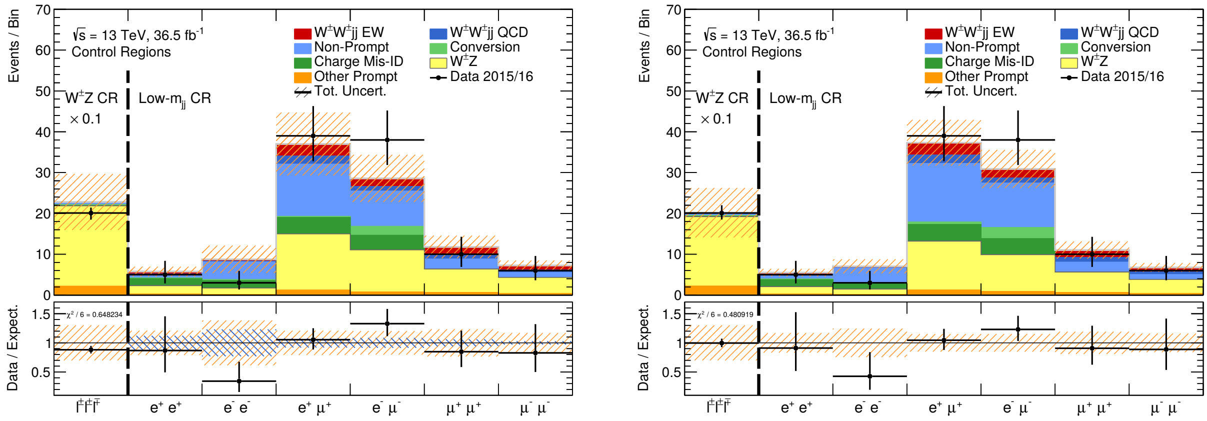

(a) Pre-fit (b) Post-fit

Figure 9.5: Pre-fit (a) and post-fit (b) m_{jj} distributions in the combined $\ell^\pm\ell^\pm\ell^\mp$ the $W^\pm Z$ control region and six lepton charge and flavor channels in the low-m_{jj} control region. Poisson uncertainties on the data are shown. In (a), statistical (blue) and systematic (orange) uncertainties are shown separately the ratio plot. In (b), the total statistical and systematic uncertainty is shown. Event yields in the $W^\pm Z$ control region are scaled with a factor of 0.1. Background contributions are grouped into categories as listed in Table 9.1.

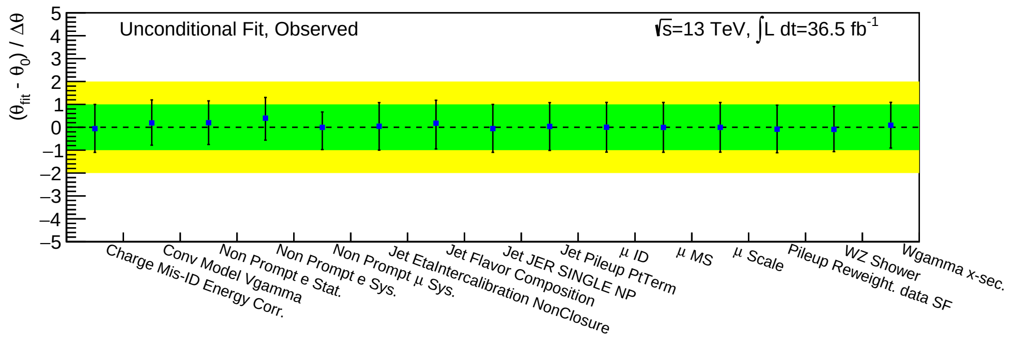

(a) Fit to Observed Data

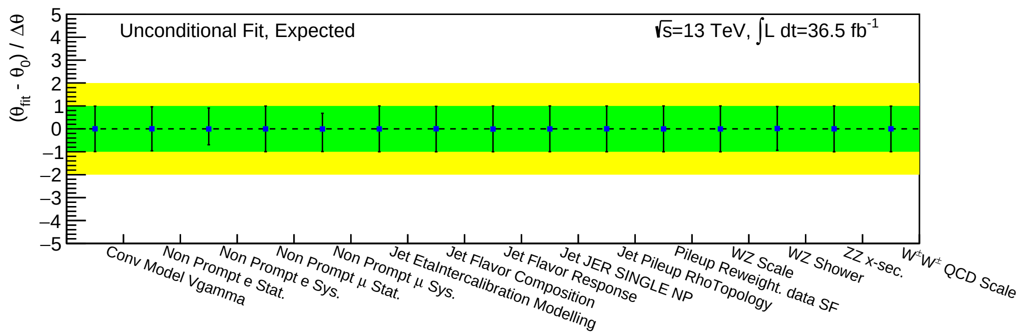

(b) Fit to Asimov Data

Figure 9.6: Nuisance parameter pulls for parameters with Gaussian constraint after the combined control region fit to observed data (a) and Asimov data (b). Only the 15 nuisance parameters showing the highest pulls or constraints are displayed.

9.2.2 Results

Pre-fit distributions in the signal region and control regions with Asimov Data are shown in Figure 9.7(a) and 9.7(c). In the signal region, only the combined $\ell^{\pm}\ell^{\pm}$ channel is shown. Invariant tagging jet mass distributions in all channels are shown in Appendix C.3.1. The previously measured value of $\mu_{WZ} = 0.88$ is applied to the $W^{\pm}Z$ background in all regions. Pre-fit event yields in the six lepton charge and flavor channels of the signal and low-m_{jj} control regions as well as the $\ell^{\pm}\ell^{\pm}\ell^{\mp}$ channel of the $W^{\pm}Z$ control region are given in Table 9.9 and 9.10, respectively. The total uncertainties are given as well.

Theory and experimental uncertainties as well as uncertainties related to the data-driven estimate of the charge mis-ID and non-prompt background are discussed in Section 8, and taken into account in the fit. A separate uncertainty group (*Bkg precision*) is defined for nuisance parameters accounting for statistical uncertainties of the simulated and data-driven backgrounds. In order to estimate the impact of each of these uncertainty groups, the fit is run with each group included separately. No further pruning of nuisance parameters is applied. An overview of expected significances for different fitting configurations is given in Table 9.8. It can be seen that theory uncertainties have the largest impact on the significance. The significance including only theory and background statistics uncertainties is 4.73 σ. The full fit including all uncertainty groups results in an expected significance of 4.6 σ. The purely statistical significance amounts to 5.4 σ.

During the full fit, the best estimator of the expected signal strength μ_{exp} is determined as

$$\mu_{\text{exp}} = 1.01 \,^{+0.25}_{-0.22}\,(\text{stat})\,^{+0.09}_{-0.09}\,(\text{theo})\,^{+0.11}_{-0.12}\,(\text{sys}), \tag{9.4}$$

$$= 1.01 \,^{+0.28}_{-0.27}\,(\text{total}). \tag{9.5}$$

The expected μ_{WZ}^{exp} after the Asimov fit is $\mu_{WZ}^{\text{exp}} = 0.88 \,^{+0.07}_{-0.07}\,(\text{stat})\,^{+0.35}_{-0.23}\,(\text{theo})\,^{+0.15}_{-0.06}\,(\text{sys})$. The total uncertainty on μ_{WZ}^{exp} is $^{+0.39}_{-0.25}$. The central value and statistical uncertainty are, as expected, identical to the values measured in the control region fit. The theory and systematic uncertainties are reduced with respect to the uncertainties obtained in the fit to the control regions, which are given in Eq. (9.3).

Nuisance parameter pulls for the 15 most affected parameters are shown in Figure 9.8(b). In contrast to post-fit pulls and constraints after the control region fit (Figure 9.6(a)), non-prompt electron nuisance parameters are highly constraint by the signal region. Moreover, smaller constraints are observed for jet nuisance parameters, which have been under-constrained after the control region fit. These constraints result in smaller uncertainties on μ_{WZ} after the full fit.

Source	Included Uncertainties								Full Result
Bkg Precision	–	✓	✓	✓	✓	✓	✓	✓	✓
Charge Mis-ID	–	–	✓	–	–	–	–	✓	✓
Non-Prompt	–	–	–	✓	–	–	✓	✓	✓
Detector	–	–	–	–	✓	–	–	–	✓
Theory	–	–	–	–	–	✓	✓	✓	✓
Exp. Significance [σ]	5.4	5.05	5.04	4.87	4.82	4.73	4.63	4.62	4.6

Table 9.8: Evolution of the expected significance when including different systematic sources. All sources marked with a ✓are included in the fit. Additionally to including different uncertainty groups separately, the expected significance is also given for settings including leading uncertainties. The full expected significance can be reproduced by including background precision, non-prompt as well as theory uncertainties. Charge mis-ID and detector uncertainties only have a minor impact on the significance.

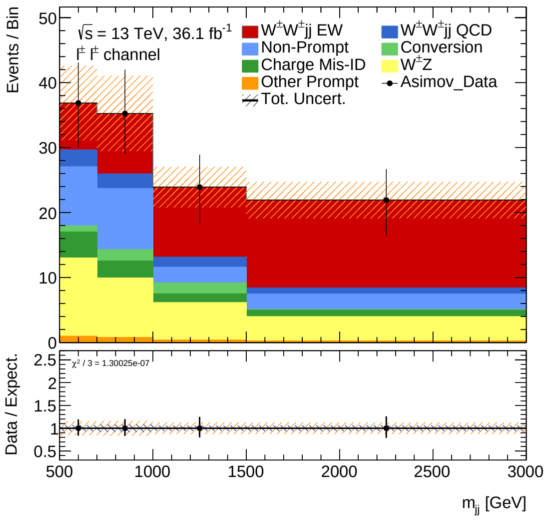

(a) Signal region, pre-fit

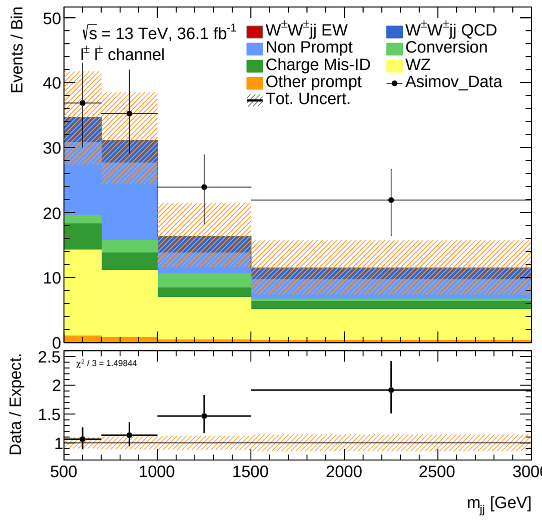

(b) Signal region, after conditional fit with $\mu = 0$

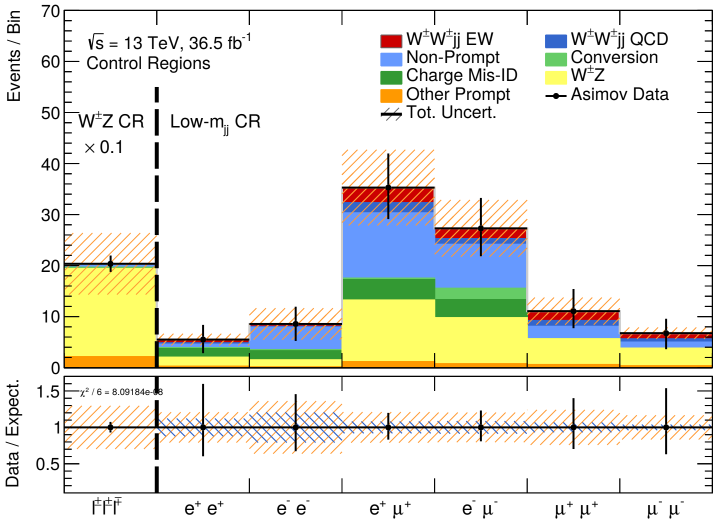

(c) Low-m_{jj} and $W^{\pm}Z$ control region

Figure 9.7: Pre-fit m_{jj} distributions for the combined $\ell^{\pm}\ell^{\pm}$ channel in the signal (a), and six lepton charge and flavor channels in the low-m_{jj} control region, as well as the $\ell^{\pm}\ell^{\pm}\ell^{\mp}$ channel in the $W^{\pm}Z$ control region (c). The m_{jj} distribution in the signal region after the condition fit is also shown (b). Poisson uncertainties on the data are shown. In the ratio plot, statistical (blue) and systematic (orange) uncertainties are shown separately. Event yields in the $W^{\pm}Z$ control region are scaled with a factor 0.1. Background contributions are grouped into categories as listed in Table 9.1.

In addition to the nuisance parameter pulls after the unconditional[1] fit, pulls after the conditional fit are shown in Figure 9.8(a). In the conditional fit, the signal strength is fixed at $\mu = 0$ and the fit determines the compatibility of the data and the background-only theory. The m_{jj} distribution in the signal region after the conditional fit is shown in Figure 9.7(b). It can be seen that the signal contribution is scaled to zero in all bins. During the conditional fit, the $W^{\pm}Z$ background is scaled up with $\mu_{WZ} = 1.03 \pm 0.38$. The $W^{\pm}W^{\pm}jj$-QCD and non-prompt nuisance parameters are pulled up as well to increase the number of events predicted by the background template. Nevertheless, the disagreement between data and template is large. Therefore, the expected significance is also relatively large.

Pre- and post-fit event yields in the signal and low-m_{jj} control regions for all categories are given in Tables 9.9 and 9.11. Event yields in the $W^{\pm}Z$ control region before and after the fit to Asimov data are listed in Table 9.10. In all tables, the total uncertainty, which is defined as the squared sum of the statistical, theory and systematic uncertainty is given. Tables with event yields and separate statistical, theory and other systematic uncertainties are shown in Appendix C.4.

In all tables, yields for the charge mis-ID background are missing in the $\mu\mu$ channels, as the charge mis-ID probability for muons is very small and therefore no data-driven estimate is derived (cf. Section 6.2.2). It is also noticeable that $W^{\pm}Z$ and $W^{\pm}W^{\pm}$ production are asymmetric in lepton charge. More events are expected in the $\ell^{+}\ell^{+}$ channel than in the corresponding $\ell^{-}\ell^{-}$ channel. This is due to the quark content of the proton.

When comparing the pre- and post-fit $W^{\pm}Z$ uncertainties in the $W^{\pm}Z$ region, it can be seen that the total uncertainty on the $W^{\pm}Z$ prediction is drastically reduced. The final uncertainty on the total prediction corresponds approximately to square root of the total predicted yield. It can be inferred that the theory and systematic uncertainties are constrained to the statistical uncertainty of the (here still Asimov) data yield. This introduces anti-correlations between the $W^{\pm}Z$ strength μ_{WZ} and $W^{\pm}Z$ theory uncertainties, which are larger than 60 %. Additionally, correlations between μ_{WZ} and some jet and non-prompt nuisance parameters of the order of 10 % are observed. Similarly, in the signal and low-m_{jj} control regions mainly the systematic uncertainties on the non-prompt background are reduced by the fit. Correlations between non-prompt nuisance parameters and the signal strength μ of 10 % to 20 % are introduced. In Table 9.12, pair-wise correlation factors between nuisance parameters are shown. Only nuisance parameter pairs with an absolute correlation larger than 7 % are listed. However, nuisance parameter correlations down to 2 % are given in Appendix C.5. The large correlations between nuisance parameters are compatible with the constraints observed in Figure 9.8(b).

Nuisance parameters accounting for statistical uncertainties on the precision of the simulated background are discussed in Section 8.4. The corresponding relative uncertainties before the fit are listed in Table 8.9, and vary between 5 % and approximately 60 % in the signal region. During the fit to Asimov data these uncertainties are constrained due to correlations with non-prompt and jet nuisance parameters in the first two bins of the signal region, as well as the low-m_{jj} control region. The correlations are included in Table 9.12, and become as large as -20 %. The relative post-fit uncertainties in the signal region are listed in Table 9.13, and range from 1 % to 24 %. No constraints are observed for systematic uncertainties on the background precision in the control regions. A summary of the relative uncertainties in all regions at various stages of the statistical analysis is given in Appendix C.6.

[1] The full fit where the signal strength μ is unconstrained and non-fixed.

	e^+e^+	e^-e^-	$e^+\mu^+/\mu^+e^+$	$e^-\mu^-/\mu^-e^-$	$\mu^+\mu^+$	$\mu^-\mu^-$	$\ell^\pm\ell^\pm$
			Signal region				
Other Prompt	0.17 ± 0.05	0.14 ± 0.05	0.90 ± 0.19	0.60 ± 0.14	0.36 ± 0.10	0.19 ± 0.06	2.36 ± 0.48
$W^\pm Z$	1.64 ± 0.53	1.14 ± 0.38	12.08 ± 3.66	7.81 ± 2.37	4.81 ± 1.50	3.19 ± 1.04	30.67 ± 9.21
Charge Mis-ID	1.33 ± 0.15	1.17 ± 0.13	3.48 ± 0.37	2.95 ± 0.33	–	–	8.93 ± 0.71
Conversion	0.41 ± 0.26	0.62 ± 0.37	2.65 ± 1.60	0.80 ± 0.72	< 0.01	< 0.01	4.47 ± 2.44
Non-Prompt	4.08 ± 2.30	2.31 ± 1.71	9.35 ± 4.87	6.34 ± 3.74	0.57 ± 0.15	0.67 ± 0.25	23.32 ± 9.68
$W^\pm W^\pm$jj QCD	0.38 ± 0.13	0.16 ± 0.05	3.02 ± 1.02	1.21 ± 0.41	1.80 ± 0.61	0.76 ± 0.26	7.34 ± 2.47
$W^\pm W^\pm$jj EW	3.80 ± 0.25	1.49 ± 0.10	16.49 ± 1.07	6.45 ± 0.40	9.14 ± 0.63	3.50 ± 0.24	40.88 ± 2.63
Asimov Data	11.81	7.03	47.97	26.17	16.69	8.31	117.97
Data 2015/16	10	4	44	28	25	11	122
Total Expected	11.81 ± 2.41	7.03 ± 1.81	47.97 ± 6.57	26.17 ± 4.61	16.69 ± 1.84	8.31 ± 1.18	117.97 ± 14.38
			Low-m_{jj} control region				
Other Prompt	0.28 ± 0.09	0.16 ± 0.07	1.20 ± 0.25	0.77 ± 0.20	0.63 ± 0.14	0.37 ± 0.12	3.40 ± 0.64
$W^\pm Z$	1.77 ± 0.57	1.37 ± 0.42	12.07 ± 3.43	9.02 ± 2.62	5.04 ± 1.44	3.46 ± 1.02	32.72 ± 9.23
Charge Mis-ID	1.70 ± 0.19	1.77 ± 0.17	4.00 ± 0.42	3.56 ± 0.48	–	–	11.03 ± 1.04
Conversion	0.18 ± 0.10	0.26 ± 0.19	0.28 ± 1.04	2.20 ± 1.20	< 0.01	< 0.01	2.93 ± 1.90
Non-Prompt	0.71 ± 0.68	4.37 ± 2.48	12.78 ± 5.68	8.62 ± 4.04	2.43 ± 2.05	1.18 ± 0.27	30.08 ± 11.09
$W^\pm W^\pm$jj QCD	0.24 ± 0.07	0.15 ± 0.05	1.99 ± 0.56	1.15 ± 0.32	1.16 ± 0.33	0.64 ± 0.18	5.32 ± 1.50
$W^\pm W^\pm$jj EW	0.64 ± 0.11	0.47 ± 0.10	2.97 ± 0.50	1.99 ± 0.35	1.83 ± 0.31	1.11 ± 0.19	9.01 ± 1.53
Asimov Data	5.51	8.56	35.28	27.30	11.08	6.76	94.48
Data 2015/16	5	3	39	38	10	6	101
Total Expected	5.51 ± 0.93	8.56 ± 2.53	35.28 ± 6.85	27.30 ± 5.05	11.08 ± 2.56	6.76 ± 1.10	94.48 ± 14.97

Table 9.9: Pre-fit event yields and total uncertainties for all signal and background contributions as well as for Asimov and observed data in lepton channels in the signal and low-m_{jj} control regions. Background contributions are grouped into categories as listed in Table 9.1.

	Pre-fit	Post-fit
Other Prompt	21.55 ± 4.11	21.53 ± 4.07
$W^\pm Z$	172.45 ± 59.88	172.39 ± 15.59
Charge Mis-ID	0.02 ± 0.01	0.02 ± 0.00
Conversion	2.68 ± 2.25	2.69 ± 2.02
Non-Prompt	6.82 ± 1.73	6.82 ± 0.16
$W^\pm W^\pm$jj QCD	–	–
$W^\pm W^\pm$jj EW	< 0.01	< 0.01
Asimov Data	203.52	203.52
Total Expectation	203.52 ± 60.30	203.44 ± 14.88

Table 9.10: Pre- and post-fit event yields in the $\ell^\pm\ell^\pm\ell^\mp$ channel of the $W^\pm Z$ control region for the fit to Asimov data. In addition, the total uncertainty on the event yield is given. Background contributions are grouped into categories as listed in Table 9.1.

	e^+e^+	e^-e^-	$e^+\mu^+/\mu^+e^+$	$e^-\mu^-/\mu^-e^-$	$\mu^+\mu^+$	$\mu^-\mu^-$	$\ell^\pm\ell^\pm$
			Signal region				
Other Prompt	0.17 ± 0.05	0.14 ± 0.04	0.90 ± 0.19	0.60 ± 0.14	0.36 ± 0.09	0.19 ± 0.05	2.35 ± 0.47
$W^\pm Z$	1.64 ± 0.33	1.14 ± 0.27	12.07 ± 1.81	7.81 ± 1.33	4.81 ± 0.57	3.18 ± 0.54	30.64 ± 3.93
Charge Mis-ID	1.33 ± 0.26	1.17 ± 0.23	3.48 ± 0.36	2.95 ± 0.38	–	–	8.93 ± 0.79
Conversion	0.41 ± 0.21	0.62 ± 0.34	2.64 ± 1.36	0.80 ± 0.64	< 0.01	< 0.01	4.46 ± 2.21
Non-Prompt	4.07 ± 1.20	2.30 ± 0.82	9.30 ± 2.29	6.31 ± 1.68	0.57 ± 0.06	0.67 ± 0.15	23.22 ± 4.79
$W^\pm W^\pm$jj QCD	0.38 ± 0.14	0.16 ± 0.06	3.02 ± 1.04	1.21 ± 0.43	1.80 ± 0.61	0.76 ± 0.26	7.32 ± 2.47
$W^\pm W^\pm$jj EW	3.82 ± 0.26	1.50 ± 0.10	16.58 ± 1.12	6.49 ± 0.42	9.19 ± 0.65	3.52 ± 0.25	41.10 ± 2.75
Asimov Data	11.82	7.03	47.97	26.17	16.69	8.31	117.97
Total Expected	11.82 ± 1.69	7.03 ± 1.35	47.98 ± 3.86	26.17 ± 2.65	16.72 ± 1.11	8.32 ± 0.69	118.03 ± 7.36
			Low-m_{jj} control region				
Other Prompt	0.28 ± 0.09	0.16 ± 0.06	1.20 ± 0.25	0.76 ± 0.19	0.63 ± 0.14	0.37 ± 0.11	3.39 ± 0.64
$W^\pm Z$	1.76 ± 0.36	1.37 ± 0.38	12.06 ± 2.05	9.00 ± 1.51	5.03 ± 0.84	3.45 ± 0.53	32.68 ± 4.83
Charge Mis-ID	1.70 ± 0.29	1.77 ± 0.40	4.01 ± 0.46	3.56 ± 0.51	–	–	11.03 ± 1.15
Conversion	0.18 ± 0.09	0.26 ± 0.13	0.29 ± 0.97	2.19 ± 1.07	< 0.01	< 0.01	2.93 ± 1.76
Non-Prompt	0.71 ± 0.22	4.37 ± 1.25	12.73 ± 2.84	8.60 ± 2.22	2.41 ± 1.14	1.17 ± 0.17	29.99 ± 5.90
$W^\pm W^\pm$jj QCD	0.24 ± 0.07	0.15 ± 0.05	1.99 ± 0.58	1.14 ± 0.34	1.16 ± 0.34	0.64 ± 0.18	5.31 ± 1.50
$W^\pm W^\pm$jj EW	0.64 ± 0.11	0.48 ± 0.09	2.99 ± 0.50	2.00 ± 0.34	1.84 ± 0.31	1.12 ± 0.19	9.07 ± 1.52
Asimov Data	5.51	8.56	35.28	27.30	11.08	6.76	94.48
Total Expected	5.51 ± 0.78	8.56 ± 1.79	35.25 ± 3.54	27.26 ± 3.03	11.06 ± 1.39	6.76 ± 0.60	94.40 ± 6.89

Table 9.11: Post-fit event yields and total uncertainties for the fit to Asimov data in lepton channels in the signal and low-m_{jj} control regions. Background contributions are grouped into categories as listed in Table 9.1.

Parameter 1	Parameter 2	Correlation [%]
$W^{\pm}Z$ Shower	μ_{WZ}	−67.1
$W^{\pm}Z$ Scale	μ_{WZ}	−66.6
Non Prompt e Stat.	Non Prompt e Sys.	−26.1
$W^{\pm}W^{\pm}jj$-Ew Shower	μ	21.3
Non Prompt e Sys.	Bkg Prec. Low-m_{jj} CR, e^-e^- Chan, Bin 1	−19.2
Non Prompt μ Sys.	μ	−18.2
Non Prompt e Sys.	Bkg Prec. SR, e^-e^- Chan, Bin 2	−16.6
$W^{\pm}W^{\pm}jj$-QCD Scale	μ	−16.2
Jet Flavor Composition	μ_{WZ}	−14.9
Non Prompt e Sys.	Bkg Prec. SR, e^+e^+ Chan, Bin 2	−14.0
Non Prompt e Sys.	μ	−13.7
Bkg Prec. SR, $e^+\mu^+/\mu^+e^+$ Chan, Bin 4	μ	−13.4
Non Prompt μ Sys.	Bkg Prec. SR, $e^-\mu^-/\mu^-e^-$ Chan, Bin 1	−13.1
Non Prompt μ Sys.	$W^{\pm}Z$ Shower	12.7
Non Prompt e Sys.	Non Prompt μ Sys.	−12.3
Jet Energy Resolution	Bkg Prec. SR, $e^+\mu^+/\mu^+e^+$ Chan, Bin 2	−12.1
Non Prompt e Sys.	Bkg Prec. Low-m_{jj} CR, $e^-\mu^-/\mu^-e^-$ Chan, Bin 1	−11.8
Non Prompt μ Sys.	μ_{WZ}	−11.4
Non Prompt μ Sys.	Bkg Prec. Low-m_{jj} CR, $e^+\mu^+/\mu^+e^+$ Chan, Bin 1	−11.1
Non Prompt e Sys.	Bkg Prec. Low-m_{jj} CR, $e^+\mu^+/\mu^+e^+$ Chan, Bin 1	−9.5
Jet Flavor Composition	μ	−9.3
Non Prompt e Sys.	$W^{\pm}Z$ Shower	8.9
$W^{\pm}W^{\pm}jj$-Ew Ew Corr.	μ	8.8
Luminosity	μ	−8.7
Jet Energy Resolution	Bkg Prec. SR, $e^+\mu^+/\mu^+e^+$ Chan, Bin 1	8.6
Bkg Prec. SR, $e^+\mu^+/\mu^+e^+$ Chan, Bin 3	μ	−8.4
Non Prompt μ Stat.	Non Prompt μ Sys.	−8.2
Non Prompt μ Sys.	Jet Energy Resolution	−8.1
Conversion Model $V\gamma$	Non Prompt e Sys.	−7.9
Pile-up Reweight. data SF	μ	7.8
Non Prompt μ Sys.	Bkg Prec. SR, $e^+\mu^+/\mu^+e^+$ Chan, Bin 2	−7.8
Flavor Tag Eff. Eigen Light 1	μ	−7.7
$W^{\pm}Z$ Shower	μ	7.2
Non Prompt μ Sys.	Bkg Prec. Low-m_{jj} CR, $\mu^+\mu^+$ Chan, Bin 1	−7.0
Jet Flavor Composition	Bkg Prec. SR, $e^-\mu^-/\mu^-e^-$ Chan, Bin 4	−7.0

Table 9.12: Pair-wise correlation factors between two nuisance parameters after the fit to Asimov data. Parameter pairs are sorted by descending absolute correlation value. Only correlations larger than 7 % are shown.

Lower Bin Boundary [GeV]	Background Precision Uncertainty [%]					
	e^-e^-	e^+e^+	$e^-\mu^-/\mu^-e^-$	$e^+\mu^+/\mu^+e^+$	$\mu^-\mu^-$	$\mu^+\mu^+$
500	5.05 −4.38	13.99 −11.51	7.50 −6.86	4.62 −4.28	3.22 −3.06	2.11 −2.03
700	23.74 −18.53	15.71 −12.57	6.89 −5.97	5.15 −4.70	3.08 −2.90	2.15 −2.04
1000	10.42 −7.39	1.18 −1.09	2.97 −2.58	3.89 −3.42	2.87 −2.56	1.59 −1.50
1500	2.43 −1.73	1.52 −1.29	4.52 −3.65	3.38 −2.82	1.54 −1.41	0.99 −0.94

Table 9.13: Overview of relative systematic uncertainties on the simulated background precision in the signal region after the fit to Asimov data.

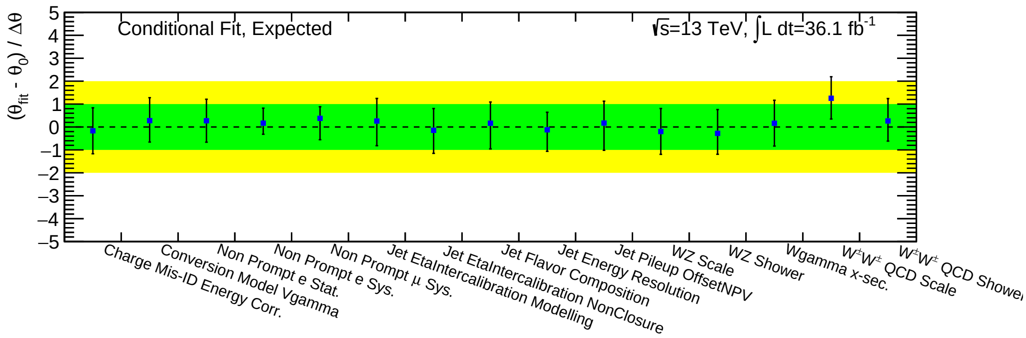

(a) Conditional Fit

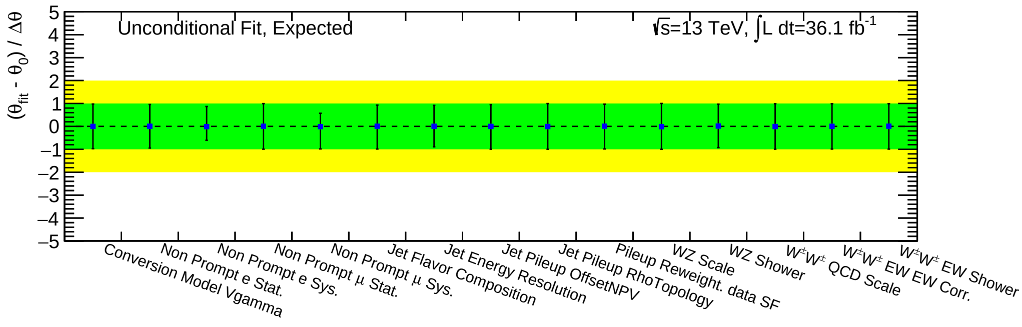

(b) Unconditional Fit

Figure 9.8: Nuisance parameter pulls after the full fit to Asimov data for nuisance parameters with Gaussian constraints. In the conditional fit (a), the signal strength is fixed at $\mu = 0$. Thus, the compatibility of the Asimov data with the background-only theory is tested. In the unconditional fit (b), μ is kept floating to determine the best estimator for the Asimov dataset. Only the 15 nuisance parameters showing the highest pulls or constraints are displayed.

9.3 Results using Observed Data

The statistical analysis using measured data is only performed after all selection criteria and fitting configurations are finalized. In the combined fit to observed data in signal and control regions, the $W^{\pm}Z$ strength μ_{WZ} is determined directly during the fit, since observed data are included in all three regions. Therefore, no separate control region fit is necessary. The previously measured normalization factor μ_{WZ} of 0.88 is applied to the $W^{\pm}Z$ estimate before the fit.

The m_{jj} distributions in the signal region in all six lepton channels before the fit is shown in Figure 9.9. The corresponding distributions in the combined $\ell^{\pm}\ell^{\pm}$ channel are presented in Appendix C.3.2. In all channels, there is an consistent excess of measured events in the last bin from 1500 GeV to 3000 GeV. In the bin from 700 GeV to 1000 GeV, the data fall short of the prediction. Sizable systematic uncertainties in the first m_{jj} bins in the ee channels are observed. These are mainly due to the statistical and systematic uncertainties on the non-prompt estimate. Pre-fit event yields in the control regions are shown in Figure 9.11(a).

In all regions, the expected pre-fit event yields are identical to the pre-fit yields of the fit to Asimov data. Pre-fit event yields in the signal and low-m_{jj} control regions are presented in Table 9.9. In the signal region, there is an excess of data especially in the $\mu^+\mu^+$ channel, which is partially compensated by other channels. In total, 122 data events are observed in the signal region with an expectation of 118 ± 14 events from the signal+background, and 77 ± 14 events from the background-only hypothesis. In the low-m_{jj} control region, a total of 101 events is observed where 94 are expected. The difference is mainly caused by an excess in data in the $e^-\mu^-/\mu^-e^-$ channel. Event yields in the $W^{\pm}Z$ control region before and after the fit to observed data are listed in Table 9.14. As the measured μ_{WZ} is already applied, the agreement between data and prediction is good.

In the combined fit, an observed signal strength of

$$\mu_{\text{obs}} = 1.46\ ^{+0.26}_{-0.24}\ \text{(stat)}\ ^{+0.10}_{-0.08}\ \text{(theo)}\ ^{+0.13}_{-0.11}\ \text{(sys)}, \tag{9.6}$$

$$= 1.46\ ^{+0.31}_{-0.28}\ \text{(total)}, \tag{9.7}$$

is measured. Statistical uncertainties are dominating.
The observed μ_{WZ}^{obs} after the fit is $\mu_{WZ}^{\text{obs}} = 0.85\ ^{+0.07}_{-0.07}$ (stat) $^{+0.32}_{-0.21}$ (theo) $^{+0.22}_{-0.09}$ (sys), with a total uncertainty of $^{+0.40}_{-0.24}$. The uncertainties on μ_{obs} and μ_{WZ}^{obs} are comparable to the uncertainties on μ_{exp} and μ_{WZ}^{exp}. An observed significance of 6.7 σ is calculated. Therefore, the observation of $W^{\pm}W^{\pm}jj$-Ew production is claimed. The purely statistical significance amounts to 7.8 σ.

The value of the negative logarithmic likelihood ratio $-\Delta\ln(L)$ as a function of the signal strength μ is shown in Figure 9.10. The negative logarithmic likelihood ratio is defined as $\frac{1}{2}\,q_0$, where q_0 is the discovery test statistics given in Eq. (2.40). The Asimov and observed datasets are compared to theory hypotheses corresponding to different values of μ. As μ_{exp} and μ_{obs} are the best estimators of μ for the respective datasets, the minima of the expected and observed curves are located by construction at exactly μ_{exp} and μ_{obs}. A signal strength of zero represents the background-only theory. Therefore, the discovery significance of a specific dataset can be calculated from the intersection of the curve with $\mu = 0$, analogous to Eq. (2.34). The total uncertainty on μ_{exp} and μ_{obs} can be read from the μ values where the expected and observed curves surpass the 1-σ level, at $-\Delta\ln(L) = 0.5$. In Figure 9.10 (b), the likelihood curves are shown for μ values between 0.70 and 1.85. The uncertainties on μ_{exp} and μ_{obs} agree with the total uncertainties given in Eq. (9.5) and Eq. (9.7), respectively.

It is evident from Figure 9.10(a) that the likelihood curve is asymmetric for both datasets. This can be understood by considering what each point in the likelihood curve represents. $-\Delta\ln(L(\mu))$ is a measure of the compatibility between the dataset and the theory generated by μ. Let N_{obs} be the observed number of events in a one-bin measurement, and μ_{obs} the corresponding signal strength. The predicted number of events, N_{exp} grows with μ, as it is defined as the scaled sum

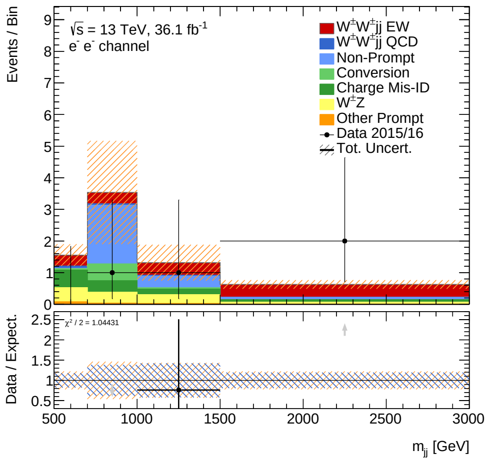

(a) e^-e^-

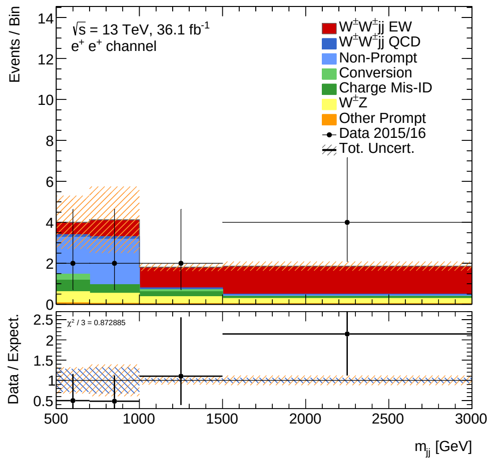

(b) e^+e^+

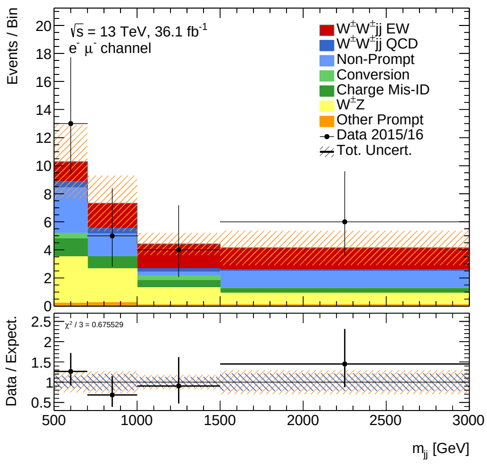

(c) $e^-\mu^-/\mu^-e^-$

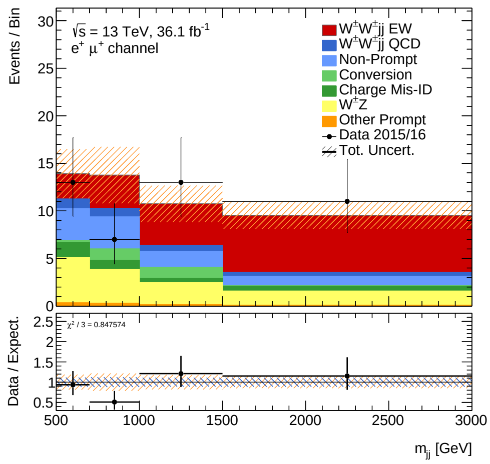

(d) $e^+\mu^+/\mu^+e^+$

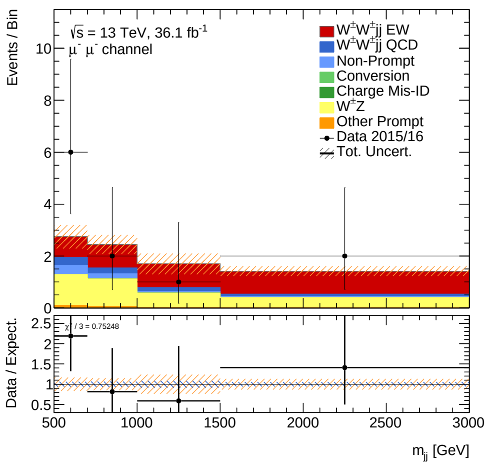

(e) $\mu^-\mu^-$

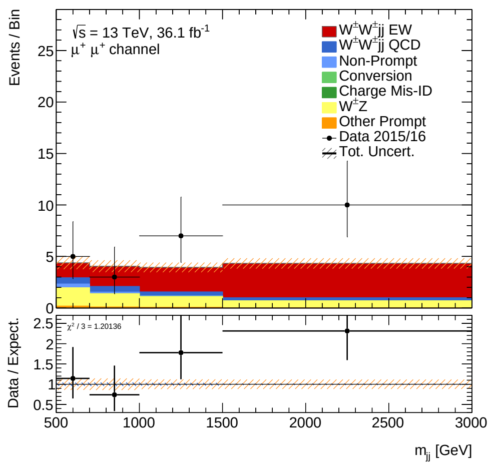

(f) $\mu^+\mu^+$

Figure 9.9: Pre-fit m_{jj} distributions in six lepton charge and flavor channels in the signal region. Poisson uncertainties are shown for the Asimov data points. In the ratio plot, statistical (blue) and systematic (orange) uncertainties are shown separately. Background contributions are grouped into categories as listed in Table 9.1.

of signal and background, $N_{\text{exp}} = \mu N_{\text{sig}} + N_{\text{bkg}}$ (see Eq. (2.35)). In the Poissonian regime, the statistical uncertainty on the theory prediction grows with $\sqrt{N_{\text{exp}}}$. Therefore, the observation of N_{obs} events is more compatible with theories where $\mu > \mu_{\text{obs}}$ than with theories predicting less events than N_{obs}. This translates into a steeper likelihood curve for $\mu < \mu_{\text{obs}}$, while the slope decreases for $\mu > \mu_{\text{obs}}$. Hence, the asymmetry of the likelihood scan increases with the predicted signal-to-background ratio. In other words, the likelihood scan becomes asymmetric if the predicted number of signal events is large relative to the statistical uncertainty on the background prediction. The asymmetry can be cured by introducing systematic uncertainties on the background of similar size as the statistical uncertainties on the total prediction, as the background uncertainties are not scaled with μ. This however also results in a loss of significance. The introduction of systematic normalization uncertainties on the signal, on the contrary enhances the asymmetry. But as the significance is calculated from the background-only theory, signal normalization uncertainties have no impact on the significance. From the large asymmetry observed in Figure 9.10(a) it is seen that the analysis is very sensitive to $W^{\pm}W^{\pm}jj$-EW production and limited by statistical uncertainties. This confirms the high observed significance of 6.7 σ and the statistical uncertainties on μ_{obs} given in Eq. (9.6). Implications of asymmetric negative logarithmic likelihood functions are briefly discussed in Section 2.2.2.

Post-fit m_{jj} distributions in the control regions and the signal region are shown in Figure 9.11(b) and 9.13, respectively. Note that, in contrast to the pre-fit distributions, statistical uncertainties on the background precision cannot be shown separately in the ratio panel, as the corresponding nuisance parameters are highly correlated with other sources of uncertainty. Event yields including the total uncertainty[1] after the fit to observed data in the $W^{\pm}Z$ control region are given in Table 9.14. Event yields in the signal and low-m_{jj} control regions are presented in Table 9.15. It can be seen that the overall agreement between data and prediction, especially in the signal region, is greatly improved after the fit. In all channels except for the $\mu^{+}\mu^{+}$ channel, data and prediction agree within their uncertainties.

Nuisance parameter pulls after the fit are shown in Figure 9.12. In addition to μ_{obs}, the signal prediction is adapted by nuisance parameters related the interference between $W^{\pm}W^{\pm}jj$-EW and $W^{\pm}W^{\pm}jj$-QCD production as well as EW NLO corrections and scale uncertainties. The discrepancy in the ee channels in the signal region below 1000 GeV is attenuated by a large negative pull on the non-prompt electron nuisance parameter. The overall shape of the m_{jj} distribution in the signal region differs between the total pre-fit prediction and the observation. Therefore, the disagreement cannot be cured by simply scaling the signal by a uniform factor. Nuisance parameters having a larger effect in the high-m_{jj} regions, like the Jet Flavor Composition and Energy Resolution parameters are used to flatten the shape of the total prediction.

Pair-wise correlation factors between nuisance parameters are shown in Table 9.16 for all parameter pairs with an absolute correlation larger[2] than 7 %. Correlations of nuisance parameters to the signal strength are significantly reduced with respect to values calculated in the fit to Asimov data given Table 9.12. This can be interpreted such that the pull exerted by the observed data on the signal strength is large compared to the shifts introduced by nuisance parameters. This means that it is more efficient, in terms of minimizing $-\Delta\ln(L)$, for the fit to adjust the signal prediction using the unconstrained normalization factor μ rather than pulling the signal prediction using constrained nuisance parameters. Thus, the impact a variation of the signal strength has on the nuisance parameters is reduced. Overall, sizable correlations between muon and electron non-prompt nuisance parameters, and between $W^{\pm}Z$ theory parameters and jet, as well as $V\gamma$ parameters are observed. Correlations between non-prompt and background precision nuisance parameters are comparable to the results of the fit to Asimov data. Therefore, the post-fit background precision uncertainties are similar to those presented in Table 9.13. A complete overview of background precision uncertainties before and after all fits is given in Appendix C.6.

[1] For event yields with separate statistical, theory and other systematic uncertainties see Appendix C.4.

[2] A more complete list containing correlations down to 2 % is given in Appendix C.5.

	Pre-fit	Post-fit
Other Prompt	21.55 ± 4.11	22.89 ± 4.29
$W^{\pm}Z$	172.45 ± 59.88	170.87 ± 15.58
Charge Mis-ID	0.02 ± 0.01	0.02 ± 0.00
Conversion	2.68 ± 2.25	1.70 ± 1.75
Non-Prompt	6.82 ± 1.73	6.82 ± 0.16
$W^{\pm}W^{\pm}$jj QCD	–	–
$W^{\pm}W^{\pm}$jj EW	< 0.01	< 0.01
Data 2015/16	201	201
Total Expectation	203.52 ± 60.30	202.31 ± 14.87

Table 9.14: Pre- and post-fit event yields in the $\ell^{\pm}\ell^{\pm}\ell^{\mp}$ channel of the $W^{\pm}Z$ control region for the fit to observed data. In addition, the total uncertainty on the event yield is given. Background contributions are grouped into categories as listed in Table 9.1.

	e^+e^+	e^-e^-	$e^+\mu^+/\mu^+e^+$	$e^-\mu^-/\mu^-e^-$	$\mu^+\mu^+$	$\mu^-\mu^-$	$\ell^{\pm}\ell^{\pm}$
			Signal region				
Other prompt	0.16 ± 0.04	0.14 ± 0.04	0.90 ± 0.20	0.62 ± 0.14	0.39 ± 0.09	0.22 ± 0.05	2.43 ± 0.48
WZ	1.44 ± 0.29	1.05 ± 0.25	11.26 ± 1.68	7.73 ± 1.32	4.80 ± 0.59	3.31 ± 0.56	29.60 ± 3.81
Charge Mis-ID	1.20 ± 0.25	1.05 ± 0.22	3.38 ± 0.36	2.97 ± 0.38	0.00 ± 0.00	0.00 ± 0.00	8.60 ± 0.77
Conversion	0.42 ± 0.22	0.53 ± 0.32	2.92 ± 1.52	1.38 ± 1.02	0.00 ± 0.00	0.00 ± 0.00	5.26 ± 2.75
Non Prompt	2.28 ± 1.26	1.21 ± 0.70	5.86 ± 2.85	4.63 ± 1.81	0.58 ± 0.06	0.65 ± 0.14	15.20 ± 6.16
$W^{\pm}W^{\pm}$jj QCD	0.35 ± 0.13	0.15 ± 0.05	2.93 ± 0.99	1.21 ± 0.41	1.79 ± 0.60	0.76 ± 0.25	7.18 ± 2.37
$W^{\pm}W^{\pm}$jj EW	5.65 ± 0.37	2.24 ± 0.15	24.52 ± 1.61	9.54 ± 0.62	13.60 ± 0.94	5.23 ± 0.37	60.77 ± 3.99
Data 2015/16	10	4	44	28	25	11	122
Total Expected	11.50 ± 1.56	6.36 ± 1.09	51.76 ± 4.10	28.08 ± 2.75	21.16 ± 1.32	10.17 ± 0.75	129.04 ± 8.35
			Low-m_{jj} control region				
Other prompt	0.25 ± 0.09	0.15 ± 0.06	1.24 ± 0.25	0.96 ± 0.23	0.62 ± 0.14	0.32 ± 0.10	3.52 ± 0.67
WZ	1.80 ± 0.38	1.11 ± 0.34	11.99 ± 2.05	9.93 ± 1.71	4.87 ± 0.81	3.51 ± 0.55	33.20 ± 5.01
Charge Mis-ID	1.68 ± 0.29	1.47 ± 0.37	4.15 ± 0.48	3.91 ± 0.55	0.00 ± 0.00	0.00 ± 0.00	11.21 ± 1.19
Conversion	0.17 ± 0.09	0.24 ± 0.13	1.74 ± 1.79	2.65 ± 1.32	0.00 ± 0.00	0.00 ± 0.00	4.80 ± 2.93
Non Prompt	0.92 ± 0.30	2.18 ± 1.38	9.67 ± 3.31	6.56 ± 2.80	2.22 ± 0.91	1.16 ± 0.16	22.71 ± 7.19
$W^{\pm}W^{\pm}$jj QCD	0.23 ± 0.07	0.13 ± 0.05	2.03 ± 0.58	1.24 ± 0.36	1.18 ± 0.33	0.65 ± 0.18	5.45 ± 1.51
$W^{\pm}W^{\pm}$jj EW	0.90 ± 0.16	0.61 ± 0.13	4.14 ± 0.70	2.74 ± 0.49	2.51 ± 0.44	1.55 ± 0.27	12.46 ± 2.14
Data 2015/16	5	3	39	38	10	6	101
Total Expected	5.94 ± 0.84	5.89 ± 1.61	34.96 ± 3.73	27.99 ± 3.28	11.39 ± 1.32	7.18 ± 0.64	93.35 ± 7.45

Table 9.15: Post-fit event yields and total uncertainties for the fit to observed data in lepton channels in the signal and low-m_{jj} control regions. Background contributions are grouped into categories as listed in Table 9.1.

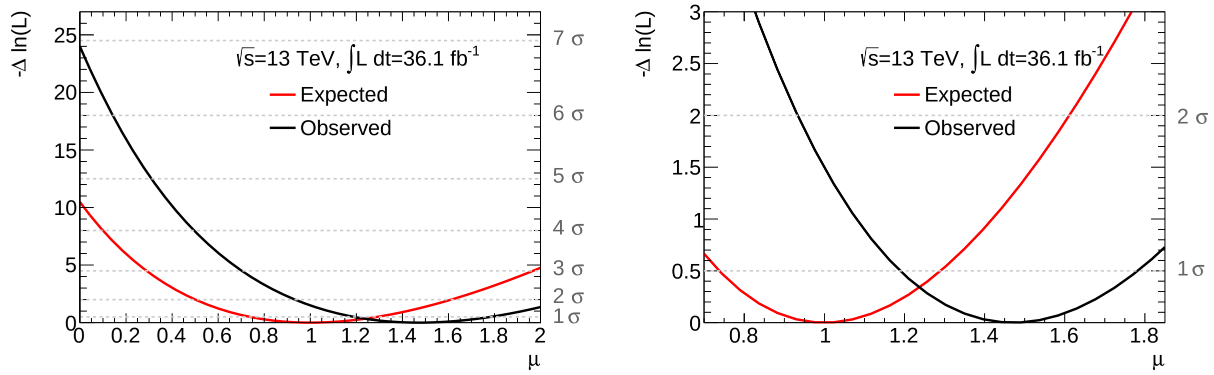

(a) Full range (b) For 0.70 $\leq \mu \leq$ 1.85

Figure 9.10: Likelihood scan of the signal strength μ for the combined fit of the signal, low-m_{jj} and $W^{\pm}Z$ control region. The red line corresponds the negative logarithmic likelihood ratio $-\Delta\ln(L)$ of the Asimov data, while the observed dataset is represented by the black line. The discovery significance is calculated as $Z = \sqrt{-2 \cdot \Delta\ln(L)}$. Dashed lines are drawn at $-\Delta\ln(L)$ values equivalent to integer significances. In (a), the full μ range is shown, such that the expected and observed significances can be read of the intersection of the red and black line with the y axis, respectively. In (b), the range around the expected and observed minima is shown.

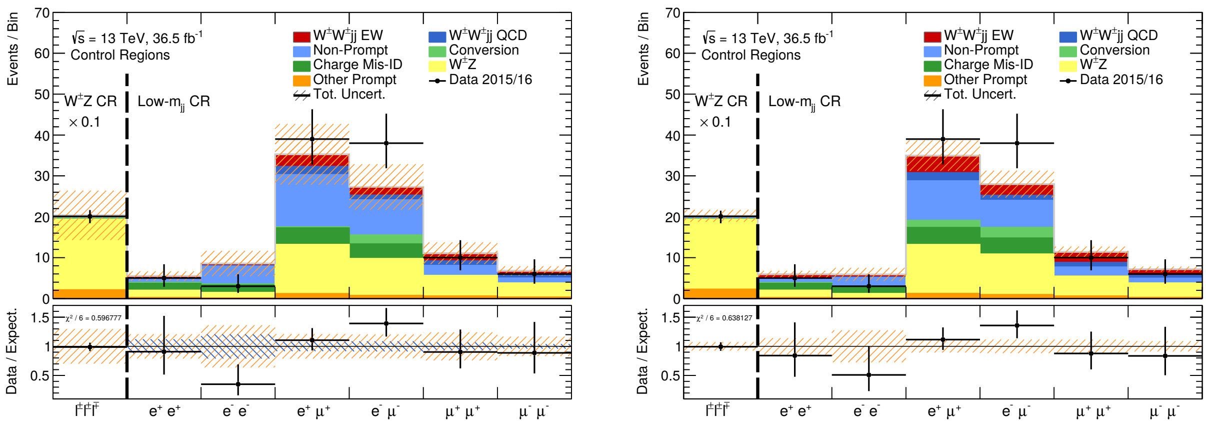

(a) Pre-fit (b) Post-fit

Figure 9.11: Pre- (a) and post-fit m_{jj} distributions (b) for fit to observe data in six lepton charge and flavor channels in thelow-m_{jj} control region, as well as the $\ell^{\pm}\ell^{\pm}\ell^{\mp}$ channel in the $W^{\pm}Z$ control region. Poisson uncertainties on the data are shown. In (a), statistical (blue) and systematic (orange) uncertainties are shown separately the ratio plot. In (b), the total statistical and systematic uncertainty is shown. Event yields in the $W^{\pm}Z$ control region are scaled with a factor of 0.1. Background contributions are grouped into categories as listed in Table 9.1.

The impact of a specific nuisance parameter on the final result is estimated by measuring the effect each parameter has on the signal strength, μ_{obs}. In order to do so, a series of four separate fits is performed for each nuisance parameter. Starting at its best estimate, $\hat{\theta}_{\text{post}}$, after the fit to observed data, each nuisance parameter is varied up and down by its pre- and post-fit uncertainties, and fixed at this value. The resulting variations are denoted as $(\hat{\theta}_{\text{post}} + \Delta^{\text{up}}_{\text{pre(post)}}\theta)$ and $(\hat{\theta}_{\text{post}} - \Delta^{\text{down}}_{\text{pre(post)}}\theta)$ for the up- and down variations, respectively. For each of these variations, the tested nuisance parameter is fixed, while all others are optimized. The difference between the resulting μ'_{obs} and the nominal μ_{obs} is used to estimate the impact on the signal strength. After applying this procedure to all nuisance parameters[1], the nuisance parameters are ranked according to their pre-fit impact, $\Delta_{\text{pre}}\mu_{\text{obs}}$, on μ_{obs}, given as

$$\Delta_{\text{pre}}\mu_{\text{obs}} = (\mu'_{\text{obs}})_{\text{pre}} - \mu_{\text{obs}}. \tag{9.8}$$

The pre- and post fit impact on the signal strength, as well as the post-fit nuisance parameter pulls and uncertainties are shown in Figure 9.14 for the 19 highest ranked nuisance parameters. Detailed information on all nuisance parameters is listed in Appendix C.7, Table C.19. It is seen that the nuisance parameter accounting for the $W^{\pm}W^{\pm}jj$-EW shower uncertainties, which are the leading uncertainties on the signal prediction (see Table 8.8), is the parameter with the largest impact on the signal strength. Generally, it is observed that nuisance parameters with a high correlation to the signal strength, such as nuisance parameters attributed to the systematic uncertainty on the non-prompt electron and muon estimate, the $W^{\pm}W^{\pm}jj$-QCD scale uncertainty and the jet flavor composition uncertainty are also amongst the highest ranked parameters.

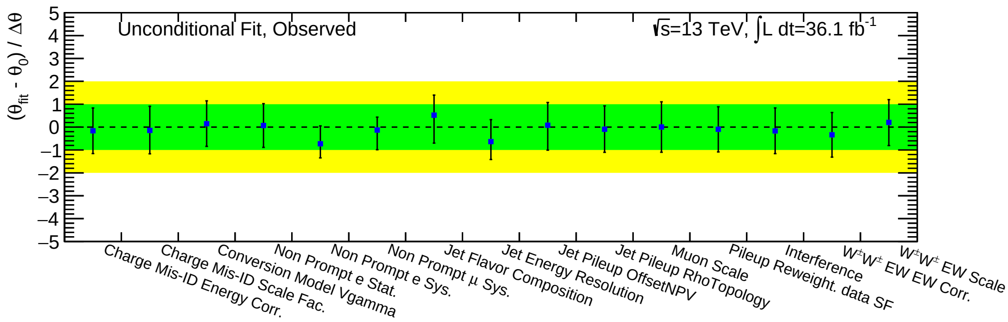

Figure 9.12: Nuisance parameter pulls after the full fit to observed data. Only the 15 nuisance parameters showing the highest pulls or constraints are displayed.

[1]Nuisance parameters accounting for background precision uncertainties are not included.

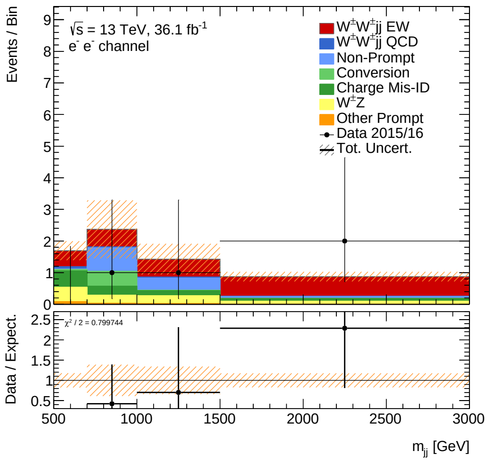

(a) e^-e^-

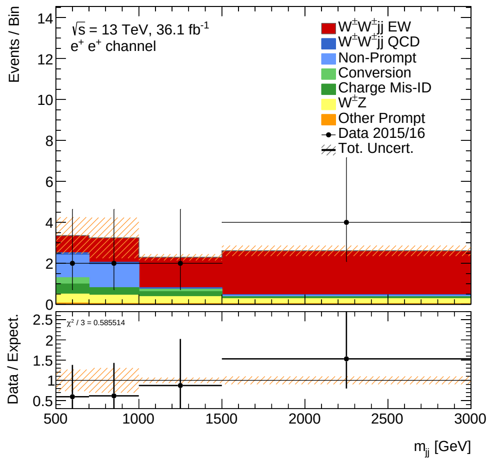

(b) e^+e^+

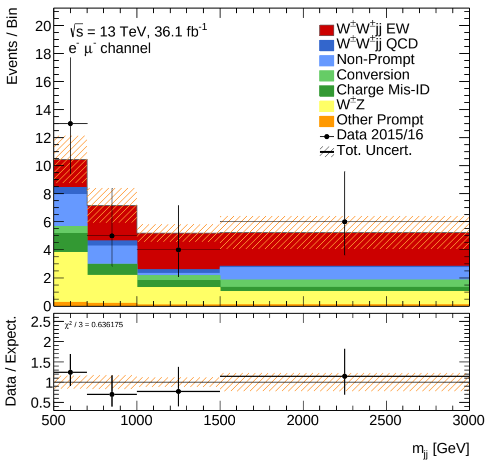

(c) $e^-\mu^-/\mu^-e^-$

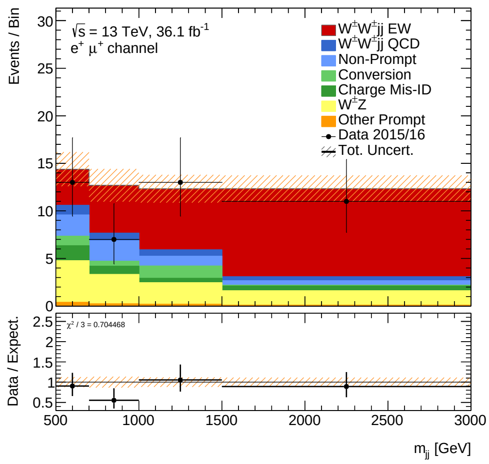

(d) $e^+\mu^+/\mu^+e^+$

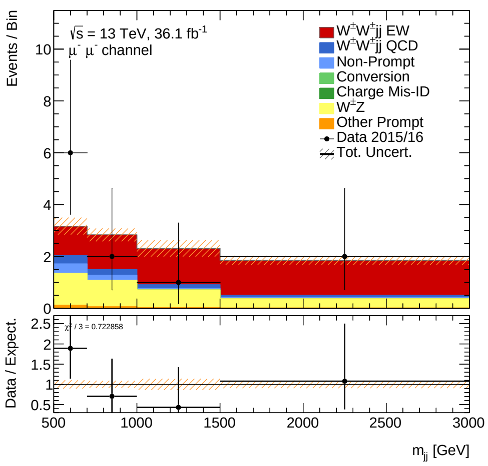

(e) $\mu^-\mu^-$

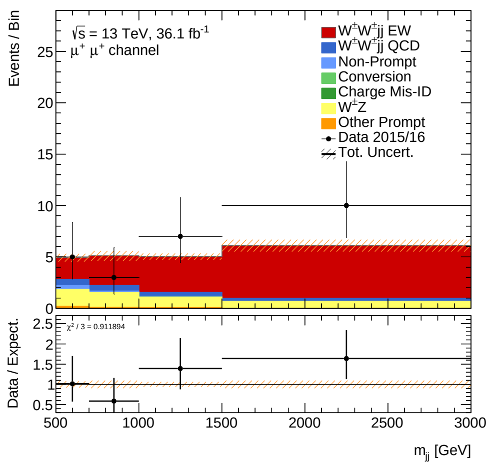

(f) $\mu^+\mu^+$

Figure 9.13: Post-fit m_{jj} distributions in six lepton charge and flavor channels in the signal region. Poisson uncertainties are shown for the Asimov data points. In the ratio plot, the total statistical and systematic uncertainties are shown. Background contributions are grouped into categories as listed in Table 9.1.

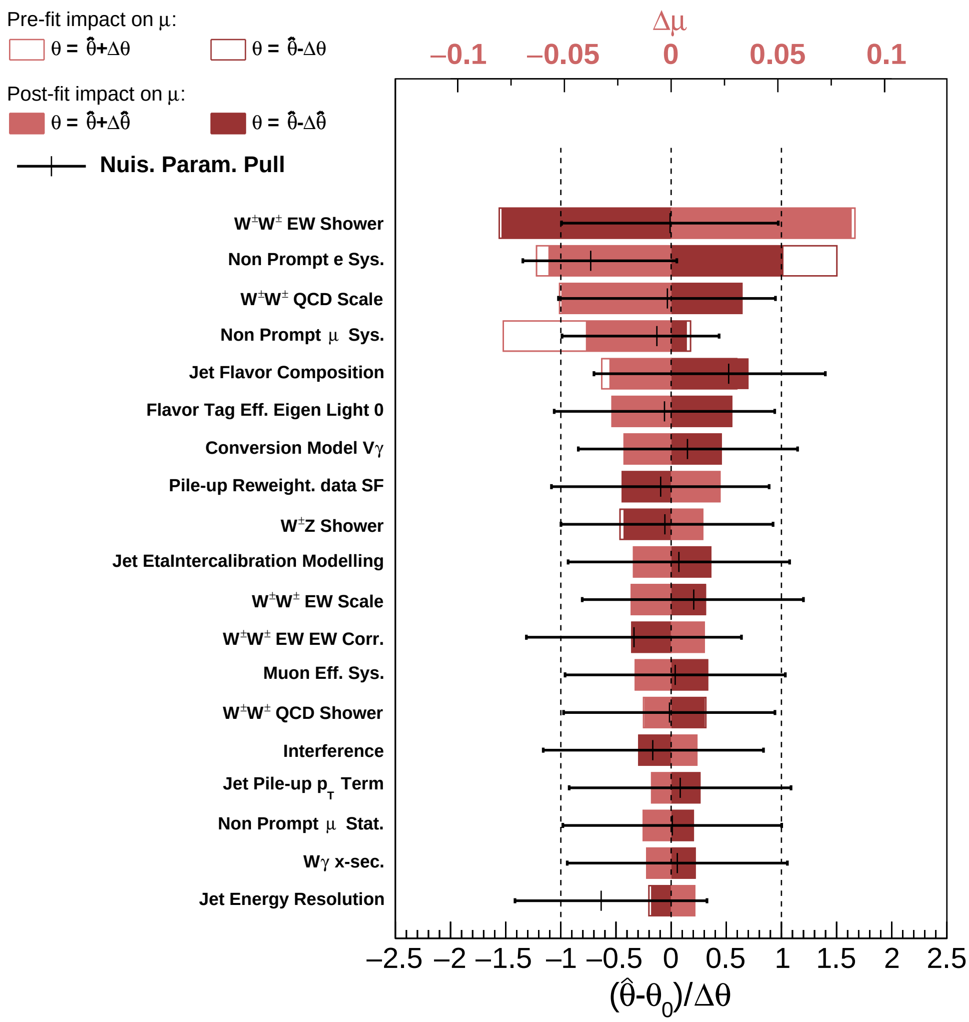

Figure 9.14: Ranking of nuisance parameters according to their pre-fit impact on the signal strength. Only the 19 most important parameters are shown. Nuisance parameters accounting for background precision and luminosity uncertainties are not included. For each nuisance parameter, the pre- and post-fit impact on the signal strength (red, top axis) as well as the post-fit parameter pull and uncertainty (black, bottom axis) are shown. The pre-fit uncertainties on the nuisance parameter pulls are ± 1 for all parameters.

Parameter 1	Parameter 2	Correlation [%]
$W^{\pm}Z$ Shower	μ_{WZ}	−69.2
$W^{\pm}Z$ Scale	μ_{WZ}	−66.7
$W^{\pm}W^{\pm}jj$-Ew Shower	μ	28.2
Non Prompt e Sys.	Bkg Prec. Low-m_{jj} Cr, $e^{-}e^{-}$ Chan, Bin 1	−25.4
Non Prompt e Stat.	Non Prompt e Sys.	−24.8
Non Prompt e Sys.	Bkg Prec. SR, $e^{-}e^{-}$ Chan, Bin 2	−21.0
Non Prompt e Sys.	Bkg Prec. SR, $e^{+}e^{+}$ Chan, Bin 2	−18.7
Non Prompt e Sys.	μ	−18.5
Conversion Model $V\gamma$	Jet Energy Resolution	−15.7
Jet Flavor Composition	μ_{WZ}	−15.5
Conversion Model $V\gamma$	Non Prompt e Sys.	−15.2
Jet Energy Resolution	Bkg Prec. SR, $e^{+}\mu^{+}/\mu^{+}e^{+}$ Chan, Bin 2	−15.0
Non Prompt e Sys.	Jet Flavor Composition	−14.5
$W^{\pm}W^{\pm}jj$-Qcd Scale	μ	−13.9
Non Prompt e Sys.	$W^{\pm}Z$ Shower	12.1
Jet Flavor Composition	Bkg Prec. SR, $e^{-}\mu^{-}/\mu^{-}e^{-}$ Chan, Bin 4	−12.0
Jet Flavor Composition	Jet Pile-up OffsetNPV	−11.7
Luminosity	μ	−11.6
Jet Flavor Composition	μ	−11.3
Non Prompt e Sys.	Non Prompt μ Sys.	−11.2
Non Prompt e Sys.	Bkg Prec. Low-m_{jj} Cr, $e^{-}\mu^{-}/\mu^{-}e^{-}$ Chan, Bin 1	−9.9
Flavor Tag Eff. Eigen Light 1	μ	−9.6
Non Prompt e Sys.	Bkg Prec. SR, $e^{+}e^{+}$ Chan, Bin 1	−9.2
Non Prompt e Sys.	Bkg Prec. Low-m_{jj} Cr, $e^{+}\mu^{+}/\mu^{+}e^{+}$ Chan, Bin 1	−8.9
Jet Energy Resolution	Bkg Prec. SR, $e^{+}\mu^{+}/\mu^{+}e^{+}$ Chan, Bin 1	8.7
Jet Flavor Composition	Bkg Prec. Low-m_{jj} Cr, $e^{+}\mu^{+}/\mu^{+}e^{+}$ Chan, Bin 1	−8.7
Non Prompt e Sys.	Jet Energy Resolution	8.7
Non Prompt μ Sys.	μ	−8.5
Jet Pile-up RhoTopology	μ_{WZ}	−8.4
Conversion Model $V\gamma$	Jet Flavor Composition	8.4
Bkg Prec. SR, $e^{+}\mu^{+}/\mu^{+}e^{+}$ Chan, Bin 3	μ	−8.0
Jet EtaIntercalibration Modeling	μ_{WZ}	−8.0
Non Prompt e Sys.	μ_{WZ}	−8.0
Bkg Prec. SR, $e^{+}\mu^{+}/\mu^{+}e^{+}$ Chan, Bin 4	μ	−7.9
Pile-up Reweight. data SF	μ	7.8
Jet Pile-up OffsetNPV	Bkg Prec. SR, $e^{-}\mu^{-}/\mu^{-}e^{-}$ Chan, Bin 4	−7.6
Non Prompt e Sys.	$W^{\pm}\gamma$ x-sec.	−7.5
Jet EffectiveNP 2	μ_{WZ}	−7.3
Non Prompt e Stat.	Jet Flavor Composition	−7.1

Table 9.16: Pair-wise correlation factors between two nuisance parameters after the fit to observed data. Parameter pairs are sorted by descending absolute correlation value. Only correlations large than 7 % are shown.

9.4 Cross Section Calculation

As described above, a profile likelihood fit is done to determine the best estimator of the signal strength for the Asimov and observed dataset, denoted as μ_{exp} and μ_{obs}, respectively. In order to extract the measured fiducial cross section based on the results of a profile likelihood fit, the predicted theory cross section $\sigma^{\text{fid}}_{\text{theo}}$ in the fiducial region needs to be known with theory normalization uncertainties. Further shape uncertainties on the m_{jj} distribution are taken into account in the fitting template and are therefore included in the uncertainty on the signal strength. The signal normalization and shape uncertainties are discussed in detail in Section 4.2.1. The measured fiducial cross section $\sigma^{\text{fid}}_{\text{meas}}$ is then calculated as

$$\sigma^{\text{fid}}_{\text{meas}} = \hat{\mu} \cdot \sigma^{\text{fid}}_{\text{theo}} = \hat{\mu} \cdot \sigma^{\text{tot}}_{\text{theo}} \cdot \mathcal{A}, \tag{9.9}$$

where $\mathcal{A}$ is the acceptance factor of the fiducial phase space as defined in Eq. (4.2). The best estimate of the signal strength, $\hat{\mu}$ is replaced with either μ_{exp} or μ_{obs} when calculating the expected or observed measured fiducial cross section, respectively.

The predicted total and fiducial cross sections, as well as the acceptance are given in Section 4.2. The acceptance and its uncertainties are properly propagated to the predicted fiducial cross section at leading order, resulting in a fiducial cross section $\sigma^{\text{fid}}_{\text{theo}}$ [97] of

$$\sigma^{\text{fid}}_{\text{theo}} = \Big(2.01 \pm 0.02(\text{stat}) \,^{+0.29}_{-0.23}\,(\text{scale}) \,^{+0.16}_{-0.02}\,(\text{parton shower}) \,^{+0.05}_{-0.03}\,(\text{PDF}{+}\alpha_{\text{s}})\Big) \text{ fb}. \tag{9.10}$$

As described in Eq. (9.9), $\sigma^{\text{fid}}_{\text{theo}}$ is used to derive the measured expected fiducial cross section. The best estimator of the expected signal strength μ_{exp} (see Eq. (9.4)) is used

$$\mu_{\text{exp}} = 1.01 \,^{+0.25}_{-0.22}\,(\text{stat}) \,^{+0.09}_{-0.09}\,(\text{theo}) \,^{+0.11}_{-0.12}\,(\text{sys}).$$

This results in a measured expected fiducial cross section $\sigma^{\text{fid}}_{\text{meas,exp}}$ of

$$\sigma^{\text{fid}}_{\text{meas,exp}} = \Big(2.02 \,^{+0.50}_{-0.45}\,(\text{stat}) \,^{+0.18}_{-0.17}\,(\text{theo}) \,^{+0.22}_{-0.24}\,(\text{sys})\Big) \text{ fb}, \tag{9.11}$$

$$= \Big(2.02 \,^{+0.57}_{-0.54}\,(\text{total})\Big) \text{ fb}. \tag{9.12}$$

For the fit to observed data, μ_{obs} was determined to (see Eq. (9.6))

$$\mu_{\text{obs}} = 1.46 \,^{+0.26}_{-0.24}\,(\text{stat}) \,^{+0.10}_{-0.08}\,(\text{theo}) \,^{+0.13}_{-0.11}\,(\text{sys}),$$

corresponding to a measured observed fiducial cross section $\sigma^{\text{fid}}_{\text{meas,obs}}$ of

$$\sigma^{\text{fid}}_{\text{meas,obs}} = \Big(2.94 \,^{+0.52}_{-0.48}\,(\text{stat}) \,^{+0.19}_{-0.16}\,(\text{theo}) \,^{+0.27}_{-0.23}\,(\text{sys})\Big) \text{ fb}, \tag{9.13}$$

$$= \Big(2.94 \,^{+0.62}_{-0.56}\,(\text{total})\Big) \text{ fb}. \tag{9.14}$$

In Figure 9.15, a comparison of the predicted and measured fiducial cross sections is shown. The total uncertainties are depicted by a light blue error band. In the case of the predicted fiducial cross section, the largest source of uncertainties, i. e. the renormalization and factorization scale uncertainties are shown separately. For the measured fiducial cross section, the dominant statistical uncertainty is shown separately.

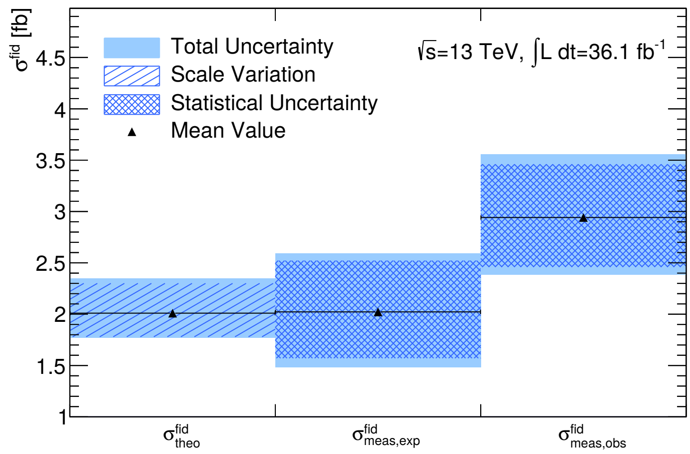

Figure 9.15: Comparison of predicted and measured fiducial cross sections $\sigma^{\text{fid}}_{\text{theo}}$ and $\sigma^{\text{fid}}_{\text{meas}}$. The total uncertainties are depicted by a light blue error band. For the predicted fiducial cross section the largest source of uncertainties, the renormalization and factorization scale uncertainties are shown separately. For the measured fiducial cross section, the dominant statistical uncertainty is shown separately.

9.5 Discussion of the Validity of Expected and Observed Results

In the previous sections, an expected and observed significance of 4.6 σ and 6.7 σ is calculated, respectively. The corresponding expected and observed measured fiducial cross sections amount to $(2.02 \pm {}^{0.57}_{0.54})$ fb and $(2.94 \pm {}^{0.62}_{0.56})$ fb. Although these values agree within their uncertainties, there is some tension between expected and observed results. However, the observed measured fiducial cross section is in good agreement with PowhegBox+Py8 and MG_aMC+Py8 predictions presented in Reference [99]. It is therefore a valid assumption that the Sherpa signal sample does not describe electroweak $W^{\pm}W^{\pm}$ production accurately and the question can be raised if the observed results depend on the choice of the nominal signal prediction.

The validity of the observed results is tested by using a set of four different signal hypotheses to fit an arbitrary dataset. If the statistical analyses yields the same results for all different signal templates applied to the same dataset, it is shown that the uncertainties on the background and signal distributions are sufficient to compensate possible inaccuracies in the Sherpa signal prediction and that the final observed result is reasonably independent of the choice of the signal sample. In all of these cross-checks, a pruning with $t = 0.1$ % and $p_{\text{b}} = 20$ % is applied to shape nuisance parameters (cf. Section 9.1.3).

All signal templates used in this test are derived from the nominal Sherpa signal. In the following, the different configurations are referred to as

Nominal: The nominal Sherpa signal prediction including all systematic uncertainties[1].

Scaled: The nominal Sherpa signal is normalized to the MG_aMC+Py8 fiducial cross section. Using a fiducial cross section of (3.106 ± 0.015) fb, corresponding to the MG_aMC+Py8 $W^{\pm}W^{\pm}jj$-Ew prediction with Pythia 8 parton showering [99], a scale factor of $f_s = 1.54$ is calculated. The scaling is applied uniformly in all bins.

Variation 1: The signal template is constructed from the nominal signal prediction. A scale factor $f_1 \in [1.5, 2.0]$ is applied to all m_{jj} bins. The scale factor increases with m_{jj}, such that high-m_{jj} bins receive a higher weight. This choice is motivated by the m_{jj} distributions for the

[1] All nuisance parameters are included, except for those not passing the pruning selection of $t = 0.1$ % and $p_{\text{b}} = 20$ %.

SHERPA, POWHEGBOX+PY8 and MG_AMC+PY8 generators on truth level [99], where the disagreement with SHERPA increases with m_{jj} as well. Systematic uncertainties are scaled using the same, m_{jj}-dependent factor, such that the relative impact is not changed.

Variation 2: This variation is very similar to the construction of the *Variation 1* scenario, however, a scale factor $f_2 \in [3.0, 4.0]$ is used.

The test dataset is constructed in a way such that shape and normalization differences exists with respect to any of the varied signal predictions. Thus, the ability of the profile likelihood fit to adapt to random data distributions is probed. The test dataset is defined as the sum of all background contributions, where the nominal signal prediction scaled with f_1 is added on top. The resulting dataset is not identical to the Asimov dataset corresponding to the *Variation 1* scenario, as no scale factors on the backgrounds, especially the $W^{\pm}Z$ background estimate, are considered.

A comparison of the four different fitting configurations is shown in Figure 9.16. Only the signal distributions are varied between the different scenarios, and are shown in red. The k-factors for different signal templates with respect to the nominal distribution are defined as

$$k = \frac{\sum_{n=1}^{4} N_n^{\text{var}}}{\sum_{n=1}^{4} N_n^{\text{nom}}},$$

where n runs over all m_{jj} bins in the signal region, and $N_n^{\text{nom(var)}}$ denotes the number of events in the nominal and varied signal distribution in bin n, respectively. The k-factors for all varied signal templates are summarized in Table 9.17. For the signal templates scaled with f_1 and f_2, k-factors of 1.71 and 3.43 are calculated, respectively. Thus, the normalization of the *Scaled* and *Variation 1* scenarios are of comparable size.

Post-fit distributions are shown in Figure 9.17. It can be seen that good agreement between test dataset and prediction is achieved for all four scenarios. Detailed fit results are summarized in Table 9.17, where the best estimator of the signal strength, $\hat{\mu}$ as well as the corresponding measured fiducial cross section, $\sigma_{\text{meas}}^{\text{fid}}$, and the significance are listed. The measured cross section is calculated taking into account the k-factor for each signal template as

$$\sigma_{\text{meas}}^{\text{fid}} = k\,\hat{\mu}\,\sigma_{\text{theo}}^{\text{fid}},$$

where the leading order SHERPA fiducial cross section $\sigma_{\text{theo}}^{\text{fid}} = (2.01 \pm 0.34)\,\text{fb}$ is used. In addition to the central values, the relative uncertainty on $\hat{\mu}$ separated into statistical, theory and other systematic contributions is given. Statistical and systematic uncertainties are found to be similar in all four cases. It is, however, observed that theory uncertainties are reduced by approximately 1 % in the scenarios *Variation 1* and *Variation 2*, where the shape of the signal template was modified. This is due to a slight constraint on the $W^{\pm}W^{\pm}jj$-EW Shower nuisance parameter which has post-fit uncertainties of $^{+0.98}_{-0.98}$ for the *Nominal* and *Scaled* scenario, while the uncertainty corresponds to $^{+0.96}_{-0.97}$ for the other two variations.

All cross section measurements are in good agreement. Almost identical results are obtained in the *Nominal* and *Scaled*, as well as *Variation 1* and *Variation 2* scenarios, respectively. The cross section values reported in Table 9.17 differ only in the third digit. For each variation, the difference of the measured cross section with respect to the *Nominal* configuration is given in Table 9.17. Between the scenarios with and without shape change, the difference between the measured cross sections amounts to approximately 3 %, which is much smaller than the statistical uncertainty. Furthermore, the significances derived for the test dataset is all scenarios are compatible with each other.

As only minor differences are observed between the four signal hypotheses, the observed results presented in Section 9.3 are assumed to be reliable.

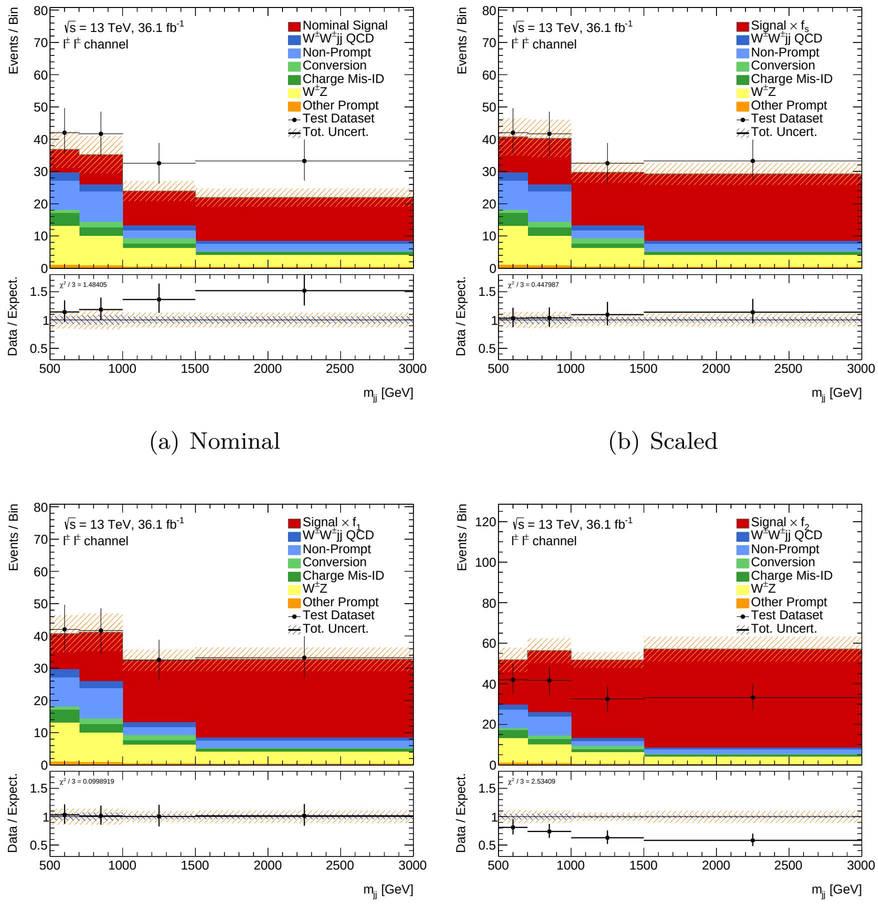

(a) Nominal (b) Scaled

(c) Variation 1 (d) Variation 2

Figure 9.16: Pre-fit m_{jj} distributions in the combined $\ell^{\pm}\ell^{\pm}$ channel of the signal region, using different versions of the signal template and the same modified dataset. Background contributions are grouped into categories as listed in Table 9.1.

Quantity	Unit	Nominal	Scaled	Variation 1	Variation 2
k-Factor		–	1.54	1.71	3.43
$\hat{\mu}$		1.75	1.14	0.99	0.50
$\Delta_{\text{stat}}\ \hat{\mu}$	[%]	15.90	15.98	15.87	15.96
$\Delta_{\text{theo}}\ \hat{\mu}$	[%]	7.11	7.13	6.27	6.26
$\Delta_{\text{sys}}\ \hat{\mu}$	[%]	8.71	8.65	8.80	8.79
$\sigma^{\text{fid}}_{\text{meas}}$	[fb]	3.52	3.52	3.41	3.41
$\Delta_{\text{stat}}\ \sigma^{\text{fid}}_{\text{meas}}$	[fb]	0.56	0.53	0.54	0.54
$\Delta_{\text{theo}}\ \sigma^{\text{fid}}_{\text{meas}}$	[fb]	0.25	0.25	0.21	0.22
$\Delta_{\text{sys}}\ \sigma^{\text{fid}}_{\text{meas}}$	[fb]	0.31	0.30	0.30	0.30
$\Delta\ \sigma^{\text{Nom}}_{\text{fid}}$	[%]	–	0.06	3.12	3.07
Significance		7.05	7.05	7.07	7.07

Table 9.17: Comparison of fit results for all four scenarios. The bottom row shows the relative difference of the measured fiducial cross sections of all scenarios w.r.t. the nominal settings.

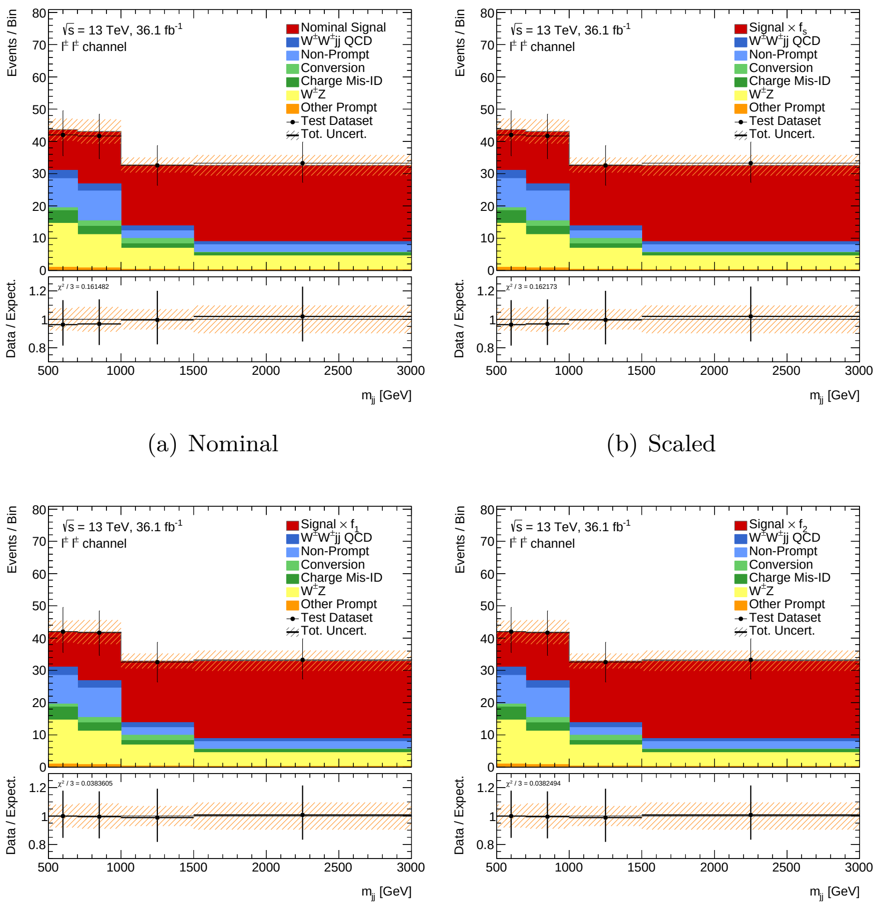

(a) Nominal

(b) Scaled

(c) Variation 1

(d) Variation 2

Figure 9.17: Post-fit m_{jj} distributions in the combined $\ell^{\pm}\ell^{\pm}$ channel of the signal region, using different versions of the signal template and the same modified dataset. Background contributions are grouped into categories as listed in Table 9.1.

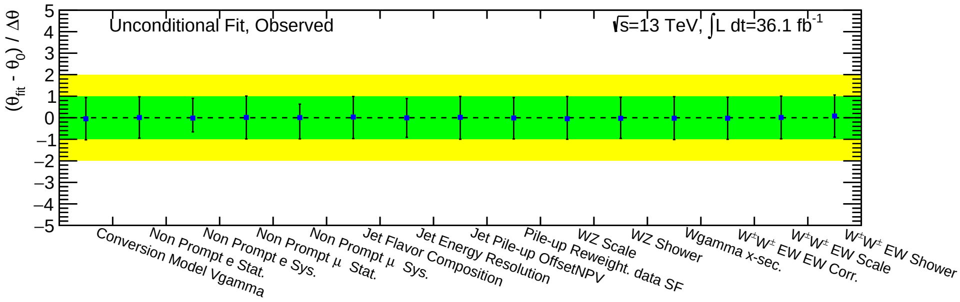

(a) Nominal

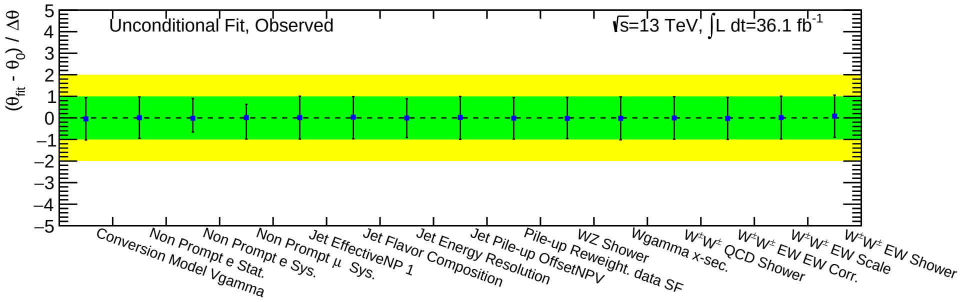

(b) Scaled

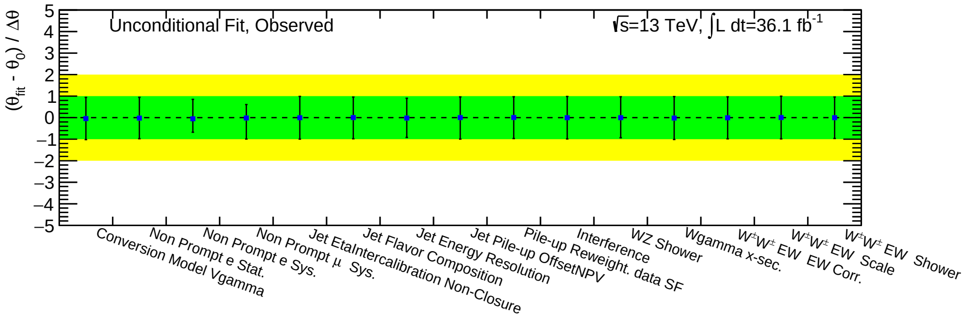

(c) Variation 1

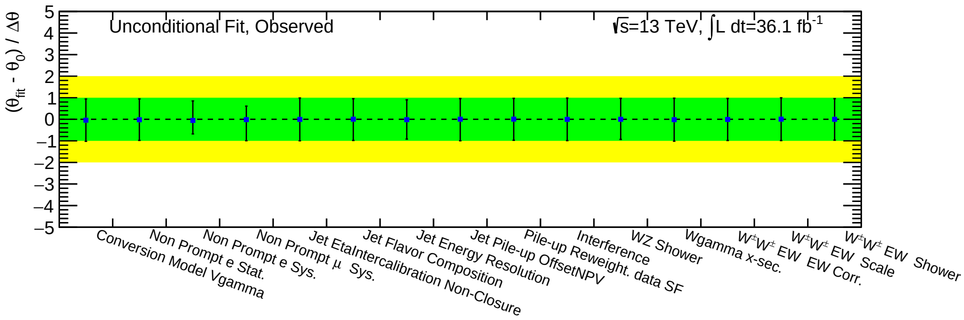

(d) Variation 2

Figure 9.18: Nuisance parameter pulls for parameters with Gaussian constraint after the fits to a test dataset, using different signal template shapes.

10 Summary and Outlook

In this thesis, the measurement of the electroweak $pp \to W^{\pm}W^{\pm}jj \to \ell^{\pm}\nu\ell'^{\pm}\nu' jj$ production is presented. The measurement is based on a total integrated luminosity of 36.1 fb^{-1} of proton-proton collision data, recorded at a center-of-mass energy of 13 TeV. All processes involving purely electroweak couplings, that are at least of the order $\mathcal{O}(\alpha_{\text{ew}}^6)$ with $W^{\pm}$-bosons decaying into electrons or muons are considered as $W^{\pm}W^{\pm}$ electroweak production.

Signal event candidates are selected by requiring at least two jets, exactly two same-charge leptons as well as high missing transverse momentum in the event. The signal region is constrained to a Vbs-like topology with a high invariant mass m_{jj} of the leading and subleading jets of $m_{jj} > 500$ GeV and a large angular separation $\Delta Y_{jj} > 2$ between them. The m_{jj} binning in the signal region is optimized based on the signal-to-background ratio in each bin, as well as relative statistical uncertainties of the signal and total background estimate. In the optimal configuration, the signal region is split into four bins.

The main background contributions are generated by events from $W^{\pm}Z$ production as well as events with wrongly measured or mis-reconstructed leptons. These can be either electrons with a mis-reconstructed charge, called charge mis-ID background; or jets that are mis-reconstructed as electrons or muons, denoted as non-prompt background. Both contributions mainly depend on detector effects which cannot be modeled with high accuracy. Therefore, these backgrounds are estimated using observed data in control regions. In the statistical analysis, low-m_{jj} and $W^{\pm}Z$ control regions are used to constrain the non-prompt and $W^{\pm}Z$ backgrounds, respectively.

The expected and observed significances as well as the respective signal strengths are determined in a combined profile likelihood fit of the signal and control regions. The normalization of the $W^{\pm}Z$ background, μ_{WZ}, is measured in a separate fit of the $W^{\pm}Z$ and low-m_{jj} control regions to observed data, prior to the full fit to expected Asimov data. In order to propagate the measurement of μ_{WZ} to the expected results, μ_{WZ} is then used to scale the $W^{\pm}Z$ estimate in all regions for the composition of the expected Asimov dataset and in the full fit. This increases the comparability of the expected and observed significance.

The measured expected and observed fiducial cross sections are compared to the leading order prediction of the Sherpa generator. Theory uncertainties on the signal prediction due to variations of the renormalization and factorization scales, the strong coupling α_{s}, as well as variations of the parton shower (PS) scheme and the parton density (PDF) of the proton are taken into account. The theory uncertainties on the signal m_{jj} distribution are separated into a normalization effect on particle level and and normalization and shape uncertainty on reconstruction level. The normalization uncertainty on particle level is assigned to the predicted fiducial cross section $\sigma_{\text{theo}}^{\text{fid}}$. On detector level, residual normalization effects as well as remaining shape effects are assigned to the signal template in the profile likelihood fit and therefore included in the uncertainty on the measured fiducial cross section $\sigma_{\text{meas}}^{\text{fid}}$.

A summary of the expected and observed significances and measured fiducial cross sections as well as the cross section prediction is given in Table 10.1. The observed significance is 6.7 σ; which is one of the most significant observations of $W^{\pm}W^{\pm}jj$-Ew production up to now. An expected significance of 4.6 σ is measured. The expected and observed measured fiducial cross sections agree within their uncertainties. It is seen that the predictions from the PowhegBox and MadGraph5_aMC@NLO (MG_aMC) generators differ from the Sherpa prediction in terms of cross section and differential m_{jj} distribution. It has been shown, however, that the observed

	Significance [σ]	$\sigma^{\text{fid}}_{\text{meas}}$ [fb]
Expected	4.6	$2.02\ ^{+0.50}_{-0.45}$ (stat) $^{+0.18}_{-0.17}$ (theo) $^{+0.22}_{-0.24}$ (sys)
Observed	6.7	$2.94\ ^{+0.52}_{-0.48}$ (stat) $^{+0.19}_{-0.16}$ (theo) $^{+0.27}_{-0.23}$ (sys)
$\sigma^{\text{fid}}_{\text{theo}}$ [fb]	2.01 $\pm$ 0.02 (stat) $^{+0.29}_{-0.23}$ (scale) $^{+0.16}_{-0.02}$ (PS) $^{+0.05}_{-0.03}$ (PDF+α_s)	

Table 10.1: Summary of the expected and observed significances as well as measured fiducial cross sections $\sigma^{\text{fid}}_{\text{meas}}$. In addition, predicted fiducial cross section $\sigma^{\text{fid}}_{\text{theo}}$ is given.

results are not expected to be depended on the exact value of the predicted signal normalization and shape in the signal region.

The CMS experiment has reported an expected and observed significance of 5.7 σ and 5.5 σ, respectively [91]. However, the definition of the signal region slightly differs from the definition applied in this analysis. Furthermore, the CMS results are based on the leading order MG_aMC+Py8 $W^{\pm}W^{\pm}jj$-EW prediction. Therefore, the results are not easily comparable.

Based on the data recorded in 2015 and 2016, the ATLAS collaboration reported expected and observed significances of 4.6 σ and 6.9 σ, respectively [11]. The analysis strategy is almost identical to the one employed in this thesis. Minor differences in the observed significance occur, as one-sided nuisance parameters are symmetrized in this thesis, which was not done for the ATLAS publication.

In future analyses using the full LHC Run 2 dataset, which corresponds to approximately 140 fb^{-1} [58], limits on non-SM contributions will be set. These anomalous quartic couplings are parametrized in the effective field theory approach using dimension-eight operators [46]. In contrast to the 8 TeV analyses, a unified unitarization method will be applied in CMS and ATLAS measurements to gain comparability and open the option for combined measurements. The unitarization method is proposed in Reference [152]. Following this prescription, limits will be set on a partial dataset which is clipped at variable cut-off values in the relevant energy scale. The energy scale is determined by the momentum transfer of the interaction at particle level. Limiting the energy range simultaneously assures the validity of the effective field theory, which would break at energies close to the new resonance. Compared to the K-matrix unitarization [95] used in the 8 TeV analysis by the ATLAS collaboration, the clipping method enables theorists to reinterpret the analysis results.

$W^{\pm}W^{\pm}jj$-EW production has now been successfully observed by the ATLAS and CMS collaborations and is compatible with Standard Model predictions. Up to now, no conclusive implications regarding the electroweak symmetry breaking mechanism can be inferred. Including more data or even combining ATLAS and CMS results will be crucial for reducing the currently dominating statistical uncertainties and gaining deeper insights. The most interesting result would be to exclude the Standard Model at 3 σ or more. Even though there is a certain tension between the current measurement and the SHERPA leading order prediction, the question of which value the ratio of observed to predicted cross section will take in future measurements can currently not be answered with certainty. It is seen that the current observation is in very good agreement with other generators. However, at the moment no Monte-Carlo program is able to generate $W^{\pm}W^{\pm}jj$-EW events including higher-order electroweak corrections. These corrections are known to have a negative effect on the total cross section and are especially important in high m_{jj} regions, where the sensitivity of VBS measurements is largest. Therefore, there are still highly interesting times to come in the scope of VBS analyses.

11 Bibliography

[1] McDonnell, J.J. *The concept of an atom from Democritus to John Dalton*. Distinguished Dissertations Series. Edwin Mellen Press, 1992. URL: https://books.google.de/books?id=IGkgAQAAIAAJ.

[2] Thomson J. J. *XL. Cathode Rays*. In: *The London, Edinburgh, and Dublin Philosophical Magazine and Journal of Science* 44.269 (1897), 293–316. DOI: 10.1080/14786449708621070.

[3] Geiger, Hans and Rutherford , Ernest. *The scattering of α-particles by matter*. In: *83. Proceedings of the Royal Society of London, Containing Papers of a Mathematical and Physical Character* Series A (1910). DOI: doi.org/10.1098/rspa.1910.0038.

[4] E. Rutherford. *The scattering of alpha and beta particles by matter and the structure of the atom*. In: *Phil. Mag. Ser.6* 21 (1911), pp. 669–688. DOI: 10.1080/14786440508637080.

[5] W. de Boer. *Grand unified theories and supersymmetry in particle physics and cosmology*. In: *Prog. Part. Nucl. Phys.* 33 (1994), pp. 201–302. DOI: 10.1016/0146-6410(94)90045-0. arXiv: hep-ph/9402266 [hep-ph].

[6] D. J. Griffiths. *Introduction to elementary particles; 2nd rev. version*. Physics textbook. New York, NY: Wiley, 2008. URL: https://cds.cern.ch/record/111880.

[7] J. Erler et al. *Electroweak Precision Tests of the Standard Model after the Discovery of the Higgs Boson*. In: (2019). arXiv: 1902.05142 [hep-ph].

[8] G. Aad et al. *Observation of a new particle in the search for the Standard Model Higgs boson with the ATLAS detector at the LHC*. In: *Phys. Lett.* B716 (2012), pp. 1–29. DOI: 10.1016/j.physletb.2012.08.020. arXiv: 1207.7214 [hep-ex].

[9] G. Aad et al. *Combined Measurement of the Higgs Boson Mass in pp Collisions at $\sqrt{s} = 7$ and 8 TeV with the ATLAS and CMS Experiments*. In: *Phys. Rev. Lett.* 114 (2015), p. 191803. DOI: 10.1103/PhysRevLett.114.191803. arXiv: 1503.07589 [hep-ex].

[10] *Combined measurements of Higgs boson production and decay using up to 80 fb^{-1} of proton–proton collision data at $\sqrt{s}$ = 13 TeV collected with the ATLAS experiment*. Tech. rep. ATLAS-CONF-2018-031. Geneva: CERN, July 2018. URL: http://cds.cern.ch/record/2629412.

[11] *Observation of electroweak production of a same-sign W boson pair in association with two jets in pp collisions at $\sqrt{s} = 13$ TeV with the ATLAS detector*. Tech. rep. ATLAS-CONF-2018-030. Geneva: CERN, July 2018. URL: https://cds.cern.ch/record/2629411.

[12] G. Arnison et al. *Experimental observation of isolated large transverse energy electrons with associated missing energy at s=540 GeV*. In: *Physics Letters B* 122.1 (1983), pp. 103–116. ISSN: 0370-2693. DOI: https://doi.org/10.1016/0370-2693(83)91177-2. URL: http://www.sciencedirect.com/science/article/pii/0370269383911772.

[13] *Observation of single isolated electrons of high transverse momentum in events with missing transverse energy at the CERN pp collider*. In: *Physics Letters B* 122.5 (1983), pp. 476–485. ISSN: 0370-2693. DOI: https://doi.org/10.1016/0370-2693(83)91605-2.

[14] G. Arnison et al. *Experimental Observation of Lepton Pairs of Invariant Mass Around 95-GeV/c**2 at the CERN SPS Collider*. In: *Phys. Lett.* B126 (1983). [,7.55(1983)], pp. 398–410. DOI: 10.1016/0370-2693(83)90188-0.

[15] P. Bagnaia et al. *Evidence for Z0 —> e+ e- at the CERN anti-p p Collider.* In: *Phys. Lett.* B129 (1983). [,7.69(1983)], pp. 130–140. DOI: 10.1016/0370-2693(83)90744-X.

[16] S. Abachi et al. *Observation of the top quark.* In: *Phys. Rev. Lett.* 74 (1995), pp. 2632–2637. DOI: 10.1103/PhysRevLett.74.2632. arXiv: hep-ex/9503003 [hep-ex].

[17] J. Yoh. *The Discovery of the B quark at Fermilab in 1977: The Experiment coordinator's story.* In: *AIP Conf. Proc.* 424.1 (1998), pp. 29–42. DOI: 10.1063/1.55114.

[18] G. ALTARELLI. *The Standard model of particle physics.* In: (2005). arXiv: hep-ph/0510281 [hep-ph].

[19] S. Weinberg. *A Model of Leptons.* In: *Phy. Rev. Lett.* 19 (1967).

[20] A. Salam. *Elementary Particle Theory.* In: *Almqvist and Wiksell* (1968).

[21] S. Glashow. *Partial-Symmetries of Weak Interactions.* In: *Nuclear Physics* 22 (1961).

[22] C. S. Wu et al. *Experimental Test of Parity Conservation in Beta Decay.* In: *Physical Review* 105 (Feb. 1957), pp. 1413–1415. DOI: 10.1103/PhysRev.105.1413.

[23] N. Cabibbo. *Unitary Symmetry and Leptonic Decays.* In: *Phys. Rev. Lett.* 10 (12 June 1963), pp. 531–533. DOI: 10.1103/PhysRevLett.10.531. URL: https://link.aps.org/doi/10.1103/PhysRevLett.10.531.

[24] M. Kobayashi et al. *CP Violation in the Renormalizable Theory of Weak Interaction.* In: *Prog. Theor. Phys.* 49 (1973), pp. 652–657. DOI: 10.1143/PTP.49.652.

[25] J. H. Christenson et al. *Evidence for the 2π Decay of the K_2^0 Meson.* In: *Phys. Rev. Lett.* 13 (1964), pp. 138–140. DOI: 10.1103/PhysRevLett.13.138.

[26] B. Aubert et al. *Observation of CP Violation in the B^0 Meson System.* In: *Phys. Rev. Lett.* 87 (9 Aug. 2001), p. 091801. DOI: 10.1103/PhysRevLett.87.091801. URL: https://link.aps.org/doi/10.1103/PhysRevLett.87.091801.

[27] B. Pontecorvo. *Neutrino Experiments and the Problem of Conservation of Leptonic Charge.* In: *Sov. Phys. JETP* 26 (1968). [Zh. Eksp. Teor. Fiz.53,1717(1967)], pp. 984–988.

[28] Z. Maki et al. *Remarks on the Unified Model of Elementary Particles.* In: *Progress of Theoretical Physics* 28.5 (Nov. 1962), pp. 870–880. ISSN: 0033-068X. DOI: 10.1143/PTP.28.870. eprint: http://oup.prod.sis.lan/ptp/article-pdf/28/5/870/5258750/28-5-870.pdf. URL: https://dx.doi.org/10.1143/PTP.28.870.

[29] A. Bellerive et al. *The Sudbury Neutrino Observatory.* In: *Nucl. Phys.* B908 (2016), pp. 30–51. DOI: 10.1016/j.nuclphysb.2016.04.035. arXiv: 1602.02469 [nucl-ex].

[30] Y. Fukuda et al. *Evidence for oscillation of atmospheric neutrinos.* In: *Phys. Rev. Lett.* 81 (1998), pp. 1562–1567. DOI: 10.1103/PhysRevLett.81.1562. arXiv: hep-ex/9807003 [hep-ex].

[31] M. Tanabashi et al. *Review of Particle Physics.* In: *Phys. Rev. D* 98 (3 Aug. 2018), p. 030001. DOI: 10.1103/PhysRevD.98.030001. URL: https://link.aps.org/doi/10.1103/PhysRevD.98.030001.

[32] A. Denner et al. *Radiative corrections to W+ W- —> W+ W- in the electroweak standard model.* In: *Nucl. Phys.* B525 (1998), pp. 27–50. DOI: 10.1016/S0550-3213(98)00287-9. arXiv: hep-ph/9711302 [hep-ph].

[33] C. Balazs. *Baryogenesis: A small review of the big picture.* In: (2014). arXiv: 1411.3398 [hep-ph].

[34] P. A. R. Ade et al. *Planck 2013 results. XVI. Cosmological parameters.* In: *Astron. Astrophys.* 571 (2014), A16. DOI: 10.1051/0004-6361/201321591. arXiv: 1303.5076 [astro-ph.CO].

[35] C. Csáki et al. *Beyond the Standard Model*. In: *Proceedings, 2013 European School of High-Energy Physics (ESHEP 2013): Paradfurdo, Hungary, June 5-18, 2013*. 2015, pp. 169–268. DOI: 10.5170/CERN-2015-004.169. arXiv: 1602.04228 [hep-ph].

[36] Martin, Stephen P. *A Supersymmetry primer*. In: (1997). Adv. Ser. Direct. High Energy Phys.18,1(1998), pp. 1–98. DOI: 10.1142/9789812839657_0001,10.1142/9789814307505_0001. arXiv: hep-ph/9709356 [hep-ph].

[37] H. Georgi et al. *Doubly charged Higgs bosons*. In: *Nuclear Physics B* 262.3 (1985), pp. 463–477. ISSN: 0550-3213. DOI: https://doi.org/10.1016/0550-3213(85)90325-6. URL: http://www.sciencedirect.com/science/article/pii/0550321385903256.

[38] O. Witzel. *Review on Composite Higgs Models*. In: *36th International Symposium on Lattice Field Theory (Lattice 2018) East Lansing, MI, United States, July 22-28, 2018*. 2019. arXiv: 1901.08216 [hep-lat].

[39] C. Degrande et al. *Effective Field Theory: A Modern Approach to Anomalous Couplings*. In: *Annals Phys.* 335 (2013), pp. 21–32. DOI: 10.1016/j.aop.2013.04.016. arXiv: 1205.4231 [hep-ph].

[40] M. Aaboud et al. *$ZZ \to \ell^+\ell^-\ell'^+\ell'^-$ cross-section measurements and search for anomalous triple gauge couplings in 13 TeV pp collisions with the ATLAS detector*. In: *Phys. Rev.* D97.3 (2018), p. 032005. DOI: 10.1103/PhysRevD.97.032005. arXiv: 1709.07703 [hep-ex].

[41] M. Aaboud et al. *Measurement of $WW/WZ \to \ell\nu qq'$ production with the hadronically decaying boson reconstructed as one or two jets in pp collisions at $\sqrt{s} = 8$ TeV with ATLAS, and constraints on anomalous gauge couplings*. In: *Eur. Phys. J.* C77.8 (2017), p. 563. DOI: 10.1140/epjc/s10052-017-5084-2. arXiv: 1706.01702 [hep-ex].

[42] G. Aad et al. *Measurements of $W^{\pm}Z$ production cross sections in pp collisions at $\sqrt{s} = 8$ TeV with the ATLAS detector and limits on anomalous gauge boson self-couplings*. In: *Phys. Rev.* D93.9 (2016), p. 092004. DOI: 10.1103/PhysRevD.93.092004. arXiv: 1603.02151 [hep-ex].

[43] M. J. Herrero et al. *The Electroweak chiral Lagrangian for the Standard Model with a heavy Higgs*. In: *Nucl. Phys.* B418 (1994), pp. 431–455. DOI: 10.1016/0550-3213(94)90525-8. arXiv: hep-ph/9308276 [hep-ph].

[44] M. J. Herrero et al. *The Electroweak chiral Lagrangian as an effective field theory of the standard model with a heavy Higgs*. In: *Workshop on Electroweak Symmetry Breaking Budapest, Hungary, July 11-13, 1994*. 1994, pp. 37–54. arXiv: hep-ph/9412317 [hep-ph].

[45] A. Alboteanu et al. *Resonances and unitarity in weak boson scattering at the LHC*. In: *Journal of High Energy Physics* 2008.11 (Nov. 2008), pp. 010–010. DOI: 10.1088/1126-6708/2008/11/010. URL: https://doi.org/10.1088%2F1126-6708%2F2008%2F11%2F010.

[46] C. Degrande et al. *Monte Carlo tools for studies of non-standard electroweak gauge boson interactions in multi-boson processes: A Snowmass White Paper*. In: *Proceedings, 2013 Community Summer Study on the Future of U.S. Particle Physics: Snowmass on the Mississippi (CSS2013): Minneapolis, MN, USA, July 29-August 6, 2013*. 2013. arXiv: 1309.7890 [hep-ph]. URL: http://www.slac.stanford.edu/econf/C1307292/docs/submittedArxivFiles/1309.7890.pdf.

[47] F. James. *Statistical methods in experimental physics*. 2006. ISBN: 9789812567956.

[48] J. Adell et al. *The median of the Poisson distribution*. In: *Metrika* 61 (Feb. 2005), pp. 337–346. DOI: 10.1007/s001840400350.

[49] G. Cowan. *Statistical data analysis*. 1998. ISBN: 9780198501565.

[50] K. Cranmer et al. *HistFactory: A tool for creating statistical models for use with RooFit and RooStats*. Tech. rep. CERN-OPEN-2012-016. New York: New York U., Jan. 2012. URL: https://cds.cern.ch/record/1456844.

[51] R. J. Barlow et al. *Fitting using finite Monte Carlo samples*. In: *Comput. Phys. Commun.* 77 (1993), pp. 219–228. DOI: 10.1016/0010-4655(93)90005-W.

[52] K. Cranmer. *The HistFactory Tool*. Likelhoods for the LHC searches. 2013. URL: https://indico.cern.ch/event/218693/contributions/1520320/attachments/353580/492532/HistFactory-LikelihoodWorkshop-22-01-13.pdf.

[53] L. Lyons. *Open statistical issues in particle physics*. In: *arXiv e-prints*, arXiv:0811.1663 (Nov. 2008), arXiv:0811.1663. arXiv: 0811.1663 [stat.AP].

[54] G. Cowan et al. *Asymptotic formulae for likelihood-based tests of new physics*. In: *Eur. Phys. J.* C71 (2011). [Erratum: Eur. Phys. J.C73,2501(2013)], p. 1554. DOI: 10.1140/epjc/s10052-011-1554-0, 10.1140/epjc/s10052-013-2501-z. arXiv: 1007.1727 [physics.data-an].

[55] E. Mobs. *The CERN accelerator complex - August 2018. Complexe des accélérateurs du CERN - Août 2018*. In: (Aug. 2018). General Photo. URL: https://cds.cern.ch/record/2636343.

[56] CERN. *The accelerator complex*. 2018. URL: https://home.cern/about/accelerators (visited on 10/05/2018).

[57] CERN. *Timeline: The history of CERN - The Large Hadron Collider*. 2018. URL: https://timeline.web.cern.ch/timelines/The-Large-Hadron-Collider (visited on 10/05/2018).

[58] The Atlas Collaboration. *Public Luminosity Results Run2*. 2018. URL: https://twiki.cern.ch/twiki/bin/view/AtlasPublic/LuminosityPublicResultsRun2 (visited on 01/02/2019).

[59] M. Capeans et al. *ATLAS Insertable B-Layer Technical Design Report*. Tech. rep. CERN-LHCC-2010-013. ATLAS-TDR-19. Sept. 2010. URL: https://cds.cern.ch/record/1291633.

[60] The Atlas Collaboration. *The* Atlas *Experiment at the CERN Large Hadron Collider*. In: *JINST* 3 (2008), S08003. DOI: 10.1088/1748-0221/3/08/S08003.

[61] The Atlas Collaboration. *Performance of the ATLAS Transition Radiation Tracker in Run 1 of the LHC: tracker properties*. In: *JINST* 12.05 (2017), P05002. DOI: 10.1088/1748-0221/12/05/P05002. arXiv: 1702.06473 [hep-ex].

[62] K. Potamianos. *The upgraded Pixel detector and the commissioning of the Inner Detector tracking of the ATLAS experiment for Run-2 at the Large Hadron Collider*. Tech. rep. ATL-PHYS-PROC-2016-104. 15 pages, EPS-HEP 2015 Proceedings. Geneva: CERN, Aug. 2016. URL: https://cds.cern.ch/record/2209070.

[63] A. Ruiz-Martinez et al. *The Run-2 ATLAS Trigger System*. Tech. rep. ATL-DAQ-PROC-2016-003. Geneva: CERN, Feb. 2016. URL: https://cds.cern.ch/record/2133909.

[64] A. Buckley et al. *General-purpose event generators for LHC physics*. In: *Phys. Rept.* 504 (2011), pp. 145–233. DOI: 10.1016/j.physrep.2011.03.005. arXiv: 1101.2599 [hep-ph].

[65] T. Gleisberg et al. *Event generation with SHERPA 1.1*. In: *JHEP* 02 (2009), p. 007. DOI: 10.1088/1126-6708/2009/02/007. arXiv: 0811.4622 [hep-ph].

[66] Z. M. and. *Simulation of Pile-up in the ATLAS Experiment*. In: *Journal of Physics: Conference Series* 513.2 (June 2014), p. 022024. DOI: 10.1088/1742-6596/513/2/022024. URL: https://doi.org/10.1088%2F1742-6596%2F513%2F2%2F022024.

[67] V. V. Sudakov. *Vertex parts at very high-energies in quantum electrodynamics*. In: *Sov. Phys. JETP* 3 (1956). [Zh. Eksp. Teor. Fiz.30,87(1956)], pp. 65–71.

[68] S. Catani et al. *QCD matrix elements + parton showers*. In: *JHEP* 11 (2001), p. 063. DOI: 10.1088/1126-6708/2001/11/063. arXiv: hep-ph/0109231 [hep-ph].

[69] L. Lonnblad. *Correcting the color dipole cascade model with fixed order matrix elements.* In: *JHEP* 05 (2002), p. 046. DOI: 10.1088/1126-6708/2002/05/046. arXiv: hep-ph/0112284 [hep-ph].

[70] J. Alwall et al. *The automated computation of tree-level and next-to-leading order differential cross sections, and their matching to parton shower simulations.* In: *JHEP* 07 (2014), p. 079. DOI: 10.1007/JHEP07(2014)079. arXiv: 1405.0301 [hep-ph].

[71] N. Lavesson et al. *Merging parton showers and matrix elements: Back to basics.* In: *JHEP* 04 (2008), p. 085. DOI: 10.1088/1126-6708/2008/04/085. arXiv: 0712.2966 [hep-ph].

[72] S. Frixione et al. *Matching NLO QCD computations with Parton Shower simulations: the POWHEG method.* In: *JHEP* 11 (2007), p. 070. DOI: 10.1088/1126-6708/2007/11/070. arXiv: 0709.2092 [hep-ph].

[73] P. Nason. *A New method for combining NLO QCD with shower Monte Carlo algorithms.* In: *JHEP* 11 (2004), p. 040. DOI: 10.1088/1126-6708/2004/11/040. arXiv: hep-ph/0409146 [hep-ph].

[74] S. Alioli et al. *A general framework for implementing NLO calculations in shower Monte Carlo programs: the POWHEG BOX.* In: *Journal of High Energy Physics* 2010.6 (June 2010), p. 43. ISSN: 1029-8479. DOI: 10.1007/JHEP06(2010)043. URL: %7Bhttps://doi.org/10.1007/JHEP06(2010)043%7D.

[75] T. Melia et al. *W^+W^+ plus dijet production in the POWHEGBOX.* In: *Eur. Phys. J.* C71 (2011), p. 1670. DOI: 10.1140/epjc/s10052-011-1670-x. arXiv: 1102.4846 [hep-ph].

[76] T. Sjöstrand et al. *An Introduction to PYTHIA 8.2.* In: *Comput. Phys. Commun.* 191 (2015), pp. 159–177. DOI: 10.1016/j.cpc.2015.01.024. arXiv: 1410.3012 [hep-ph].

[77] M. Bahr et al. *Herwig++ Physics and Manual.* In: *Eur. Phys. J.* C58 (2008), pp. 639–707. DOI: 10.1140/epjc/s10052-008-0798-9. arXiv: 0803.0883 [hep-ph].

[78] J. Bellm et al. *Herwig 7.0/Herwig++ 3.0 release note.* In: *Eur. Phys. J.* C76.4 (2016), p. 196. DOI: 10.1140/epjc/s10052-016-4018-8. arXiv: 1512.01178 [hep-ph].

[79] The ATLAS Collaboration. *The ATLAS Simulation Infrastructure.* In: *The European Physical Journal C* 70.3 (Dec. 2010), pp. 823–874. DOI: 10.1140/epjc/s10052-010-1429-9. URL: https://doi.org/10.1140/epjc/s10052-010-1429-9.

[80] S. Agostinelli et al. *Geant4—a simulation toolkit.* In: *Nuclear Instruments and Methods in Physics Research Section A: Accelerators, Spectrometers, Detectors and Associated Equipment* 506.3 (2003), pp. 250–303. ISSN: 0168-9002. DOI: {https://doi.org/10.1016/S0168-9002(03)01368-8}. URL: %7Bhttp://www.sciencedirect.com/science/article/pii/S0168900203013688%7D.

[81] C. Gumpert et al. *Measurement of Electroweak Gauge Boson Scattering in the Channel $pp \to W^\pm W^\pm jj$ with the ATLAS Detector at the Large Hadron Collider.* Presented 27 Feb 2015. Dec. 2014. URL: https://cds.cern.ch/record/2003240.

[82] M. Aaboud et al. *Search for anomalous electroweak production of WW/WZ in association with a high-mass dijet system in pp collisions at $\sqrt{s} = 8$ TeV with the ATLAS detector.* In: *Phys. Rev.* D95.3 (2017), p. 032001. DOI: 10.1103/PhysRevD.95.032001. arXiv: 1609.05122 [hep-ex].

[83] M. Aaboud et al. *Observation of electroweak $W^\pm Z$ boson pair production in association with two jets in pp collisions at $\sqrt{s} = 13$ TeV with the ATLAS detector.* In: *Submitted to: Phys. Lett.* (2018). arXiv: 1812.09740 [hep-ex].

[84] A. M. Sirunyan et al. *Measurement of vector boson scattering and constraints on anomalous quartic couplings from events with four leptons and two jets in proton–proton collisions at $\sqrt{s} = 13$ TeV.* In: *Phys. Lett.* B774 (2017), pp. 682–705. DOI: 10.1016/j.physletb.2017.10.020. arXiv: 1708.02812 [hep-ex].

[85] M. Aaboud et al. *Search for heavy resonances decaying into WW in the $e\nu\mu\nu$ final state in pp collisions at $\sqrt{s} = 13$ TeV with the ATLAS detector.* In: *Eur. Phys. J.* C78.1 (2018), p. 24. DOI: 10.1140/epjc/s10052-017-5491-4. arXiv: 1710.01123 [hep-ex].

[86] V. Khachatryan et al. *Evidence for exclusive $\gamma\gamma \to W^+W^-$ production and constraints on anomalous quartic gauge couplings in pp collisions at $\sqrt{s} = 7$ and 8 TeV.* In: *JHEP* 08 (2016), p. 119. DOI: 10.1007/JHEP08(2016)119. arXiv: 1604.04464 [hep-ex].

[87] M. Aaboud et al. *Measurement of exclusive $\gamma\gamma \to W^+W^-$ production and search for exclusive Higgs boson production in pp collisions at $\sqrt{s} = 8$ TeV using the ATLAS detector.* In: *Phys. Rev.* D94.3 (2016), p. 032011. DOI: 10.1103/PhysRevD.94.032011. arXiv: 1607.03745 [hep-ex].

[88] F. Speiser. *Study of Opposite Sign WWjj Production using Boosted Decision Trees with the ATLAS Detector at the LHC.* MA thesis. Dresden, Tech. U., 2014-10-28.

[89] M. Aaboud et al. *Measurement of $W^\pm W^\pm$ vector-boson scattering and limits on anomalous quartic gauge couplings with the ATLAS detector.* In: *Phys. Rev.* D96.1 (2017), p. 012007. DOI: 10.1103/PhysRevD.96.012007. arXiv: 1611.02428 [hep-ex].

[90] V. Khachatryan et al. *Study of vector boson scattering and search for new physics in events with two same-sign leptons and two jets.* In: *Phys. Rev. Lett.* 114.5 (2015), p. 051801. DOI: 10.1103/PhysRevLett.114.051801. arXiv: 1410.6315 [hep-ex].

[91] A. M. Sirunyan et al. *Observation of electroweak production of same-sign W boson pairs in the two jet and two same-sign lepton final state in proton-proton collisions at $\sqrt{s} = 13$ TeV.* In: *Phys. Rev. Lett.* 120.8 (2018), p. 081801. DOI: 10.1103/PhysRevLett.120.081801. arXiv: 1709.05822 [hep-ex].

[92] J. Baglio et al. *VBFNLO: A Parton Level Monte Carlo for Processes with Electroweak Bosons – Manual for Version 2.7.0.* In: (2011). arXiv: 1107.4038 [hep-ph].

[93] J. Baglio et al. *Release Note - VBFNLO 2.7.0.* In: (2014). arXiv: 1404.3940 [hep-ph].

[94] K. Arnold et al. *VBFNLO: A Parton level Monte Carlo for processes with electroweak bosons.* In: *Comput. Phys. Commun.* 180 (2009), pp. 1661–1670. DOI: 10.1016/j.cpc.2009.03.006. arXiv: 0811.4559 [hep-ph].

[95] A. Alboteanu et al. *Resonances and Unitarity in Weak Boson Scattering at the LHC.* In: *JHEP* 11 (2008), p. 010. DOI: 10.1088/1126-6708/2008/11/010. arXiv: 0806.4145 [hep-ph].

[96] D. L. Rainwater et al. *Probing color singlet exchange in Z + two jet events at the CERN LHC.* In: *Phys. Rev.* D54 (1996), pp. 6680–6689. DOI: 10.1103/PhysRevD.54.6680. arXiv: hep-ph/9605444 [hep-ph].

[97] S. Todt et al. *Support note for measurement of electroweak $W^\pm W^\pm jj$ production at $\sqrt{s} =$ 13 TeV.* Tech. rep. ATL-COM-PHYS-2018-252. Geneva: CERN, Mar. 2018. URL: https://cds.cern.ch/record/2309552.

[98] R. D. Ball et al. *Parton distributions for the LHC Run II.* In: *JHEP* 04 (2015), p. 040. DOI: 10.1007/JHEP04(2015)040. arXiv: 1410.8849 [hep-ph].

[99] *Modelling of the vector boson scattering process $pp \to W^\pm W^\pm jj$ in Monte Carlo generators in ATLAS.* Tech. rep. ATL-PHYS-PUB-2019-004. Geneva: CERN, Jan. 2019. URL: https://cds.cern.ch/record/2655303.

[100] A. Ballestrero et al. *Precise predictions for same-sign W-boson scattering at the LHC.* In: *Eur. Phys. J.* C78.8 (2018), p. 671. DOI: 10.1140/epjc/s10052-018-6136-y. arXiv: 1803.07943 [hep-ph].

[101] Stefan Hoeche. *Status of Sherpa event generator.* Presentation at the Multi-Boson Interactions workshop, University of Michigan. 2018.

[102] M. Mittal et al. *Support note for measurement of electroweak $W^\pm W^\pm jj$ production at $\sqrt{s}$ = 13 TeV*. Tech. rep. ATL-COM-PHYS-2018-252. Geneva: CERN, Mar. 2018. URL: https://cds.cern.ch/record/2309552.

[103] B. Biedermann et al. *Complete NLO corrections to W^+W^+ scattering and its irreducible background at the LHC*. In: *JHEP* 10 (2017), p. 124. DOI: 10.1007/JHEP10(2017)124. arXiv: 1708.00268 [hep-ph].

[104] T. Herrmann et al. *Study of Different Unfolding Methods of Kinematic Distributions of the $WZ \rightarrow WZ$ Scattering with Data and Simulations of the ATLAS Detector at the LHC*. Presented 2017. Mar. 2017. URL: https://cds.cern.ch/record/2267776.

[105] C. Bittrich et al. *Support note for measurement of electroweak $W^\pm W^\pm jj$ production at $\sqrt{s}$ = 13 TeV*. Tech. rep. ATL-COM-PHYS-2018-252. Geneva: CERN, Mar. 2018. URL: https://cds.cern.ch/record/2309552.

[106] The ATLAS Collaboration. *Tracking CP Pre-Recommendations for 2017 Winter Conferences, 2015+2016/20.7*. 2018. URL: https://twiki.cern.ch/twiki/bin/view/AtlasProtected/TrackingCPMoriond2017#Vertexing (visited on 10/26/2018).

[107] W. Buttinger. *Using Event Weights to account for differences in Instantaneous Luminosity and Trigger Prescale in Monte Carlo and Data*. Tech. rep. ATL-COM-SOFT-2015-119. Geneva: CERN, May 2015. URL: https://cds.cern.ch/record/2014726.

[108] The Atlas Collaboration. *Extended Pileup Reweighting MC15 - Recommended settings*. 2017. URL: https://twiki.cern.ch/twiki/bin/view/AtlasProtected/ExtendedPileupReweightingMC15#Recommended_settings_for_version (visited on 01/02/2019).

[109] S. M. Mazza. *Search for new physics in the diphoton channel at the ATLAS experiment at the LHC*. PhD thesis. Milan U., 2017. URL: http://www.infn.it/thesis/thesis_dettaglio.php?tid=11559.

[110] The ATLAS Collaboration. *Isolation Working Points used for Release 20.7 Studies*. 2018. URL: https://twiki.cern.ch/twiki/bin/view/AtlasProtected/IsolationSelectionTool#WPs%20used%20for%20Rel20.7%20studies%20and (visited on 11/16/2018).

[111] B. Pok Ho Tam. *Primary Vertex Reconstruction in ATLAS Experiment*. 2014. URL: http://www.phy.cuhk.edu.hk/sure/comments_2014/tph_pre.pdf.

[112] *Electron and photon energy calibration with the ATLAS detector using data collected in 2015 at* $\sqrt{s}$ = 13 TeV. Tech. rep. ATL-PHYS-PUB-2016-015. Geneva: CERN, Aug. 2016. URL: https://cds.cern.ch/record/2203514.

[113] G. Aad et al. *Electron and photon energy calibration with the ATLAS detector using LHC Run 1 data*. In: *Eur. Phys. J.* C74.10 (2014), p. 3071. DOI: 10.1140/epjc/s10052-014-3071-4. arXiv: 1407.5063 [hep-ex].

[114] *Electron efficiency measurements with the ATLAS detector using the 2015 LHC proton-proton collision data*. Tech. rep. ATLAS-CONF-2016-024. Geneva: CERN, June 2016. URL: http://cds.cern.ch/record/2157687.

[115] G. Tarna. *Electron identification with the ATLAS detector*. Tech. rep. ATL-PHYS-PROC-2017-173. Geneva: CERN, Sept. 2017. URL: https://cds.cern.ch/record/2286383.

[116] G. Aad et al. *Muon reconstruction performance of the ATLAS detector in proton–proton collision data at $\sqrt{s}$ =13 TeV*. In: *Eur. Phys. J.* C76.5 (2016), p. 292. DOI: 10.1140/epjc/s10052-016-4120-y. arXiv: 1603.05598 [hep-ex].

[117] M. Cacciari et al. *The anti-k_t jet clustering algorithm*. In: *JHEP* 04 (2008), p. 063. DOI: 10.1088/1126-6708/2008/04/063. arXiv: 0802.1189 [hep-ph].

[118] M. Aaboud et al. *Jet energy scale measurements and their systematic uncertainties in proton-proton collisions at $\sqrt{s} = 13$ TeV with the ATLAS detector*. In: *Phys. Rev.* D96.7 (2017), p. 072002. DOI: 10.1103/PhysRevD.96.072002. arXiv: 1703.09665 [hep-ex].

[119] *Tagging and suppression of pileup jets with the ATLAS detector*. Tech. rep. ATLAS-CONF-2014-018. Geneva: CERN, May 2014. URL: https://cds.cern.ch/record/1700870.

[120] M. Aaboud et al. *Identification and rejection of pile-up jets at high pseudorapidity with the ATLAS detector*. In: *Eur. Phys. J.* C77.9 (2017). [Erratum: Eur. Phys. J.C77,no.10,712(2017)], p. 580. DOI: 10.1140/epjc/s10052-017-5081-5,10.1140/epjc/s10052-017-5245-3. arXiv: 1705.02211 [hep-ex].

[121] G. Aad et al. *Performance of pile-up mitigation techniques for jets in pp collisions at $\sqrt{s} = 8$ TeV using the ATLAS detector*. In: *Eur. Phys. J.* C76.11 (2016), p. 581. DOI: 10.1140/epjc/s10052-016-4395-z. arXiv: 1510.03823 [hep-ex].

[122] M. Cacciari et al. *Pileup subtraction using jet areas*. In: *Phys. Lett.* B659 (2008), pp. 119–126. DOI: 10.1016/j.physletb.2007.09.077. arXiv: 0707.1378 [hep-ph].

[123] M. Cacciari et al. *The Catchment Area of Jets*. In: *JHEP* 04 (2008), p. 005. DOI: 10.1088/1126-6708/2008/04/005. arXiv: 0802.1188 [hep-ph].

[124] S. Catani et al. *Longitudinally-invariant $k_\perp$-clustering algorithms for hadron-hadron collisions*. In: *Nuclear Physics B* 406.1 (1993), pp. 187–224. ISSN: 0550-3213. DOI: https://doi.org/10.1016/0550-3213(93)90166-M. URL: http://www.sciencedirect.com/science/article/pii/055032139390166M.

[125] A. Hoecker et al. *TMVA: Toolkit for Multivariate Data Analysis*. In: *PoS* ACAT (2007), p. 040. arXiv: physics/0703039.

[126] The ATLAS Collaboration. *JVT Public Plots for ICHEP 2016*. 2016. URL: https://atlas.web.cern.ch/Atlas/GROUPS/PHYSICS/PLOTS/JETM-2016-011/ (visited on 01/04/2019).

[127] Atlas Collaboration. *Jet energy measurement and its systematic uncertainty in proton–proton collisions at $\sqrt{s} = 7$ TeV with the ATLAS detector*. In: *The European Physical Journal C* 75.1 (Jan. 2015), p. 17. ISSN: 1434-6052. DOI: 10.1140/epjc/s10052-014-3190-y. URL: https://doi.org/10.1140/epjc/s10052-014-3190-y.

[128] G. Aad et al. *Jet energy measurement with the ATLAS detector in proton-proton collisions at $\sqrt{s} = 7$ TeV*. In: *Eur. Phys. J.* C73.3 (2013), p. 2304. DOI: 10.1140/epjc/s10052-013-2304-2. arXiv: 1112.6426 [hep-ex].

[129] *Data-driven determination of the energy scale and resolution of jets reconstructed in the ATLAS calorimeters using dijet and multijet events at $\sqrt{s} = 8$ TeV*. Tech. rep. ATLAS-CONF-2015-017. Geneva: CERN, Apr. 2015. URL: http://cds.cern.ch/record/2008678.

[130] *Optimisation of the ATLAS b-tagging performance for the 2016 LHC Run*. Tech. rep. ATL-PHYS-PUB-2016-012. Geneva: CERN, June 2016. URL: https://cds.cern.ch/record/2160731.

[131] G. Gonella. *Observation and Measurement of the Electroweak $W^\pm W^\pm$ Production in pp Collisions at $\sqrt{s} = 13$ TeV with the ATLAS Detector*. PhD thesis. Albert-Ludwigs-Universität Freiburg, 2019. Unpublished doctoral thesis.

[132] M. Aaboud et al. *Performance of missing transverse momentum reconstruction with the ATLAS detector using proton-proton collisions at $\sqrt{s} = 13$ TeV*. In: *Eur. Phys. J.* C78.11 (2018), p. 903. DOI: 10.1140/epjc/s10052-018-6288-9. arXiv: 1802.08168 [hep-ex].

[133] D. Adams et al. *Recommendations of the Physics Objects and Analysis Harmonisation Study Groups 2014*. Tech. rep. ATL-PHYS-INT-2014-018. Geneva: CERN, July 2014. URL: https://cds.cern.ch/record/1743654.

[134] W. Buttinger. *Overlap Removal Working Points.* 2016. URL: https://indico.cern.ch/event/587852/contributions/2369263/attachments/1371264/2079878/OR_NotesNov2016.pdf.

[135] H. Reisin Carretero et al. *Ghost association of tracks performance plots for BOOST2012.* Tech. rep. ATL-COM-GEN-2012-013. Geneva: CERN, July 2012. URL: https://cds.cern.ch/record/1461321.

[136] G. Aad et al. *Evidence for Electroweak Production of $W^{\pm}W^{\pm}jj$ in pp Collisions at $\sqrt{s} = 8$ TeV with the ATLAS Detector.* In: *Phys. Rev. Lett.* 113.14 (2014), p. 141803. DOI: 10.1103/PhysRevLett.113.141803. arXiv: 1405.6241 [hep-ex].

[137] W. Di Clemente. *Measurement of electroweak production of same-sign W-boson pairs with ATLAS.* PhD thesis. University of Pennsylvania, 2020. Unpublished doctoral thesis.

[138] H. Bethe et al. *On the Stopping of Fast Particles and on the Creation of Positive Electrons.* In: *Proceedings of the Royal Society of London Series A* 146 (Aug. 1934), pp. 83–112. DOI: 10.1098/rspa.1934.0140.

[139] J. Almond et al. *Search for heavy neutrino, W_R and Z_R gauge bosons in events with two high-P_T leptons and jets with the ATLAS detector in pp collisions at $\sqrt{s} = 8$ TeV.* Tech. rep. ATL-COM-PHYS-2013-810. This is the supporting note for EXOT-2012-24, which is now published as JHEP07 (2015) 162. Geneva: CERN, June 2013. URL: https://cds.cern.ch/record/1555805.

[140] J.-F. Arguin et al. *Support Note for Electron ID: charge mis-identification.* Tech. rep. ATL-COM-PHYS-2017-1014. Geneva: CERN, July 2017. URL: https://cds.cern.ch/record/2273365.

[141] P. Laycock et al. *ATLAS data preparation in run 2.* In: *Journal of Physics: Conference Series* 898.4 (2017), p. 042050. URL: http://stacks.iop.org/1742-6596/898/i=4/a=042050.

[142] The ATLAS Collaboration. *How To Clean Jets 2016.* 2019. URL: https://twiki.cern.ch/twiki/bin/view/AtlasProtected/HowToCleanJets2016#IsBadBatMan_Event_Flag_and_EMEC (visited on 02/28/2019).

[143] The ATLAS Collaboration. *EGamma Identification Run2.* 2019. URL: https://twiki.cern.ch/twiki/bin/view/AtlasProtected/EGammaIdentificationRun2#Bad_Electron_Photon_Cluster (visited on 01/05/2019).

[144] *Selection of jets produced in 13TeV proton-proton collisions with the ATLAS detector.* Tech. rep. ATLAS-CONF-2015-029. Geneva: CERN, July 2015. URL: https://cds.cern.ch/record/2037702.

[145] C. Mwewa. *Observation of the electroweak production of $W^{\pm}W^{\pm}jj$ in pp collisions at $\sqrt{s} = 13$ TeV with the ATLAS detector.* University of Cape Town, 2019. Unpublished doctoral thesis.

[146] E. Gross. *Practical Statistics for High Energy Physics.* In: *CERN Yellow Reports: School Proceedings* 4 (2017), p. 165. ISSN: 2519-805X. URL: https://e-publishing.cern.ch/index.php/CYRSP/article/view/303.

[147] S. Dulat et al. *New parton distribution functions from a global analysis of quantum chromodynamics.* In: *Phys. Rev.* D93.3 (2016), p. 033006. DOI: 10.1103/PhysRevD.93.033006. arXiv: 1506.07443 [hep-ph].

[148] L. A. Harland-Lang et al. *Parton distributions in the LHC era: MMHT 2014 PDFs.* In: *Eur. Phys. J.* C75.5 (2015), p. 204. DOI: 10.1140/epjc/s10052-015-3397-6. arXiv: 1412.3989 [hep-ph].

[149] M. Aaboud et al. *Luminosity determination in pp collisions at $\sqrt{s} = 8$ TeV using the ATLAS detector at the LHC.* In: *Eur. Phys. J.* C76.12 (2016), p. 653. DOI: 10.1140/epjc/s10052-016-4466-1. arXiv: 1608.03953 [hep-ex].

[150] G. Avoni et al. *The new LUCID-2 detector for luminosity measurement and monitoring in ATLAS*. In: *JINST* 13.07 (2018), P07017. DOI: 10.1088/1748-0221/13/07/P07017.

[151] S. van der Meer. *Calibration of the Effective Beam Height in the ISR*. In: (1968).

[152] A. Falkowski et al. *Global constraints on anomalous triple gauge couplings in effective field theory approach*. In: *Phys. Rev. Lett.* 116.1 (2016), p. 011801. DOI: 10.1103/PhysRevLett.116.011801. arXiv: 1508.00581 [hep-ph].

A Additional Material on Charge Mis-ID Estimation

A.1 Validaton of Anti-ID Charge Mis-ID Estimate

The ID-AntiID charge mis-ID procedure, as explained in Section 6.2.2.4, is validated in a separate region, which is designed to be especially pure charge mis-ID processes. The definition of the ID-AntiID validation region is given in Table A.1, and follows the definition of the region, where the charge mis-ID estimate is derived closely, with and additional truth level requirement to reject non-prompt contributions.

Criterion	Value	Reference
Preselection	Nominal	Table 7.1
Channel	ee	
Charge	same-charge	
Lead e object selection	Analysis level	Table 5.1
Sub-lead e object selection	Anti-ID	Table 5.1
Truth selection	requiring prompt leptons	
$m_{\ell\ell}$	Nominal	Table 7.2
N_{jet}	< 2	
$m_{\ell\ell}$	$80\,\mathrm{GeV} < m_{\ell\ell} < 100\,\mathrm{GeV}$	
$E_{\mathrm{T}}^{\mathrm{miss}}$	$> 30\,\mathrm{GeV}$	
$N_{b-\mathrm{jet}}$	$= 0$	

Table A.1: Definition of Nominal + anti-ID validation region, used for validating data-driven charge mis-ID estimate in the ID-AntiID region.

Figure A.1 shows kinematic distributions in this validation region. The charge mis-ID estimate is in good agreement with the observed data. An disagreement of 10 % is observed in the integral, which is assigned as a systematic uncertainty.

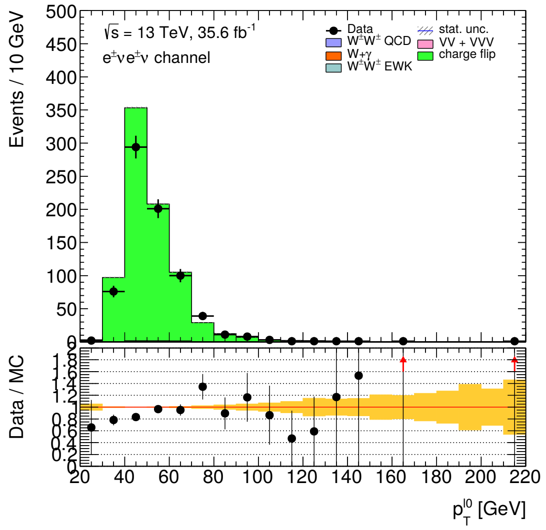

(a) p_{T}

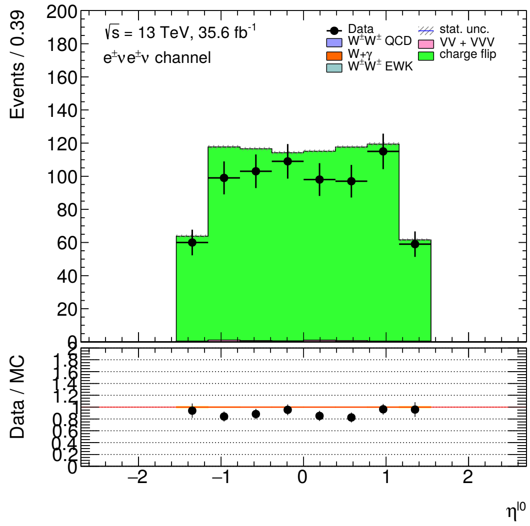

(b) η

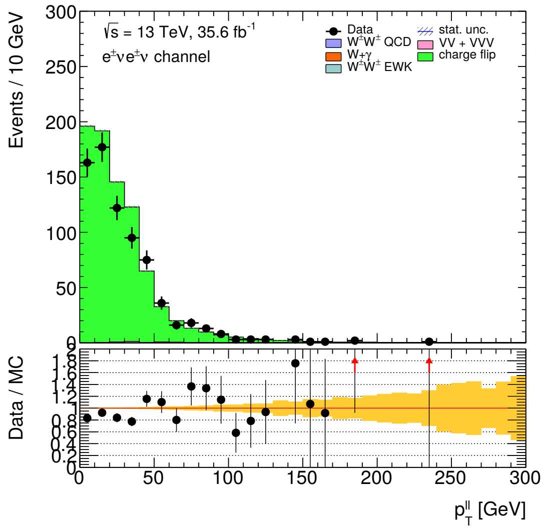

(c) $p_{\mathrm{T}}^{\ell\ell}$

Figure A.1: Kinematic distributions in the ID-AntiID validation region to check the modeling of the estimation procedure for the ee channel [131].

A.2 Anti-ID Charge Mis-ID Rates

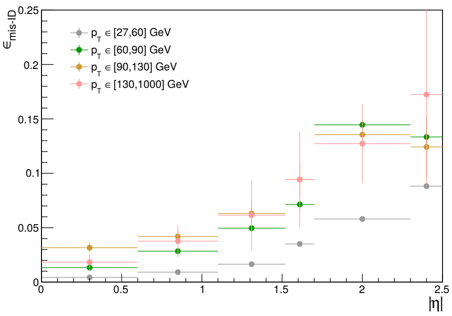

(a) $\varepsilon(|\eta|)$ for anti-ID e, using charge

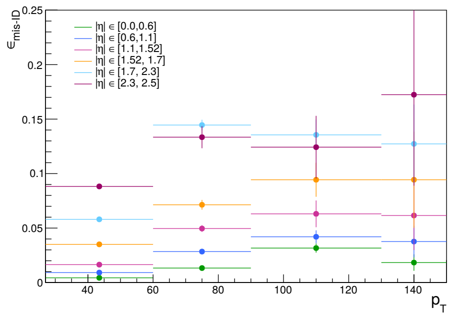

(b) $\varepsilon(p_{\mathrm{T}})$ for anti-ID e, using charge

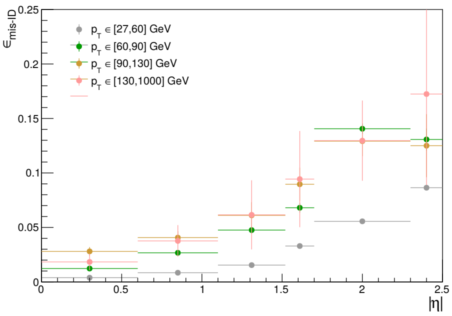

(c) $\varepsilon(p_{\mathrm{T}})$ for anti-ID e, using truth information

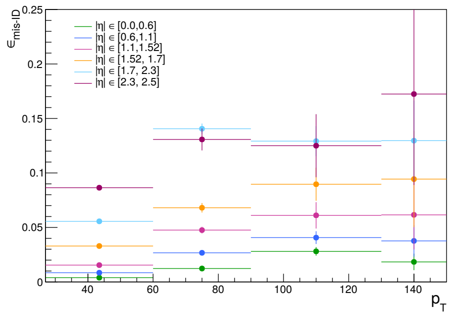

(d) $\varepsilon(|\eta|)$ for anti-ID e, using truth information

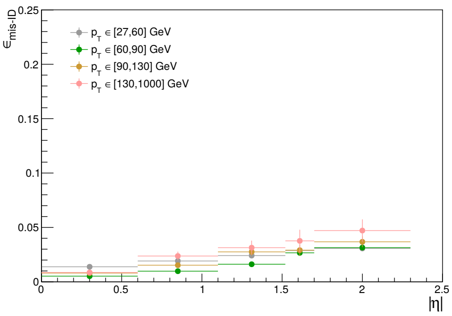

(e) $\varepsilon(|\eta|)$ for nominal e, using truth information

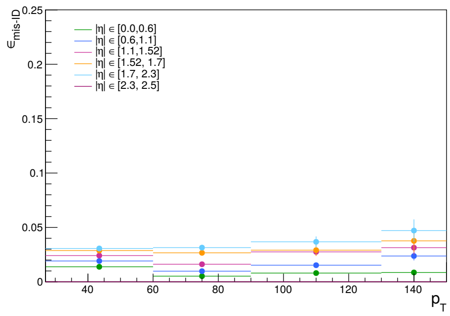

(f) $\varepsilon(p_{\mathrm{T}})$ for nominal e, using truth information

Figure A.2: Charge Mis-ID rates are retrieved on simulated events under the assumption, that the anti-ID electron has the wrong reconstructed charge and are shown as a function of $|\eta|$ (a) and p_{T} (b). As a validation of this assumption, charge mis-ID rates are also retrieved by exploiting the truth information in simulation for nominal (c and d) and anti-ID electrons (d and f). The rates for tag (nominal) electrons are negligible compared to the ones for probe electrons (anti-ID) [131].

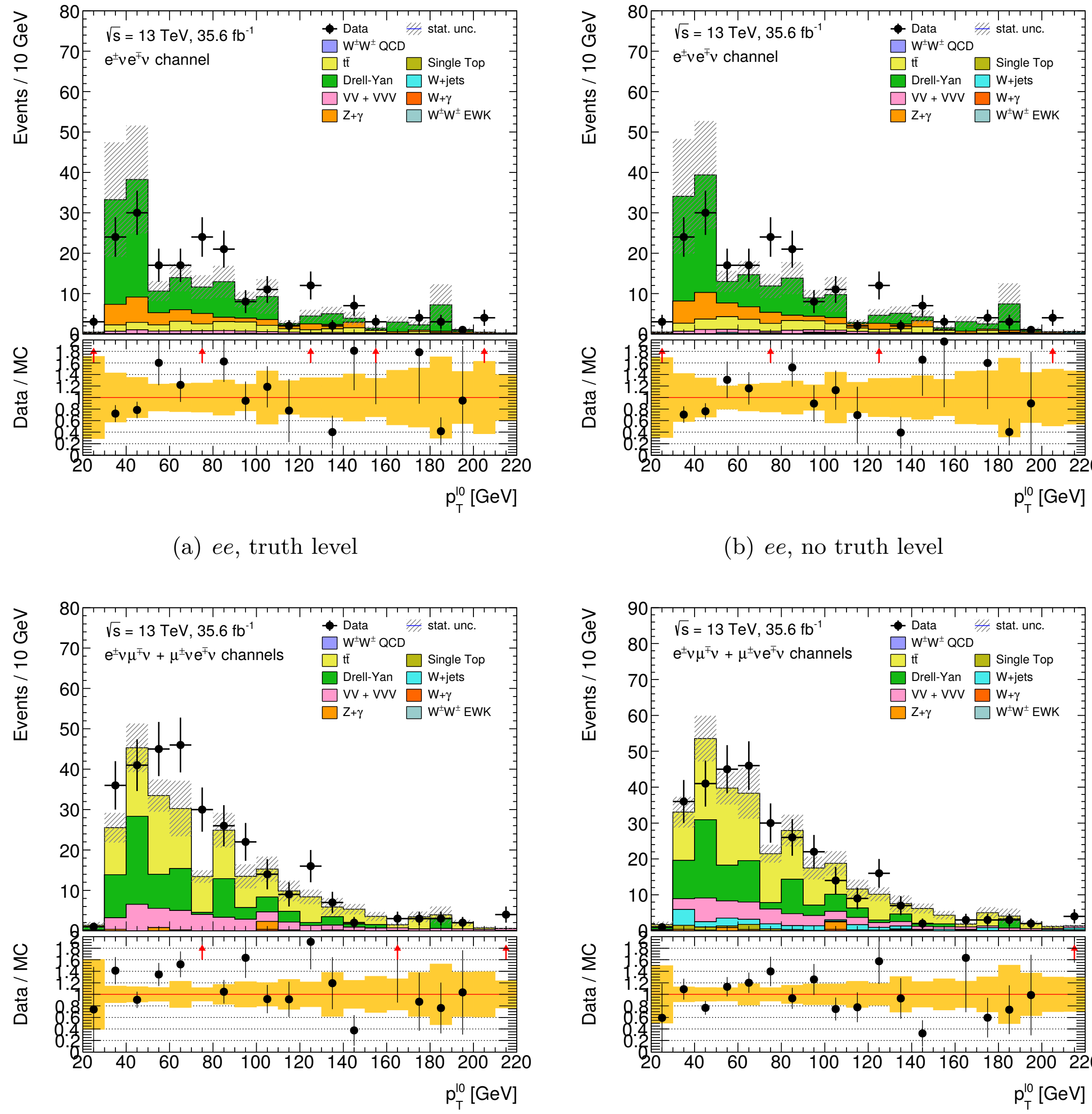

(a) ee, truth level

(b) ee, no truth level

(c) $e\mu/\mu e$, truth level

(d) $e\mu/\mu e$, no truth level

Figure A.3: Leading lepton p_{T} distributions in opposite-charge Nominal + anti-ID region in the ee (top) and $e\mu/\mu e$ channel (bottom). Events are select with (left) and without (right) requiring prompt leptons on truth level [131].

B Additional Material on Systematic Uncertainties

B.1 Complete List of Experimental Uncertainties

- Charge Mis-ID Energy Corr., Scale Fac.
- Non-Prompt e Stat., e Sys., μ Stat., μ Sys.
- e/γ RESOLUTION ALL
- e/γ Scale ALLCORR, E4SCINTILLATOR, LARCALIB EXTRA2015PRE
- e/γ Scale LARTEMPERATURE EXTRA2015PRE, EXTRA2016PRE
- Electron Eff. ID CorrUncertainty(NP0-NP14)
- Electron Eff. ID SIMPLIFIED UncorrUncertainty(NP0-NP15)
- Electron Eff. Iso TOTAL 1NPCOR PLUS UNCOR
- Electron Eff. Reco TOTAL 1NPCOR PLUS UNCOR
- Electron Eff. Trigger TOTAL 1NPCOR PLUS UNCOR
- Muon Eff. Stat., Sys.
- Muon Eff. Stat. low p_{T}, Sys. low p_{T}
- Muon Eff. TrigStatUncertainty, TrigSystUncertainty
- Muon ID, MS, Scale
- Muon Iso Stat., Sys.
- Muon TTVA Stat., Sys.
- Jet BJES Response
- Jet EffectiveNP 1-7, 8restTerm
- Jet EtaIntercalibration Modelling, Non-Closure, Total Stat.
- Jet Flavor Composition, Response
- Jet Energy Resolution
- Jet PunchThrough MC15
- Jet SingleParticle HighPt
- Jet JVT Efficiency
- Flavor Tag Eff. Eigen B 0-2
- Flavor Tag Eff. Eigen C 0-2
- Flavor Tag Eff. Eigen Light 0-4
- Flavor Tag Eff. extrapolation (from charm)
- Jet Pile-up OffsetMu, OffsetNPV, p_{T} Term, RhoTopology

- Pile-up Reweight. data SF
- MET Soft Trk. Resolution, ResoPerp, Scale
- Conversion Model Vgamma

B.2 Complete List of Theory Uncertainties

- $W^{\pm}Z$ α_{s}, PDF, Scale, Shower
- $W^{\pm}W^{\pm}jj$-QCD α_{s}, PDF, Scale, Shower
- $W^{\pm}W^{\pm}jj$-Ew α_{s}, PDF, Scale, Shower
- $W^{\pm}W^{\pm}jj$-Ew Ew Correction
- $W^{\pm}W^{\pm}jj$-Ew-$W^{\pm}W^{\pm}jj$-QCD Interference
- $W^{\pm}\gamma$, $Z\gamma$, ZZ, top, and tri-boson cross section

B.3 Relative Effect of Nuisance Parameters

B.3.1 e^+e^+ Channel, Signal Region

Nuisance Parameter	Relativ Effect on Sample [%]									
	$W^\pm W^\pm jj$-Ew	top	tri-boson	$Z\gamma$	$W^\pm\gamma$	ZZ	$W^\pm W^\pm jj$-QCD	Charge Mis-ID	Non-Prompt	$W^\pm Z$
Jet Pile-up OffsetMu	0.29	1.82	0.00	0.00	0.00	11.65	1.01	0.00	0.00	0.74
e/γ Scale ALLCORR	0.12	1.56	0.01	0.00	0.00	1.15	0.70	0.00	0.00	1.14
Jet EffectiveNP 3	0.30	1.86	0.01	0.00	0.00	0.00	0.59	0.00	0.00	0.27
$W^\pm W^\pm$ EW Scale	2.28	0.00	0.00	0.00	0.00	0.00	0.00	0.00	0.00	0.00
Flavor Tag Eff. Eigen C 1	0.21	0.43	0.30	0.00	0.00	0.23	0.27	0.00	0.00	0.23
Jet PunchThrough MC15	0.06	0.00	0.00	0.00	0.00	0.00	0.16	0.00	0.00	0.00
Jet Pile-up RhoTopology	0.66	8.50	5.14	0.01	0.01	1.46	0.83	0.00	0.00	3.28
Jet EffectiveNP 8restTerm	0.16	0.05	0.00	0.00	0.00	0.00	0.22	0.00	0.00	0.04
Interference	2.43	0.00	0.00	0.00	0.00	0.00	0.00	0.00	0.00	0.00
e/γ Scale LARTEMPERATURE EXTRA2015PRE	0.00	0.00	0.00	0.00	0.00	0.00	0.00	0.00	0.00	0.50
Jet BJES Response	0.02	0.10	0.00	0.00	0.00	0.00	0.00	0.00	0.00	0.00
Electron Eff. ID SIMPLIFIED UncorrUncertaintyNP8	0.73	0.68	0.82	0.70	0.59	0.71	0.76	0.00	0.00	0.60
Electron Eff. ID SIMPLIFIED UncorrUncertaintyNP5	0.03	0.04	0.02	0.00	0.00	0.06	0.04	0.00	0.00	0.05
Electron Eff. ID SIMPLIFIED UncorrUncertaintyNP7	0.10	0.06	0.08	0.00	0.32	0.13	0.09	0.00	0.00	0.09
Electron Eff. ID SIMPLIFIED UncorrUncertaintyNP6	0.13	0.25	0.11	0.18	0.00	0.13	0.14	0.00	0.00	0.16
Jet EtaIntercalibration Total Stat.	0.25	1.86	0.23	0.00	0.00	2.03	0.60	0.00	0.00	0.36
e/γ RESOLUTION ALL	0.27	3.92	0.01	0.25	0.00	5.60	0.67	0.00	0.00	0.95
MET Soft Trk. Resolution	0.55	1.79	0.00	0.00	0.00	3.86	0.39	0.00	0.00	0.25
$W^\pm W^\pm$ EW Shower	5.55	0.00	0.00	0.00	0.00	0.00	0.00	0.00	0.00	0.00
Electron Eff. Iso TOTAL 1NPCOR PLUS UNCOR	0.80	0.90	1.21	0.46	0.43	0.85	0.90	0.00	0.00	0.65
e/γ Scale LARTEMPERATURE EXTRA2016PRE	0.00	0.00	0.00	0.00	0.00	0.00	0.00	0.00	0.00	0.50
Flavor Tag Eff. Eigen Light 2	0.17	0.21	0.16	0.13	0.21	0.23	0.24	0.00	0.00	0.24
Flavor Tag Eff. Eigen Light 1	0.38	0.51	0.28	0.27	0.46	0.50	0.55	0.00	0.00	0.52
Flavor Tag Eff. Eigen Light 0	1.68	2.06	1.29	1.03	1.82	1.92	2.42	0.00	0.00	2.16
Flavor Tag Eff. Eigen Light 4	0.08	0.07	0.03	0.11	0.27	0.07	0.16	0.00	0.00	0.06
Pile-up Reweight. data SF	2.94	11.68	23.94	12.57	17.75	6.80	6.47	0.00	0.00	4.25
$W^\pm W^\pm$ EW PDF	0.65	0.00	0.00	0.00	0.00	0.00	0.00	0.00	0.00	0.00
Electron Eff. Trigger TOTAL 1NPCOR PLUS UNCOR	0.02	0.03	0.02	0.02	0.00	0.03	0.02	0.00	0.00	0.03
Electron Eff. ID CorrUncertaintyNP6	0.01	0.03	0.02	0.03	0.02	0.04	0.01	0.00	0.00	0.01
Electron Eff. ID CorrUncertaintyNP7	0.01	0.03	0.03	0.03	0.04	0.03	0.02	0.00	0.00	0.03
Flavor Tag Eff. Eigen B 1	0.00	4.42	0.00	0.00	0.00	0.09	0.04	0.00	0.00	0.03
Flavor Tag Eff. Eigen B 0	0.01	17.11	0.00	0.00	0.00	0.12	0.06	0.00	0.00	0.17
Flavor Tag Eff. Eigen B 2	0.00	1.85	0.00	0.00	0.00	0.06	0.02	0.00	0.00	0.00
Electron Eff. ID CorrUncertaintyNP8	0.02	0.04	0.12	0.06	0.04	0.05	0.02	0.00	0.00	0.04
Electron Eff. ID CorrUncertaintyNP9	0.06	0.08	0.13	0.06	0.16	0.07	0.05	0.00	0.00	0.05
$W^\pm W^\pm$ EW α_s	0.22	0.00	0.00	0.00	0.00	0.00	0.00	0.00	0.00	0.00
$W^\pm W^\pm$ EW EW Corr.	3.64	0.00	0.00	0.00	0.00	0.00	0.00	0.00	0.00	0.00
e/γ Scale E4SCINTILLATOR	0.00	0.00	0.00	0.00	0.00	0.00	0.00	0.00	0.00	0.50

Nuisance Parameter	Relativ Effect on Sample [%]									
	$W^{\pm}W^{\pm}jj$-Ew	top	tri-boson	$Z\gamma$	$W^{\pm}\gamma$	ZZ	$W^{\pm}W^{\pm}jj$-QCD	Charge Mis-ID	Non-Prompt	$W^{\pm}Z$
Jet Flavor Response	1.01	1.88	5.14	0.02	0.00	2.68	0.73	0.00	0.00	4.04
Flavor Tag Eff. extrapolation	0.05	0.43	0.10	0.00	0.00	0.06	0.10	0.00	0.00	0.09
Jet Pile-up p_{T} Term	1.02	7.62	5.14	0.00	0.01	4.99	0.90	0.00	0.00	4.84
Jet Energy Resolution	1.99	18.79	7.24	0.06	0.06	13.20	2.93	0.00	0.00	6.25
Jet EtaIntercalibration Non-Closure	0.93	7.65	5.14	0.00	0.00	3.77	0.53	0.00	0.00	4.09
Electron Eff. ID CorrUncertaintyNP14	0.76	0.66	0.48	0.82	1.25	0.92	0.73	0.00	0.00	0.86
Electron Eff. ID CorrUncertaintyNP12	0.01	0.11	0.07	0.04	0.07	0.04	0.01	0.00	0.00	0.01
Electron Eff. ID CorrUncertaintyNP13	0.06	0.13	0.50	0.03	0.04	0.05	0.08	0.00	0.00	0.05
Electron Eff. ID CorrUncertaintyNP10	0.18	0.19	0.14	0.18	0.23	0.19	0.16	0.00	0.00	0.20
Electron Eff. ID CorrUncertaintyNP11	0.00	0.06	0.05	0.08	0.10	0.06	0.01	0.00	0.00	0.02
e/γ Scale LARCALIB EXTRA2015PRE	0.10	0.00	0.00	0.00	0.00	0.00	0.19	0.00	0.00	0.76
MET Soft Trk. Scale	0.11	1.79	0.00	0.00	0.00	0.59	0.53	0.00	0.00	0.25
Jet EffectiveNP 4	0.10	1.86	0.00	0.00	0.00	0.00	0.36	0.00	0.00	0.32
Jet EffectiveNP 7	0.11	0.07	0.00	0.00	0.00	0.00	0.22	0.00	0.00	0.04
Jet EffectiveNP 6	0.11	0.05	0.00	0.00	0.00	0.00	0.41	0.00	0.00	0.04
Jet EffectiveNP 1	0.48	6.08	0.36	0.00	0.01	2.68	0.74	0.00	0.00	2.52
Jet JVT Efficiency	0.02	0.31	0.09	0.00	0.35	0.31	0.12	0.00	0.00	0.07
Jet EffectiveNP 2	0.54	0.09	0.23	0.00	0.00	2.08	0.92	0.00	0.00	1.09
Flavor Tag Eff. Eigen C 0	0.33	0.97	1.72	0.00	0.00	0.70	0.52	0.00	0.00	0.81
Flavor Tag Eff. Eigen C 2	0.10	0.25	0.26	0.00	0.00	0.13	0.14	0.00	0.00	0.11
Flavor Tag Eff. Eigen Light 3	0.05	0.62	0.04	0.09	0.39	0.30	0.11	0.00	0.00	0.26
Jet EtaIntercalibration Modelling	1.21	3.75	5.14	11.50	0.00	14.26	1.73	0.00	0.00	6.63
Electron Eff. Reco TOTAL 1NPCOR PLUS UNCOR	0.30	0.39	0.74	0.29	0.28	0.31	0.33	0.00	0.00	0.32
MET Soft Trk. ResoPerp	0.25	1.79	0.00	0.00	0.00	0.00	0.21	0.00	0.00	0.20
Flavor Tag Eff. extrapolation from charm	0.00	0.14	1.67	0.00	0.00	0.43	0.00	0.00	0.00	0.37
Jet EffectiveNP 5	0.13	0.03	0.00	0.00	0.00	0.00	0.22	0.00	0.00	0.12
Jet Pile-up OffsetNPV	0.71	10.52	5.14	0.00	0.00	2.10	0.24	0.00	0.00	2.37
Jet Flavor Composition	1.95	9.56	10.51	11.50	14.36	5.36	2.15	0.00	0.00	9.21
Charge Mis-ID Energy Corr.	0.00	0.00	0.00	0.00	0.00	0.00	0.00	4.20	0.00	0.00
Charge Mis-ID Scale Fac.	0.00	0.00	0.00	0.00	0.00	0.00	0.00	9.32	0.00	0.00
Non-Prompt e Sys.	0.00	0.00	0.00	0.00	0.00	0.00	0.00	0.00	52.04	0.00
Non-Prompt e Stat.	0.00	0.00	0.00	0.00	0.00	0.00	0.00	0.00	14.87	0.00

Table B.1: Summary of the relative effects of all shape nuisance parameters in the $e^{+}e^{+}$ channel of the signal region.

B.3.2 e^-e^- Channel, Signal Region

Nuisance Parameter	Relativ Effect on Sample [%]									
	$W^\pm W^\pm jj$-Ew	top	tri-boson	$Z\gamma$	$W^\pm\gamma$	ZZ	$W^\pm W^\pm jj$-Qcd	Charge Mis-ID	Non-Prompt	$W^\pm Z$
Jet Pile-up OffsetMu	0.67	2.47	1.10	0.00	0.00	0.69	0.91	0.00	0.00	4.67
e/γ Scale ALLCORR	0.51	2.08	0.00	0.00	0.00	2.89	0.44	0.00	0.00	0.56
Jet EffectiveNP 3	0.42	2.51	0.01	0.00	0.00	2.18	0.89	0.00	0.00	0.76
$W^\pm W^\pm$ EW Scale	2.09	0.00	0.00	0.00	0.00	0.00	0.00	0.00	0.00	0.00
Flavor Tag Eff. Eigen C 1	0.31	0.22	0.77	0.00	0.32	0.21	0.50	0.00	0.00	0.16
Jet PunchThrough MC15	0.00	0.00	0.00	0.00	0.00	0.00	0.00	0.00	0.00	0.05
Jet Pile-up RhoTopology	1.03	11.22	3.03	0.00	7.61	7.54	3.37	0.00	0.00	7.92
Jet EffectiveNP 8restTerm	0.17	0.00	0.00	0.00	0.00	0.71	0.44	0.00	0.00	0.71
Interference	2.42	0.00	0.00	0.00	0.00	0.00	0.00	0.00	0.00	0.00
e/γ Scale LARTEMPERATURE EXTRA2015PRE	0.07	0.00	0.00	0.00	0.00	0.00	0.00	0.00	0.00	0.48
Jet BJES Response	0.00	4.45	0.00	0.00	0.00	0.00	0.00	0.00	0.00	0.00
Electron Eff. ID SIMPLIFIED UncorrUncertaintyNP8	0.89	0.56	1.20	0.00	0.51	0.68	0.94	0.00	0.00	0.77
Electron Eff. ID SIMPLIFIED UncorrUncertaintyNP5	0.02	0.04	0.00	0.00	0.00	0.04	0.01	0.00	0.00	0.04
Electron Eff. ID SIMPLIFIED UncorrUncertaintyNP7	0.10	0.05	0.07	0.00	0.12	0.07	0.08	0.00	0.00	0.08
Electron Eff. ID SIMPLIFIED UncorrUncertaintyNP6	0.11	0.17	0.10	0.00	0.17	0.16	0.13	0.00	0.00	0.14
Jet EtaIntercalibration Total Stat.	0.49	2.48	1.10	0.00	0.01	2.18	0.41	0.00	0.00	4.80
e/γ RESOLUTION ALL	0.35	2.09	0.01	0.00	0.00	1.01	0.45	0.00	0.00	1.27
MET Soft Trk. Resolution	0.73	0.00	0.00	0.00	0.00	4.45	0.41	0.00	0.00	2.34
$W^\pm W^\pm$ EW Shower	5.29	0.00	0.00	0.00	0.00	0.00	0.00	0.00	0.00	0.00
Electron Eff. Iso TOTAL 1NPCOR PLUS UNCOR	1.06	0.44	0.91	0.00	0.44	0.79	1.16	0.00	0.00	0.87
e/γ Scale LARTEMPERATURE EXTRA2016PRE	0.07	0.00	0.00	0.00	0.00	0.00	0.00	0.00	0.00	0.48
Flavor Tag Eff. Eigen Light 2	0.18	0.16	0.26	0.00	0.21	0.22	0.24	0.00	0.00	0.25
Flavor Tag Eff. Eigen Light 1	0.41	0.39	0.57	0.00	0.47	0.48	0.52	0.00	0.00	0.55
Flavor Tag Eff. Eigen Light 0	1.72	1.61	2.34	0.00	1.80	1.86	2.28	0.00	0.00	2.21
Flavor Tag Eff. Eigen Light 4	0.10	0.12	0.14	0.00	0.24	0.11	0.10	0.00	0.00	0.05
Pile-up Reweight. data SF	2.55	8.93	14.90	0.00	9.12	5.71	1.91	0.00	0.00	5.59
$W^\pm W^\pm$ EW PDF	0.58	0.00	0.00	0.00	0.00	0.00	0.00	0.00	0.00	0.00
Electron Eff. Trigger TOTAL 1NPCOR PLUS UNCOR	0.02	0.03	0.02	0.00	0.02	0.03	0.02	0.00	0.00	0.03
Electron Eff. ID CorrUncertaintyNP6	0.01	0.02	0.04	0.00	0.02	0.02	0.01	0.00	0.00	0.02
Electron Eff. ID CorrUncertaintyNP7	0.01	0.03	0.03	0.00	0.02	0.03	0.03	0.00	0.00	0.01
Flavor Tag Eff. Eigen B 1	0.01	4.48	0.00	0.00	0.00	0.00	0.00	0.00	0.00	0.03
Flavor Tag Eff. Eigen B 0	0.08	10.71	0.00	0.00	0.00	0.00	0.00	0.00	0.00	0.18
Flavor Tag Eff. Eigen B 2	0.01	2.19	0.00	0.00	0.00	0.00	0.00	0.00	0.00	0.02
Electron Eff. ID CorrUncertaintyNP8	0.01	0.07	0.05	0.00	0.05	0.02	0.02	0.00	0.00	0.01
Electron Eff. ID CorrUncertaintyNP9	0.07	0.11	0.09	0.00	0.23	0.07	0.08	0.00	0.00	0.05
$W^\pm W^\pm$ EW α_s	0.20	0.00	0.00	0.00	0.00	0.00	0.00	0.00	0.00	0.00
$W^\pm W^\pm$ EW EW Corr.	3.57	0.00	0.00	0.00	0.00	0.00	0.00	0.00	0.00	0.00
e/γ Scale E4SCINTILLATOR	0.07	0.00	0.00	0.00	0.00	0.00	0.00	0.00	0.00	0.48
Jet Flavor Response	1.20	8.64	3.04	0.00	0.19	8.27	3.00	0.00	0.00	7.58
Flavor Tag Eff. extrapolation	0.09	0.70	0.19	0.00	0.20	0.04	0.12	0.00	0.00	0.10
Jet Pile-up p_T Term	1.04	4.58	1.10	0.00	0.01	5.91	2.68	0.00	0.00	5.97

Nuisance Parameter	Relativ Effect on Sample [%]									
	$W^{\pm}W^{\pm}jj$-Ew	top	tri-boson	$Z\gamma$	$W^{\pm}\gamma$	ZZ	$W^{\pm}W^{\pm}jj$-Qcd	Charge Mis-ID	Non-Prompt	$W^{\pm}Z$
Jet Energy Resolution	5.16	35.16	8.01	0.00	12.61	8.50	14.31	0.00	0.00	9.36
Jet EtaIntercalibration Non-Closure	1.35	8.93	3.04	0.00	0.17	2.12	2.68	0.00	0.00	4.15
Electron Eff. ID CorrUncertaintyNP14	0.70	0.98	0.74	0.00	1.08	0.85	0.63	0.00	0.00	0.78
Electron Eff. ID CorrUncertaintyNP12	0.01	0.05	0.05	0.00	0.01	0.02	0.01	0.00	0.00	0.02
Electron Eff. ID CorrUncertaintyNP13	0.06	0.10	0.11	0.00	0.03	0.02	0.04	0.00	0.00	0.05
Electron Eff. ID CorrUncertaintyNP10	0.17	0.25	0.18	0.00	0.29	0.21	0.17	0.00	0.00	0.18
Electron Eff. ID CorrUncertaintyNP11	0.02	0.05	0.09	0.00	0.10	0.02	0.01	0.00	0.00	0.04
e/γ Scale LARCALIB EXTRA2015PRE	0.15	0.00	0.00	0.00	0.00	0.00	0.43	0.00	0.00	0.43
MET Soft Trk. Scale	0.15	0.00	0.00	0.00	0.00	3.68	0.84	0.00	0.00	0.61
Jet EffectiveNP 4	0.28	2.47	0.00	0.00	0.00	2.88	0.87	0.00	0.00	0.53
Jet EffectiveNP 7	0.31	0.00	0.00	0.00	0.00	2.18	0.43	0.00	0.00	0.29
Jet EffectiveNP 6	0.24	0.00	0.00	0.00	0.00	2.18	0.87	0.00	0.00	0.28
Jet EffectiveNP 1	1.05	8.82	1.11	0.00	0.19	2.33	2.11	0.00	0.00	6.91
Jet Jvt Efficiency	0.03	0.76	0.65	0.00	0.07	0.21	0.05	0.00	0.00	0.41
Jet EffectiveNP 2	0.42	8.95	0.01	0.00	0.01	2.95	1.23	0.00	0.00	0.91
Flavor Tag Eff. Eigen C 0	0.49	0.48	1.77	0.00	0.36	1.01	0.81	0.00	0.00	0.94
Flavor Tag Eff. Eigen C 2	0.13	0.17	0.48	0.00	0.21	0.06	0.26	0.00	0.00	0.07
Flavor Tag Eff. Eigen Light 3	0.06	0.30	0.40	0.00	0.47	0.31	0.15	0.00	0.00	0.28
Jet EtaIntercalibration Modelling	1.20	8.71	3.04	0.00	0.02	10.52	3.46	0.00	0.00	7.45
Electron Eff. Reco TOTAL 1NPCOR PLUS UNCOR	0.32	0.26	0.38	0.00	0.24	0.30	0.30	0.00	0.00	0.31
MET Soft Trk. ResoPerp	0.47	0.00	0.00	0.00	0.00	3.68	0.79	0.00	0.00	0.76
Flavor Tag Eff. extrapolation from charm	0.00	0.29	0.96	0.00	0.00	0.59	0.00	0.00	0.00	0.50
Jet EffectiveNP 5	0.33	0.01	0.00	0.00	0.00	2.88	0.77	0.00	0.00	0.45
Jet Pile-up OffsetNPV	0.57	7.16	0.01	0.00	0.03	2.20	1.00	0.00	0.00	1.47
Jet Flavor Composition	2.38	6.01	9.29	0.00	7.65	12.38	4.18	0.00	0.00	10.03
Charge Mis-ID Energy Corr.	0.00	0.00	0.00	0.00	0.00	0.00	0.00	2.04	0.00	0.00
Charge Mis-ID Scale Fac.	0.00	0.00	0.00	0.00	0.00	0.00	0.00	8.68	0.00	0.00
Non-Prompt e Sys.	0.00	0.00	0.00	0.00	0.00	0.00	0.00	0.00	60.74	0.00
Non-Prompt e Stat.	0.00	0.00	0.00	0.00	0.00	0.00	0.00	0.00	14.62	0.00

Table B.2: Summary of the relative effects of all shape nuisance parameters in the $e^{-}e^{-}$ channel of the signal region.

B.3.3 $e^+\mu^+/\mu^+e^+$ Channel, Signal Region

Nuisance Parameter	Relativ Effect on Sample [%]									
	$W^\pm W^\pm jj$-Ew	top	tri-boson	$Z\gamma$	$W^\pm\gamma$	ZZ	$W^\pm W^\pm jj$-QCD	Charge Mis-ID	Non-Prompt	$W^\pm Z$
Jet Pile-up OffsetMu	0.21	3.92	0.69	0.00	0.01	2.93	0.30	0.00	0.00	1.70
Muon Iso Sys.	0.21	0.21	0.21	0.21	0.21	0.21	0.21	0.00	0.00	0.21
e/γ Scale ALLCORR	0.10	0.73	0.07	0.00	0.00	0.24	0.19	0.00	0.00	0.26
Muon Eff. Stat.	0.19	0.23	0.16	0.20	0.14	0.16	0.19	0.00	0.00	0.18
Jet EffectiveNP 3	0.28	5.60	0.34	0.00	0.00	1.91	0.52	0.00	0.00	0.69
$W^\pm W^\pm$ EW Scale	2.30	0.00	0.00	0.00	0.00	0.00	0.00	0.00	0.00	0.00
Flavor Tag Eff. Eigen C 1	0.17	0.32	0.15	0.00	0.00	0.14	0.24	0.00	0.00	0.12
Jet PunchThrough MC15	0.02	0.00	0.00	0.00	0.00	0.00	0.00	0.00	0.00	0.02
Jet Pile-up RhoTopology	0.65	2.36	8.58	0.01	3.69	4.66	0.63	0.00	0.00	1.79
Jet EffectiveNP 8restTerm	0.12	0.03	0.01	0.00	0.00	2.39	0.26	0.00	0.00	0.39
Interference	2.45	0.00	0.00	0.00	0.00	0.00	0.00	0.00	0.00	0.00
e/γ Scale LARTEMPERATURE EXTRA2015PRE	0.00	0.00	0.00	0.00	0.00	0.00	0.00	0.00	0.00	0.05
Jet BJES Response	0.01	6.27	0.00	0.00	0.00	0.00	0.07	0.00	0.00	0.02
Electron Eff. ID SIMPLIFIED UncorrUncertaintyNP8	0.28	0.19	0.27	0.52	0.04	0.11	0.19	0.00	0.00	0.20
Electron Eff. ID SIMPLIFIED UncorrUncertaintyNP5	0.01	0.01	0.01	0.00	0.00	0.01	0.01	0.00	0.00	0.01
Electron Eff. ID SIMPLIFIED UncorrUncertaintyNP7	0.04	0.05	0.01	0.00	0.00	0.02	0.03	0.00	0.00	0.03
Electron Eff. ID SIMPLIFIED UncorrUncertaintyNP6	0.06	0.05	0.03	0.00	0.09	0.05	0.05	0.00	0.00	0.04
Jet EtaIntercalibration Total Stat.	0.26	6.29	1.19	0.00	0.01	2.78	0.43	0.00	0.00	1.06
e/γ RESOLUTION ALL	0.09	0.78	0.05	0.00	0.00	0.43	0.17	0.00	0.00	0.26
MET Soft Trk. Resolution	0.10	0.00	0.09	0.00	0.00	1.11	0.36	0.00	0.00	0.58
$W^\pm W^\pm$ EW Shower	5.55	0.00	0.00	0.00	0.00	0.00	0.00	0.00	0.00	0.00
Electron Eff. Iso TOTAL 1NPCOR PLUS UNCOR	0.35	0.26	0.49	1.43	0.35	0.29	0.32	0.00	0.00	0.36
e/γ Scale LARTEMPERATURE EXTRA2016PRE	0.00	0.00	0.00	0.00	0.00	0.00	0.00	0.00	0.00	0.05
Muon ID	0.21	1.18	0.00	0.00	0.00	1.12	0.17	0.00	0.00	0.61
Flavor Tag Eff. Eigen Light 2	0.17	0.19	0.27	0.31	0.39	0.19	0.25	0.00	0.00	0.23
Flavor Tag Eff. Eigen Light 1	0.38	0.42	0.61	0.60	0.82	0.43	0.54	0.00	0.00	0.50
Flavor Tag Eff. Eigen Light 0	1.65	1.65	2.44	2.26	3.17	1.64	2.36	0.00	0.00	2.02
Flavor Tag Eff. Eigen Light 4	0.09	0.08	0.08	0.18	0.35	0.08	0.14	0.00	0.00	0.08
Pile-up Reweight. data SF	0.84	7.49	21.37	13.64	18.39	7.89	1.73	0.00	0.00	2.31
$W^\pm W^\pm$ EW PDF	0.65	0.00	0.00	0.00	0.00	0.00	0.00	0.00	0.00	0.00
Electron Eff. Trigger TOTAL 1NPCOR PLUS UNCOR	0.05	0.05	0.06	0.06	0.12	0.05	0.05	0.00	0.00	0.06
Muon Eff. TrigStatUncertainty	0.03	0.03	0.02	0.01	0.09	0.03	0.03	0.00	0.00	0.03
Muon Eff. Sys.	0.84	0.85	0.80	0.76	0.85	0.83	0.87	0.00	0.00	0.85
Electron Eff. ID SIMPLIFIED UncorrUncertaintyNP15	0.03	0.03	0.03	0.00	0.00	0.08	0.06	0.00	0.00	0.07
Electron Eff. ID SIMPLIFIED UncorrUncertaintyNP14	0.01	0.00	0.00	0.00	0.00	0.01	0.01	0.00	0.00	0.01
Electron Eff. ID CorrUncertaintyNP6	0.00	0.02	0.03	0.04	0.04	0.01	0.00	0.00	0.00	0.01
Electron Eff. ID CorrUncertaintyNP7	0.01	0.01	0.03	0.03	0.05	0.03	0.02	0.00	0.00	0.02
Flavor Tag Eff. Eigen B 1	0.01	4.14	0.00	0.00	0.00	0.03	0.04	0.00	0.00	0.04
Flavor Tag Eff. Eigen B 0	0.06	8.60	0.00	0.00	0.00	0.24	0.12	0.00	0.00	0.15
Flavor Tag Eff. Eigen B 2	0.00	1.40	0.00	0.00	0.00	0.01	0.01	0.00	0.00	0.01
Electron Eff. ID CorrUncertaintyNP8	0.01	0.01	0.02	0.06	0.03	0.02	0.00	0.00	0.00	0.00

Nuisance Parameter	Relativ Effect on Sample [%]									
	$W^{\pm}W^{\pm}jj$-EW	top	tri-boson	$Z\gamma$	$W^{\pm}\gamma$	ZZ	$W^{\pm}W^{\pm}jj$-QCD	Charge Mis-ID	Non-Prompt	$W^{\pm}Z$
Electron Eff. ID CorrUncertaintyNP9	0.03	0.03	0.04	0.11	0.07	0.06	0.03	0.00	0.00	0.03
$W^{\pm}W^{\pm}$ EW α_s	0.23	0.00	0.00	0.00	0.00	0.00	0.00	0.00	0.00	0.00
Muon TTVA Stat.	0.08	0.08	0.07	0.06	0.07	0.07	0.07	0.00	0.00	0.08
$W^{\pm}W^{\pm}$ EW EW Corr.	3.67	0.00	0.00	0.00	0.00	0.00	0.00	0.00	0.00	0.00
Muon Scale	0.16	1.17	0.00	0.00	0.00	0.75	0.13	0.00	0.00	0.39
e/γ Scale E4SCINTILLATOR	0.01	0.00	0.00	0.00	0.00	0.00	0.04	0.00	0.00	0.08
Jet Flavor Response	0.73	3.74	7.48	0.01	3.70	6.05	1.02	0.00	0.00	1.78
Flavor Tag Eff. extrapolation	0.05	0.71	0.03	0.00	0.00	0.05	0.08	0.00	0.00	0.04
Jet Pile-up p_{T} Term	0.88	3.95	6.80	0.01	3.71	3.42	0.97	0.00	0.00	1.72
Jet Energy Resolution	0.42	26.97	9.66	232.69	87.31	25.20	1.52	0.00	0.00	2.57
Jet EtaIntercalibration Non-Closure	0.62	10.43	2.22	0.00	3.71	5.05	0.51	0.00	0.00	2.18
Electron Eff. ID CorrUncertaintyNP14	0.41	0.49	0.28	0.36	0.52	0.48	0.45	0.00	0.00	0.46
Electron Eff. ID CorrUncertaintyNP12	0.01	0.03	0.05	0.02	0.05	0.10	0.04	0.00	0.00	0.04
Electron Eff. ID CorrUncertaintyNP13	0.02	0.01	0.05	0.03	0.05	0.08	0.01	0.00	0.00	0.02
Electron Eff. ID CorrUncertaintyNP10	0.10	0.11	0.08	0.11	0.17	0.13	0.11	0.00	0.00	0.11
Electron Eff. ID CorrUncertaintyNP11	0.00	0.01	0.07	0.10	0.08	0.03	0.02	0.00	0.00	0.02
e/γ Scale LARCALIB EXTRA2015PRE	0.03	0.00	0.05	0.00	0.00	0.08	0.07	0.00	0.00	0.13
Muon MS	0.21	1.17	0.00	36.55	0.00	0.86	0.36	0.00	0.00	0.64
Muon Iso Stat.	0.02	0.03	0.02	0.02	0.02	0.02	0.02	0.00	0.00	0.02
MET Soft Trk. Scale	0.11	0.76	0.63	0.00	0.00	2.19	0.16	0.00	0.00	0.72
Jet EffectiveNP 4	0.13	7.03	0.01	0.00	0.00	2.23	0.53	0.00	0.00	0.42
Jet EffectiveNP 7	0.05	0.02	0.01	0.00	0.00	2.50	0.15	0.00	0.00	0.22
Jet EffectiveNP 6	0.09	6.30	0.01	0.00	0.00	0.28	0.22	0.00	0.00	0.17
Jet EffectiveNP 1	0.54	4.69	2.23	0.01	3.70	2.22	0.45	0.00	0.00	1.38
Jet JVT Efficiency	0.03	0.13	0.52	0.11	0.36	0.19	0.04	0.00	0.00	0.10
Jet EffectiveNP 2	0.28	5.61	1.42	0.00	3.71	2.41	0.60	0.00	0.00	0.97
Flavor Tag Eff. Eigen C 0	0.31	1.20	2.10	0.00	0.00	0.85	0.40	0.00	0.00	0.64
Muon Eff. TrigSystUncertainty	0.05	0.04	0.05	0.02	0.05	0.08	0.06	0.00	0.00	0.06
Flavor Tag Eff. Eigen C 2	0.08	0.11	0.12	0.00	0.00	0.05	0.13	0.00	0.00	0.04
Flavor Tag Eff. Eigen Light 3	0.06	0.39	0.50	0.10	0.56	0.41	0.09	0.00	0.00	0.31
Jet EtaIntercalibration Modelling	0.96	5.14	8.14	263.60	3.71	6.91	1.00	0.00	0.00	3.23
Electron Eff. Reco TOTAL 1NPCOR PLUS UNCOR	0.16	0.18	0.20	0.20	0.13	0.14	0.16	0.00	0.00	0.16
MET Soft Trk. ResoPerp	0.11	0.57	0.56	0.00	0.00	1.08	0.32	0.00	0.00	0.92
Flavor Tag Eff. extrapolation from charm	0.00	0.18	1.89	0.00	0.00	0.52	0.00	0.00	0.00	0.31
Muon TTVA Sys.	0.07	0.04	0.02	0.00	0.01	0.02	0.04	0.00	0.00	0.05
Jet EffectiveNP 5	0.11	7.01	0.00	0.00	0.00	2.49	0.31	0.00	0.00	0.36
Jet Pile-up OffsetNPV	0.19	6.93	1.20	0.00	0.01	2.60	0.22	0.00	0.00	2.10
Jet Flavor Composition	1.52	14.73	22.24	263.59	3.71	12.32	2.10	0.00	0.00	3.18
Charge Mis-ID Energy Corr.	0.00	0.00	0.00	0.00	0.00	0.00	0.00	5.91	0.00	0.00
Charge Mis-ID Scale Fac.	0.00	0.00	0.00	0.00	0.00	0.00	0.00	3.64	0.00	0.00
Non-Prompt μ Sys.	0.00	0.00	0.00	0.00	0.00	0.00	0.00	0.00	63.72	0.00
Non-Prompt e Sys.	0.00	0.00	0.00	0.00	0.00	0.00	0.00	0.00	44.29	0.00
Non-Prompt μ Stat.	0.00	0.00	0.00	0.00	0.00	0.00	0.00	0.00	4.78	0.00
Non-Prompt e Stat.	0.00	0.00	0.00	0.00	0.00	0.00	0.00	0.00	10.14	0.00

Nuisance Parameter	Relativ Effect on Sample [%]									
	$W^{\pm}W^{\pm}jj$-EW	top	tri-boson	$Z\gamma$	$W^{\pm}\gamma$	ZZ	$W^{\pm}W^{\pm}jj$-QCD	Charge Mis-ID	Non-Prompt	$W^{\pm}Z$

Table B.3: Summary of the relative effects of all shape nuisance parameters in the $e^{+}\mu^{+}/\mu^{+}e^{+}$ channel of the signal region.

B.3.4 $e^-\mu^-/\mu^-e^-$ Channel, Signal Region

Nuisance Parameter	Relativ Effect on Sample [%]									
	$W^\pm W^\pm jj$-Ew	top	tri-boson	$Z\gamma$	$W^\pm\gamma$	ZZ	$W^\pm W^\pm jj$-QCD	Charge Mis-ID	Non-Prompt	$W^\pm Z$
Jet Pile-up OffsetMu	0.19	7.17	4.01	0.39	0.02	4.60	0.30	0.00	0.00	1.20
Muon Iso Sys.	0.22	0.21	0.21	0.21	0.21	0.21	0.22	0.00	0.00	0.21
e/γ Scale ALLCORR	0.07	4.91	0.10	0.00	0.00	3.41	0.29	0.00	0.00	0.19
Muon Eff. Stat.	0.20	0.17	0.19	0.14	0.18	0.18	0.20	0.00	0.00	0.19
Jet EffectiveNP 3	0.40	4.88	2.82	0.39	0.00	5.79	0.22	0.00	0.00	0.48
$W^\pm W^\pm$ EW Scale	1.98	0.00	0.00	0.00	0.00	0.00	0.00	0.00	0.00	0.00
Flavor Tag Eff. Eigen C 1	0.28	0.28	1.21	0.00	0.12	0.22	0.32	0.00	0.00	0.16
Jet PunchThrough MC15	0.03	0.00	0.00	0.00	0.00	0.15	0.05	0.00	0.00	0.00
Jet Pile-up RhoTopology	0.52	4.37	4.86	0.39	0.02	5.75	0.94	0.00	0.00	1.36
Jet EffectiveNP 8restTerm	0.17	2.89	0.00	0.39	0.00	1.74	0.11	0.00	0.00	0.34
Interference	2.31	0.00	0.00	0.00	0.00	0.00	0.00	0.00	0.00	0.00
e/γ Scale LARTEMPERATURE EXTRA2015PRE	0.00	0.00	0.00	0.00	0.00	1.54	0.00	0.00	0.00	0.03
Jet BJES Response	0.02	3.76	0.00	0.39	0.00	0.00	0.00	0.00	0.00	0.03
Electron Eff. ID SIMPLIFIED UncorrUncertaintyNP8	0.31	0.14	0.56	0.00	0.56	0.17	0.26	0.00	0.00	0.23
Electron Eff. ID SIMPLIFIED UncorrUncertaintyNP5	0.01	0.02	0.00	0.00	0.00	0.01	0.01	0.00	0.00	0.01
Electron Eff. ID SIMPLIFIED UncorrUncertaintyNP7	0.04	0.02	0.01	0.00	0.00	0.02	0.03	0.00	0.00	0.04
Electron Eff. ID SIMPLIFIED UncorrUncertaintyNP6	0.05	0.10	0.03	0.00	0.00	0.04	0.04	0.00	0.00	0.04
Jet EtaIntercalibration Total Stat.	0.29	2.91	2.81	0.39	0.01	3.79	0.24	0.00	0.00	0.54
e/γ RESOLUTION ALL	0.23	4.79	0.51	0.00	0.00	4.34	0.27	0.00	0.00	0.67
MET Soft Trk. Resolution	0.20	9.43	0.00	0.00	0.00	2.39	0.35	0.00	0.00	0.34
$W^\pm W^\pm$ EW Shower	5.24	0.00	0.00	0.00	0.00	0.00	0.00	0.00	0.00	0.00
Electron Eff. Iso TOTAL 1NPCOR PLUS UNCOR	0.43	0.22	0.52	1.07	0.35	0.30	0.45	0.00	0.00	0.45
e/γ Scale LARTEMPERATURE EXTRA2016PRE	0.00	0.00	0.00	0.00	0.00	1.54	0.00	0.00	0.00	0.03
Muon ID	0.12	3.12	0.67	0.00	0.00	4.20	0.53	0.00	0.00	0.73
Flavor Tag Eff. Eigen Light 2	0.18	0.21	0.15	0.19	0.16	0.25	0.25	0.00	0.00	0.23
Flavor Tag Eff. Eigen Light 1	0.40	0.48	0.34	0.37	0.38	0.56	0.55	0.00	0.00	0.50
Flavor Tag Eff. Eigen Light 0	1.68	1.90	1.34	1.46	1.38	2.23	2.31	0.00	0.00	1.99
Flavor Tag Eff. Eigen Light 4	0.10	0.06	0.07	0.20	0.38	0.11	0.17	0.00	0.00	0.07
Pile-up Reweight. data SF	1.32	31.60	48.21	17.48	21.31	8.42	2.65	0.00	0.00	7.79
$W^\pm W^\pm$ EW PDF	0.56	0.00	0.00	0.00	0.00	0.00	0.00	0.00	0.00	0.00
Electron Eff. Trigger TOTAL 1NPCOR PLUS UNCOR	0.05	0.05	0.07	0.07	0.07	0.06	0.05	0.00	0.00	0.06
Muon Eff. TrigStatUncertainty	0.02	0.03	0.02	0.01	0.01	0.03	0.03	0.00	0.00	0.03
Muon Eff. Sys.	0.90	0.80	0.74	1.23	0.98	0.88	0.98	0.00	0.00	0.83
Electron Eff. ID SIMPLIFIED UncorrUncertaintyNP15	0.02	0.04	0.02	0.00	0.00	0.09	0.04	0.00	0.00	0.05
Electron Eff. ID SIMPLIFIED UncorrUncertaintyNP14	0.00	0.00	0.01	0.00	0.00	0.02	0.01	0.00	0.00	0.01
Electron Eff. ID CorrUncertaintyNP6	0.00	0.02	0.02	0.21	0.04	0.02	0.00	0.00	0.00	0.01
Electron Eff. ID CorrUncertaintyNP7	0.01	0.03	0.03	0.17	0.05	0.02	0.01	0.00	0.00	0.02
Flavor Tag Eff. Eigen B 1	0.01	3.40	0.18	3.32	0.00	0.05	0.01	0.00	0.00	0.02
Flavor Tag Eff. Eigen B 0	0.06	6.88	0.25	4.66	0.00	0.07	0.02	0.00	0.00	0.07
Flavor Tag Eff. Eigen B 2	0.00	0.38	0.14	1.24	0.00	0.02	0.01	0.00	0.00	0.00
Electron Eff. ID CorrUncertaintyNP8	0.00	0.02	0.02	0.22	0.11	0.02	0.01	0.00	0.00	0.01

Nuisance Parameter	Relativ Effect on Sample [%]									
	$W^{\pm}W^{\pm}jj$-Ew	top	tri-boson	$Z\gamma$	$W^{\pm}\gamma$	ZZ	$W^{\pm}W^{\pm}jj$-Qcd	Charge Mis-ID	Non-Prompt	$W^{\pm}Z$
Electron Eff. ID CorrUncertaintyNP9	0.03	0.04	0.04	0.30	0.10	0.05	0.03	0.00	0.00	0.03
$W^{\pm}W^{\pm}$ EW α_s	0.20	0.00	0.00	0.00	0.00	0.00	0.00	0.00	0.00	0.00
Muon TTVA Stat.	0.08	0.07	0.07	0.08	0.08	0.07	0.08	0.00	0.00	0.08
$W^{\pm}W^{\pm}$ EW EW Corr.	3.44	0.00	0.00	0.00	0.00	0.00	0.00	0.00	0.00	0.00
Muon Scale	0.15	2.10	0.64	0.00	0.00	0.96	0.26	0.00	0.00	0.64
e/γ Scale E4SCINTILLATOR	0.00	0.00	0.00	0.00	0.00	1.54	0.05	0.00	0.00	0.08
Jet Flavor Response	0.78	11.19	72.85	0.01	0.02	6.54	1.00	0.00	0.00	1.41
Flavor Tag Eff. extrapolation	0.08	0.19	0.94	0.00	0.08	0.05	0.10	0.00	0.00	0.05
Jet Pile-up p_T Term	0.81	2.60	73.65	0.00	0.01	7.84	1.14	0.00	0.00	1.55
Jet Energy Resolution	0.93	12.86	85.21	390.48	0.20	15.81	2.59	0.00	0.00	8.18
Jet EtaIntercalibration Non-Closure	0.85	7.36	73.66	0.39	0.01	5.09	0.94	0.00	0.00	1.08
Electron Eff. ID CorrUncertaintyNP14	0.39	0.41	0.58	0.78	0.40	0.56	0.43	0.00	0.00	0.44
Electron Eff. ID CorrUncertaintyNP12	0.01	0.02	0.05	0.05	0.05	0.04	0.02	0.00	0.00	0.04
Electron Eff. ID CorrUncertaintyNP13	0.02	0.03	0.01	0.09	0.02	0.02	0.02	0.00	0.00	0.02
Electron Eff. ID CorrUncertaintyNP10	0.10	0.10	0.07	0.18	0.04	0.13	0.10	0.00	0.00	0.11
Electron Eff. ID CorrUncertaintyNP11	0.00	0.03	0.06	0.58	0.01	0.03	0.01	0.00	0.00	0.02
e/γ Scale LARCALIB EXTRA2015PRE	0.10	0.02	0.09	0.00	0.00	1.90	0.11	0.00	0.00	0.09
Muon MS	0.23	0.68	1.33	0.00	0.00	4.08	0.29	0.00	0.00	0.87
Muon Iso Stat.	0.03	0.02	0.03	0.05	0.04	0.02	0.03	0.00	0.00	0.02
MET Soft Trk. Scale	0.14	4.87	0.00	0.00	0.00	2.99	0.41	0.00	0.00	0.20
Jet EffectiveNP 4	0.36	2.42	2.82	0.39	0.00	2.10	0.17	0.00	0.00	0.47
Jet EffectiveNP 7	0.10	2.90	0.00	0.39	0.00	0.01	0.11	0.00	0.00	0.38
Jet EffectiveNP 6	0.20	4.87	0.00	0.39	0.00	1.74	0.11	0.00	0.00	0.07
Jet EffectiveNP 1	0.35	6.90	4.86	0.39	0.02	5.23	0.60	0.00	0.00	0.81
Jet Jvt Efficiency	0.04	0.29	0.19	0.00	0.10	0.21	0.04	0.00	0.00	0.12
Jet EffectiveNP 2	0.47	4.91	4.01	0.39	0.01	2.71	0.43	0.00	0.00	0.53
Flavor Tag Eff. Eigen C 0	0.46	0.86	3.08	0.00	0.14	1.38	0.53	0.00	0.00	0.61
Muon Eff. TrigSystUncertainty	0.05	0.06	0.04	0.03	0.02	0.06	0.05	0.00	0.00	0.05
Flavor Tag Eff. Eigen C 2	0.13	0.18	0.84	0.00	0.08	0.07	0.16	0.00	0.00	0.08
Flavor Tag Eff. Eigen Light 3	0.09	0.56	0.33	0.15	0.68	0.46	0.10	0.00	0.00	0.31
Jet EtaIntercalibration Modelling	1.19	10.98	4.00	0.38	0.01	6.59	1.85	0.00	0.00	1.86
Electron Eff. Reco TOTAL 1NPCOR PLUS UNCOR	0.16	0.16	0.21	0.21	0.26	0.18	0.17	0.00	0.00	0.18
MET Soft Trk. ResoPerp	0.36	6.98	0.00	0.00	0.00	2.89	0.54	0.00	0.00	0.74
Flavor Tag Eff. extrapolation from charm	0.00	0.44	1.34	0.00	0.00	0.75	0.00	0.00	0.00	0.26
Muon TTVA Sys.	0.07	0.05	0.06	0.00	0.18	0.04	0.04	0.00	0.00	0.05
Jet EffectiveNP 5	0.23	4.87	0.00	0.39	0.00	0.95	0.11	0.00	0.00	0.38
Jet Pile-up OffsetNPV	0.31	4.46	72.84	0.39	100.49	5.13	0.48	0.00	0.00	0.71
Jet Flavor Composition	1.89	40.96	69.57	102.99	100.51	9.03	2.64	0.00	0.00	4.00
Charge Mis-ID Energy Corr.	0.00	0.00	0.00	0.00	0.00	0.00	0.00	6.46	0.00	0.00
Charge Mis-ID Scale Fac.	0.00	0.00	0.00	0.00	0.00	0.00	0.00	2.98	0.00	0.00
Non-Prompt μ Sys.	0.00	0.00	0.00	0.00	0.00	0.00	0.00	0.00	70.34	0.00
Non-Prompt e Sys.	0.00	0.00	0.00	0.00	0.00	0.00	0.00	0.00	34.27	0.00
Non-Prompt μ Stat.	0.00	0.00	0.00	0.00	0.00	0.00	0.00	0.00	5.08	0.00
Non-Prompt e Stat.	0.00	0.00	0.00	0.00	0.00	0.00	0.00	0.00	11.50	0.00

Nuisance Parameter	Relativ Effect on Sample [%]									
	$W^\pm W^\pm jj$-Ew	top	tri-boson	$Z\gamma$	$W^\pm\gamma$	ZZ	$W^\pm W^\pm jj$-Qcd	Charge Mis-ID	Non-Prompt	$W^\pm Z$

Table B.4: Summary of the relative effects of all shape nuisance parameters in the $e^-\mu^-/\mu^-e^-$ channel of the signal region.

B.3.5 $\mu^+\mu^+$ Channel, Signal Region

Nuisance Parameter	Relativ Effect on Sample [%]									
	$W^\pm W^\pm jj$-Ew	top	tri-boson	$Z\gamma$	$W^\pm\gamma$	ZZ	$W^\pm W^\pm jj$-Qcd	Charge Mis-ID	Non-Prompt	$W^\pm Z$
Jet Pile-up OffsetMu	0.36	6.00	11.42	0.00	0.00	7.53	0.73	0.00	0.00	1.80
Muon Iso Sys.	0.42	0.42	0.42	0.00	0.00	0.41	0.42	0.00	0.00	0.42
e/γ Scale ALLCORR	0.01	0.00	0.00	0.00	0.00	0.00	0.00	0.00	0.00	0.04
Muon Eff. Stat.	0.38	0.34	0.75	0.00	0.00	0.33	0.37	0.00	0.00	0.37
Jet EffectiveNP 3	0.31	1.87	0.00	0.00	0.00	1.76	0.43	0.00	0.00	0.30
$W^\pm W^\pm$ EW Scale	2.29	0.00	0.00	0.00	0.00	0.00	0.00	0.00	0.00	0.00
Flavor Tag Eff. Eigen C 1	0.17	0.46	1.01	0.00	0.00	0.30	0.25	0.00	0.00	0.17
Jet PunchThrough MC15	0.02	0.01	0.00	0.00	0.00	0.00	0.08	0.00	0.00	0.10
Jet Pile-up RhoTopology	0.53	11.67	11.47	0.00	0.00	5.17	1.04	0.00	0.00	2.14
Jet EffectiveNP 8restTerm	0.22	0.03	0.00	0.00	0.00	0.48	0.35	0.00	0.00	0.32
Interference	2.45	0.00	0.00	0.00	0.00	0.00	0.00	0.00	0.00	0.00
Jet BJES Response	0.01	1.04	0.00	0.00	0.00	0.01	0.00	0.00	0.00	0.06
Jet EtaIntercalibration Total Stat.	0.29	0.81	0.03	0.00	0.00	1.99	0.62	0.00	0.00	0.96
e/γ RESOLUTION ALL	0.00	0.00	0.00	0.00	0.00	0.46	0.00	0.00	0.00	0.04
MET Soft Trk. Resolution	0.16	0.94	0.00	0.00	0.00	1.20	0.34	0.00	0.00	0.52
$W^\pm W^\pm$ EW Shower	5.56	0.00	0.00	0.00	0.00	0.00	0.00	0.00	0.00	0.00
Muon ID	0.28	4.38	0.00	0.00	0.00	7.14	0.42	0.00	0.00	1.50
Flavor Tag Eff. Eigen Light 2	0.16	0.17	0.24	0.00	0.00	0.23	0.24	0.00	0.00	0.24
Flavor Tag Eff. Eigen Light 1	0.38	0.38	0.52	0.00	0.00	0.53	0.54	0.00	0.00	0.53
Flavor Tag Eff. Eigen Light 0	1.63	1.52	2.07	0.00	0.00	2.12	2.34	0.00	0.00	2.15
Flavor Tag Eff. Eigen Light 4	0.09	0.03	0.10	0.00	0.00	0.09	0.15	0.00	0.00	0.06
Pile-up Reweight. data SF	2.20	7.46	13.77	0.00	0.00	7.77	2.16	0.00	0.00	4.23
$W^\pm W^\pm$ EW PDF	0.65	0.00	0.00	0.00	0.00	0.00	0.00	0.00	0.00	0.00
Muon Eff. TrigStatUncertainty	0.24	0.15	0.28	0.00	0.00	0.16	0.20	0.00	0.00	0.23
Muon Eff. Sys.	1.68	1.66	2.08	0.00	0.00	1.65	1.70	0.00	0.00	1.72
Flavor Tag Eff. Eigen B 1	0.01	4.40	0.00	0.00	0.00	0.12	0.03	0.00	0.00	0.02
Flavor Tag Eff. Eigen B 0	0.04	10.58	0.00	0.00	0.00	0.18	0.09	0.00	0.00	0.14
Flavor Tag Eff. Eigen B 2	0.00	1.25	0.00	0.00	0.00	0.04	0.02	0.00	0.00	0.01
$W^\pm W^\pm$ EW α_s	0.23	0.00	0.00	0.00	0.00	0.00	0.00	0.00	0.00	0.00
Muon TTVA Stat.	0.16	0.14	0.15	0.00	0.00	0.15	0.15	0.00	0.00	0.15
$W^\pm W^\pm$ EW EW Corr.	3.67	0.00	0.00	0.00	0.00	0.00	0.00	0.00	0.00	0.00
Muon Scale	0.17	2.65	0.00	0.00	0.00	8.86	0.38	0.00	0.00	1.18
Jet Flavor Response	0.74	13.53	0.05	0.00	0.00	4.44	1.35	0.00	0.00	3.13
Flavor Tag Eff. extrapolation	0.04	0.21	0.02	0.00	0.00	0.03	0.09	0.00	0.00	0.05
Jet Pile-up p_T Term	1.06	10.88	0.03	0.00	0.00	2.77	1.34	0.00	0.00	3.34
Jet Energy Resolution	1.02	15.94	17.92	0.00	0.00	37.43	1.53	0.00	0.00	8.47
Jet EtaIntercalibration Non-Closure	0.63	6.22	0.02	0.00	0.00	2.61	0.82	0.00	0.00	1.68
Muon MS	0.25	4.37	0.00	0.00	0.00	7.35	0.50	0.00	0.00	1.58
Muon Iso Stat.	0.05	0.05	0.06	0.00	0.00	0.04	0.04	0.00	0.00	0.05
MET Soft Trk. Scale	0.12	1.74	0.00	0.00	0.00	2.22	0.14	0.00	0.00	0.45
Jet EffectiveNP 4	0.18	0.03	0.00	0.00	0.00	0.52	0.34	0.00	0.00	0.15

Nuisance Parameter	Relativ Effect on Sample [%]									
	$W^{\pm}W^{\pm}jj$-EW	top	tri-boson	$Z\gamma$	$W^{\pm}\gamma$	ZZ	$W^{\pm}W^{\pm}jj$-QCD	Charge Mis-ID	Non-Prompt	$W^{\pm}Z$
Jet EffectiveNP 7	0.06	0.01	0.00	0.00	0.00	0.01	0.27	0.00	0.00	0.58
Jet EffectiveNP 6	0.09	0.03	0.00	0.00	0.00	0.01	0.34	0.00	0.00	0.22
Jet EffectiveNP 1	0.50	2.63	0.06	0.00	0.00	2.67	1.09	0.00	0.00	1.21
Jet JVT Efficiency	0.03	0.36	0.31	0.00	0.00	0.31	0.04	0.00	0.00	0.06
Jet EffectiveNP 2	0.42	1.88	0.02	0.00	0.00	2.29	0.70	0.00	0.00	1.15
Flavor Tag Eff. Eigen C 0	0.28	1.20	2.98	0.00	0.00	1.39	0.42	0.00	0.00	0.84
Muon Eff. TrigSystUncertainty	0.40	0.36	0.44	0.00	0.00	0.32	0.36	0.00	0.00	0.37
Flavor Tag Eff. Eigen C 2	0.07	0.28	0.06	0.00	0.00	0.07	0.13	0.00	0.00	0.06
Flavor Tag Eff. Eigen Light 3	0.05	0.31	0.30	0.00	0.00	0.54	0.12	0.00	0.00	0.37
Jet EtaIntercalibration Modelling	1.02	12.60	11.73	0.00	0.00	12.06	1.32	0.00	0.00	3.99
MET Soft Trk. ResoPerp	0.19	0.94	0.00	0.00	0.00	2.01	0.45	0.00	0.00	1.49
Flavor Tag Eff. extrapolation from charm	0.00	0.47	1.22	0.00	0.00	0.48	0.00	0.00	0.00	0.42
Muon TTVA Sys.	0.14	0.09	0.11	0.00	0.00	0.07	0.09	0.00	0.00	0.09
Jet EffectiveNP 5	0.22	0.02	0.00	0.00	0.00	1.00	0.22	0.00	0.00	0.55
Jet Pile-up OffsetNPV	0.26	1.93	0.03	0.00	0.00	1.39	0.53	0.00	0.00	1.52
Jet Flavor Composition	1.62	18.22	13.43	0.00	0.00	14.38	2.67	0.00	0.00	5.38
Non-Prompt μ Sys.	0.00	0.00	0.00	0.00	0.00	0.00	0.00	0.00	17.18	0.00
Non-Prompt μ Stat.	0.00	0.00	0.00	0.00	0.00	0.00	0.00	0.00	9.26	0.00

Table B.5: Summary of the relative effects of all shape nuisance parameters in the $\mu^{+}\mu^{+}$ channel of the signal region.

B.3.6 $\mu^-\mu^-$ Channel, Signal Region

Nuisance Parameter	Relativ Effect on Sample [%]									
	$W^\pm W^\pm jj$-Ew	top	tri-boson	$Z\gamma$	$W^\pm\gamma$	ZZ	$W^\pm W^\pm jj$-QCD	Charge Mis-ID	Non-Prompt	$W^\pm Z$
Jet Pile-up OffsetMu	0.41	1.24	3.81	0.00	0.00	1.77	0.60	0.00	0.00	2.05
Muon Iso Sys.	0.43	0.42	0.58	0.00	0.00	0.42	0.44	0.00	0.00	0.43
Muon Eff. Stat.	0.38	0.38	0.33	0.00	0.00	0.36	0.37	0.00	0.00	0.37
Jet EffectiveNP 3	0.63	2.83	3.81	0.00	0.00	0.85	0.46	0.00	0.00	0.57
$W^\pm W^\pm$ EW Scale	2.04	0.00	0.00	0.00	0.00	0.00	0.00	0.00	0.00	0.00
Flavor Tag Eff. Eigen C 1	0.30	0.30	1.37	0.00	0.00	0.12	0.42	0.00	0.00	0.23
Jet PunchThrough MC15	0.00	0.00	0.00	0.00	0.00	0.00	0.25	0.00	0.00	0.00
Jet Pile-up RhoTopology	0.84	19.71	4.01	0.00	0.00	5.71	0.65	0.00	0.00	3.13
Jet EffectiveNP 8restTerm	0.27	2.89	3.81	0.00	0.00	0.66	0.29	0.00	0.00	0.17
Interference	2.38	0.00	0.00	0.00	0.00	0.00	0.00	0.00	0.00	0.00
Jet BJES Response	0.00	7.42	0.00	0.00	0.00	0.01	0.07	0.00	0.00	0.00
Jet EtaIntercalibration Total Stat.	0.33	2.93	3.79	0.00	0.00	3.16	0.36	0.00	0.00	0.33
MET Soft Trk. Resolution	0.40	0.00	0.00	0.00	0.00	3.73	0.32	0.00	0.00	1.10
$W^\pm W^\pm$ EW Shower	5.26	0.00	0.00	0.00	0.00	0.00	0.00	0.00	0.00	0.00
Muon ID	0.48	7.74	1.26	0.00	0.00	5.61	0.47	0.00	0.00	1.93
Flavor Tag Eff. Eigen Light 2	0.18	0.25	0.22	0.00	0.00	0.27	0.25	0.00	0.00	0.22
Flavor Tag Eff. Eigen Light 1	0.39	0.55	0.48	0.00	0.00	0.60	0.55	0.00	0.00	0.49
Flavor Tag Eff. Eigen Light 0	1.63	2.08	1.92	0.00	0.00	2.35	2.32	0.00	0.00	1.96
Flavor Tag Eff. Eigen Light 4	0.11	0.16	0.15	0.00	0.00	0.07	0.14	0.00	0.00	0.07
Pile-up Reweight. data SF	3.09	15.77	23.19	0.00	0.00	15.57	3.31	0.00	0.00	6.80
$W^\pm W^\pm$ EW PDF	0.57	0.00	0.00	0.00	0.00	0.00	0.00	0.00	0.00	0.00
Muon Eff. TrigStatUncertainty	0.24	0.19	0.16	0.00	0.00	0.19	0.19	0.00	0.00	0.22
Muon Eff. Sys.	1.81	1.57	2.30	0.00	0.00	1.89	1.87	0.00	0.00	1.85
Flavor Tag Eff. Eigen B 1	0.01	5.26	0.00	0.00	0.00	0.40	0.03	0.00	0.00	0.04
Flavor Tag Eff. Eigen B 0	0.04	17.95	0.00	0.00	0.00	1.28	0.08	0.00	0.00	0.12
Flavor Tag Eff. Eigen B 2	0.00	2.13	0.00	0.00	0.00	0.25	0.01	0.00	0.00	0.01
$W^\pm W^\pm$ EW α_s	0.20	0.00	0.00	0.00	0.00	0.00	0.00	0.00	0.00	0.00
Muon TTVA Stat.	0.16	0.17	0.15	0.00	0.00	0.14	0.15	0.00	0.00	0.15
$W^\pm W^\pm$ EW EW Corr.	3.52	0.00	0.00	0.00	0.00	0.00	0.00	0.00	0.00	0.00
Muon Scale	0.19	7.80	1.22	0.00	0.00	3.09	0.45	0.00	0.00	1.43
Jet Flavor Response	0.96	4.45	4.04	0.00	0.00	3.65	2.29	0.00	0.00	3.77
Flavor Tag Eff. extrapolation	0.08	0.42	0.30	0.00	0.00	0.02	0.13	0.00	0.00	0.07
Jet Pile-up p_T Term	0.84	9.48	3.82	0.00	0.00	15.59	2.02	0.00	0.00	2.66
Jet Energy Resolution	1.91	14.24	19.68	0.00	0.00	35.86	3.19	0.00	0.00	13.36
Jet EtaIntercalibration Non-Closure	1.05	4.57	3.82	0.00	0.00	4.33	1.88	0.00	0.00	3.17
Muon MS	0.51	7.80	1.26	0.00	0.00	3.60	0.46	0.00	0.00	1.19
Muon Iso Stat.	0.05	0.05	0.08	0.00	0.00	0.04	0.05	0.00	0.00	0.05
MET Soft Trk. Scale	0.40	0.00	0.00	0.00	0.00	3.36	0.47	0.00	0.00	0.48
Jet EffectiveNP 4	0.14	2.89	3.81	0.00	0.00	0.66	0.37	0.00	0.00	0.25
Jet EffectiveNP 7	0.09	2.90	0.00	0.00	0.00	0.66	0.32	0.00	0.00	0.17
Jet EffectiveNP 6	0.09	2.90	0.00	0.00	0.00	0.51	0.21	0.00	0.00	0.17

Nuisance Parameter	Relativ Effect on Sample [%]									
	$W^\pm W^\pm jj$-Ew	top	tri-boson	$Z\gamma$	$W^\pm\gamma$	ZZ	$W^\pm W^\pm jj$-Qcd	Charge Mis-ID	Non-Prompt	$W^\pm Z$
Jet EffectiveNP 1	0.86	19.56	4.04	0.00	0.00	3.95	2.38	0.00	0.00	2.64
Jet Jvt Efficiency	0.03	0.18	0.30	0.00	0.00	0.34	0.05	0.00	0.00	0.06
Jet EffectiveNP 2	1.03	2.67	0.01	0.00	0.00	1.82	0.77	0.00	0.00	0.35
Flavor Tag Eff. Eigen C 0	0.48	1.70	5.03	0.00	0.00	1.37	0.64	0.00	0.00	0.89
Muon Eff. TrigSystUncertainty	0.40	0.39	0.37	0.00	0.00	0.31	0.35	0.00	0.00	0.37
Flavor Tag Eff. Eigen C 2	0.14	0.43	0.74	0.00	0.00	0.03	0.21	0.00	0.00	0.11
Flavor Tag Eff. Eigen Light 3	0.08	0.42	0.37	0.00	0.00	0.35	0.11	0.00	0.00	0.30
Jet EtaIntercalibration Modelling	1.19	8.57	6.18	0.00	0.00	11.26	2.18	0.00	0.00	5.05
MET Soft Trk. ResoPerp	0.23	0.00	0.00	0.00	0.00	2.19	0.30	0.00	0.00	1.27
Flavor Tag Eff. extrapolation from charm	0.01	0.49	3.14	0.00	0.00	0.97	0.00	0.00	0.00	0.39
Muon TTVA Sys.	0.14	0.15	0.04	0.00	0.00	0.05	0.09	0.00	0.00	0.10
Jet EffectiveNP 5	0.30	0.01	0.00	0.00	0.00	0.66	0.26	0.00	0.00	0.21
Jet Pile-up OffsetNPV	0.48	2.93	3.82	0.00	0.00	8.47	2.27	0.00	0.00	1.34
Jet Flavor Composition	2.03	9.37	2.84	0.00	0.00	9.38	3.30	0.00	0.00	4.37
Non-Prompt μ Sys.	0.00	0.00	0.00	0.00	0.00	0.00	0.00	0.00	34.70	0.00
Non-Prompt μ Stat.	0.00	0.00	0.00	0.00	0.00	0.00	0.00	0.00	16.13	0.00

Table B.6: Summary of the relative effects of all shape nuisance parameters in the $\mu^-\mu^-$ channel of the signal region.

B.3.7 $\ell^{\pm}\ell^{\pm}$ Channel, $W^{\pm}Z$ Control Region

Nuisance Parameter	Relativ Effect on Sample [%]											
	$W^{\pm}W^{\pm}jj$-Ew	top	tri-boson	$Z\gamma$	$W^{\pm}\gamma$	ZZ	$W^{\pm}W^{\pm}jj$-Qcd	$W^{\pm}Z$	$W^{\pm}W^{\pm}$	$t\bar{t}$	Z+jets	$W^{\pm}$+jets
Jet Pile-up OffsetMu	0.00	0.34	0.70	0.34	0.00	0.43	0.00	0.47	0.00	0.00	0.00	0.00
Muon Iso Sys.	0.20	0.30	0.29	0.35	0.00	0.29	0.00	0.30	0.00	0.00	0.00	0.00
e/γ Scale ALLCORR	0.00	0.33	0.27	0.34	0.00	0.15	0.00	0.06	0.00	0.00	0.00	0.00
Muon Eff. Stat.	0.13	0.28	0.26	0.25	0.00	0.26	0.00	0.27	0.00	0.00	0.00	0.00
Jet EffectiveNP 3	0.00	0.26	0.07	0.00	0.00	0.20	0.00	0.25	0.00	0.00	0.00	0.00
$W^{\pm}W^{\pm}$ EW Scale	5.46	0.00	0.00	0.00	0.00	0.00	0.00	0.00	0.00	0.00	0.00	0.00
Flavor Tag Eff. Eigen C 1	0.00	0.11	0.13	0.12	0.00	0.12	0.00	0.18	0.00	0.00	0.00	0.00
Jet PunchThrough MC15	0.00	0.02	0.01	0.00	0.00	0.02	0.00	0.01	0.00	0.00	0.00	0.00
Jet Pile-up RhoTopology	0.01	1.32	1.85	0.27	0.00	2.52	0.00	1.54	0.00	0.00	0.00	0.00
Jet EffectiveNP 8restTerm	0.00	0.27	0.05	0.00	0.00	0.20	0.00	0.10	0.00	0.00	0.00	0.00
e/γ Scale LARTEMPERATURE EXTRA2015PRE	0.00	0.02	0.00	0.00	0.00	0.01	0.00	0.00	0.00	0.00	0.00	0.00
Jet BJES Response	0.00	0.38	0.03	0.00	0.00	0.03	0.00	0.01	0.00	0.00	0.00	0.00
Electron Eff. ID SIMPLIFIED UncorrUncertaintyNP8	0.70	0.22	0.36	0.04	0.00	0.18	0.00	0.23	0.00	0.00	0.00	0.00
Electron Eff. ID SIMPLIFIED UncorrUncertaintyNP7	0.00	0.02	0.03	0.04	0.00	0.03	0.00	0.03	0.00	0.00	0.00	0.00
Electron Eff. ID SIMPLIFIED UncorrUncertaintyNP6	0.00	0.03	0.02	0.00	0.00	0.02	0.00	0.02	0.00	0.00	0.00	0.00
Jet EtaIntercalibration Total Stat.	0.00	0.19	0.18	0.05	0.00	0.65	0.00	0.54	0.00	0.00	0.00	0.00
e/γ RESOLUTION ALL	0.00	0.30	0.34	0.00	0.00	0.23	0.00	0.04	0.00	0.00	0.00	0.00
MET Soft Trk. Resolution	0.00	0.21	0.32	23.15	0.00	2.38	0.00	0.48	0.00	0.00	0.00	0.00
Electron Eff. Iso TOTAL 1NPCOR PLUS UNCOR	0.10	0.22	0.44	0.17	0.00	0.24	0.00	0.27	0.00	0.00	0.00	0.00
e/γ Scale LARTEMPERATURE EXTRA2016PRE	0.00	0.02	0.00	0.00	0.00	0.01	0.00	0.00	0.00	0.00	0.00	0.00
Muon ID	0.00	0.33	0.42	0.33	0.00	0.15	0.00	0.36	0.00	0.00	0.00	0.00
Flavor Tag Eff. Eigen Light 2	0.13	0.15	0.21	0.21	0.00	0.19	0.00	0.21	0.00	0.00	0.00	0.00
Flavor Tag Eff. Eigen Light 1	0.27	0.33	0.46	0.44	0.00	0.42	0.00	0.46	0.00	0.00	0.00	0.00
Flavor Tag Eff. Eigen Light 0	1.07	1.29	1.84	1.74	0.00	1.63	0.00	1.82	0.00	0.00	0.00	0.00
Flavor Tag Eff. Eigen Light 4	0.06	0.02	0.05	0.02	0.00	0.03	0.00	0.06	0.00	0.00	0.00	0.00
Pile-up Reweight. data SF	42.73	1.61	0.46	7.01	0.00	3.67	0.00	1.46	0.00	0.00	0.00	0.00
$W^{\pm}W^{\pm}$ EW PDF	3.52	0.00	0.00	0.00	0.00	0.00	0.00	0.00	0.00	0.00	0.00	0.00
Electron Eff. Trigger TOTAL 1NPCOR PLUS UNCOR	0.01	0.02	0.02	0.02	0.00	0.02	0.00	0.02	0.00	0.00	0.00	0.00
Muon Eff. TrigStatUncertainty	0.00	0.13	0.10	0.09	0.00	0.11	0.00	0.12	0.00	0.00	0.00	0.00
Muon Eff. Sys.	0.83	1.24	1.31	1.01	0.00	1.22	0.00	1.28	0.00	0.00	0.00	0.00
Electron Eff. ID SIMPLIFIED UncorrUncertaintyNP15	0.00	0.01	0.01	0.07	0.00	0.02	0.00	0.01	0.00	0.00	0.00	0.00
Electron Eff. ID CorrUncertaintyNP6	0.01	0.00	0.00	0.02	0.00	0.00	0.00	0.00	0.00	0.00	0.00	0.00
Electron Eff. ID CorrUncertaintyNP7	0.03	0.00	0.00	0.03	0.00	0.00	0.00	0.00	0.00	0.00	0.00	0.00
Flavor Tag Eff. Eigen B 1	0.00	3.89	0.02	0.02	0.00	0.04	0.00	0.03	0.00	0.00	0.00	0.00
Flavor Tag Eff. Eigen B 0	0.00	12.63	0.06	0.20	0.00	0.21	0.00	0.17	0.00	0.00	0.00	0.00
Flavor Tag Eff. Eigen B 2	0.00	1.79	0.01	0.02	0.00	0.02	0.00	0.01	0.00	0.00	0.00	0.00
Electron Eff. ID CorrUncertaintyNP8	0.07	0.00	0.00	0.00	0.00	0.00	0.00	0.00	0.00	0.00	0.00	0.00
Electron Eff. ID CorrUncertaintyNP9	0.04	0.02	0.02	0.01	0.00	0.02	0.00	0.02	0.00	0.00	0.00	0.00
$W^{\pm}W^{\pm}$ EW α_s	1.26	0.00	0.00	0.00	0.00	0.00	0.00	0.00	0.00	0.00	0.00	0.00
Muon TTVA Stat.	0.08	0.11	0.10	0.11	0.00	0.11	0.00	0.11	0.00	0.00	0.00	0.00
Muon Scale	0.00	0.57	0.29	0.00	0.00	0.12	0.00	0.45	0.00	0.00	0.00	0.00

Nuisance Parameter	Relativ Effect on Sample [%]											
	$W^{\pm}W^{\pm}jj$-Ew	top	tri-boson	$Z\gamma$	$W^{\pm}\gamma$	ZZ	$W^{\pm}W^{\pm}jj$-Qcd	$W^{\pm}Z$	$W^{\pm}W^{\pm}$	$t\bar{t}$	Z+jets	$W^{\pm}$+jets
e/γ Scale E4SCINTILLATOR	0.00	0.05	0.01	0.00	0.00	0.03	0.00	0.02	0.00	0.00	0.00	0.00
Jet Flavor Response	0.01	1.45	1.40	0.06	0.00	2.27	0.00	1.51	0.00	0.00	0.00	0.00
Flavor Tag Eff. extrapolation	0.00	0.11	0.04	0.00	0.00	0.02	0.00	0.04	0.00	0.00	0.00	0.00
Jet Pile-up p_{T} Term	0.01	1.81	1.38	0.05	0.00	2.01	0.00	0.99	0.00	0.00	0.00	0.00
Jet Energy Resolution	0.12	4.91	7.55	61.18	0.00	6.40	0.00	2.56	0.00	0.00	0.00	0.00
Jet EtaIntercalibration Non-Closure	0.02	0.50	0.56	0.05	0.00	0.25	0.00	0.29	0.00	0.00	0.00	0.00
Electron Eff. ID CorrUncertaintyNP14	0.36	0.22	0.24	0.14	0.00	0.27	0.00	0.23	0.00	0.00	0.00	0.00
Electron Eff. ID CorrUncertaintyNP12	0.01	0.00	0.00	0.01	0.00	0.02	0.00	0.00	0.00	0.00	0.00	0.00
Electron Eff. ID CorrUncertaintyNP13	0.01	0.01	0.02	0.02	0.00	0.00	0.00	0.01	0.00	0.00	0.00	0.00
Electron Eff. ID CorrUncertaintyNP10	0.09	0.05	0.06	0.05	0.00	0.06	0.00	0.05	0.00	0.00	0.00	0.00
Electron Eff. ID CorrUncertaintyNP11	0.09	0.00	0.01	0.02	0.00	0.00	0.00	0.00	0.00	0.00	0.00	0.00
e/γ Scale LARCALIB EXTRA2015PRE	0.00	0.02	0.00	0.00	0.00	0.03	0.00	0.02	0.00	0.00	0.00	0.00
Muon MS	0.00	0.44	0.65	0.00	0.00	0.13	0.00	0.47	0.00	0.00	0.00	0.00
Muon Iso Stat.	0.01	0.03	0.04	0.03	0.00	0.03	0.00	0.04	0.00	0.00	0.00	0.00
MET Soft Trk. Scale	0.00	0.07	0.09	0.00	0.00	2.68	0.00	0.51	0.00	0.00	0.00	0.00
Jet EffectiveNP 4	0.00	0.33	0.02	0.00	0.00	0.24	0.00	0.16	0.00	0.00	0.00	0.00
Jet EffectiveNP 7	0.00	0.28	0.06	0.00	0.00	0.11	0.00	0.07	0.00	0.00	0.00	0.00
Jet EffectiveNP 6	0.00	0.13	0.05	0.00	0.00	0.08	0.00	0.05	0.00	0.00	0.00	0.00
Jet EffectiveNP 1	0.01	0.82	0.52	0.28	0.00	1.26	0.00	1.06	0.00	0.00	0.00	0.00
Jet Jvt Efficiency	0.00	0.08	0.06	0.26	0.00	0.15	0.00	0.08	0.00	0.00	0.00	0.00
Jet EffectiveNP 2	0.00	0.45	0.05	0.00	0.00	0.30	0.00	0.18	0.00	0.00	0.00	0.00
Flavor Tag Eff. Eigen C 0	0.00	0.41	0.89	0.73	0.00	0.70	0.00	0.42	0.00	0.00	0.00	0.00
Muon Eff. TrigSystUncertainty	0.01	0.23	0.18	0.21	0.00	0.20	0.00	0.20	0.00	0.00	0.00	0.00
Flavor Tag Eff. Eigen C 2	0.00	0.01	0.04	0.17	0.00	0.02	0.00	0.05	0.00	0.00	0.00	0.00
Flavor Tag Eff. Eigen Light 3	0.02	0.28	0.35	0.27	0.00	0.35	0.00	0.31	0.00	0.00	0.00	0.00
Jet EtaIntercalibration Modelling	0.01	2.00	3.01	0.34	0.00	3.24	0.00	2.11	0.00	0.00	0.00	0.00
Electron Eff. Reco TOTAL 1NPCOR PLUS UNCOR	0.11	0.09	0.12	0.09	0.00	0.10	0.00	0.10	0.00	0.00	0.00	0.00
MET Soft Trk. ResoPerp	0.00	0.40	0.05	0.00	0.00	2.05	0.00	0.45	0.00	0.00	0.00	0.00
Flavor Tag Eff. extrapolation from charm	0.00	0.06	0.55	0.00	0.00	0.40	0.00	0.00	0.00	0.00	0.00	0.00
Muon TTVA Sys.	0.00	0.10	0.09	0.11	0.00	0.08	0.00	0.09	0.00	0.00	0.00	0.00
Jet EffectiveNP 5	0.00	0.27	0.07	0.00	0.00	0.25	0.00	0.09	0.00	0.00	0.00	0.00
Jet Pile-up OffsetNPV	0.01	0.19	0.56	0.05	0.00	0.63	0.00	0.34	0.00	0.00	0.00	0.00
Jet Flavor Composition	0.03	4.04	5.85	2.82	0.00	6.62	0.00	4.57	0.00	0.00	0.00	0.00

Table B.7: Summary of the relative effects of all shape nuisance parameters in the $\ell^{\pm}\ell^{\pm}$ channel of the $W^{\pm}Z$ control region.

B.3.8 e^+e^+ Channel, Low-m_{jj} Control Region

Nuisance Parameter	Relativ Effect on Sample [%]									
	$W^\pm W^\pm jj$-EW	top	tri-boson	$Z\gamma$	$W^\pm\gamma$	ZZ	$W^\pm W^\pm jj$-QCD	Charge Mis-ID	Non-Prompt	$W^\pm Z$
Jet Pile-up OffsetMu	0.81	4.14	0.65	0.00	0.01	11.53	0.13	0.00	0.00	1.50
e/γ Scale ALLCORR	0.19	1.02	0.00	0.00	0.00	15.73	0.50	0.00	0.00	0.61
Jet EffectiveNP 3	0.16	0.03	0.01	0.00	0.00	11.16	0.51	0.00	0.00	1.02
$W^\pm W^\pm$ EW Scale	4.17	0.00	0.00	0.00	0.00	0.00	0.00	0.00	0.00	0.00
Flavor Tag Eff. Eigen C 1	0.20	0.14	0.14	0.00	0.00	0.01	0.23	0.00	0.00	0.19
Jet Pile-up RhoTopology	1.25	10.76	2.43	0.00	0.02	15.62	1.75	0.00	0.00	5.64
Jet EffectiveNP 8restTerm	0.17	0.00	0.01	0.00	0.00	0.00	0.16	0.00	0.00	0.28
Interference	8.26	0.00	0.00	0.00	0.00	0.00	0.00	0.00	0.00	0.00
Jet BJES Response	0.00	0.51	0.00	0.00	0.00	0.00	0.00	0.00	0.00	0.00
Electron Eff. ID SIMPLIFIED UncorrUncertaintyNP8	0.59	0.38	0.90	0.00	1.75	0.47	0.59	0.00	0.00	0.64
Electron Eff. ID SIMPLIFIED UncorrUncertaintyNP5	0.03	0.11	0.02	0.00	0.00	0.07	0.03	0.00	0.00	0.03
Electron Eff. ID SIMPLIFIED UncorrUncertaintyNP7	0.11	0.14	0.04	0.00	0.05	0.06	0.11	0.00	0.00	0.12
Electron Eff. ID SIMPLIFIED UncorrUncertaintyNP6	0.16	0.12	0.18	0.00	0.09	0.21	0.16	0.00	0.00	0.16
Jet EtaIntercalibration Total Stat.	0.65	0.10	0.01	0.00	0.00	11.17	0.41	0.00	0.00	1.69
e/γ RESOLUTION ALL	0.13	1.98	0.00	0.00	0.00	4.20	1.99	0.00	0.00	0.44
MET Soft Trk. Resolution	0.52	1.02	0.00	0.00	0.00	10.68	0.30	0.00	0.00	2.29
$W^\pm W^\pm$ EW Shower	12.06	0.00	0.00	0.00	0.00	0.00	0.00	0.00	0.00	0.00
Electron Eff. Iso TOTAL 1NPCOR PLUS UNCOR	0.51	0.37	1.04	0.00	2.62	0.53	0.59	0.00	0.00	0.61
Muon ID	0.00	0.00	1.06	0.00	0.00	0.00	0.00	0.00	0.00	0.00
Flavor Tag Eff. Eigen Light 2	0.21	0.17	0.19	0.00	0.23	0.16	0.23	0.00	0.00	0.20
Flavor Tag Eff. Eigen Light 1	0.44	0.37	0.42	0.00	0.49	0.35	0.49	0.00	0.00	0.43
Flavor Tag Eff. Eigen Light 0	1.66	1.35	1.53	0.00	1.86	1.31	1.85	0.00	0.00	1.62
Flavor Tag Eff. Eigen Light 4	0.11	0.11	0.11	0.00	0.04	0.01	0.10	0.00	0.00	0.07
Pile-up Reweight. data SF	4.21	5.41	11.31	0.00	9.28	6.70	1.90	0.00	0.00	5.20
$W^\pm W^\pm$ EW PDF	0.51	0.00	0.00	0.00	0.00	0.00	0.00	0.00	0.00	0.00
Electron Eff. Trigger TOTAL 1NPCOR PLUS UNCOR	0.02	0.04	0.02	0.00	0.00	0.03	0.03	0.00	0.00	0.03
Electron Eff. ID CorrUncertaintyNP6	0.01	0.00	0.01	0.00	0.03	0.01	0.00	0.00	0.00	0.01
Electron Eff. ID CorrUncertaintyNP7	0.01	0.03	0.01	0.00	0.01	0.01	0.02	0.00	0.00	0.02
Flavor Tag Eff. Eigen B 1	0.00	4.74	0.00	0.00	0.00	0.00	0.00	0.00	0.00	0.01
Flavor Tag Eff. Eigen B 0	0.00	9.92	0.00	0.00	0.00	0.00	0.00	0.00	0.00	0.01
Flavor Tag Eff. Eigen B 2	0.00	3.09	0.00	0.00	0.00	0.00	0.00	0.00	0.00	0.01
Electron Eff. ID CorrUncertaintyNP8	0.01	0.03	0.02	0.00	0.07	0.01	0.02	0.00	0.00	0.01
Electron Eff. ID CorrUncertaintyNP9	0.05	0.00	0.07	0.00	0.04	0.06	0.06	0.00	0.00	0.06
$W^\pm W^\pm$ EW α_s	0.28	0.00	0.00	0.00	0.00	0.00	0.00	0.00	0.00	0.00
$W^\pm W^\pm$ EW EW Corr.	7.64	0.00	0.00	0.00	0.00	0.00	0.00	0.00	0.00	0.00
Muon Scale	0.00	0.00	1.06	0.00	0.00	0.00	0.00	0.00	0.00	0.00
Jet Flavor Response	0.76	10.55	2.04	0.00	0.01	16.64	1.35	0.00	0.00	4.49
Flavor Tag Eff. extrapolation	0.02	0.03	0.00	0.00	0.00	0.00	0.04	0.00	0.00	0.03
Jet Pile-up p_T Term	0.54	5.18	1.38	0.00	0.00	11.44	0.84	0.00	0.00	1.80
Jet Energy Resolution	1.01	5.44	5.47	0.00	0.00	20.87	0.27	0.00	0.00	4.36
Jet EtaIntercalibration Non-Closure	0.53	1.79	2.44	0.00	0.01	8.85	1.66	0.00	0.00	4.05

Nuisance Parameter	Relativ Effect on Sample [%]									
	$W^{\pm}W^{\pm}jj$-Ew	top	tri-boson	$Z\gamma$	$W^{\pm}\gamma$	ZZ	$W^{\pm}W^{\pm}jj$-QCD	Charge Mis-ID	Non-Prompt	$W^{\pm}Z$
Electron Eff. ID CorrUncertaintyNP14	0.79	1.26	0.86	0.00	0.15	0.95	0.80	0.00	0.00	0.77
Electron Eff. ID CorrUncertaintyNP12	0.00	0.02	0.01	0.00	0.02	0.00	0.01	0.00	0.00	0.00
Electron Eff. ID CorrUncertaintyNP13	0.05	0.05	0.00	0.00	0.02	0.04	0.05	0.00	0.00	0.03
Electron Eff. ID CorrUncertaintyNP10	0.20	0.25	0.17	0.00	0.07	0.21	0.20	0.00	0.00	0.21
Electron Eff. ID CorrUncertaintyNP11	0.02	0.07	0.05	0.00	0.20	0.02	0.01	0.00	0.00	0.01
e/γ Scale LARCALIB EXTRA2015PRE	0.17	0.00	0.00	0.00	0.00	11.95	0.00	0.00	0.00	0.14
Muon MS	0.00	0.00	1.06	0.00	0.00	0.00	0.00	0.00	0.00	0.00
MET Soft Trk. Scale	0.17	1.02	0.00	0.00	0.00	12.47	0.27	0.00	0.00	0.53
Jet EffectiveNP 4	0.16	0.02	0.01	0.00	0.00	11.18	0.16	0.00	0.00	0.77
Jet EffectiveNP 7	0.15	0.03	0.00	0.00	0.00	0.00	0.51	0.00	0.00	0.10
Jet EffectiveNP 6	0.16	0.03	0.01	0.00	0.00	0.00	0.36	0.00	0.00	0.28
Jet EffectiveNP 1	1.60	9.52	0.66	0.00	0.01	15.55	1.34	0.00	0.00	5.12
Jet JVT Efficiency	0.11	0.35	0.30	0.00	0.25	0.14	0.06	0.00	0.00	0.16
Jet EffectiveNP 2	0.50	0.09	0.01	0.00	0.00	11.16	0.73	0.00	0.00	1.00
Flavor Tag Eff. Eigen C 0	0.53	0.57	1.63	0.00	0.00	0.57	0.56	0.00	0.00	1.20
Flavor Tag Eff. Eigen C 2	0.01	0.02	0.00	0.00	0.00	0.06	0.08	0.00	0.00	0.08
Flavor Tag Eff. Eigen Light 3	0.30	0.32	0.72	0.00	0.31	0.36	0.38	0.00	0.00	0.44
Jet EtaIntercalibration Modelling	1.16	8.65	6.87	0.00	0.01	16.80	1.89	0.00	0.00	3.98
Electron Eff. Reco TOTAL 1NPCOR PLUS UNCOR	0.31	0.37	0.26	0.00	0.30	0.29	0.30	0.00	0.00	0.29
MET Soft Trk. ResoPerp	0.03	0.00	0.00	0.00	0.00	18.16	0.26	0.00	0.00	0.44
Flavor Tag Eff. extrapolation from charm	0.00	0.59	1.59	0.00	0.00	0.34	0.00	0.00	0.00	0.69
Jet EffectiveNP 5	0.31	0.00	0.01	0.00	0.00	0.37	0.51	0.00	0.00	0.29
Jet Pile-up OffsetNPV	1.01	0.10	0.02	0.00	0.01	5.97	0.77	0.00	0.00	1.26
Jet Flavor Composition	0.64	13.52	17.37	0.00	25.67	28.82	1.44	0.00	0.00	11.97
Charge Mis-ID Energy Corr.	0.00	0.00	0.00	0.00	0.00	0.00	0.00	7.83	0.00	0.00
Charge Mis-ID Scale Fac.	0.00	0.00	0.00	0.00	0.00	0.00	0.00	7.40	0.00	0.00
Non-Prompt e Sys.	0.00	0.00	0.00	0.00	0.00	0.00	0.00	0.00	42.14	0.00
Non-Prompt e Stat.	0.00	0.00	0.00	0.00	0.00	0.00	0.00	0.00	20.41	0.00

Table B.8: Summary of the relative effects of all shape nuisance parameters in the $e^{+}e^{+}$ channel of the low-m_{jj} control region.

B.3.9 e^-e^- Channel, Low-m_{jj} Control Region

Nuisance Parameter	Relativ Effect on Sample [%]									
	$W^\pm W^\pm jj$-Ew	top	tri-boson	$Z\gamma$	$W^\pm\gamma$	ZZ	$W^\pm W^\pm jj$-Qcd	Charge Mis-ID	Non-Prompt	$W^\pm Z$
Jet Pile-up OffsetMu	0.95	4.08	17.38	0.00	0.01	0.01	0.51	0.00	0.00	2.28
e/γ Scale ALLCORR	0.53	0.00	0.00	0.00	0.00	1.24	0.76	0.00	0.00	2.61
Jet EffectiveNP 3	0.64	4.07	0.01	0.00	0.00	0.00	1.24	0.00	0.00	2.72
$W^\pm W^\pm$ EW Scale	4.17	0.00	0.00	0.00	0.00	0.00	0.00	0.00	0.00	0.00
Flavor Tag Eff. Eigen C 1	0.34	0.02	0.07	0.00	0.00	0.10	0.43	0.00	0.00	0.31
Jet PunchThrough MC15	0.00	0.00	0.00	0.00	0.00	0.00	0.00	0.00	0.00	0.19
Jet Pile-up RhoTopology	0.69	4.56	17.35	0.00	0.09	11.35	1.30	0.00	0.00	3.49
Jet EffectiveNP 8restTerm	0.21	0.00	0.00	0.00	0.00	0.00	0.51	0.00	0.00	0.17
Interference	8.26	0.00	0.00	0.00	0.00	0.00	0.00	0.00	0.00	0.00
e/γ Scale LARTEMPERATURE EXTRA2015PRE	0.00	0.00	0.00	0.00	0.00	1.23	0.00	0.00	0.00	0.00
Jet BJES Response	0.00	17.62	0.00	0.00	0.00	0.00	0.00	0.00	0.00	1.24
Electron Eff. ID SIMPLIFIED UncorrUncertaintyNP8	0.63	0.37	1.01	0.00	0.36	0.52	0.79	0.00	0.00	0.70
Electron Eff. ID SIMPLIFIED UncorrUncertaintyNP5	0.05	0.05	0.00	0.00	0.00	0.00	0.04	0.00	0.00	0.02
Electron Eff. ID SIMPLIFIED UncorrUncertaintyNP7	0.09	0.21	0.04	0.00	0.26	0.18	0.11	0.00	0.00	0.10
Electron Eff. ID SIMPLIFIED UncorrUncertaintyNP6	0.16	0.14	0.14	0.00	0.00	0.16	0.12	0.00	0.00	0.16
Jet EtaIntercalibration Total Stat.	0.42	4.08	0.01	0.00	0.02	2.77	0.41	0.00	0.00	3.32
e/γ RESOLUTION ALL	0.84	4.39	0.00	0.00	0.00	2.09	1.66	0.00	0.00	3.40
MET Soft Trk. Resolution	0.35	7.08	0.00	0.00	0.00	0.18	0.38	0.00	0.00	0.39
$W^\pm W^\pm$ EW Shower	12.06	0.00	0.00	0.00	0.00	0.00	0.00	0.00	0.00	0.00
Electron Eff. Iso TOTAL 1NPCOR PLUS UNCOR	0.66	0.11	1.51	0.00	0.15	0.34	0.85	0.00	0.00	0.73
e/γ Scale LARTEMPERATURE EXTRA2016PRE	0.00	0.00	0.00	0.00	0.00	1.23	0.00	0.00	0.00	0.00
Flavor Tag Eff. Eigen Light 2	0.21	0.16	0.22	0.00	0.23	0.22	0.21	0.00	0.00	0.20
Flavor Tag Eff. Eigen Light 1	0.45	0.35	0.50	0.00	0.61	0.46	0.46	0.00	0.00	0.43
Flavor Tag Eff. Eigen Light 0	1.68	1.29	1.86	0.00	2.23	1.70	1.73	0.00	0.00	1.63
Flavor Tag Eff. Eigen Light 4	0.06	0.25	0.01	0.00	0.41	0.16	0.05	0.00	0.00	0.05
Pile-up Reweight. data SF	3.81	5.20	16.19	0.00	12.57	61.27	2.09	0.00	0.00	3.68
$W^\pm W^\pm$ EW PDF	0.51	0.00	0.00	0.00	0.00	0.00	0.00	0.00	0.00	0.00
Electron Eff. Trigger TOTAL 1NPCOR PLUS UNCOR	0.03	0.03	0.02	0.00	0.00	0.03	0.02	0.00	0.00	0.03
Electron Eff. ID CorrUncertaintyNP6	0.00	0.02	0.01	0.00	0.02	0.01	0.01	0.00	0.00	0.01
Electron Eff. ID CorrUncertaintyNP7	0.01	0.01	0.04	0.00	0.00	0.01	0.01	0.00	0.00	0.01
Flavor Tag Eff. Eigen B 1	0.01	2.96	0.00	0.00	0.00	0.00	0.00	0.00	0.00	0.05
Flavor Tag Eff. Eigen B 0	0.17	15.37	0.00	0.00	0.00	0.00	0.00	0.00	0.00	0.12
Flavor Tag Eff. Eigen B 2	0.01	2.42	0.00	0.00	0.00	0.00	0.00	0.00	0.00	0.04
Electron Eff. ID CorrUncertaintyNP8	0.01	0.02	0.04	0.00	0.04	0.02	0.03	0.00	0.00	0.03
Electron Eff. ID CorrUncertaintyNP9	0.04	0.13	0.07	0.00	0.20	0.07	0.07	0.00	0.00	0.08
$W^\pm W^\pm$ EW α_s	0.28	0.00	0.00	0.00	0.00	0.00	0.00	0.00	0.00	0.00
$W^\pm W^\pm$ EW EW Corr.	7.64	0.00	0.00	0.00	0.00	0.00	0.00	0.00	0.00	0.00
e/γ Scale E4SCINTILLATOR	0.00	0.00	0.00	0.00	0.00	1.23	0.00	0.00	0.00	0.00
Jet Flavor Response	0.35	6.00	17.35	0.00	0.07	5.00	1.32	0.00	0.00	6.14
Flavor Tag Eff. extrapolation	0.02	0.06	0.00	0.00	0.00	0.02	0.06	0.00	0.00	0.02
Jet Pile-up p_T Term	0.23	3.95	17.37	0.00	0.02	5.61	0.47	0.00	0.00	4.18

Nuisance Parameter	Relativ Effect on Sample [%]									
	$W^{\pm}W^{\pm}jj$-Ew	top	tri-boson	$Z\gamma$	$W^{\pm}\gamma$	ZZ	$W^{\pm}W^{\pm}jj$-Qcd	Charge Mis-ID	Non-Prompt	$W^{\pm}Z$
Jet Energy Resolution	10.21	26.82	20.44	0.00	0.14	19.80	5.75	0.00	0.00	0.44
Jet EtaIntercalibration Non-Closure	3.06	10.09	17.38	0.00	0.04	1.41	0.47	0.00	0.00	0.63
Electron Eff. ID CorrUncertaintyNP14	0.84	1.30	0.44	0.00	1.51	0.76	0.67	0.00	0.00	0.81
Electron Eff. ID CorrUncertaintyNP12	0.01	0.00	0.01	0.00	0.07	0.04	0.01	0.00	0.00	0.01
Electron Eff. ID CorrUncertaintyNP13	0.05	0.04	0.03	0.00	0.02	0.01	0.12	0.00	0.00	0.04
Electron Eff. ID CorrUncertaintyNP10	0.19	0.28	0.10	0.00	0.30	0.22	0.17	0.00	0.00	0.19
Electron Eff. ID CorrUncertaintyNP11	0.02	0.06	0.13	0.00	0.04	0.01	0.02	0.00	0.00	0.02
e/γ Scale LARCALIB EXTRA2015PRE	0.20	0.00	0.00	0.00	0.00	1.23	1.19	0.00	0.00	2.37
MET Soft Trk. Scale	0.08	0.00	0.00	0.00	0.00	6.56	1.22	0.00	0.00	2.83
Jet EffectiveNP 4	0.64	4.07	0.01	0.00	0.00	0.01	0.91	0.00	0.00	2.72
Jet EffectiveNP 7	0.00	0.00	0.00	0.00	0.00	0.00	0.03	0.00	0.00	0.14
Jet EffectiveNP 6	0.21	0.00	0.00	0.00	0.00	0.00	0.45	0.00	0.00	0.15
Jet EffectiveNP 1	0.63	4.28	17.36	0.00	0.07	8.75	0.33	0.00	0.00	6.17
Jet Jvt Efficiency	0.11	0.12	0.35	0.00	0.00	0.28	0.23	0.00	0.00	0.10
Jet EffectiveNP 2	0.47	4.04	0.01	0.00	0.01	0.01	1.21	0.00	0.00	2.87
Flavor Tag Eff. Eigen C 0	0.74	0.94	0.38	0.00	0.00	0.64	0.87	0.00	0.00	0.95
Flavor Tag Eff. Eigen C 2	0.01	0.09	0.00	0.00	0.00	0.02	0.10	0.00	0.00	0.10
Flavor Tag Eff. Eigen Light 3	0.30	0.39	0.52	0.00	1.87	0.43	0.31	0.00	0.00	0.36
Jet EtaIntercalibration Modelling	1.97	18.62	17.38	0.00	0.08	7.39	1.63	0.00	0.00	2.76
Electron Eff. Reco TOTAL 1NPCOR PLUS UNCOR	0.32	0.32	0.23	0.00	0.22	0.24	0.33	0.00	0.00	0.31
MET Soft Trk. ResoPerp	0.59	0.00	0.00	0.00	0.00	0.65	1.00	0.00	0.00	2.58
Flavor Tag Eff. extrapolation from charm	0.00	0.00	0.22	0.00	0.00	0.39	0.00	0.00	0.00	0.32
Jet EffectiveNP 5	0.00	0.01	0.00	0.00	0.00	0.01	0.73	0.00	0.00	2.87
Jet Pile-up OffsetNPV	0.25	4.16	0.01	0.00	0.06	2.77	0.69	0.00	0.00	2.39
Jet Flavor Composition	1.23	9.61	17.33	0.00	0.16	9.98	4.01	0.00	0.00	3.14
Charge Mis-ID Energy Corr.	0.00	0.00	0.00	0.00	0.00	0.00	0.00	0.89	0.00	0.00
Charge Mis-ID Scale Fac.	0.00	0.00	0.00	0.00	0.00	0.00	0.00	10.65	0.00	0.00
Non-Prompt e Sys.	0.00	0.00	0.00	0.00	0.00	0.00	0.00	0.00	58.04	0.00
Non-Prompt e Stat.	0.00	0.00	0.00	0.00	0.00	0.00	0.00	0.00	14.00	0.00

Table B.9: Summary of the relative effects of all shape nuisance parameters in the $e^{-}e^{-}$ channel of the low-m_{jj} control region.

B.3.10 $e^+\mu^+/\mu^+e^+$ Channel, Low-m_{jj} Control Region

Nuisance Parameter	Relativ Effect on Sample [%]									
	$W^\pm W^\pm jj$-Ew	top	tri-boson	$Z\gamma$	$W^\pm\gamma$	ZZ	$W^\pm W^\pm jj$-Qcd	Charge Mis-ID	Non-Prompt	$W^\pm Z$
Jet Pile-up OffsetMu	0.21	1.47	2.24	0.00	0.01	1.94	0.46	0.00	0.00	0.19
Muon Iso Sys.	0.21	0.21	0.21	0.00	0.20	0.21	0.21	0.00	0.00	0.21
e/γ Scale ALLCORR	0.27	0.62	0.04	0.00	0.00	0.74	0.13	0.00	0.00	0.14
Muon Eff. Stat.	0.20	0.20	0.18	0.00	0.15	0.17	0.19	0.00	0.00	0.18
Jet EffectiveNP 3	0.46	0.45	0.26	0.00	0.01	0.50	0.32	0.00	0.00	0.26
$W^\pm W^\pm$ EW Scale	4.17	0.00	0.00	0.00	0.00	0.00	0.00	0.00	0.00	0.00
Flavor Tag Eff. Eigen C 1	0.24	0.26	0.10	0.00	0.00	0.01	0.25	0.00	0.00	0.12
Jet PunchThrough MC15	0.00	0.00	0.00	0.00	0.00	0.00	0.00	0.00	0.00	0.02
Jet Pile-up RhoTopology	0.07	2.22	5.25	0.00	14.97	7.99	1.53	0.00	0.00	0.91
Jet EffectiveNP 8restTerm	0.20	0.01	0.00	0.00	0.00	0.00	0.06	0.00	0.00	0.09
Interference	8.26	0.00	0.00	0.00	0.00	0.00	0.00	0.00	0.00	0.00
e/γ Scale LARTEMPERATURE EXTRA2015PRE	0.06	0.24	0.00	0.00	0.00	0.10	0.00	0.00	0.00	0.01
Jet BJES Response	0.06	0.94	0.00	0.00	0.08	0.00	0.03	0.00	0.00	0.18
Electron Eff. ID SIMPLIFIED UncorrUncertaintyNP8	0.20	0.15	0.16	0.00	0.56	0.12	0.14	0.00	0.00	0.14
Electron Eff. ID SIMPLIFIED UncorrUncertaintyNP5	0.02	0.02	0.03	0.00	0.00	0.02	0.01	0.00	0.00	0.01
Electron Eff. ID SIMPLIFIED UncorrUncertaintyNP7	0.04	0.04	0.04	0.00	0.00	0.04	0.03	0.00	0.00	0.03
Electron Eff. ID SIMPLIFIED UncorrUncertaintyNP6	0.07	0.05	0.04	0.00	0.00	0.03	0.06	0.00	0.00	0.06
Jet EtaIntercalibration Total Stat.	0.18	2.38	2.23	0.00	0.01	1.47	0.32	0.00	0.00	0.16
e/γ RESOLUTION ALL	0.08	0.25	0.01	0.00	0.00	1.01	0.05	0.00	0.00	0.17
MET Soft Trk. Resolution	0.01	0.52	0.69	0.00	0.00	1.64	0.04	0.00	0.00	0.35
$W^\pm W^\pm$ EW Shower	12.06	0.00	0.00	0.00	0.00	0.00	0.00	0.00	0.00	0.00
Electron Eff. Iso TOTAL 1NPCOR PLUS UNCOR	0.26	0.24	0.22	0.00	1.43	0.19	0.20	0.00	0.00	0.26
e/γ Scale LARTEMPERATURE EXTRA2016PRE	0.06	0.24	0.00	0.00	0.00	0.10	0.00	0.00	0.00	0.01
Muon ID	0.15	2.09	0.07	0.00	0.02	4.93	0.11	0.00	0.00	0.30
Flavor Tag Eff. Eigen Light 2	0.20	0.17	0.15	0.00	0.29	0.19	0.21	0.00	0.00	0.20
Flavor Tag Eff. Eigen Light 1	0.42	0.37	0.32	0.00	0.62	0.41	0.45	0.00	0.00	0.43
Flavor Tag Eff. Eigen Light 0	1.60	1.37	1.17	0.00	2.47	1.53	1.70	0.00	0.00	1.62
Flavor Tag Eff. Eigen Light 4	0.08	0.01	0.01	0.00	0.13	0.02	0.08	0.00	0.00	0.04
Pile-up Reweight. data SF	1.80	12.82	7.80	0.00	14.47	9.59	1.29	0.00	0.00	1.77
$W^\pm W^\pm$ EW PDF	0.51	0.00	0.00	0.00	0.00	0.00	0.00	0.00	0.00	0.00
Electron Eff. Trigger TOTAL 1NPCOR PLUS UNCOR	0.05	0.04	0.03	0.00	0.06	0.05	0.06	0.00	0.00	0.06
Muon Eff. TrigStatUncertainty	0.03	0.03	0.02	0.00	0.02	0.04	0.03	0.00	0.00	0.03
Muon Eff. Sys.	0.79	0.80	0.85	0.00	0.78	0.86	0.79	0.00	0.00	0.76
Electron Eff. ID SIMPLIFIED UncorrUncertaintyNP15	0.04	0.04	0.06	0.00	0.00	0.11	0.06	0.00	0.00	0.06
Electron Eff. ID SIMPLIFIED UncorrUncertaintyNP14	0.01	0.00	0.01	0.00	0.00	0.02	0.01	0.00	0.00	0.01
Electron Eff. ID CorrUncertaintyNP6	0.00	0.00	0.02	0.00	0.04	0.06	0.01	0.00	0.00	0.01
Electron Eff. ID CorrUncertaintyNP7	0.02	0.02	0.02	0.00	0.06	0.04	0.02	0.00	0.00	0.02
Flavor Tag Eff. Eigen B 1	0.02	3.22	0.00	0.00	0.79	0.04	0.00	0.00	0.00	0.02
Flavor Tag Eff. Eigen B 0	0.07	14.26	0.00	0.00	1.15	0.26	0.26	0.00	0.00	0.14
Flavor Tag Eff. Eigen B 2	0.01	1.85	0.00	0.00	0.54	0.03	0.01	0.00	0.00	0.01
Electron Eff. ID CorrUncertaintyNP8	0.01	0.01	0.00	0.00	0.18	0.03	0.00	0.00	0.00	0.00

Nuisance Parameter	Relativ Effect on Sample [%]									
	$W^{\pm}W^{\pm}jj$-EW	top	tri-boson	$Z\gamma$	$W^{\pm}\gamma$	ZZ	$W^{\pm}W^{\pm}jj$-QCD	Charge Mis-ID	Non-Prompt	$W^{\pm}Z$
Electron Eff. ID CorrUncertaintyNP9	0.03	0.02	0.01	0.00	0.09	0.01	0.03	0.00	0.00	0.03
$W^{\pm}W^{\pm}$ EW α_s	0.28	0.00	0.00	0.00	0.00	0.00	0.00	0.00	0.00	0.00
Muon TTVA Stat.	0.08	0.08	0.07	0.00	0.07	0.08	0.08	0.00	0.00	0.08
$W^{\pm}W^{\pm}$ EW EW Corr.	7.64	0.00	0.00	0.00	0.00	0.00	0.00	0.00	0.00	0.00
Muon Scale	0.07	2.11	0.07	0.00	0.00	1.25	0.07	0.00	0.00	0.29
e/γ Scale E4SCINTILLATOR	0.06	0.25	0.00	0.00	0.00	0.10	0.00	0.00	0.00	0.01
Jet Flavor Response	0.58	2.95	4.27	0.00	0.01	6.66	0.95	0.00	0.00	0.47
Flavor Tag Eff. extrapolation	0.02	0.06	0.02	0.00	0.00	0.01	0.03	0.00	0.00	0.01
Jet Pile-up p_T Term	0.73	0.65	2.26	0.00	0.07	1.16	0.21	0.00	0.00	0.70
Jet Energy Resolution	0.08	1.50	5.41	0.00	108.34	5.87	0.59	0.00	0.00	2.16
Jet EtaIntercalibration Non-Closure	0.73	1.71	0.23	0.00	0.07	2.77	0.60	0.00	0.00	0.91
Electron Eff. ID CorrUncertaintyNP14	0.43	0.39	0.59	0.00	0.25	0.57	0.47	0.00	0.00	0.48
Electron Eff. ID CorrUncertaintyNP12	0.03	0.01	0.04	0.00	0.02	0.06	0.04	0.00	0.00	0.06
Electron Eff. ID CorrUncertaintyNP13	0.00	0.03	0.02	0.00	0.18	0.04	0.01	0.00	0.00	0.02
Electron Eff. ID CorrUncertaintyNP10	0.11	0.11	0.13	0.00	0.01	0.19	0.12	0.00	0.00	0.11
Electron Eff. ID CorrUncertaintyNP11	0.01	0.01	0.01	0.00	0.10	0.02	0.02	0.00	0.00	0.01
e/γ Scale LARCALIB EXTRA2015PRE	0.09	0.24	0.00	0.00	0.00	0.10	0.06	0.00	0.00	0.02
Muon MS	0.18	2.64	0.27	0.00	0.02	0.92	0.21	0.00	0.00	0.18
Muon Iso Stat.	0.02	0.02	0.02	0.00	0.02	0.02	0.02	0.00	0.00	0.02
MET Soft Trk. Scale	0.24	1.17	0.00	0.00	0.00	0.89	0.20	0.00	0.00	0.58
Jet EffectiveNP 4	0.33	0.45	0.00	0.00	0.00	0.24	0.16	0.00	0.00	0.22
Jet EffectiveNP 7	0.15	0.21	0.00	0.00	0.00	0.01	0.03	0.00	0.00	0.08
Jet EffectiveNP 6	0.18	0.24	0.00	0.00	0.00	0.01	0.05	0.00	0.00	0.08
Jet EffectiveNP 1	0.18	0.89	4.90	0.00	14.89	7.33	0.78	0.00	0.00	0.10
Jet JVT Efficiency	0.13	0.05	0.07	0.00	0.52	0.13	0.13	0.00	0.00	0.03
Jet EffectiveNP 2	0.64	0.95	2.24	0.00	0.00	1.19	0.40	0.00	0.00	0.36
Flavor Tag Eff. Eigen C 0	0.68	1.11	2.42	0.00	0.00	1.00	0.60	0.00	0.00	0.74
Muon Eff. TrigSystUncertainty	0.06	0.06	0.06	0.00	0.03	0.07	0.06	0.00	0.00	0.06
Flavor Tag Eff. Eigen C 2	0.00	0.08	0.01	0.00	0.00	0.00	0.02	0.00	0.00	0.00
Flavor Tag Eff. Eigen Light 3	0.27	0.37	0.30	0.00	0.22	0.40	0.29	0.00	0.00	0.40
Jet EtaIntercalibration Modelling	0.25	2.11	2.45	0.00	0.07	5.99	0.78	0.00	0.00	0.23
Electron Eff. Reco TOTAL 1NPCOR PLUS UNCOR	0.15	0.16	0.16	0.00	0.34	0.14	0.15	0.00	0.00	0.16
MET Soft Trk. ResoPerp	0.02	0.05	0.00	0.00	0.00	0.78	0.31	0.00	0.00	0.10
Flavor Tag Eff. extrapolation from charm	0.00	0.50	2.26	0.00	0.00	0.88	0.00	0.00	0.00	0.40
Muon TTVA Sys.	0.06	0.04	0.03	0.00	0.00	0.04	0.05	0.00	0.00	0.05
Jet EffectiveNP 5	0.23	0.52	0.00	0.00	0.00	0.00	0.01	0.00	0.00	0.12
Jet Pile-up OffsetNPV	0.20	1.19	4.68	0.00	0.01	1.16	0.22	0.00	0.00	1.63
Jet Flavor Composition	0.62	2.76	8.34	0.00	588.29	5.53	2.74	0.00	0.00	4.47
Charge Mis-ID Energy Corr.	0.00	0.00	0.00	0.00	0.00	0.00	0.00	7.80	0.00	0.00
Charge Mis-ID Scale Fac.	0.00	0.00	0.00	0.00	0.00	0.00	0.00	2.81	0.00	0.00
Non-Prompt μ Sys.	0.00	0.00	0.00	0.00	0.00	0.00	0.00	0.00	46.16	0.00
Non-Prompt e Sys.	0.00	0.00	0.00	0.00	0.00	0.00	0.00	0.00	34.12	0.00
Non-Prompt μ Stat.	0.00	0.00	0.00	0.00	0.00	0.00	0.00	0.00	3.83	0.00
Non-Prompt e Stat.	0.00	0.00	0.00	0.00	0.00	0.00	0.00	0.00	13.08	0.00

Nuisance Parameter	Relativ Effect on Sample [%]									
	$W^{\pm}W^{\pm}jj$-Ew	top	tri-boson	$Z\gamma$	$W^{\pm}\gamma$	ZZ	$W^{\pm}W^{\pm}jj$-Qcd	Charge Mis-ID	Non-Prompt	$W^{\pm}Z$

Table B.10: Summary of the relative effects of all shape nuisance parameters in the $e^+\mu^+/\mu^+e^+$ channel of the low-m_{jj} control region.

B.3.11 $e^-\mu^-/\mu^-e^-$ Channel, Low-m_{jj} Control Region

Nuisance Parameter	Relativ Effect on Sample [%]								
	$W^\pm W^\pm jj$-Ew	top	tri-boson	$Z\gamma$	$W^\pm\gamma$	ZZ	$W^\pm W^\pm jj$-QCD	Charge Mis-ID	Non-Prompt	$W^\pm Z$
Jet Pile-up OffsetMu	0.25	1.02	2.84	0.00	0.11	3.70	0.18	0.00	0.00	2.20
Muon Iso Sys.	0.21	0.21	0.21	0.20	0.20	0.21	0.21	0.00	0.00	0.21
e/γ Scale ALLCORR	0.19	0.00	0.00	0.00	0.00	0.24	0.14	0.00	0.00	0.25
Muon Eff. Stat.	0.20	0.15	0.21	0.19	0.17	0.17	0.18	0.00	0.00	0.18
Jet EffectiveNP 3	0.05	0.03	2.35	0.01	0.00	1.75	0.11	0.00	0.00	0.44
$W^\pm W^\pm$ EW Scale	4.17	0.00	0.00	0.00	0.00	0.00	0.00	0.00	0.00	0.00
Flavor Tag Eff. Eigen C 1	0.33	0.47	0.21	0.00	0.70	0.06	0.29	0.00	0.00	0.13
Jet PunchThrough MC15	0.00	4.42	0.00	0.00	0.00	0.00	0.06	0.00	0.00	0.05
Jet Pile-up RhoTopology	2.16	4.76	7.77	5.68	0.11	7.11	1.24	0.00	0.00	3.75
Jet EffectiveNP 8restTerm	0.12	0.02	0.00	0.00	0.00	0.91	0.06	0.00	0.00	0.61
Interference	8.26	0.00	0.00	0.00	0.00	0.00	0.00	0.00	0.00	0.00
e/γ Scale LARTEMPERATURE EXTRA2015PRE	0.00	0.00	0.00	0.00	0.00	0.11	0.00	0.00	0.00	0.05
Jet BJES Response	0.00	4.35	0.00	0.00	0.00	0.01	0.00	0.00	0.00	0.05
Electron Eff. ID SIMPLIFIED UncorrUncertaintyNP8	0.24	0.26	0.26	0.00	0.15	0.08	0.20	0.00	0.00	0.15
Electron Eff. ID SIMPLIFIED UncorrUncertaintyNP5	0.01	0.02	0.02	0.00	0.00	0.01	0.01	0.00	0.00	0.02
Electron Eff. ID SIMPLIFIED UncorrUncertaintyNP7	0.04	0.02	0.03	0.00	0.00	0.01	0.04	0.00	0.00	0.03
Electron Eff. ID SIMPLIFIED UncorrUncertaintyNP6	0.06	0.04	0.06	0.00	0.00	0.05	0.05	0.00	0.00	0.05
Jet EtaIntercalibration Total Stat.	0.31	0.03	2.84	5.65	0.01	2.17	0.42	0.00	0.00	0.77
e/γ RESOLUTION ALL	0.12	0.02	0.02	0.00	0.00	0.97	0.54	0.00	0.00	0.42
MET Soft Trk. Resolution	0.61	4.14	7.34	0.00	0.00	1.35	0.21	0.00	0.00	1.75
$W^\pm W^\pm$ EW Shower	12.06	0.00	0.00	0.00	0.00	0.00	0.00	0.00	0.00	0.00
Electron Eff. Iso TOTAL 1NPCOR PLUS UNCOR	0.31	0.39	0.37	0.22	0.32	0.21	0.31	0.00	0.00	0.23
e/γ Scale LARTEMPERATURE EXTRA2016PRE	0.00	0.00	0.00	0.00	0.00	0.11	0.00	0.00	0.00	0.05
Muon ID	0.20	0.36	0.10	0.00	13.81	1.23	0.10	0.00	0.00	0.10
Flavor Tag Eff. Eigen Light 2	0.19	0.12	0.18	0.17	0.22	0.18	0.21	0.00	0.00	0.19
Flavor Tag Eff. Eigen Light 1	0.42	0.26	0.40	0.37	0.51	0.39	0.45	0.00	0.00	0.40
Flavor Tag Eff. Eigen Light 0	1.57	1.00	1.49	1.33	1.81	1.46	1.71	0.00	0.00	1.49
Flavor Tag Eff. Eigen Light 4	0.07	0.06	0.05	0.21	0.39	0.00	0.09	0.00	0.00	0.04
Pile-up Reweight. data SF	1.96	6.01	8.57	19.93	24.73	6.22	0.79	0.00	0.00	0.99
$W^\pm W^\pm$ EW PDF	0.51	0.00	0.00	0.00	0.00	0.00	0.00	0.00	0.00	0.00
Electron Eff. Trigger TOTAL 1NPCOR PLUS UNCOR	0.05	0.05	0.07	0.02	0.14	0.06	0.05	0.00	0.00	0.06
Muon Eff. TrigStatUncertainty	0.03	0.03	0.03	0.01	0.04	0.04	0.03	0.00	0.00	0.03
Muon Eff. Sys.	0.84	0.71	0.92	0.55	1.38	0.76	0.84	0.00	0.00	0.78
Electron Eff. ID SIMPLIFIED UncorrUncertaintyNP15	0.03	0.07	0.04	0.00	0.00	0.08	0.05	0.00	0.00	0.06
Electron Eff. ID SIMPLIFIED UncorrUncertaintyNP14	0.01	0.00	0.00	0.00	0.00	0.03	0.01	0.00	0.00	0.01
Electron Eff. ID CorrUncertaintyNP6	0.00	0.02	0.00	0.02	0.01	0.03	0.00	0.00	0.00	0.00
Electron Eff. ID CorrUncertaintyNP7	0.01	0.01	0.01	0.04	0.01	0.03	0.02	0.00	0.00	0.02
Flavor Tag Eff. Eigen B 1	0.03	2.69	0.00	0.00	0.00	0.04	0.01	0.00	0.00	0.03
Flavor Tag Eff. Eigen B 0	0.12	10.01	0.00	0.00	0.00	0.64	0.06	0.00	0.00	0.12
Flavor Tag Eff. Eigen B 2	0.00	1.96	0.00	0.00	0.00	0.01	0.01	0.00	0.00	0.02
Electron Eff. ID CorrUncertaintyNP8	0.00	0.03	0.01	0.04	0.02	0.01	0.00	0.00	0.00	0.02

Nuisance Parameter	Relativ Effect on Sample [%]									
	$W^{\pm}W^{\pm}jj$-EW	top	tri-boson	$Z\gamma$	$W^{\pm}\gamma$	ZZ	$W^{\pm}W^{\pm}jj$-QCD	Charge Mis-ID	Non-Prompt	$W^{\pm}Z$
Electron Eff. ID CorrUncertaintyNP9	0.03	0.06	0.05	0.00	0.02	0.02	0.03	0.00	0.00	0.04
$W^{\pm}W^{\pm}$ EW α_s	0.28	0.00	0.00	0.00	0.00	0.00	0.00	0.00	0.00	0.00
Muon TTVA Stat.	0.08	0.08	0.08	0.05	0.08	0.08	0.08	0.00	0.00	0.08
$W^{\pm}W^{\pm}$ EW EW Corr.	7.64	0.00	0.00	0.00	0.00	0.00	0.00	0.00	0.00	0.00
Muon Scale	0.12	1.04	0.10	0.00	13.81	0.07	0.16	0.00	0.00	0.18
e/γ Scale E4SCINTILLATOR	0.00	0.00	0.00	0.00	0.00	0.11	0.05	0.00	0.00	0.05
Jet Flavor Response	1.48	2.45	2.30	5.67	0.11	6.50	0.96	0.00	0.00	2.38
Flavor Tag Eff. extrapolation	0.03	0.02	0.03	0.00	0.01	0.00	0.03	0.00	0.00	0.02
Jet Pile-up p_T Term	0.17	2.60	1.12	5.66	0.01	4.85	0.59	0.00	0.00	1.87
Jet Energy Resolution	2.33	20.70	6.41	4.54	0.96	11.60	0.79	0.00	0.00	2.80
Jet EtaIntercalibration Non-Closure	0.72	6.57	1.59	0.01	0.02	9.02	0.09	0.00	0.00	3.59
Electron Eff. ID CorrUncertaintyNP14	0.43	0.51	0.49	0.30	0.48	0.60	0.46	0.00	0.00	0.54
Electron Eff. ID CorrUncertaintyNP12	0.02	0.06	0.04	0.07	0.20	0.13	0.03	0.00	0.00	0.05
Electron Eff. ID CorrUncertaintyNP13	0.00	0.04	0.00	0.06	0.03	0.07	0.01	0.00	0.00	0.01
Electron Eff. ID CorrUncertaintyNP10	0.11	0.12	0.12	0.21	0.19	0.12	0.11	0.00	0.00	0.12
Electron Eff. ID CorrUncertaintyNP11	0.01	0.01	0.02	0.06	0.07	0.03	0.02	0.00	0.00	0.02
e/γ Scale LARCALIB EXTRA2015PRE	0.13	0.00	0.00	0.00	0.00	0.11	0.06	0.00	0.00	0.04
Muon MS	0.16	1.04	0.10	0.00	13.81	0.63	0.27	0.00	0.00	0.29
Muon Iso Stat.	0.02	0.02	0.03	0.01	0.02	0.02	0.02	0.00	0.00	0.02
MET Soft Trk. Scale	0.45	0.00	0.00	0.00	0.00	1.85	0.17	0.00	0.00	0.79
Jet EffectiveNP 4	0.07	0.02	2.36	0.00	0.00	1.74	0.12	0.00	0.00	0.63
Jet EffectiveNP 7	0.11	0.01	0.00	0.00	0.01	0.01	0.01	0.00	0.00	0.30
Jet EffectiveNP 6	0.22	0.01	0.00	0.00	0.01	0.91	0.07	0.00	0.00	0.34
Jet EffectiveNP 1	1.04	5.06	7.85	5.67	0.11	4.43	0.87	0.00	0.00	2.10
Jet JVT Efficiency	0.08	0.82	0.39	2.17	0.20	0.08	0.14	0.00	0.00	0.02
Jet EffectiveNP 2	0.25	0.07	2.36	5.67	0.01	0.69	0.55	0.00	0.00	1.76
Flavor Tag Eff. Eigen C 0	0.93	0.59	2.36	0.00	1.10	0.93	0.68	0.00	0.00	0.71
Muon Eff. TrigSystUncertainty	0.05	0.07	0.05	0.03	0.02	0.09	0.05	0.00	0.00	0.07
Flavor Tag Eff. Eigen C 2	0.01	0.07	0.01	0.00	0.02	0.03	0.04	0.00	0.00	0.00
Flavor Tag Eff. Eigen Light 3	0.31	0.20	0.46	0.52	0.99	0.37	0.30	0.00	0.00	0.35
Jet EtaIntercalibration Modelling	1.28	3.16	0.54	0.01	0.11	15.76	1.06	0.00	0.00	3.51
Electron Eff. Reco TOTAL 1NPCOR PLUS UNCOR	0.15	0.15	0.18	0.14	0.25	0.17	0.16	0.00	0.00	0.16
MET Soft Trk. ResoPerp	0.43	0.00	2.19	0.00	0.00	0.15	0.08	0.00	0.00	1.00
Flavor Tag Eff. extrapolation from charm	0.00	0.08	2.06	0.00	0.00	0.72	0.00	0.00	0.00	0.29
Muon TTVA Sys.	0.06	0.12	0.04	0.01	0.06	0.03	0.04	0.00	0.00	0.04
Jet EffectiveNP 5	0.10	0.01	0.00	0.00	0.00	0.91	0.06	0.00	0.00	0.37
Jet Pile-up OffsetNPV	0.46	1.06	11.13	5.66	0.10	1.78	0.14	0.00	0.00	1.79
Jet Flavor Composition	2.40	2.43	13.30	10.18	13.20	19.94	1.44	0.00	0.00	7.93
Charge Mis-ID Energy Corr.	0.00	0.00	0.00	0.00	0.00	0.00	0.00	11.20	0.00	0.00
Charge Mis-ID Scale Fac.	0.00	0.00	0.00	0.00	0.00	0.00	0.00	2.78	0.00	0.00
Non-Prompt μ Sys.	0.00	0.00	0.00	0.00	0.00	0.00	0.00	0.00	1.83	0.00
Non-Prompt e Sys.	0.00	0.00	0.00	0.00	0.00	0.00	0.00	0.00	42.60	0.00
Non-Prompt μ Stat.	0.00	0.00	0.00	0.00	0.00	0.00	0.00	0.00	1.63	0.00
Non-Prompt e Stat.	0.00	0.00	0.00	0.00	0.00	0.00	0.00	0.00	18.06	0.00

Nuisance Parameter	Relativ Effect on Sample [%]									
	$W^{\pm}W^{\pm}jj$-EW	top	tri-boson	$Z\gamma$	$W^{\pm}\gamma$	ZZ	$W^{\pm}W^{\pm}jj$-QCD	Charge Mis-ID	Non-Prompt	$W^{\pm}Z$

Table B.11: Summary of the relative effects of all shape nuisance parameters in the $e^{-}\mu^{-}/\mu^{-}e^{-}$ channel of the low-m_{jj} control region.

B.3.12 $\mu^+\mu^+$ Channel, Low-m_{jj} Control Region

Nuisance Parameter	Relativ Effect on Sample [%]									
	$W^\pm W^\pm jj$-EW	top	tri-boson	$Z\gamma$	$W^\pm\gamma$	ZZ	$W^\pm W^\pm jj$-QCD	Charge Mis-ID	Non-Prompt	$W^\pm Z$
Jet Pile-up OffsetMu	0.61	1.46	3.77	0.00	0.00	5.80	0.18	0.00	0.00	0.41
Muon Iso Sys.	0.41	0.41	0.42	0.00	0.00	0.41	0.41	0.00	0.00	0.41
Muon Eff. Stat.	0.37	0.39	0.36	0.00	0.00	0.33	0.37	0.00	0.00	0.36
Jet EffectiveNP 3	0.45	1.32	0.00	0.00	0.00	1.40	0.60	0.00	0.00	0.29
$W^\pm W^\pm$ EW Scale	4.17	0.00	0.00	0.00	0.00	0.00	0.00	0.00	0.00	0.00
Flavor Tag Eff. Eigen C 1	0.25	0.09	0.21	0.00	0.00	0.00	0.20	0.00	0.00	0.14
Jet Pile-up RhoTopology	0.62	0.29	4.34	0.00	0.00	5.01	1.73	0.00	0.00	2.06
Jet EffectiveNP 8restTerm	0.27	1.32	0.00	0.00	0.00	1.40	0.06	0.00	0.00	0.48
Interference	8.26	0.00	0.00	0.00	0.00	0.00	0.00	0.00	0.00	0.00
Jet BJES Response	0.06	0.61	0.00	0.00	0.00	0.00	0.00	0.00	0.00	0.25
Jet EtaIntercalibration Total Stat.	0.28	1.41	0.45	0.00	0.00	1.93	0.22	0.00	0.00	0.99
MET Soft Trk. Resolution	0.20	1.17	0.00	0.00	0.00	1.86	0.03	0.00	0.00	0.13
$W^\pm W^\pm$ EW Shower	12.06	0.00	0.00	0.00	0.00	0.00	0.00	0.00	0.00	0.00
Muon ID	0.33	0.88	0.06	0.00	0.00	2.09	0.10	0.00	0.00	1.08
Flavor Tag Eff. Eigen Light 2	0.20	0.20	0.19	0.00	0.00	0.19	0.22	0.00	0.00	0.21
Flavor Tag Eff. Eigen Light 1	0.43	0.45	0.43	0.00	0.00	0.41	0.46	0.00	0.00	0.45
Flavor Tag Eff. Eigen Light 0	1.62	1.65	1.62	0.00	0.00	1.56	1.75	0.00	0.00	1.69
Flavor Tag Eff. Eigen Light 4	0.07	0.04	0.05	0.00	0.00	0.01	0.09	0.00	0.00	0.04
Pile-up Reweight. data SF	1.89	1.96	7.91	0.00	0.00	3.39	3.18	0.00	0.00	0.58
$W^\pm W^\pm$ EW PDF	0.51	0.00	0.00	0.00	0.00	0.00	0.00	0.00	0.00	0.00
Muon Eff. TrigStatUncertainty	0.23	0.23	0.20	0.00	0.00	0.22	0.21	0.00	0.00	0.21
Muon Eff. Sys.	1.59	1.53	1.66	0.00	0.00	1.61	1.55	0.00	0.00	1.61
Flavor Tag Eff. Eigen B 1	0.01	2.80	0.00	0.00	0.00	0.06	0.03	0.00	0.00	0.02
Flavor Tag Eff. Eigen B 0	0.01	17.45	0.00	0.00	0.00	0.38	0.13	0.00	0.00	0.35
Flavor Tag Eff. Eigen B 2	0.00	2.11	0.00	0.00	0.00	0.05	0.01	0.00	0.00	0.02
$W^\pm W^\pm$ EW α_s	0.28	0.00	0.00	0.00	0.00	0.00	0.00	0.00	0.00	0.00
Muon TTVA Stat.	0.16	0.15	0.15	0.00	0.00	0.16	0.15	0.00	0.00	0.15
$W^\pm W^\pm$ EW EW Corr.	7.64	0.00	0.00	0.00	0.00	0.00	0.00	0.00	0.00	0.00
Muon Scale	0.57	0.76	0.06	0.00	0.00	0.28	0.32	0.00	0.00	1.01
Jet Flavor Response	0.74	1.93	4.33	0.00	0.00	6.39	1.45	0.00	0.00	0.81
Flavor Tag Eff. extrapolation	0.02	0.02	0.00	0.00	0.00	0.01	0.01	0.00	0.00	0.01
Jet Pile-up p_T Term	0.96	4.48	0.77	0.00	0.00	1.72	0.54	0.00	0.00	1.02
Jet Energy Resolution	1.10	0.05	30.56	0.00	0.00	2.35	2.68	0.00	0.00	2.21
Jet EtaIntercalibration Non-Closure	0.98	1.30	0.46	0.00	0.00	8.52	0.94	0.00	0.00	0.26
Muon MS	0.57	0.76	0.06	0.00	0.00	0.39	0.32	0.00	0.00	1.34
Muon Iso Stat.	0.04	0.04	0.04	0.00	0.00	0.04	0.04	0.00	0.00	0.04
MET Soft Trk. Scale	0.17	1.17	0.00	0.00	0.00	3.46	0.23	0.00	0.00	0.71
Jet EffectiveNP 4	0.51	1.31	0.00	0.00	0.00	1.40	0.05	0.00	0.00	0.40
Jet EffectiveNP 7	0.10	1.24	0.00	0.00	0.00	1.70	0.05	0.00	0.00	0.04
Jet EffectiveNP 6	0.17	2.15	0.00	0.00	0.00	1.24	0.12	0.00	0.00	0.18
Jet EffectiveNP 1	0.63	1.30	4.33	0.00	0.00	5.18	1.02	0.00	0.00	1.19

Nuisance Parameter	Relativ Effect on Sample [%]									
	$W^{\pm}W^{\pm}jj$-Ew	top	tri-boson	$Z\gamma$	$W^{\pm}\gamma$	ZZ	$W^{\pm}W^{\pm}jj$-Qcd	Charge Mis-ID	Non-Prompt	$W^{\pm}Z$
Jet Jvt Efficiency	0.11	0.22	0.19	0.00	0.00	0.19	0.13	0.00	0.00	0.14
Jet EffectiveNP 2	0.32	1.91	0.00	0.00	0.00	1.01	0.84	0.00	0.00	0.22
Flavor Tag Eff. Eigen C 0	0.63	1.37	1.35	0.00	0.00	1.09	0.51	0.00	0.00	0.83
Muon Eff. TrigSystUncertainty	0.38	0.33	0.32	0.00	0.00	0.42	0.36	0.00	0.00	0.37
Flavor Tag Eff. Eigen C 2	0.01	0.10	0.02	0.00	0.00	0.14	0.00	0.00	0.00	0.02
Flavor Tag Eff. Eigen Light 3	0.32	0.57	0.44	0.00	0.00	0.42	0.27	0.00	0.00	0.44
Jet EtaIntercalibration Modelling	0.61	2.03	8.54	0.00	0.00	4.99	0.94	0.00	0.00	0.64
MET Soft Trk. ResoPerp	0.19	0.62	0.00	0.00	0.00	1.46	0.11	0.00	0.00	0.11
Flavor Tag Eff. extrapolation from charm	0.00	0.51	1.17	0.00	0.00	0.82	0.00	0.00	0.00	0.42
Muon TTVA Sys.	0.12	0.05	0.13	0.00	0.00	0.12	0.09	0.00	0.00	0.12
Jet EffectiveNP 5	0.11	1.28	0.00	0.00	0.00	1.40	0.14	0.00	0.00	0.54
Jet Pile-up OffsetNPV	0.76	1.15	0.76	0.00	0.00	5.97	0.18	0.00	0.00	1.61
Jet Flavor Composition	1.09	7.00	3.99	0.00	0.00	8.42	2.41	0.00	0.00	6.08
Non-Prompt μ Sys.	0.00	0.00	0.00	0.00	0.00	0.00	0.00	0.00	137.56	0.00
Non-Prompt μ Stat.	0.00	0.00	0.00	0.00	0.00	0.00	0.00	0.00	14.73	0.00

Table B.12: Summary of the relative effects of all shape nuisance parameters in the $\mu^+\mu^+$ channel of the low-m_{jj} control region.

B.3.13 $\mu^-\mu^-$ Channel, Low-m_{jj} Control Region

Nuisance Parameter	Relativ Effect on Sample [%]									
	$W^\pm W^\pm jj$-EW	top	tri-boson	$Z\gamma$	$W^\pm\gamma$	ZZ	$W^\pm W^\pm jj$-QCD	Charge Mis-ID	Non-Prompt	$W^\pm Z$
Jet Pile-up OffsetMu	1.04	0.50	0.03	0.00	0.00	5.83	0.32	0.00	0.00	1.13
Muon Iso Sys.	0.42	0.44	0.42	0.00	0.00	0.41	0.41	0.00	0.00	0.42
e/γ Scale ALLCORR	0.00	3.26	0.00	0.00	0.00	0.00	0.00	0.00	0.00	0.06
Muon Eff. Stat.	0.38	0.50	0.40	0.00	0.00	0.37	0.37	0.00	0.00	0.38
Jet EffectiveNP 3	0.19	1.15	0.00	0.00	0.00	0.34	0.44	0.00	0.00	0.07
$W^\pm W^\pm$ EW Scale	4.17	0.00	0.00	0.00	0.00	0.00	0.00	0.00	0.00	0.00
Flavor Tag Eff. Eigen C 1	0.38	0.33	0.06	0.00	0.00	0.07	0.33	0.00	0.00	0.17
Jet PunchThrough MC15	0.00	0.00	0.00	0.00	0.00	0.00	0.11	0.00	0.00	0.02
Jet Pile-up RhoTopology	1.22	8.30	6.73	0.00	0.00	3.30	0.70	0.00	0.00	4.98
Jet EffectiveNP 8restTerm	0.07	1.14	0.00	0.00	0.00	1.28	0.35	0.00	0.00	0.16
Interference	8.26	0.00	0.00	0.00	0.00	0.00	0.00	0.00	0.00	0.00
e/γ Scale LARTEMPERATURE EXTRA2015PRE	0.00	3.26	0.00	0.00	0.00	0.00	0.00	0.00	0.00	0.06
Jet BJES Response	0.00	4.12	0.00	0.00	0.00	0.01	0.09	0.00	0.00	0.06
Jet EtaIntercalibration Total Stat.	0.48	1.12	0.02	0.00	0.00	2.11	0.46	0.00	0.00	1.01
e/γ RESOLUTION ALL	0.00	3.26	0.00	0.00	0.00	0.00	0.00	0.00	0.00	0.06
MET Soft Trk. Resolution	0.34	0.77	0.00	0.00	0.00	2.73	0.00	0.00	0.00	0.16
$W^\pm W^\pm$ EW Shower	12.06	0.00	0.00	0.00	0.00	0.00	0.00	0.00	0.00	0.00
e/γ Scale LARTEMPERATURE EXTRA2016PRE	0.00	3.26	0.00	0.00	0.00	0.00	0.00	0.00	0.00	0.06
Muon ID	0.20	8.10	0.00	0.00	0.00	1.43	0.19	0.00	0.00	0.71
Flavor Tag Eff. Eigen Light 2	0.19	0.19	0.19	0.00	0.00	0.20	0.21	0.00	0.00	0.21
Flavor Tag Eff. Eigen Light 1	0.40	0.39	0.41	0.00	0.00	0.45	0.45	0.00	0.00	0.45
Flavor Tag Eff. Eigen Light 0	1.52	1.47	1.51	0.00	0.00	1.70	1.68	0.00	0.00	1.67
Flavor Tag Eff. Eigen Light 4	0.06	0.05	0.02	0.00	0.00	0.06	0.07	0.00	0.00	0.03
Pile-up Reweight. data SF	0.48	2.51	7.05	0.00	0.00	4.93	1.45	0.00	0.00	0.72
$W^\pm W^\pm$ EW PDF	0.51	0.00	0.00	0.00	0.00	0.00	0.00	0.00	0.00	0.00
Muon Eff. TrigStatUncertainty	0.23	0.18	0.23	0.00	0.00	0.18	0.21	0.00	0.00	0.19
Muon Eff. Sys.	1.69	1.47	1.89	0.00	0.00	1.61	1.70	0.00	0.00	1.58
Flavor Tag Eff. Eigen B 1	0.02	1.33	0.16	0.00	0.00	0.02	0.01	0.00	0.00	0.01
Flavor Tag Eff. Eigen B 0	0.15	13.00	0.23	0.00	0.00	0.69	0.08	0.00	0.00	0.29
Flavor Tag Eff. Eigen B 2	0.01	1.17	0.01	0.00	0.00	0.01	0.01	0.00	0.00	0.01
$W^\pm W^\pm$ EW α_s	0.28	0.00	0.00	0.00	0.00	0.00	0.00	0.00	0.00	0.00
Muon TTVA Stat.	0.16	0.16	0.16	0.00	0.00	0.15	0.15	0.00	0.00	0.15
$W^\pm W^\pm$ EW EW Corr.	7.64	0.00	0.00	0.00	0.00	0.00	0.00	0.00	0.00	0.00
Muon Scale	0.44	5.82	0.00	0.00	0.00	0.84	0.23	0.00	0.00	0.90
e/γ Scale E4SCINTILLATOR	0.00	3.26	0.00	0.00	0.00	0.00	0.00	0.00	0.00	0.06
Jet Flavor Response	0.90	3.54	6.91	0.00	0.00	1.41	0.69	0.00	0.00	3.57
Flavor Tag Eff. extrapolation	0.03	0.01	0.00	0.00	0.00	0.00	0.03	0.00	0.00	0.02
Jet Pile-up p_T Term	0.90	2.16	6.94	0.00	0.00	3.18	0.72	0.00	0.00	2.55
Jet Energy Resolution	0.15	20.11	8.39	0.00	0.00	29.70	2.81	0.00	0.00	4.54
Jet EtaIntercalibration Non-Closure	0.67	3.43	0.02	0.00	0.00	2.00	0.74	0.00	0.00	1.39
e/γ Scale LARCALIB EXTRA2015PRE	0.00	3.26	0.00	0.00	0.00	0.00	0.00	0.00	0.00	0.06

Nuisance Parameter	Relativ Effect on Sample [%]									
	$W^{\pm}W^{\pm}jj$-Ew	top	tri-boson	$Z\gamma$	$W^{\pm}\gamma$	ZZ	$W^{\pm}W^{\pm}jj$-QCD	Charge Mis-ID	Non-Prompt	$W^{\pm}Z$
Muon MS	0.29	6.48	0.00	0.00	0.00	1.13	0.37	0.00	0.00	0.55
Muon Iso Stat.	0.04	0.04	0.05	0.00	0.00	0.04	0.04	0.00	0.00	0.04
MET Soft Trk. Scale	0.46	3.98	0.00	0.00	0.00	1.02	0.21	0.00	0.00	0.29
Jet EffectiveNP 4	0.20	1.15	0.00	0.00	0.00	0.34	0.34	0.00	0.00	0.25
Jet EffectiveNP 7	0.11	1.14	0.00	0.00	0.00	0.00	0.11	0.00	0.00	0.07
Jet EffectiveNP 6	0.09	1.14	0.00	0.00	0.00	1.28	0.14	0.00	0.00	0.11
Jet EffectiveNP 1	0.80	4.32	6.91	0.00	0.00	1.40	0.65	0.00	0.00	3.38
Jet JVT Efficiency	0.10	0.25	0.32	0.00	0.00	0.28	0.17	0.00	0.00	0.15
Jet EffectiveNP 2	0.35	1.99	0.01	0.00	0.00	0.93	0.57	0.00	0.00	0.75
Flavor Tag Eff. Eigen C 0	0.89	1.33	2.89	0.00	0.00	1.54	0.72	0.00	0.00	0.96
Muon Eff. TrigSystUncertainty	0.39	0.33	0.38	0.00	0.00	0.37	0.36	0.00	0.00	0.38
Flavor Tag Eff. Eigen C 2	0.01	0.05	0.09	0.00	0.00	0.11	0.03	0.00	0.00	0.01
Flavor Tag Eff. Eigen Light 3	0.27	0.25	0.39	0.00	0.00	0.51	0.31	0.00	0.00	0.44
Jet EtaIntercalibration Modelling	0.35	2.00	6.91	0.00	0.00	10.36	1.04	0.00	0.00	3.70
MET Soft Trk. ResoPerp	0.30	3.98	0.00	0.00	0.00	1.53	0.41	0.00	0.00	0.21
Flavor Tag Eff. extrapolation from charm	0.00	0.42	2.14	0.00	0.00	1.11	0.00	0.00	0.00	0.45
Muon TTVA Sys.	0.14	0.13	0.17	0.00	0.00	0.05	0.09	0.00	0.00	0.10
Jet EffectiveNP 5	0.29	0.01	0.00	0.00	0.00	1.29	0.22	0.00	0.00	0.16
Jet Pile-up OffsetNPV	0.36	2.78	0.03	0.00	0.00	7.43	0.29	0.00	0.00	2.50
Jet Flavor Composition	1.14	9.74	7.55	0.00	0.00	4.21	1.84	0.00	0.00	6.56
Non-Prompt μ Sys.	0.00	0.00	0.00	0.00	0.00	0.00	0.00	0.00	18.08	0.00
Non-Prompt μ Stat.	0.00	0.00	0.00	0.00	0.00	0.00	0.00	0.00	11.50	0.00

Table B.13: Summary of the relative effects of all shape nuisance parameters in the $\mu^{-}\mu^{-}$ channel of the low-m_{jj} control region.

C Additional Material on the Fitting

C.1 Pruning of Nuisance Parameters

This section contains the exact nuisance parameter usage for the pruning settings $t = 0.1$ % and $p_{\mathrm{b}} = 20$ %. These are shown in Figure C.1, C.2, and C.3 for the signal region, low-m_{jj}, and $W^{\pm}Z$ control regions, respectively. For each channel in each sample, the usage of nuisance parameters is indicated with a yellow (included) and blue (excluded) bin.

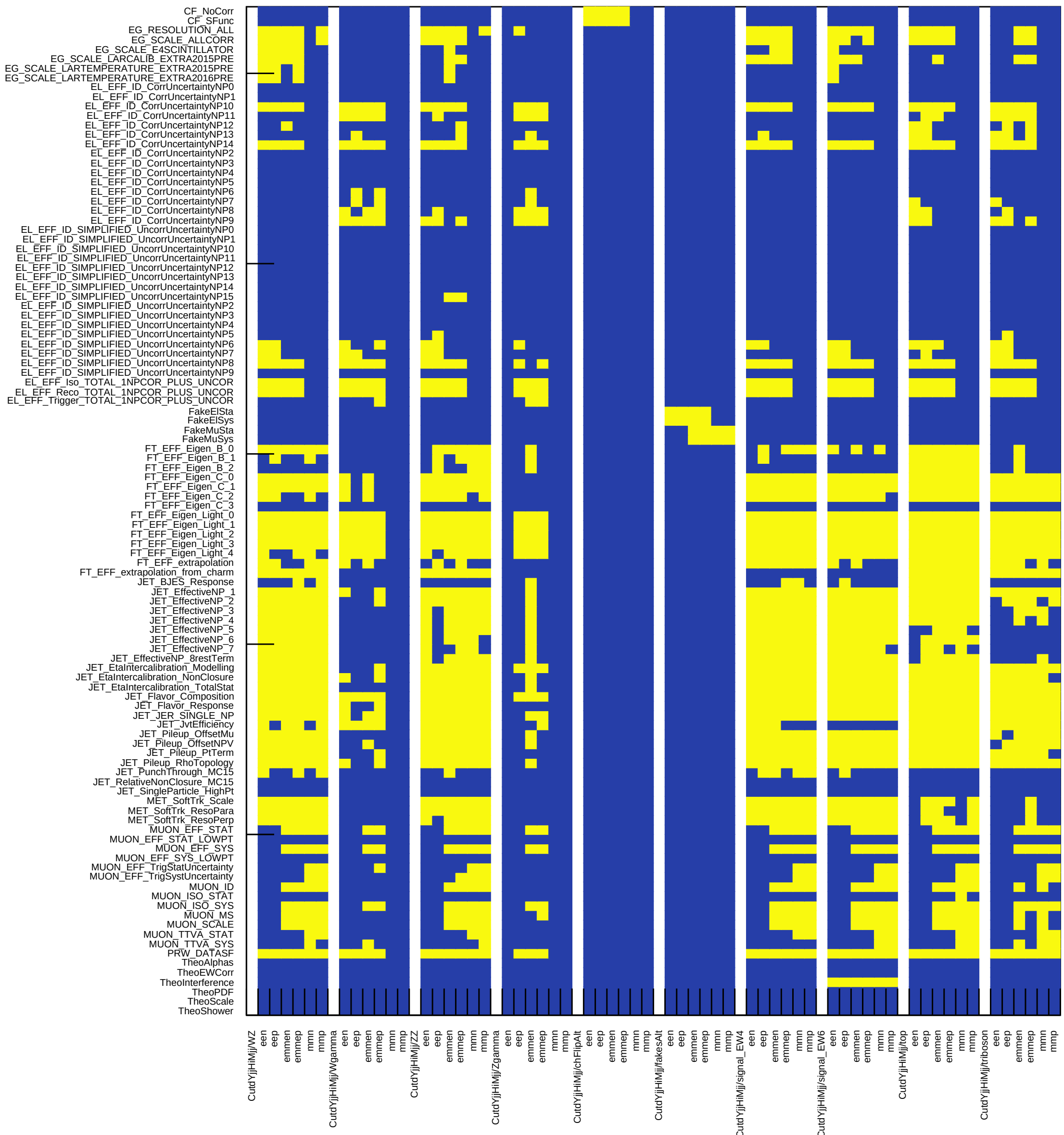

Figure C.1: Overview of the usage of nuisance parameters (ordinate) in the signal region, in different samples and channels (abscissa). Unused systematic variations are depicted by blue fields, yellow bins represented systematics used in the fit.

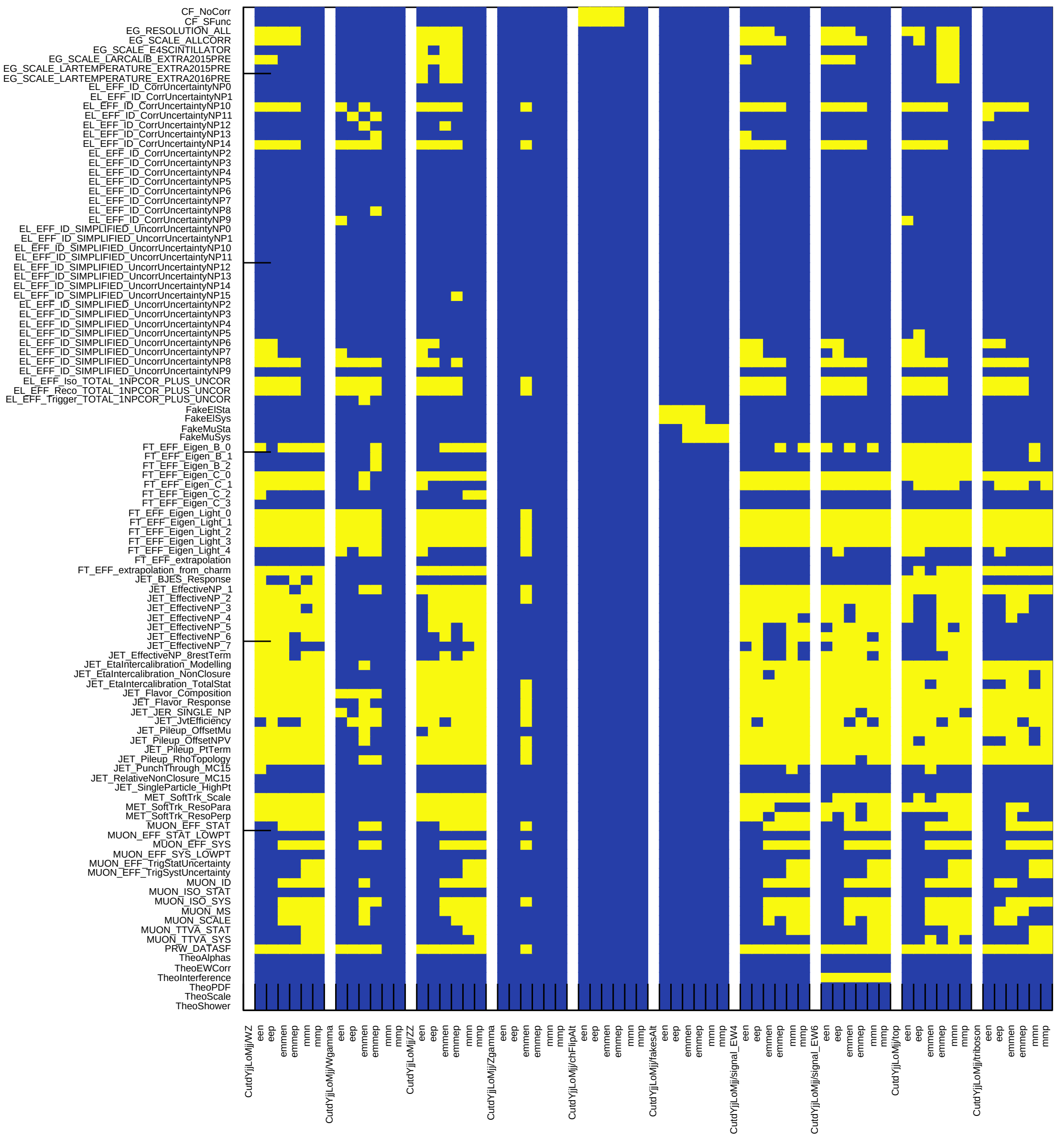

Figure C.2: Overview of the usage of nuisance parameters (ordinate) in the low-m_{jj} control region, in different samples and channels (abscissa). Unused systematic variations are depicted by blue fields, yellow bins represented systematics used in the fit.

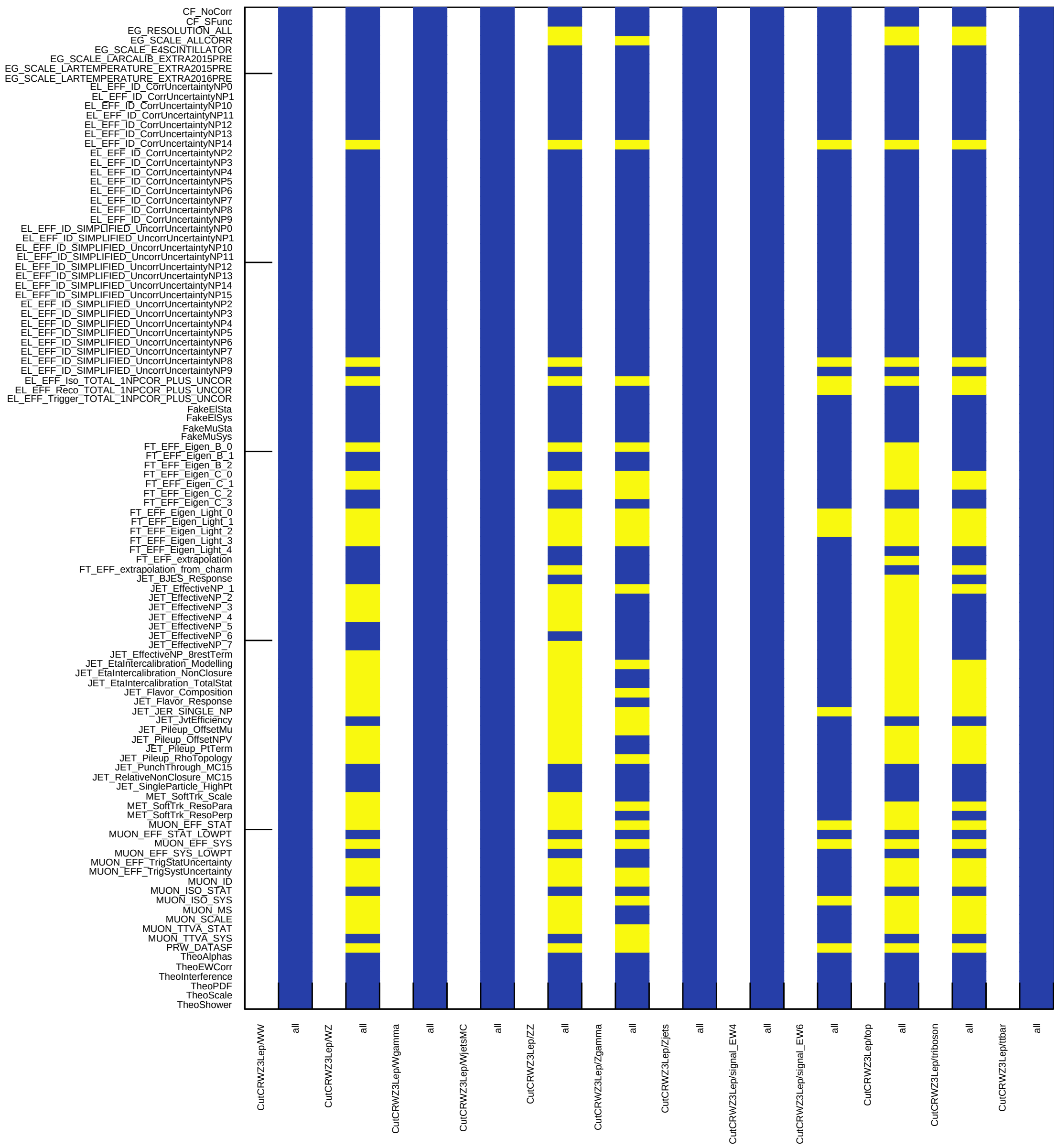

Figure C.3: Overview of the usage of nuisance parameters (ordinate) in the $W^{\pm}Z$ region, in different samples and channels (abscissa). Unused systematic variations are depicted by blue fields, yellow bins represented systematics used in the fit.

C.2 Optimizing the Signal Region

In this section, bin-wise event yields and statistical uncertainties in the signal, low-m_{jj} and $W^{\pm}Z$ control regions are reported. Signal region yields for all lepton channels are listed in Table C.2 to C.5. All six lepton channels in the low-m_{jj} control region are summarized in Table C.7. Event yields for the combined $\ell^{\pm}\ell^{\pm}$ channel in the $W^{\pm}Z$ control region are given in Table C.8.

Lower Bin Edges [GeV]	500	700	1000	1500
Charge Mis-ID	0.56 ± 0.05	0.43 ± 0.04	0.24 ± 0.03	0.10 ± 0.03
$W\gamma$	0.16 ± 0.16	–	0.02 ± 0.02	–
top	0.04 ± 0.02	0.03 ± 0.01	0.02 ± 0.01	0.01 ± 0.01
$Z\gamma$	0.01 ± 0.01	–	0.04 ± 0.04	–
$W^{\pm}Z$	0.63 ± 0.10	0.56 ± 0.07	0.39 ± 0.07	0.30 ± 0.04
tri-boson	0.01 ± 0.00	0.00 ± 0.00	–	0.01 ± 0.01
non-prompt	0.56 ± 0.05	0.43 ± 0.04	0.24 ± 0.03	0.10 ± 0.03
ZZ	0.03 ± 0.01	0.02 ± 0.01	0.01 ± 0.01	0.01 ± 0.01
$W^{\pm}W^{\pm}jj$-Ew	0.60 ± 0.03	0.82 ± 0.04	1.01 ± 0.04	1.37 ± 0.05
$W^{\pm}W^{\pm}jj$-QCD	0.14 ± 0.01	0.13 ± 0.01	0.08 ± 0.01	0.04 ± 0.01

Table C.1: Pre-fit event yields and statistical uncertainties in bins of invariant tagging jet mass m_{jj} the signal region, e^+e^+ channel.

Lower Bin Edges [GeV]	500	700	1000	1500
Charge Mis-ID	0.56 ± 0.05	0.36 ± 0.04	0.17 ± 0.03	0.08 ± 0.02
$W\gamma$	0.03 ± 0.03	0.30 ± 0.21	0.02 ± 0.02	–
top	0.34 ± 0.02	0.36 ± 0.02	0.39 ± 0.02	0.40 ± 0.03
$Z\gamma$	–	–	–	–
$W^{\pm}Z$	0.52 ± 0.06	0.39 ± 0.05	0.32 ± 0.05	0.07 ± 0.04
tri-boson	0.00 ± 0.00	0.01 ± 0.00	0.01 ± 0.00	0.00 ± 0.00
non-prompt	0.01 ± 0.26	1.86 ± 1.33	0.37 ± 0.55	0.07 ± 0.11
ZZ	0.04 ± 0.01	0.01 ± 0.00	0.00 ± 0.00	0.00 ± 0.00
$W^{\pm}W^{\pm}jj$-Ew	0.34 ± 0.02	0.36 ± 0.02	0.39 ± 0.02	0.40 ± 0.03
$W^{\pm}W^{\pm}jj$-QCD	0.07 ± 0.01	0.05 ± 0.01	0.03 ± 0.01	0.01 ± 0.00

Table C.2: Pre-fit event yields and statistical uncertainties in bins of invariant tagging jet mass m_{jj} the signal region, e^-e^- channel.

Lower Bin Edges [GeV]	500	700	1000	1500
Charge Mis-ID	1.59 ± 0.22	0.95 ± 0.15	0.44 ± 0.09	0.50 ± 0.13
$W\gamma$	0.10 ± 0.05	0.68 ± 0.65	0.67 ± 0.35	0.03 ± 0.03
top	0.14 ± 0.03	0.15 ± 0.04	0.05 ± 0.03	0.04 ± 0.01
$Z\gamma$	0.01 ± 0.01	0.01 ± 0.01	–	–
$W^{\pm}Z$	5.43 ± 0.35	4.03 ± 0.21	2.65 ± 0.16	1.70 ± 0.15
tri-boson	0.04 ± 0.02	0.04 ± 0.01	0.02 ± 0.01	0.02 ± 0.01
non-prompt	3.36 ± 1.52	3.37 ± 1.50	1.64 ± 1.11	0.98 ± 1.05
ZZ	0.16 ± 0.02	0.13 ± 0.02	0.07 ± 0.03	0.04 ± 0.01
$W^{\pm}W^{\pm}jj$-Ew	2.65 ± 0.07	3.49 ± 0.08	4.34 ± 0.09	6.02 ± 0.10
$W^{\pm}W^{\pm}jj$-QCD	1.02 ± 0.03	0.91 ± 0.03	0.67 ± 0.03	0.42 ± 0.02

Table C.3: Pre-fit event yields and statistical uncertainties in bins of invariant tagging jet mass m_{jj} the signal region, $e^+\mu^+/\mu^+e^+$ channel.

Lower Bin Edges [GeV]	500	700	1000	1500
Charge Mis-ID	1.28 ± 0.18	0.86 ± 0.13	0.51 ± 0.10	0.31 ± 0.08
$W\gamma$	0.23 ± 0.21	–	0.18 ± 0.16	0.03 ± 0.03
top	0.06 ± 0.02	0.10 ± 0.04	0.03 ± 0.01	0.04 ± 0.01
$Z\gamma$	–	0.01 ± 0.01	0.01 ± 0.01	–
$W^{\pm}Z$	3.79 ± 0.24	2.77 ± 0.28	1.41 ± 0.12	0.96 ± 0.09
tri-boson	0.03 ± 0.01	0.05 ± 0.04	0.02 ± 0.01	0.01 ± 0.00
non-prompt	3.24 ± 1.56	1.62 ± 1.47	0.28 ± 0.52	1.21 ± 0.89
ZZ	0.11 ± 0.02	0.08 ± 0.01	0.04 ± 0.02	0.04 ± 0.01
$W^{\pm}W^{\pm}jj$-Ew	1.39 ± 0.05	1.76 ± 0.06	1.76 ± 0.05	1.54 ± 0.05
$W^{\pm}W^{\pm}jj$-QCD	0.46 ± 0.02	0.41 ± 0.02	0.24 ± 0.02	0.12 ± 0.01

Table C.4: Pre-fit event yields and statistical uncertainties in bins of invariant tagging jet mass m_{jj} the signal region, $e^-\mu^-/\mu^-e^-$ channel.

Lower Bin Edges [GeV]	500	700	1000	1500
Charge Mis-ID	–	–	–	–
top	0.10 ± 0.03	0.06 ± 0.02	0.03 ± 0.02	0.01 ± 0.00
$Z\gamma/W\gamma$	–	–	–	–
$W^{\pm}Z$	2.04 ± 0.13	1.49 ± 0.15	1.19 ± 0.11	0.78 ± 0.08
tri-boson	0.03 ± 0.01	0.00 ± 0.00	0.01 ± 0.00	0.01 ± 0.00
non-prompt	–	–	–	–
ZZ	0.05 ± 0.01	0.02 ± 0.01	0.03 ± 0.01	0.01 ± 0.00
$W^{\pm}W^{\pm}jj$-Ew	1.45 ± 0.05	1.97 ± 0.06	2.39 ± 0.06	3.33 ± 0.08
$W^{\pm}W^{\pm}jj$-QCD	0.60 ± 0.03	0.54 ± 0.02	0.38 ± 0.02	0.28 ± 0.02

Table C.5: Pre-fit event yields and statistical uncertainties in bins of invariant tagging jet mass m_{jj} the signal region, $\mu^+\mu^+$ channel.

Lower Bin Edges [GeV]	500	700	1000	1500
Charge Mis-ID	–	–	–	–
top	0.80 ± 0.03	0.91 ± 0.04	0.91 ± 0.04	0.88 ± 0.04
$Z\gamma/W\gamma$	–	–	–	–
$W^{\pm}Z$	1.36 ± 0.11	1.21 ± 0.12	0.64 ± 0.14	0.44 ± 0.07
tri-boson	0.01 ± 0.01	0.01 ± 0.00	0.01 ± 0.01	0.00 ± 0.00
non-prompt	0.36 ± 0.12	0.20 ± 0.10	0.06 ± 0.04	0.06 ± 0.04
ZZ	0.03 ± 0.02	0.04 ± 0.01	0.01 ± 0.01	0.01 ± 0.01
$W^{\pm}W^{\pm}jj$-Ew	0.80 ± 0.03	0.91 ± 0.04	0.91 ± 0.04	0.88 ± 0.04
$W^{\pm}W^{\pm}jj$-QCD	0.30 ± 0.02	0.23 ± 0.02	0.15 ± 0.01	0.08 ± 0.01

Table C.6: Pre-fit event yields and statistical uncertainties in bins of invariant tagging jet mass m_{jj} the signal region, $\mu^-\mu^-$ channel.

Channel	e^+e^+	e^-e^-	$e^+\mu^+/\mu^+e^+$	$e^-\mu^-/\mu^-e^-$	$\mu^+\mu^+$	$\mu^-\mu^-$
Charge Mis-ID	1.38 ± 0.08	1.46 ± 0.09	3.07 ± 0.27	3.04 ± 0.25	–	–
$W\gamma$	0.08 ± 0.05	0.15 ± 0.15	0.16 ± 0.07	0.95 ± 0.48	–	–
top	0.13 ± 0.03	0.05 ± 0.02	0.49 ± 0.07	0.17 ± 0.04	0.27 ± 0.05	0.15 ± 0.04
$Z\gamma$	–	–	–	0.04 ± 0.04	–	–
$W^{\pm}Z$	1.67 ± 0.18	1.27 ± 0.13	11.23 ± 0.52	8.48 ± 0.46	4.61 ± 0.22	3.24 ± 0.19
tri-boson	0.03 ± 0.01	0.02 ± 0.01	0.13 ± 0.02	0.09 ± 0.02	0.12 ± 0.03	0.04 ± 0.01
non-prompt	0.42 ± 0.64	3.46 ± 1.77	10.73 ± 2.80	7.04 ± 2.24	2.19 ± 0.71	0.95 ± 0.18
ZZ	0.10 ± 0.02	0.10 ± 0.03	0.34 ± 0.06	0.38 ± 0.06	0.15 ± 0.02	0.12 ± 0.02
$W^{\pm}W^{\pm}jj$-Ew	0.60 ± 0.03	0.44 ± 0.05	2.71 ± 0.07	1.76 ± 0.06	1.65 ± 0.09	1.00 ± 0.04
$W^{\pm}W^{\pm}jj$-QCD	0.20 ± 0.02	0.14 ± 0.01	1.71 ± 0.04	0.98 ± 0.03	1.00 ± 0.03	0.56 ± 0.03

Table C.7: Pre-fit event yields and statistical uncertainties in the low-m_{jj} control region in a range from 200 GeV to 3000 GeV.

Channel	$\ell^{\pm}\ell^{\pm}$
$W\gamma$	–
top	6.17 ± 0.25
$Z\gamma$	1.52 ± 0.60
tri-boson	1.26 ± 0.06
$W^{\pm}Z$	197.09 ± 1.42
WW	0.02 ± 0.01
ZZ	14.12 ± 0.27
$t\bar{t}$	4.27 ± 1.02
Zjets	2.54 ± 1.40
Wjets	–
$W^{\pm}W^{\pm}jj$-Ew	0.00 ± 0.00
$W^{\pm}W^{\pm}jj$-QCD	–

Table C.8: Pre-fit event yields and statistical uncertainties in the $W^{\pm}Z$ control region in the combined $\ell^{\pm}\ell^{\pm}$ channel in a range from 200 GeV to 3000 GeV.

C.3 Pre- and Post-Fit Invariant Tagging Jet Mass Distribution

C.3.1 Invariant Tagging Jet Mass Distributions with Asimov Data

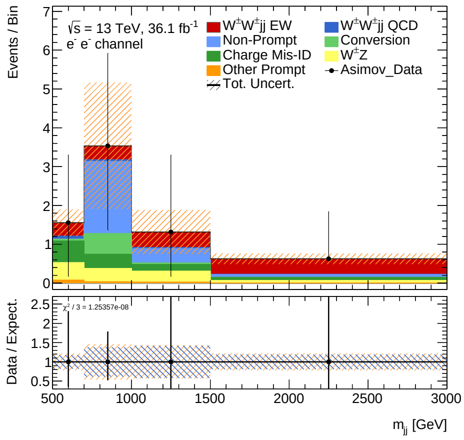

(a) e^-e^-

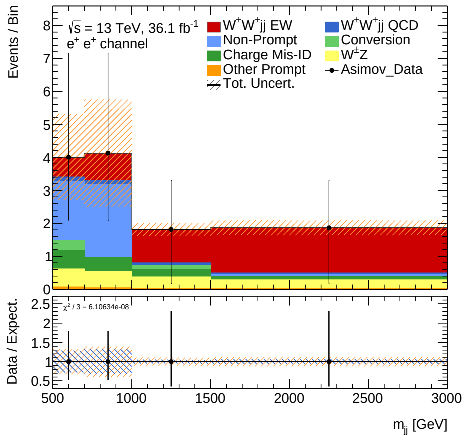

(b) e^+e^+

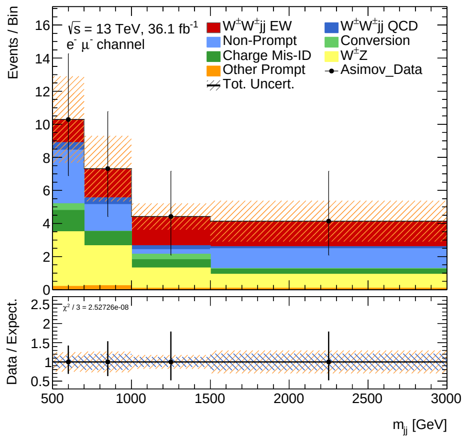

(c) $e^-\mu^-/\mu^-e^-$

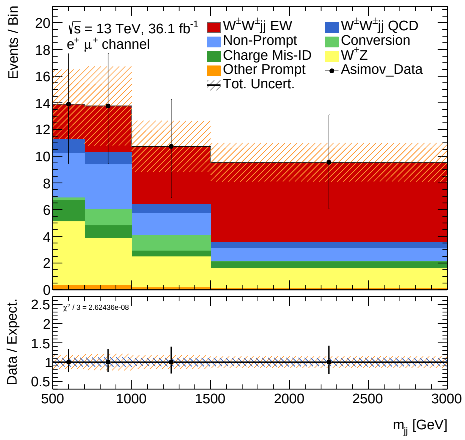

(d) $e^+\mu^+/\mu^+e^+$

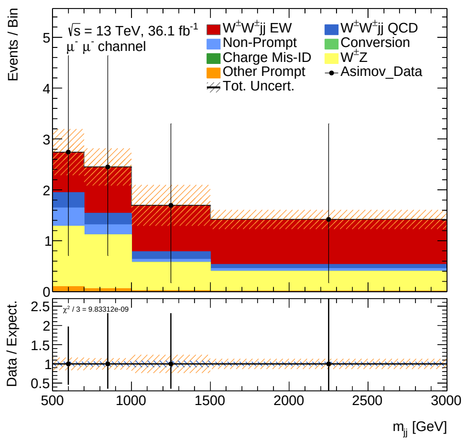

(e) $\mu^-\mu^-$

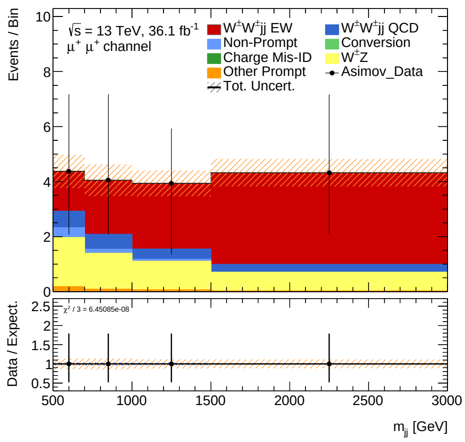

(f) $\mu^+\mu^+$

Figure C.4: Pre-fit m_{jj} distributions in six lepton charge and flavor channels in the signal region. Poisson uncertainties are shown for the Asimov data points. In the ratio plot, statistical (blue) and systematic (orange) uncertainties are shown separately. Background contributions are grouped into categories as listed in Table 9.1.

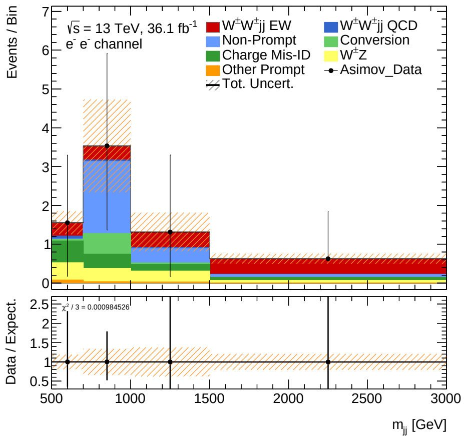

(a) e^-e^-

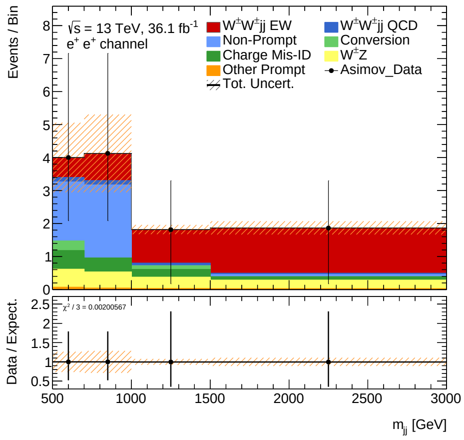

(b) e^+e^+

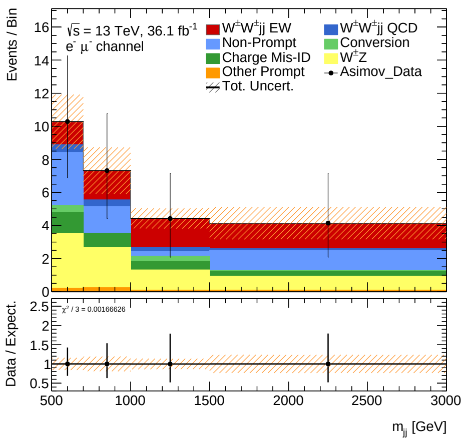

(c) $e^-\mu^-/\mu^-e^-$

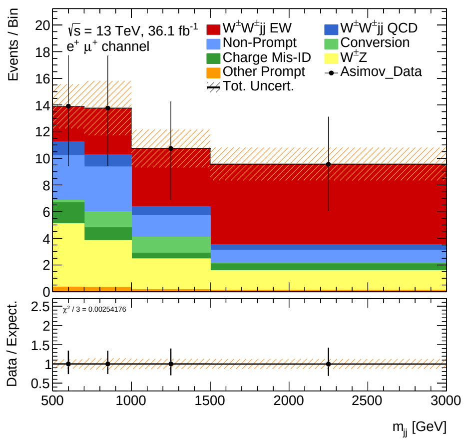

(d) $e^+\mu^+/\mu^+e^+$

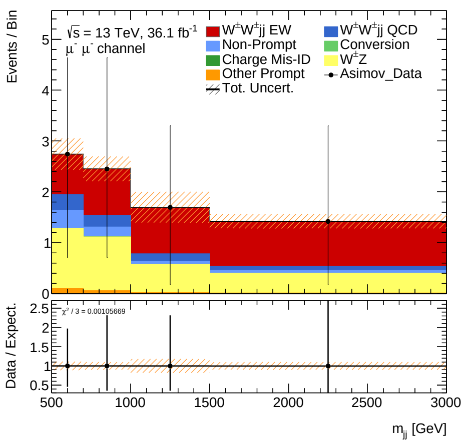

(e) $\mu^-\mu^-$

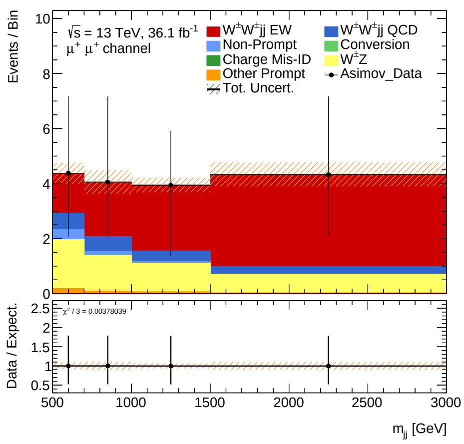

(f) $\mu^+\mu^+$

Figure C.5: Post-fit m_{jj} distributions in six lepton charge and flavor channels in the signal region. Poisson uncertainties are shown for the Asimov data points. In the ratio plot, the combined statistical and systematic uncertainty is shown. Background contributions are grouped into categories as listed in Table 9.1.

C.3.2 Invariant Tagging Jet Mass Distributions with Observed Data

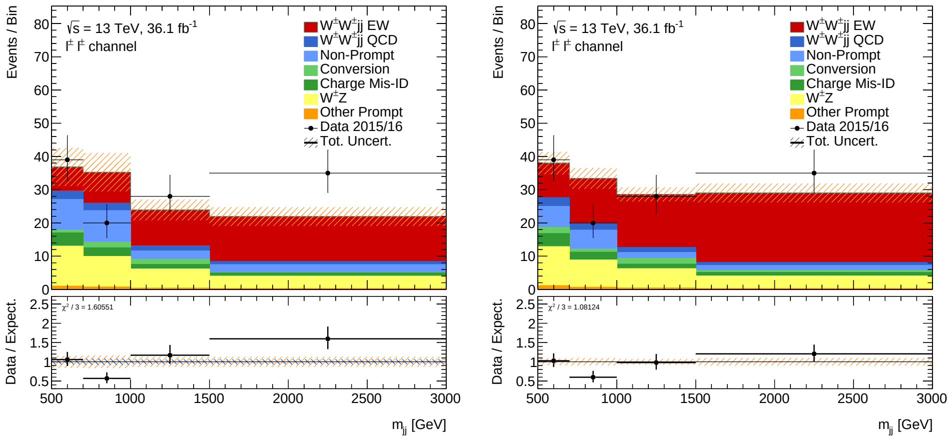

(a) Pre-Fit (b) Post-Fit

Figure C.6: Pre- and post-fit m_{jj} distributions in the combined $\ell^\pm\ell^\pm$ channel in the signal region, including observed data. Poisson uncertainties are shown for the data points. In (a), statistical (blue) and systematic (orange) uncertainties are shown separately the ratio plot. In (b), the combined statistical and systematic uncertainty is shown. Background contributions are grouped into categories as listed in Table 9.1.

C.4 Pre- and Post-Fit Event Yields

In this section, event yields at different stages of the fit are presented Event yields from different contributions are summarized in groups. These are

Other Prompt: This category contains top, tri-boson, ZZ production in all regions.

Charge Mis-ID: In the signal region, this corresponds the to data-driven charge mis-ID estimate. As no data-driven estimate is available in the $W^\pm Z$ control region, Z and WW production are listed.

Non-Prompt: In the signal region, this corresponds the to data-driven non-prompt estimate. As no data-driven estimate is available in the $W^\pm Z$ control region, $t\bar{t}$ and W production are listed.

Conversion: This category contains $V\gamma$ production in all regions.

In addition to these groups, event yields for the $W^\pm Z$ and $W^\pm W^\pm jj$-QCD background as well as $W^\pm W^\pm jj$-EW production are given. Pre- and post-fit yields in the $W^\pm Z$ control region for the fit to Asimov and observed data are shown in Table C.9 and C.10. Pre-fit event yields in the signal and low-m_{jj} control region are listed in Table C.11. Moreover, post-fit event yields after both fits are shown in Table C.12 and C.13. In addition to the central yields, uncertainties broken into statistical, theory and systematic sources are presented.

	Asimov, pre-fit	Asimov, post-fit
Other Prompt	$21.545 \pm 0.369 \pm 0.000 \pm 21.929$	$21.527 \pm 0.223 \pm 0.000 \pm 4.064$
$W^{\pm}Z$	$172.451 \pm 1.423 \pm 58.703 \pm 11.718$	$172.390 \pm 1.784 \pm 20.478 \pm 11.235$
Charge Mis-ID	$0.019 \pm 0.013 \pm 0.000 \pm 0.019$	$0.019 \pm 0.000 \pm 0.000 \pm 0.000$
Conversion	$2.683 \pm 0.602 \pm 0.000 \pm 3.452$	$2.685 \pm 0.028 \pm 0.000 \pm 2.020$
Non-Prompt	$6.816 \pm 1.729 \pm 0.000 \pm 6.816$	$6.816 \pm 0.071 \pm 0.000 \pm 0.143$
$W^{\pm}W^{\pm}$jj QCD	$0.000 \pm 0.000 \pm 0.000 \pm 0.000$	$0.000 \pm 0.000 \pm 0.000 \pm 0.000$
$W^{\pm}W^{\pm}$jj EW	$0.002 \pm 0.000 \pm 0.000 \pm 0.002$	$0.002 \pm 0.000 \pm 0.000 \pm 0.001$
Asimov Data	203.52	203.52
Total Expectation	$203.516 \pm 2.348 \pm 58.703 \pm 33.901$	$203.439 \pm 2.106 \pm 20.478 \pm 13.132$

Table C.9: Event yields in the $\ell^{\pm}\ell^{\pm}\ell^{\mp}$ channel of the $W^{\pm}Z$ control region at different stages in the fit to Asimov Data. In addition, statistical, theory and systematic uncertainties are given.

	Observed, pre-fit	Observed, post-fit
Other Prompt	$21.545 \pm 0.369 \pm 0.000 \pm 21.929$	$22.892 \pm 0.237 \pm 0.000 \pm 4.287$
$W^{\pm}Z$	$172.451 \pm 1.423 \pm 58.703 \pm 11.718$	$170.872 \pm 1.767 \pm 20.623 \pm 11.476$
Charge Mis-ID	$0.019 \pm 0.013 \pm 0.000 \pm 0.019$	$0.019 \pm 0.000 \pm 0.000 \pm 0.000$
Conversion	$2.683 \pm 0.602 \pm 0.000 \pm 3.452$	$1.703 \pm 0.018 \pm 0.000 \pm 1.747$
Non-Prompt	$6.816 \pm 1.729 \pm 0.000 \pm 6.816$	$6.816 \pm 0.070 \pm 0.000 \pm 0.143$
$W^{\pm}W^{\pm}$jj QCD	$0.000 \pm 0.000 \pm 0.000 \pm 0.000$	$0.000 \pm 0.000 \pm 0.000 \pm 0.000$
$W^{\pm}W^{\pm}$jj EW	$0.002 \pm 0.000 \pm 0.000 \pm 0.002$	$0.003 \pm 0.000 \pm 0.000 \pm 0.001$
Data 2015/16	201	201
Total Expectation	$203.516 \pm 2.348 \pm 58.703 \pm 33.901$	$202.305 \pm 2.092 \pm 20.623 \pm 13.586$

Table C.10: Event yields in the $\ell^{\pm}\ell^{\pm}\ell^{\mp}$ channel of the $W^{\pm}Z$ control region at different stages in the fit to observed Data. In addition, statistical, theory and systematic uncertainties are given.

	e^+e^+	e^-e^-	$e^+\mu^+/\mu^+e^+$	$e^-\mu^-/\mu^-e^-$	$\mu^+\mu^+$	$\mu^-\mu^-$	$\ell^\pm\ell^\pm$
				Signal region			
Other Prompt	0.169 ± 0.027 ± 0.000 ± 0.174	0.141 ± 0.025 ± 0.000 ± 0.146	0.896 ± 0.077 ± 0.000 ± 0.913	0.600 ± 0.073 ± 0.000 ± 0.612	0.361 ± 0.044 ± 0.000 ± 0.371	0.187 ± 0.031 ± 0.000 ± 0.194	2.355 ± 0.125 ± 0.000 ± 2.399
$W^\pm Z$	1.637 ± 0.145 ± 0.485 ± 0.153	1.142 ± 0.103 ± 0.339 ± 0.132	12.082 ± 0.465 ± 3.549 ± 0.748	7.811 ± 0.404 ± 2.268 ± 0.562	4.813 ± 0.241 ± 1.427 ± 0.387	3.189 ± 0.221 ± 0.931 ± 0.414	30.674 ± 0.720 ± 8.998 ± 1.838
Charge Mis-ID	1.332 ± 0.080 ± 0.000 ± 0.120	1.173 ± 0.075 ± 0.000 ± 0.101	3.475 ± 0.309 ± 0.000 ± 0.211	2.950 ± 0.258 ± 0.000 ± 0.205	0.000 ± 0.000 ± 0.000 ± 0.000	0.000 ± 0.000 ± 0.000 ± 0.000	8.931 ± 0.417 ± 0.000 ± 0.574
Conversion	0.406 ± 0.168 ± 0.000 ± 0.449	0.618 ± 0.216 ± 0.000 ± 0.685	2.650 ± 0.745 ± 0.000 ± 3.004	0.795 ± 0.264 ± 0.000 ± 1.038	0.000 ± 0.000 ± 0.000 ± 0.000	0.000 ± 0.000 ± 0.000 ± 0.000	4.468 ± 0.837 ± 0.000 ± 5.023
Non Prompt	4.078 ± 1.746 ± 0.000 ± 1.504	2.308 ± 1.469 ± 0.000 ± 0.884	9.347 ± 2.624 ± 0.000 ± 4.101	6.344 ± 2.375 ± 0.000 ± 2.887	0.573 ± 0.133 ± 0.000 ± 0.057	0.668 ± 0.168 ± 0.000 ± 0.186	23.318 ± 4.227 ± 0.000 ± 8.709
$W^\pm W^\pm$jj QCD	0.384 ± 0.018 ± 0.128 ± 0.385	0.157 ± 0.013 ± 0.052 ± 0.157	3.023 ± 0.057 ± 1.013 ± 3.025	1.214 ± 0.035 ± 0.403 ± 1.215	1.800 ± 0.043 ± 0.604 ± 1.802	0.760 ± 0.029 ± 0.252 ± 0.761	7.338 ± 0.088 ± 2.451 ± 7.343
$W^\pm W^\pm$jj EW	3.801 ± 0.000 ± 0.218 ± 3.803	1.492 ± 0.000 ± 0.079 ± 1.493	16.494 ± 0.000 ± 0.949 ± 16.501	6.452 ± 0.000 ± 0.339 ± 6.456	9.139 ± 0.000 ± 0.526 ± 9.146	3.503 ± 0.000 ± 0.185 ± 3.506	40.881 ± 0.000 ± 2.282 ± 40.902
Asimov Data	11.81	7.03	47.97	26.17	16.69	8.31	117.97
Data 2015/16	10	4	44	28	25	11	122
Total Expectation	11.808 ± 1.762 ± 0.547 ± 5.007	7.031 ± 1.491 ± 0.351 ± 2.594	47.966 ± 2.786 ± 3.811 ± 23.509	26.167 ± 2.439 ± 2.329 ± 9.591	16.686 ± 0.283 ± 1.637 ± 11.328	8.307 ± 0.281 ± 0.982 ± 4.489	117.965 ± 4.391 ± 9.602 ± 55.901
				Low-m_{jj} Control Region			
Other Prompt	0.276 ± 0.040 ± 0.000 ± 0.289	0.159 ± 0.034 ± 0.000 ± 0.168	1.200 ± 0.090 ± 0.000 ± 1.221	0.765 ± 0.076 ± 0.000 ± 0.788	0.626 ± 0.058 ± 0.000 ± 0.639	0.370 ± 0.044 ± 0.000 ± 0.386	3.395 ± 0.148 ± 0.000 ± 3.452
$W^\pm Z$	1.765 ± 0.179 ± 0.485 ± 0.232	1.373 ± 0.128 ± 0.378 ± 0.130	12.067 ± 0.516 ± 3.319 ± 0.670	9.021 ± 0.459 ± 2.481 ± 0.686	5.039 ± 0.223 ± 1.386 ± 0.338	3.459 ± 0.185 ± 0.952 ± 0.327	32.723 ± 0.780 ± 9.001 ± 1.905
Charge Mis-ID	1.697 ± 0.078 ± 0.000 ± 0.171	1.768 ± 0.085 ± 0.000 ± 0.144	4.004 ± 0.265 ± 0.000 ± 0.330	3.558 ± 0.247 ± 0.000 ± 0.408	0.000 ± 0.000 ± 0.000 ± 0.000	0.000 ± 0.000 ± 0.000 ± 0.000	11.027 ± 0.380 ± 0.000 ± 0.967
Conversion	0.183 ± 0.046 ± 0.000 ± 0.205	0.262 ± 0.148 ± 0.000 ± 0.290	0.284 ± 0.066 ± 0.000 ± 1.075	2.200 ± 0.482 ± 0.000 ± 2.457	0.000 ± 0.000 ± 0.000 ± 0.000	0.000 ± 0.000 ± 0.000 ± 0.000	2.929 ± 0.511 ± 0.000 ± 3.451
Non Prompt	0.712 ± 0.638 ± 0.000 ± 0.229	4.374 ± 1.765 ± 0.000 ± 1.747	12.775 ± 2.804 ± 0.000 ± 4.945	8.619 ± 2.241 ± 0.000 ± 3.363	2.425 ± 0.710 ± 0.000 ± 1.919	1.175 ± 0.179 ± 0.000 ± 0.200	30.080 ± 4.116 ± 0.000 ± 10.298
$W^\pm W^\pm$jj QCD	0.235 ± 0.015 ± 0.066 ± 0.236	0.153 ± 0.012 ± 0.043 ± 0.154	1.988 ± 0.044 ± 0.554 ± 1.989	1.146 ± 0.032 ± 0.319 ± 1.147	1.160 ± 0.030 ± 0.323 ± 1.162	0.641 ± 0.025 ± 0.179 ± 0.642	5.324 ± 0.070 ± 1.483 ± 5.328
$W^\pm W^\pm$jj EW	0.638 ± 0.000 ± 0.107 ± 0.639	0.474 ± 0.000 ± 0.079 ± 0.477	2.967 ± 0.000 ± 0.496 ± 2.968	1.988 ± 0.000 ± 0.333 ± 1.990	1.825 ± 0.000 ± 0.305 ± 1.826	1.114 ± 0.000 ± 0.186 ± 1.115	9.006 ± 0.000 ± 1.507 ± 9.009
Asimov Data	5.51	8.56	35.28	27.30	11.08	6.76	94.48
Data 2015/16	5	3	39	38	10	6	101
Total Expectation	5.507 ± 0.670 ± 0.501 ± 1.395	8.563 ± 1.778 ± 0.388 ± 2.051	35.283 ± 2.866 ± 3.402 ± 8.278	27.297 ± 2.352 ± 2.524 ± 7.128	11.075 ± 0.747 ± 1.456 ± 4.114	6.759 ± 0.262 ± 0.986 ± 2.163	94.484 ± 4.241 ± 9.246 ± 23.394

Table C.11: Pre-fit event yields in the signal and low-m_{jj} control region. In addition, statistical, theory and systematic uncertainties are given.

	e^+e^+	e^-e^-	$e^+\mu^+/\mu^+e^+$	$e^-\mu^-/\mu^-e^-$	$\mu^+\mu^+$	$\mu^-\mu^-$	$\ell^\pm\ell^\pm$
Signal region							
Other Prompt	0.169 ± 0.026 ± 0.000 ± 0.040	0.141 ± 0.025 ± 0.000 ± 0.037	0.896 ± 0.074 ± 0.000 ± 0.177	0.600 ± 0.070 ± 0.000 ± 0.120	0.361 ± 0.013 ± 0.000 ± 0.085	0.187 ± 0.010 ± 0.000 ± 0.047	2.354 ± 0.112 ± 0.000 ± 0.457
$W^\pm Z$	1.635 ± 0.247 ± 0.223 ± 0.148	1.140 ± 0.222 ± 0.156 ± 0.126	12.070 ± 0.996 ± 1.674 ± 0.737	7.807 ± 0.851 ± 1.110 ± 0.544	4.806 ± 0.166 ± 0.653 ± 0.372	3.182 ± 0.171 ± 0.446 ± 0.379	30.640 ± 1.401 ± 4.261 ± 1.780
Charge Mis-ID	1.332 ± 0.228 ± 0.000 ± 0.120	1.173 ± 0.206 ± 0.000 ± 0.101	3.476 ± 0.294 ± 0.000 ± 0.211	2.951 ± 0.318 ± 0.000 ± 0.204	0.000 ± 0.000 ± 0.000 ± 0.000	0.000 ± 0.000 ± 0.000 ± 0.000	8.932 ± 0.543 ± 0.000 ± 0.571
Conversion	0.405 ± 0.089 ± 0.000 ± 0.186	0.618 ± 0.197 ± 0.000 ± 0.287	2.641 ± 0.285 ± 0.000 ± 1.350	0.796 ± 0.095 ± 0.000 ± 0.630	0.000 ± 0.000 ± 0.000 ± 0.000	0.000 ± 0.000 ± 0.000 ± 0.000	4.461 ± 0.375 ± 0.000 ± 2.204
Non Prompt	4.069 ± 0.935 ± 0.000 ± 0.929	2.302 ± 0.711 ± 0.000 ± 0.548	9.299 ± 0.773 ± 0.000 ± 2.217	6.313 ± 0.739 ± 0.000 ± 1.596	0.574 ± 0.023 ± 0.000 ± 0.055	0.667 ± 0.035 ± 0.000 ± 0.144	23.224 ± 1.632 ± 0.000 ± 4.818
$W^\pm W^\pm$jj QCD	0.383 ± 0.062 ± 0.127 ± 0.028	0.156 ± 0.029 ± 0.051 ± 0.011	3.016 ± 0.253 ± 1.004 ± 0.124	1.212 ± 0.133 ± 0.399 ± 0.059	1.796 ± 0.063 ± 0.599 ± 0.081	0.758 ± 0.042 ± 0.250 ± 0.034	7.321 ± 0.309 ± 2.430 ± 0.314
$W^\pm W^\pm$jj EW	3.822 ± 0.000 ± 0.217 ± 0.142	1.500 ± 0.000 ± 0.079 ± 0.064	16.582 ± 0.000 ± 0.942 ± 0.597	6.487 ± 0.000 ± 0.338 ± 0.254	9.187 ± 0.000 ± 0.522 ± 0.389	3.521 ± 0.000 ± 0.184 ± 0.168	41.100 ± 0.000 ± 2.268 ± 1.553
Asimov Data	11.81	7.03	47.97	26.17	16.69	8.31	117.97
Total Expectation	11.816 ± 1.540 ± 0.340 ± 0.979	7.030 ± 1.300 ± 0.183 ± 0.636	47.980 ± 2.597 ± 2.180 ± 2.908	26.166 ± 2.145 ± 1.226 ± 1.958	16.724 ± 0.261 ± 1.035 ± 0.807	8.316 ± 0.256 ± 0.543 ± 0.557	118.032 ± 4.044 ± 5.428 ± 6.415
Low-m_{jj} Control Region							
Other Prompt	0.275 ± 0.038 ± 0.000 ± 0.084	0.160 ± 0.033 ± 0.000 ± 0.054	1.199 ± 0.098 ± 0.000 ± 0.231	0.764 ± 0.068 ± 0.000 ± 0.179	0.626 ± 0.048 ± 0.000 ± 0.131	0.370 ± 0.017 ± 0.000 ± 0.104	3.394 ± 0.142 ± 0.000 ± 0.626
$W^\pm Z$	1.760 ± 0.245 ± 0.282 ± 0.222	1.373 ± 0.288 ± 0.220 ± 0.130	12.056 ± 0.988 ± 1.929 ± 0.641	9.004 ± 0.803 ± 1.441 ± 0.658	5.032 ± 0.382 ± 0.805 ± 0.324	3.452 ± 0.162 ± 0.552 ± 0.312	32.677 ± 1.420 ± 5.229 ± 1.832
Charge Mis-ID	1.697 ± 0.236 ± 0.000 ± 0.171	1.770 ± 0.371 ± 0.000 ± 0.144	4.006 ± 0.328 ± 0.000 ± 0.329	3.558 ± 0.317 ± 0.000 ± 0.406	0.000 ± 0.000 ± 0.000 ± 0.000	0.000 ± 0.000 ± 0.000 ± 0.000	11.029 ± 0.650 ± 0.000 ± 0.963
Conversion	0.183 ± 0.025 ± 0.000 ± 0.087	0.262 ± 0.055 ± 0.000 ± 0.122	0.288 ± 0.024 ± 0.000 ± 0.965	2.194 ± 0.196 ± 0.000 ± 1.060	0.000 ± 0.000 ± 0.000 ± 0.000	0.000 ± 0.000 ± 0.000 ± 0.000	2.927 ± 0.209 ± 0.000 ± 1.757
Non Prompt	0.714 ± 0.099 ± 0.000 ± 0.198	4.366 ± 0.916 ± 0.000 ± 1.069	12.726 ± 1.043 ± 0.000 ± 2.834	8.596 ± 0.767 ± 0.000 ± 2.204	2.408 ± 0.183 ± 0.000 ± 1.139	1.174 ± 0.055 ± 0.000 ± 0.160	29.985 ± 1.645 ± 0.000 ± 6.097
$W^\pm W^\pm$jj QCD	0.235 ± 0.033 ± 0.065 ± 0.010	0.153 ± 0.032 ± 0.042 ± 0.011	1.985 ± 0.163 ± 0.549 ± 0.078	1.144 ± 0.102 ± 0.316 ± 0.046	1.158 ± 0.088 ± 0.320 ± 0.065	0.640 ± 0.030 ± 0.177 ± 0.030	5.314 ± 0.222 ± 1.471 ± 0.211
$W^\pm W^\pm$jj EW	0.643 ± 0.000 ± 0.105 ± 0.031	0.478 ± 0.000 ± 0.078 ± 0.051	2.989 ± 0.000 ± 0.489 ± 0.104	2.003 ± 0.000 ± 0.327 ± 0.104	1.838 ± 0.000 ± 0.301 ± 0.075	1.122 ± 0.000 ± 0.183 ± 0.043	9.073 ± 0.000 ± 1.483 ± 0.316
Asimov Data	5.51	8.56	35.28	27.30	11.08	6.76	94.48
Total Expectation	5.507 ± 0.676 ± 0.299 ± 0.391	8.561 ± 1.696 ± 0.231 ± 1.073	35.249 ± 2.643 ± 2.016 ± 3.172	27.263 ± 2.253 ± 1.480 ± 2.521	11.062 ± 0.701 ± 0.889 ± 1.220	6.759 ± 0.265 ± 0.591 ± 0.383	94.400 ± 4.100 ± 5.490 ± 6.923

Table C.12: Event yields in the signal low-m_{jj} control region after the fit to Asimov data. In addition, statistical, theory and systematic uncertainties are given.

	e^+e^+	e^-e^-	$e^+\mu^+/\mu^+e^+$	$e^-\mu^-/\mu^-e^-$	$\mu^+\mu^+$	$\mu^-\mu^-$	$\ell^\pm\ell^\pm$
Signal region							
Other Prompt	0.158 ± 0.027 ± 0.000 ± 0.036	0.143 ± 0.027 ± 0.000 ± 0.036	0.897 ± 0.075 ± 0.000 ± 0.179	0.624 ± 0.070 ± 0.000 ± 0.120	0.387 ± 0.014 ± 0.000 ± 0.086	0.217 ± 0.012 ± 0.000 ± 0.051	2.425 ± 0.113 ± 0.000 ± 0.464
$W^\pm Z$	1.441 ± 0.226 ± 0.193 ± 0.131	1.053 ± 0.209 ± 0.152 ± 0.125	11.257 ± 0.953 ± 1.562 ± 0.721	7.730 ± 0.835 ± 1.128 ± 0.537	4.804 ± 0.168 ± 0.675 ± 0.365	3.310 ± 0.184 ± 0.497 ± 0.359	29.596 ± 1.348 ± 4.200 ± 1.767
Charge Mis-ID	1.204 ± 0.220 ± 0.000 ± 0.112	1.046 ± 0.195 ± 0.000 ± 0.094	3.380 ± 0.292 ± 0.000 ± 0.206	2.973 ± 0.321 ± 0.000 ± 0.208	0.000 ± 0.000 ± 0.000 ± 0.000	0.000 ± 0.000 ± 0.000 ± 0.000	8.603 ± 0.536 ± 0.000 ± 0.557
Conversion	0.422 ± 0.100 ± 0.000 ± 0.199	0.530 ± 0.207 ± 0.000 ± 0.249	2.924 ± 0.284 ± 0.000 ± 1.502	1.379 ± 0.191 ± 0.000 ± 1.019	0.000 ± 0.000 ± 0.000 ± 0.000	0.000 ± 0.000 ± 0.000 ± 0.000	5.255 ± 0.419 ± 0.000 ± 2.739
Non Prompt	2.282 ± 0.571 ± 0.000 ± 1.256	1.209 ± 0.392 ± 0.000 ± 0.652	5.859 ± 0.499 ± 0.000 ± 2.851	4.626 ± 0.547 ± 0.000 ± 1.767	0.575 ± 0.023 ± 0.000 ± 0.053	0.653 ± 0.035 ± 0.000 ± 0.137	15.204 ± 1.044 ± 0.000 ± 6.325
$W^\pm W^\pm$jj QCD	0.348 ± 0.060 ± 0.114 ± 0.025	0.146 ± 0.028 ± 0.045 ± 0.011	2.926 ± 0.251 ± 0.952 ± 0.124	1.208 ± 0.132 ± 0.388 ± 0.060	1.792 ± 0.063 ± 0.587 ± 0.082	0.762 ± 0.041 ± 0.245 ± 0.036	7.182 ± 0.305 ± 2.332 ± 0.317
$W^\pm W^\pm$jj EW	5.648 ± 0.000 ± 0.309 ± 0.208	2.236 ± 0.000 ± 0.114 ± 0.097	24.518 ± 0.000 ± 1.345 ± 0.890	9.542 ± 0.000 ± 0.488 ± 0.378	13.601 ± 0.000 ± 0.745 ± 0.575	5.225 ± 0.000 ± 0.266 ± 0.250	60.771 ± 0.000 ± 3.247 ± 2.316
Data 2015/16	10	4	44	28	25	11	122
Total Expectation	11.503 ± 1.164 ± 0.391 ± 1.259	6.363 ± 0.976 ± 0.199 ± 0.684	51.760 ± 2.287 ± 2.318 ± 3.386	28.082 ± 2.024 ± 1.299 ± 2.142	21.160 ± 0.264 ± 1.188 ± 0.982	10.168 ± 0.268 ± 0.620 ± 0.597	129.037 ± 3.511 ± 5.905 ± 7.702
Low-m_{jj} Control Region							
Other Prompt	0.249 ± 0.035 ± 0.000 ± 0.078	0.145 ± 0.035 ± 0.000 ± 0.044	1.235 ± 0.101 ± 0.000 ± 0.234	0.961 ± 0.083 ± 0.000 ± 0.219	0.617 ± 0.047 ± 0.000 ± 0.132	0.316 ± 0.015 ± 0.000 ± 0.096	3.524 ± 0.151 ± 0.000 ± 0.649
$W^\pm Z$	1.799 ± 0.252 ± 0.305 ± 0.237	1.106 ± 0.266 ± 0.178 ± 0.105	11.986 ± 0.977 ± 1.938 ± 0.674	9.928 ± 0.858 ± 1.659 ± 0.805	4.870 ± 0.371 ± 0.791 ± 0.343	3.508 ± 0.165 ± 0.586 ± 0.321	33.197 ± 1.441 ± 5.452 ± 2.099
Charge Mis-ID	1.675 ± 0.234 ± 0.000 ± 0.169	1.472 ± 0.354 ± 0.000 ± 0.131	4.152 ± 0.338 ± 0.000 ± 0.339	3.914 ± 0.338 ± 0.000 ± 0.440	0.000 ± 0.000 ± 0.000 ± 0.000	0.000 ± 0.000 ± 0.000 ± 0.000	11.213 ± 0.656 ± 0.000 ± 0.998
Conversion	0.171 ± 0.024 ± 0.000 ± 0.084	0.235 ± 0.056 ± 0.000 ± 0.110	1.743 ± 0.142 ± 0.000 ± 1.791	2.647 ± 0.229 ± 0.000 ± 1.307	0.000 ± 0.000 ± 0.000 ± 0.000	0.000 ± 0.000 ± 0.000 ± 0.000	4.795 ± 0.282 ± 0.000 ± 2.924
Non Prompt	0.922 ± 0.129 ± 0.000 ± 0.271	2.184 ± 0.525 ± 0.000 ± 1.431	9.668 ± 0.788 ± 0.000 ± 3.314	6.563 ± 0.567 ± 0.000 ± 2.815	2.216 ± 0.169 ± 0.000 ± 0.902	1.157 ± 0.054 ± 0.000 ± 0.154	22.708 ± 1.157 ± 0.000 ± 7.390
$W^\pm W^\pm$jj QCD	0.228 ± 0.032 ± 0.063 ± 0.010	0.133 ± 0.032 ± 0.035 ± 0.009	2.031 ± 0.166 ± 0.555 ± 0.078	1.241 ± 0.107 ± 0.337 ± 0.051	1.176 ± 0.090 ± 0.313 ± 0.067	0.645 ± 0.030 ± 0.174 ± 0.030	5.454 ± 0.227 ± 1.477 ± 0.215
$W^\pm W^\pm$jj EW	0.897 ± 0.000 ± 0.148 ± 0.044	0.610 ± 0.000 ± 0.110 ± 0.072	4.144 ± 0.000 ± 0.688 ± 0.149	2.738 ± 0.000 ± 0.461 ± 0.150	2.513 ± 0.000 ± 0.423 ± 0.108	1.554 ± 0.000 ± 0.258 ± 0.061	12.455 ± 0.000 ± 2.089 ± 0.447
Data 2015/16	5	3	39	38	10	6	101
Total Expectation	5.941 ± 0.705 ± 0.330 ± 0.453	5.885 ± 1.268 ± 0.202 ± 1.421	34.958 ± 2.512 ± 2.050 ± 3.579	27.991 ± 2.183 ± 1.701 ± 2.964	11.392 ± 0.676 ± 0.905 ± 1.020	7.180 ± 0.264 ± 0.636 ± 0.396	93.347 ± 3.799 ± 5.789 ± 7.874

Table C.13: Event yields in the signal low-m_{jj} control region after the fit to observed data. In addition, statistical, theory and systematic uncertainties are given.

C.5 Nuisance Parameter Correlations

C.5.1 Nuisance Parameter Correlations after Fit to Asimov Data

Parameter 1	Parameter 2	Correlation [%]
$W^{\pm}Z$ Shower	μ_{WZ}	−67.1
$W^{\pm}Z$ Scale	μ_{WZ}	−66.6
Non Prompt e Stat.	Non Prompt e Sys.	−26.1
$W^{\pm}W^{\pm}jj$-Ew Shower	μ	21.3
Non Prompt e Sys.	Bkg Stat. Low-m_{jj} Cr, e^-e^- Chan, Bin 1	−19.2
Non Prompt μ Sys.	μ	−18.2
Non Prompt e Sys.	Bkg Stat. SR, e^-e^- Chan, Bin 2	−16.6
$W^{\pm}W^{\pm}jj$-Qcd Scale	μ	−16.2
Jet Flavor Composition	μ_{WZ}	−14.9
Non Prompt e Sys.	Bkg Stat. SR, e^+e^+ Chan, Bin 2	−14.0
Non Prompt e Sys.	μ	−13.7
Bkg Stat. SR, $e^+\mu^+/\mu^+e^+$ Chan, Bin 4	μ	−13.4
Non Prompt μ Sys.	Bkg Stat. SR, $e^-\mu^-/\mu^-e^-$ Chan, Bin 1	−13.1
Non Prompt μ Sys.	$W^{\pm}Z$ Shower	12.7
Non Prompt e Sys.	Non Prompt μ Sys.	−12.3
Jet Energy Resolution	Bkg Stat. SR, $e^+\mu^+/\mu^+e^+$ Chan, Bin 2	−12.1
Non Prompt e Sys.	Bkg Stat. Low-m_{jj} Cr, $e^-\mu^-/\mu^-e^-$ Chan, Bin 1	−11.8
Non Prompt μ Sys.	μ_{WZ}	−11.4
Non Prompt μ Sys.	Bkg Stat. Low-m_{jj} Cr, $e^+\mu^+/\mu^+e^+$ Chan, Bin 1	−11.1
Non Prompt e Sys.	Bkg Stat. Low-m_{jj} Cr, $e^+\mu^+/\mu^+e^+$ Chan, Bin 1	−9.5
Jet Flavor Composition	μ	−9.3
Non Prompt e Sys.	$W^{\pm}Z$ Shower	8.9
$W^{\pm}W^{\pm}jj$-Ew Ew Corr.	μ	8.8
Luminosity	μ	−8.7
Jet Energy Resolution	Bkg Stat. SR, $e^+\mu^+/\mu^+e^+$ Chan, Bin 1	8.6
Bkg Stat. SR, $e^+\mu^+/\mu^+e^+$ Chan, Bin 3	μ	−8.4
Non Prompt μ Stat.	Non Prompt μ Sys.	−8.2
Non Prompt μ Sys.	Jet Energy Resolution	−8.1
Conversion Model $V\gamma$	Non Prompt e Sys.	−7.9
Pile-up Reweight. data SF	μ	7.8
Non Prompt μ Sys.	Bkg Stat. SR, $e^+\mu^+/\mu^+e^+$ Chan, Bin 2	−7.8
Flavor Tag Eff. Eigen Light 1	μ	−7.7
$W^{\pm}Z$ Shower	μ	7.2
Non Prompt μ Sys.	Bkg Stat. Low-m_{jj} Cr, $\mu^+\mu^+$ Chan, Bin 1	−7.0
Jet Flavor Composition	Bkg Stat. SR, $e^-\mu^-/\mu^-e^-$ Chan, Bin 4	−7.0
Jet Pile-up OffsetNPV	Bkg Stat. SR, $e^-\mu^-/\mu^-e^-$ Chan, Bin 4	−7.0
$W^{\pm}W^{\pm}jj$-Ew Scale	μ	−6.9
Non Prompt e Sys.	μ_{WZ}	−6.8
Non Prompt e Sys.	Bkg Stat. SR, e^+e^+ Chan, Bin 1	−6.7
Jet EtaIntercalibration Modeling	μ	−6.3
Conversion Model $V\gamma$	μ	−6.3
Jet EtaIntercalibration Modeling	μ_{WZ}	−6.2
Jet Energy Resolution	μ_{WZ}	6.1
Non Prompt e Stat.	Bkg Stat. Low-m_{jj} Cr, $e^-\mu^-/\mu^-e^-$ Chan, Bin 1	−5.9
Flavor Tag Eff. Eigen Light 1	μ_{WZ}	−5.9
Pile-up Reweight. data SF	Bkg Stat. SR, $e^-\mu^-/\mu^-e^-$ Chan, Bin 2	−5.9
Non Prompt μ Sys.	Bkg Stat. SR, $e^-\mu^-/\mu^-e^-$ Chan, Bin 2	−5.7
Non Prompt e Stat.	μ	−5.7
μ	μ_{WZ}	−5.6
$W^{\pm}W^{\pm}jj$-Qcd Shower	μ	−5.6
Interference	μ	5.6
Bkg Stat. SR, $e^+\mu^+/\mu^+e^+$ Chan, Bin 2	μ	−5.6
Conversion Model $V\gamma$	Bkg Stat. SR, e^-e^- Chan, Bin 2	−5.1
Non Prompt μ Sys.	$W^{\pm}W^{\pm}jj$-Qcd Scale	−5.0
Non Prompt μ Sys.	$W^{\pm}W^{\pm}jj$-Ew Ew Corr.	−5.0
Bkg Stat. SR, $e^-\mu^-/\mu^-e^-$ Chan, Bin 3	μ	−4.9
Non Prompt μ Sys.	$W^{\pm}W^{\pm}jj$-Ew Shower	−4.9
Jet Energy Resolution	Bkg Stat. SR, $e^-\mu^-/\mu^-e^-$ Chan, Bin 2	−4.9
Muon Eff. Sys.	μ	−4.9
Conversion Model $V\gamma$	Bkg Stat. Low-m_{jj} Cr, $e^-\mu^-/\mu^-e^-$ Chan, Bin 1	−4.8
$W^{\pm}Z$ PDF	μ_{WZ}	−4.7
Non Prompt μ Sys.	Bkg Stat. Low-m_{jj} Cr, e^-e^- Chan, Bin 1	4.7
Bkg Stat. SR, $e^-\mu^-/\mu^-e^-$ Chan, Bin 4	μ	−4.7

Parameter 1	Parameter 2	Correlation [%]
Jet Energy Resolution	Bkg Stat. SR, $e^-\mu^-/\mu^-e^-$ Chan, Bin 1	4.7
Non Prompt e Stat.	Bkg Stat. Low-m_{jj} CR, $e^+\mu^+/\mu^+e^+$ Chan, Bin 1	−4.7
Non Prompt μ Sys.	Pile-up Reweight. data SF	−4.7
Non Prompt e Stat.	Non Prompt μ Sys.	−4.6
Jet Pile-up RhoTopology	μ_{WZ}	−4.6
Non Prompt μ Sys.	Bkg Stat. Low-m_{jj} CR, $e^-\mu^-/\mu^-e^-$ Chan, Bin 1	4.6
Jet Flavor Composition	Bkg Stat. Low-m_{jj} CR, $e^+\mu^+/\mu^+e^+$ Chan, Bin 1	−4.5
Non Prompt e Stat.	Bkg Stat. Low-m_{jj} CR, e^-e^- Chan, Bin 1	−4.4
Non Prompt e Stat.	$W^{\pm}Z$ Shower	4.4
ZZ x-sec.	μ_{WZ}	−4.3
Muon Eff. Sys.	μ_{WZ}	−4.3
Bkg Stat. SR, $e^-\mu^-/\mu^-e^-$ Chan, Bin 2	μ	−4.3
Jet Pile-up p_{T} Term	μ	−4.2
Jet Energy Resolution	μ	4.2
Jet Flavor Response	μ_{WZ}	4.1
Bkg Stat. SR, e^-e^- Chan, Bin 2	Bkg Stat. Low-m_{jj} CR, e^-e^- Chan, Bin 1	4.1
Non Prompt e Sys.	Jet Flavor Composition	−4.0
$W^{\pm}Z$ Shower	Bkg Stat. Low-m_{jj} CR, $e^-\mu^-/\mu^-e^-$ Chan, Bin 1	4.0
Non Prompt μ Sys.	Bkg Stat. SR, e^+e^+ Chan, Bin 2	3.9
Conversion Model $V\gamma$	Bkg Stat. SR, $e^+\mu^+/\mu^+e^+$ Chan, Bin 3	−3.9
Non Prompt μ Sys.	Bkg Stat. SR, e^-e^- Chan, Bin 2	3.8
Non Prompt μ Sys.	Interference	−3.7
Jet Flavor Response	μ	3.7
Non Prompt e Stat.	Bkg Stat. SR, e^+e^+ Chan, Bin 1	−3.7
Bkg Stat. Low-m_{jj} CR, e^-e^- Chan, Bin 1	Bkg Stat. Low-m_{jj} CR, $e^-\mu^-/\mu^-e^-$ Chan, Bin 1	3.6
Bkg Stat. SR, e^-e^- Chan, Bin 3	μ	−3.6
Non Prompt μ Sys.	Bkg Stat. SR, $e^+\mu^+/\mu^+e^+$ Chan, Bin 3	−3.6
Non Prompt e Sys.	$W^{\pm}\gamma$ x-sec.	−3.6
Non Prompt μ Stat.	μ	−3.6
Conversion Model $V\gamma$	Bkg Stat. SR, $e^+\mu^+/\mu^+e^+$ Chan, Bin 2	−3.6
Bkg Stat. SR, e^+e^+ Chan, Bin 2	Bkg Stat. Low-m_{jj} CR, e^-e^- Chan, Bin 1	3.6
Non Prompt μ Sys.	Bkg Stat. SR, $e^+\mu^+/\mu^+e^+$ Chan, Bin 1	−3.5
Jet EtaIntercalibration Non-Closure	μ	3.5
$W^{\pm}Z$ Shower	Bkg Stat. SR, $e^+\mu^+/\mu^+e^+$ Chan, Bin 3	−3.4
top x-sec.	μ_{WZ}	−3.3
Non Prompt e Stat.	μ_{WZ}	−3.3
Jet Flavor Composition	Jet Pile-up OffsetNPV	−3.3
Bkg Stat. SR, e^-e^- Chan, Bin 2	Bkg Stat. Low-m_{jj} CR, $e^-\mu^-/\mu^-e^-$ Chan, Bin 1	3.2
Non Prompt e Sys.	Bkg Stat. SR, $e^+\mu^+/\mu^+e^+$ Chan, Bin 1	−3.2
Non Prompt μ Sys.	Bkg Stat. SR, $e^+\mu^+/\mu^+e^+$ Chan, Bin 4	3.2
$W^{\pm}\gamma$ x-sec.	μ	−3.2
Non Prompt μ Sys.	Jet EtaIntercalibration Modeling	3.1
Conversion Model $V\gamma$	Non Prompt e Stat.	−3.1
Bkg Stat. Low-m_{jj} CR, $e^-\mu^-/\mu^-e^-$ Chan, Bin 1	μ_{WZ}	−3.1
$W^{\pm}Z$ Shower	$W^{\pm}W^{\pm}jj$-QCD Scale	3.1
$W^{\pm}Z$ Shower	$W^{\pm}W^{\pm}jj$-EW Shower	3.1
$W^{\pm}Z$ Shower	$W^{\pm}W^{\pm}jj$-EW EW Corr.	3.1
$W^{\pm}Z$ Shower	Bkg Stat. Low-m_{jj} CR, $e^+\mu^+/\mu^+e^+$ Chan, Bin 1	3.0
Jet EffectiveNP 2	μ_{WZ}	−3.0
Non Prompt μ Sys.	$W^{\pm}W^{\pm}jj$-EW Scale	2.9
Bkg Stat. SR, $e^+\mu^+/\mu^+e^+$ Chan, Bin 1	μ	−2.9
Non Prompt e Stat.	Bkg Stat. SR, e^+e^+ Chan, Bin 2	−2.9
Non Prompt e Sys.	Bkg Stat. SR, $e^-\mu^-/\mu^-e^-$ Chan, Bin 4	−2.9
CR$W^{\pm}Z$ 3Lep $\ell^{\pm}\ell^{\pm}\ell^{\mp}$ Chan, Bin 1	μ_{WZ}	−2.9
Non Prompt e Sys.	Bkg Stat. Low-m_{jj} CR, e^+e^+ Chan, Bin 1	2.9
Bkg Stat. SR, e^-e^- Chan, Bin 2	Bkg Stat. SR, e^+e^+ Chan, Bin 2	2.9
Jet Pile-up p_{T} Term	μ_{WZ}	−2.8
Bkg Stat. Low-m_{jj} CR, e^-e^- Chan, Bin 1	Bkg Stat. Low-m_{jj} CR, $e^+\mu^+/\mu^+e^+$ Chan, Bin 1	2.7
Non Prompt μ Sys.	Bkg Stat. SR, e^+e^+ Chan, Bin 1	2.7
Conversion Model $V\gamma$	Jet Energy Resolution	−2.7
Charge Mis-ID Energy Corr.	Non Prompt e Sys.	2.7
Non Prompt e Stat.	Jet Flavor Composition	−2.7
Non Prompt μ Stat.	$W^{\pm}Z$ Shower	2.6
Charge Mis-ID Energy Corr.	μ	2.6
Jet Flavor Composition	Bkg Stat. SR, $e^-\mu^-/\mu^-e^-$ Chan, Bin 1	2.6
Bkg Stat. Low-m_{jj} CR, $e^-\mu^-/\mu^-e^-$ Chan, Bin 1	Bkg Stat. Low-m_{jj} CR, $e^+\mu^+/\mu^+e^+$ Chan, Bin 1	2.6
Bkg Stat. SR, e^+e^+ Chan, Bin 2	μ	−2.6
Bkg Stat. SR, $e^-\mu^-/\mu^-e^-$ Chan, Bin 1	Bkg Stat. Low-m_{jj} CR, $e^+\mu^+/\mu^+e^+$ Chan, Bin 1	2.6

Parameter 1	Parameter 2	Correlation [%]
Bkg Stat. SR, $e^+\mu^+/\mu^+e^+$ Chan, Bin 3	μ_{WZ}	2.5
Pile-up Reweight. data SF	Bkg Stat. SR, $e^-\mu^-/\mu^-e^-$ Chan, Bin 1	−2.5
$W^\pm W^\pm jj$-EW EW Corr.	μ_{WZ}	−2.5
$W^\pm W^\pm jj$-EW Shower	μ_{WZ}	−2.5
Bkg Stat. SR, e^+e^+ Chan, Bin 2	Bkg Stat. Low-m_{jj} CR, $e^-\mu^-/\mu^-e^-$ Chan, Bin 1	2.5
$W^\pm W^\pm jj$-QCD Scale	μ_{WZ}	−2.5
MET Soft Trk. Resolution	μ_{WZ}	−2.5
Conversion Model $V\gamma$	$W^\pm\gamma$ x-sec.	−2.5
Interference	$W^\pm Z$ Shower	2.4
Bkg Stat. Low-m_{jj} CR, $e^+\mu^+/\mu^+e^+$ Chan, Bin 1	μ	2.4
Non Prompt e Sys.	$W^\pm W^\pm jj$-EW Shower	−2.4
Non Prompt μ Sys.	Bkg Stat. SR, $e^-\mu^-/\mu^-e^-$ Chan, Bin 4	2.3
$W^\pm Z$ α_s	μ_{WZ}	−2.3
$W^\pm\gamma$ x-sec.	Bkg Stat. SR, e^-e^- Chan, Bin 2	−2.3
Jet Flavor Composition	Bkg Stat. Low-m_{jj} CR, e^-e^- Chan, Bin 1	2.3
Bkg Stat. Low-m_{jj} CR, $e^+\mu^+/\mu^+e^+$ Chan, Bin 1	μ_{WZ}	−2.3
Non Prompt μ Stat.	μ_{WZ}	−2.2
Jet Flavor Composition	Bkg Stat. SR, $e^+\mu^+/\mu^+e^+$ Chan, Bin 2	2.2
Charge Mis-ID Scale Fac.	Non Prompt e Sys.	−2.2
Pile-up Reweight. data SF	Bkg Stat. SR, $e^+\mu^+/\mu^+e^+$ Chan, Bin 3	2.2
CR$W^\pm Z$ 3Lep $\ell^\pm\ell^\pm\ell^\mp$ Chan, Bin 1	μ	2.2
Conversion Model $V\gamma$	Bkg Stat. Low-m_{jj} CR, $e^+\mu^+/\mu^+e^+$ Chan, Bin 1	2.2
Conversion Model $V\gamma$	μ_{WZ}	−2.2
Pile-up Reweight. data SF	μ_{WZ}	2.1
$W^\pm Z$ Shower	Bkg Stat. SR, $e^+\mu^+/\mu^+e^+$ Chan, Bin 1	2.1
Conversion Model $V\gamma$	Bkg Stat. SR, e^+e^+ Chan, Bin 2	2.1
Charge Mis-ID Energy Corr.	Bkg Stat. Low-m_{jj} CR, $e^-\mu^-/\mu^-e^-$ Chan, Bin 1	2.1
Non Prompt e Stat.	Bkg Stat. SR, e^-e^- Chan, Bin 3	−2.1
Non Prompt e Sys.	Bkg Stat. Low-m_{jj} CR, $\mu^+\mu^+$ Chan, Bin 1	2.1
Non Prompt e Sys.	$W^\pm W^\pm jj$-EW EW Corr.	−2.1
Bkg Stat. SR, e^-e^- Chan, Bin 2	Bkg Stat. Low-m_{jj} CR, $e^+\mu^+/\mu^+e^+$ Chan, Bin 1	2.0
Non Prompt e Sys.	Pile-up Reweight. data SF	−2.0
Bkg Stat. SR, e^+e^+ Chan, Bin 1	Bkg Stat. Low-m_{jj} CR, e^-e^- Chan, Bin 1	2.0
$W^\pm\gamma$ x-sec.	Bkg Stat. Low-m_{jj} CR, $e^-\mu^-/\mu^-e^-$ Chan, Bin 1	−2.0
Jet EffectiveNP 3	μ	−2.0

Table C.14: Pair-wise correlation factors between two nuisance parameters after the fit to Asimov data. Parameter pairs are sorted by descending absolute correlation value. Only correlations larger than 2 % are given.

C.5.2 Nuisance Parameter Correlations after Fit to Observed Data

Parameter 1	Parameter 2	Correlation [%]
$W^\pm Z$ Shower	μ_{WZ}	−69.2
$W^\pm Z$ Scale	μ_{WZ}	−66.7
$W^\pm W^\pm jj$-EW Shower	μ	28.2
Non Prompt e Sys.	Bkg Stat. Low-m_{jj} CR, e^-e^- Chan, Bin 1	−25.4
Non Prompt e Stat.	Non Prompt e Sys.	−24.8
Non Prompt e Sys.	Bkg Stat. SR, e^-e^- Chan, Bin 2	−21.0
Non Prompt e Sys.	Bkg Stat. SR, e^+e^+ Chan, Bin 2	−18.7
Non Prompt e Sys.	μ	−18.5
Conversion Model $V\gamma$	Jet Energy Resolution	−15.7
Jet Flavor Composition	μ_{WZ}	−15.5
Conversion Model $V\gamma$	Non Prompt e Sys.	−15.2
Jet Energy Resolution	Bkg Stat. SR, $e^+\mu^+/\mu^+e^+$ Chan, Bin 2	−15.0
Non Prompt e Sys.	Jet Flavor Composition	−14.5
$W^\pm W^\pm jj$-QCD Scale	μ	−13.9
Non Prompt e Sys.	$W^\pm Z$ Shower	12.1
Jet Flavor Composition	Bkg Stat. SR, $e^-\mu^-/\mu^-e^-$ Chan, Bin 4	−12.0
Jet Flavor Composition	Jet Pile-up OffsetNPV	−11.7
Luminosity	μ	−11.6
Jet Flavor Composition	μ	−11.3
Non Prompt e Sys.	Non Prompt μ Sys.	−11.2
Non Prompt e Sys.	Bkg Stat. Low-m_{jj} CR, $e^-\mu^-/\mu^-e^-$ Chan, Bin 1	−9.9
Flavor Tag Eff. Eigen Light 1	μ	−9.6

Parameter 1	Parameter 2	Correlation [%]
Non Prompt e Sys.	Bkg Stat. SR, e^+e^+ Chan, Bin 1	−9.2
Non Prompt e Sys.	Bkg Stat. Low-m_{jj} CR, $e^+\mu^+/\mu^+e^+$ Chan, Bin 1	−8.9
Jet Energy Resolution	Bkg Stat. SR, $e^+\mu^+/\mu^+e^+$ Chan, Bin 1	8.7
Jet Flavor Composition	Bkg Stat. Low-m_{jj} CR, $e^+\mu^+/\mu^+e^+$ Chan, Bin 1	−8.7
Non Prompt e Sys.	Jet Energy Resolution	8.7
Non Prompt μ Sys.	μ	−8.5
Jet Pile-up RhoTopology	μ_{WZ}	−8.4
Conversion Model $V\gamma$	Jet Flavor Composition	8.4
Bkg Stat. SR, $e^+\mu^+/\mu^+e^+$ Chan, Bin 3	μ	−8.0
Jet EtaIntercalibration Modeling	μ_{WZ}	−8.0
Non Prompt e Sys.	μ_{WZ}	−8.0
Bkg Stat. SR, $e^+\mu^+/\mu^+e^+$ Chan, Bin 4	μ	−7.9
Pile-up Reweight. data SF	μ	7.8
Jet Pile-up OffsetNPV	Bkg Stat. SR, $e^-\mu^-/\mu^-e^-$ Chan, Bin 4	−7.6
Non Prompt e Sys.	$W^\pm\gamma$ x-sec.	−7.5
Jet EffectiveNP 2	μ_{WZ}	−7.3
Non Prompt e Stat.	Jet Flavor Composition	−7.1
Conversion Model $V\gamma$	μ	−7.0
Jet Flavor Response	μ_{WZ}	7.0
Jet Energy Resolution	μ_{WZ}	7.0
Jet Energy Resolution	$W^\pm\gamma$ x-sec.	−6.8
Flavor Tag Eff. Eigen Light 1	μ_{WZ}	−6.6
Non Prompt e Sys.	Bkg Stat. SR, $e^-\mu^-/\mu^-e^-$ Chan, Bin 1	−6.6
Jet EtaIntercalibration Modeling	μ	−6.4
$W^\pm W^\pm jj$-EW Scale	μ	−6.2
Jet Flavor Composition	Bkg Stat. Low-m_{jj} CR, e^-e^- Chan, Bin 1	6.2
Non Prompt μ Sys.	$W^\pm Z$ Shower	6.1
Non Prompt μ Sys.	Bkg Stat. SR, $e^-\mu^-/\mu^-e^-$ Chan, Bin 1	−6.1
Non Prompt e Sys.	Bkg Stat. SR, $e^+\mu^+/\mu^+e^+$ Chan, Bin 2	−6.1
$W^\pm Z$ Shower	μ	6.1
Bkg Stat. SR, e^-e^- Chan, Bin 2	Bkg Stat. Low-m_{jj} CR, e^-e^- Chan, Bin 1	6.0
Muon Eff. Sys.	μ	−5.8
$W^\pm W^\pm jj$-EW EW Corr.	μ	5.7
Jet Energy Resolution	Bkg Stat. SR, $e^-\mu^-/\mu^-e^-$ Chan, Bin 2	−5.7
Bkg Stat. SR, e^+e^+ Chan, Bin 2	Bkg Stat. Low-m_{jj} CR, e^-e^- Chan, Bin 1	5.5
Non Prompt μ Sys.	Bkg Stat. Low-m_{jj} CR, $e^+\mu^+/\mu^+e^+$ Chan, Bin 1	−5.5
Non Prompt μ Sys.	Bkg Stat. SR, $e^+\mu^+/\mu^+e^+$ Chan, Bin 2	−5.4
Non Prompt e Stat.	Bkg Stat. Low-m_{jj} CR, $e^-\mu^-/\mu^-e^-$ Chan, Bin 1	−5.4
Non Prompt e Stat.	$W^\pm Z$ Shower	5.3
Conversion Model $V\gamma$	Non Prompt e Stat.	−5.3
Pile-up Reweight. data SF	Bkg Stat. SR, $e^-\mu^-/\mu^-e^-$ Chan, Bin 2	−5.3
Conversion Model $V\gamma$	μ_{WZ}	−5.2
Non Prompt μ Sys.	μ_{WZ}	−5.0
ZZ x-sec.	μ_{WZ}	−4.9
$W^\pm Z$ PDF	μ_{WZ}	−4.9
Interference	μ	4.8
$W^\pm W^\pm jj$-QCD Shower	μ	−4.7
Non Prompt e Sys.	$W^\pm W^\pm jj$-EW Shower	−4.6
MET Soft Trk. Resolution	μ_{WZ}	−4.5
Muon Eff. Sys.	μ_{WZ}	−4.5
Bkg Stat. Low-m_{jj} CR, e^-e^- Chan, Bin 1	μ	4.5
Jet Flavor Composition	$W^\pm\gamma$ x-sec.	4.5
Non Prompt μ Stat.	Non Prompt μ Sys.	−4.5
Non Prompt μ Sys.	Bkg Stat. SR, $e^-\mu^-/\mu^-e^-$ Chan, Bin 2	−4.4
Bkg Stat. SR, e^-e^- Chan, Bin 2	μ	4.3
$W^\pm Z$ Shower	$W^\pm W^\pm jj$-EW Shower	4.3
Bkg Stat. SR, e^-e^- Chan, Bin 2	Bkg Stat. SR, e^+e^+ Chan, Bin 2	4.3
Non Prompt μ Sys.	Bkg Stat. Low-m_{jj} CR, $\mu^+\mu^+$ Chan, Bin 1	−4.3
Charge Mis-ID Energy Corr.	Non Prompt e Sys.	4.1
Pile-up Reweight. data SF	μ_{WZ}	4.1
Conversion Model $V\gamma$	Bkg Stat. SR, e^+e^+ Chan, Bin 2	4.1
μ	μ_{WZ}	−4.1
$W^\pm W^\pm jj$-EW EW Corr.	$W^\pm W^\pm jj$-EW Shower	−4.0
Non Prompt e Sys.	Bkg Stat. Low-m_{jj} CR, e^+e^+ Chan, Bin 1	4.0
Non Prompt μ Sys.	Bkg Stat. Low-m_{jj} CR, e^-e^- Chan, Bin 1	3.9
Jet Pile-up p_{T} Term	μ	−3.9
$W^\pm\gamma$ x-sec.	μ	−3.8
Non Prompt μ Stat.	μ	−3.8

Parameter 1	Parameter 2	Correlation [%]
Non Prompt e Sys.	Bkg Stat. SR, $e^+\mu^+/\mu^+e^+$ Chan, Bin 1	−3.8
$W^\pm Z$ Shower	$W^\pm W^\pm jj$-Ew Ew Corr.	3.8
Bkg Stat. SR, $e^-\mu^-/\mu^-e^-$ Chan, Bin 2	μ	−3.7
Jet Flavor Composition	Bkg Stat. SR, e^+e^+ Chan, Bin 2	3.7
$W^\pm W^\pm jj$-Ew Shower	μ_{WZ}	−3.7
Bkg Stat. SR, $e^-\mu^-/\mu^-e^-$ Chan, Bin 4	μ	−3.7
Non Prompt e Stat.	Bkg Stat. Low-m_{jj} Cr, $e^+\mu^+/\mu^+e^+$ Chan, Bin 1	−3.7
Bkg Stat. SR, e^-e^- Chan, Bin 4	μ	−3.7
Bkg Stat. Low-m_{jj} Cr, e^-e^- Chan, Bin 1	Bkg Stat. Low-m_{jj} Cr, $e^-\mu^-/\mu^-e^-$ Chan, Bin 1	3.7
Conversion Model $V\gamma$	Bkg Stat. Low-m_{jj} Cr, e^-e^- Chan, Bin 1	3.6
Jet Flavor Composition	Bkg Stat. SR, $e^-\mu^-/\mu^-e^-$ Chan, Bin 1	3.6
$W^\pm W^\pm jj$-Ew Ew Corr.	μ_{WZ}	−3.6
top x-sec.	μ_{WZ}	−3.5
$W^\pm Z$ Scale	$W^\pm Z$ Shower	3.5
Non Prompt e Stat.	μ_{WZ}	−3.5
Jet Energy Resolution	Bkg Stat. SR, $e^-\mu^-/\mu^-e^-$ Chan, Bin 1	3.5
Interference	$W^\pm W^\pm jj$-Ew Ew Corr.	−3.5
$W^\pm W^\pm jj$-Ew Ew Corr.	$W^\pm W^\pm jj$-Ew Scale	3.4
Non Prompt e Sys.	$W^\pm W^\pm jj$-Ew Ew Corr.	−3.4
Interference	$W^\pm Z$ Shower	3.4
Non Prompt e Stat.	μ	−3.4
Non Prompt μ Sys.	$W^\pm W^\pm jj$-Ew Shower	−3.4
Conversion Model $V\gamma$	Bkg Stat. Low-m_{jj} Cr, $e^-\mu^-/\mu^-e^-$ Chan, Bin 1	−3.3
$W^\pm Z$ Shower	Bkg Stat. Low-m_{jj} Cr, $e^-\mu^-/\mu^-e^-$ Chan, Bin 1	3.3
Non Prompt μ Sys.	Bkg Stat. SR, e^-e^- Chan, Bin 2	3.3
Non Prompt e Sys.	Interference	−3.2
Non Prompt μ Sys.	Bkg Stat. Low-m_{jj} Cr, $e^-\mu^-/\mu^-e^-$ Chan, Bin 1	3.2
Jet Flavor Response	μ	3.2
Non Prompt e Stat.	Bkg Stat. SR, $e^-\mu^-/\mu^-e^-$ Chan, Bin 2	−3.2
Non Prompt μ Sys.	$W^\pm W^\pm jj$-Ew Ew Corr.	−3.2
Bkg Stat. SR, e^-e^- Chan, Bin 2	Bkg Stat. Low-m_{jj} Cr, $e^-\mu^-/\mu^-e^-$ Chan, Bin 1	3.1
$W^\pm Z$ Shower	$W^\pm W^\pm jj$-Qcd Scale	3.1
Jet EffectiveNP 2	$W^\pm Z$ Scale	3.1
Jet Energy Resolution	Bkg Stat. Low-m_{jj} Cr, e^-e^- Chan, Bin 1	−3.1
Jet Energy Resolution	μ	3.1
Bkg Stat. Low-m_{jj} Cr, e^-e^- Chan, Bin 1	Bkg Stat. Low-m_{jj} Cr, $e^+\mu^+/\mu^+e^+$ Chan, Bin 1	3.0
Non Prompt e Sys.	Non Prompt μ Stat.	−3.0
Non Prompt e Stat.	Bkg Stat. SR, e^+e^+ Chan, Bin 1	−3.0
Interference	μ_{WZ}	−3.0
$W^\pm W^\pm jj$-Ew Shower	Bkg Stat. Low-m_{jj} Cr, $e^+\mu^+/\mu^+e^+$ Chan, Bin 1	−3.0
Jet EtaIntercalibration Non-Closure	μ	3.0
$W^\pm W^\pm jj$-Ew Shower	Bkg Stat. Low-m_{jj} Cr, $e^-\mu^-/\mu^-e^-$ Chan, Bin 1	−3.0
Bkg Stat. SR, e^+e^+ Chan, Bin 1	Bkg Stat. Low-m_{jj} Cr, e^-e^- Chan, Bin 1	3.0
Non Prompt μ Sys.	Bkg Stat. SR, e^+e^+ Chan, Bin 2	3.0
Non Prompt μ Stat.	$W^\pm Z$ Shower	3.0
Jet Flavor Composition	Bkg Stat. SR, e^-e^- Chan, Bin 2	3.0
CR$W^\pm Z$ 3Lep $\ell^\pm\ell^\pm\ell^\mp$ Chan, Bin 1	μ_{WZ}	−2.9
Bkg Stat. Low-m_{jj} Cr, $e^-\mu^-/\mu^-e^-$ Chan, Bin 1	Bkg Stat. Low-m_{jj} Cr, $e^+\mu^+/\mu^+e^+$ Chan, Bin 1	2.9
Bkg Stat. Low-m_{jj} Cr, $e^-\mu^-/\mu^-e^-$ Chan, Bin 1	μ_{WZ}	−2.9
Interference	$W^\pm W^\pm jj$-Ew Shower	−2.9
Jet EffectiveNP 2	$W^\pm Z$ Shower	2.9
Jet Pile-up RhoTopology	$W^\pm Z$ Scale	2.8
Conversion Model $V\gamma$	Bkg Stat. SR, $e^-\mu^-/\mu^-e^-$ Chan, Bin 4	−2.8
Conversion Model $V\gamma$	Bkg Stat. SR, $e^+\mu^+/\mu^+e^+$ Chan, Bin 1	−2.8
Non Prompt e Stat.	Bkg Stat. Low-m_{jj} Cr, e^-e^- Chan, Bin 1	−2.8
Jet Energy Resolution	Bkg Stat. SR, e^+e^+ Chan, Bin 2	−2.8
Pile-up Reweight. data SF	Bkg Stat. SR, $e^-\mu^-/\mu^-e^-$ Chan, Bin 1	−2.7
Non Prompt e Sys.	Bkg Stat. SR, e^-e^- Chan, Bin 3	2.7
Non Prompt μ Sys.	Interference	−2.7
$W^\pm Z$ Shower	Bkg Stat. SR, $e^+\mu^+/\mu^+e^+$ Chan, Bin 3	−2.7
Bkg Stat. SR, $e^-\mu^-/\mu^-e^-$ Chan, Bin 4	μ_{WZ}	2.7
Bkg Stat. SR, $e^-\mu^-/\mu^-e^-$ Chan, Bin 3	μ	−2.7
Non Prompt μ Sys.	$W^\pm W^\pm jj$-Qcd Scale	−2.6
Bkg Stat. SR, e^-e^- Chan, Bin 2	Bkg Stat. Low-m_{jj} Cr, $e^+\mu^+/\mu^+e^+$ Chan, Bin 1	2.6
Non Prompt e Stat.	Bkg Stat. SR, e^-e^- Chan, Bin 3	−2.6
Non Prompt e Sys.	Jet EtaIntercalibration Non-Closure	−2.6
$W^\pm Z$ Shower	Bkg Stat. SR, e^-e^- Chan, Bin 2	−2.6
Bkg Stat. SR, e^-e^- Chan, Bin 3	μ	−2.6

Parameter 1	Parameter 2	Correlation [%]
Bkg Stat. SR, e^+e^+ Chan, Bin 2	Bkg Stat. Low-m_{jj} CR, $e^-\mu^-/\mu^-e^-$ Chan, Bin 1	2.6
Non Prompt e Stat.	$W^\pm\gamma$ x-sec.	−2.6
$W^\pm Z$ Shower	Bkg Stat. Low-m_{jj} CR, $e^+\mu^+/\mu^+e^+$ Chan, Bin 1	2.6
Non Prompt e Stat.	$W^\pm W^\pm jj$-EW Shower	−2.6
Non Prompt e Sys.	$W^\pm W^\pm jj$-QCD Scale	−2.6
Conversion Model $V\gamma$	Bkg Stat. SR, e^-e^- Chan, Bin 2	−2.6
$W^\pm W^\pm jj$-QCD Scale	μ_{WZ}	−2.6
Jet Energy Resolution	Bkg Stat. SR, $\mu^-\mu^-$ Chan, Bin 3	2.6
Charge Mis-ID Scale Fac.	Bkg Stat. Low-m_{jj} CR, e^-e^- Chan, Bin 1	−2.5
$W^\pm W^\pm jj$-EW Scale	$W^\pm W^\pm jj$-EW Shower	2.5
Non Prompt μ Stat.	μ_{WZ}	−2.5
Non Prompt μ Sys.	Pile-up Reweight. data SF	−2.5
Bkg Stat. SR, e^-e^- Chan, Bin 2	Bkg Stat. SR, e^+e^+ Chan, Bin 1	2.5
Conversion Model $V\gamma$	Bkg Stat. SR, $e^+\mu^+/\mu^+e^+$ Chan, Bin 3	−2.5
Jet Flavor Composition	$W^\pm W^\pm jj$-EW EW Corr.	2.4
$W^\pm Z$ Shower	Bkg Stat. SR, $e^-\mu^-/\mu^-e^-$ Chan, Bin 2	2.4
Bkg Stat. SR, $e^+\mu^+/\mu^+e^+$ Chan, Bin 2	μ_{WZ}	−2.4
Jet Pile-up p_T Term	μ_{WZ}	−2.4
Non Prompt e Sys.	MET Soft Trk. Resolution	2.4
Bkg Stat. SR, $e^-\mu^-/\mu^-e^-$ Chan, Bin 2	μ_{WZ}	−2.3
Conversion Model $V\gamma$	Pile-up Reweight. data SF	−2.3
Jet Pile-up RhoTopology	$W^\pm Z$ Shower	2.3
Jet Pile-up OffsetNPV	μ	−2.3
Flavor Tag Eff. Eigen C 1	μ	−2.2
Interference	$W^\pm W^\pm jj$-EW Scale	2.2
Bkg Stat. SR, e^+e^+ Chan, Bin 2	Bkg Stat. Low-m_{jj} CR, $e^+\mu^+/\mu^+e^+$ Chan, Bin 1	2.2
Bkg Stat. SR, e^+e^+ Chan, Bin 4	μ	−2.2
Pile-up Reweight. data SF	Bkg Stat. SR, $e^+\mu^+/\mu^+e^+$ Chan, Bin 3	2.2
Flavor Tag Eff. Eigen Light 2	μ	2.2
Bkg Stat. SR, e^+e^+ Chan, Bin 1	Bkg Stat. SR, e^+e^+ Chan, Bin 2	2.2
Flavor Tag Eff. Eigen C 1	μ_{WZ}	−2.2
Conversion Model $V\gamma$	Bkg Stat. SR, $e^+\mu^+/\mu^+e^+$ Chan, Bin 2	2.1
$W^\pm Z$ Shower	Bkg Stat. Low-m_{jj} CR, e^-e^- Chan, Bin 1	−2.1
$W^\pm Z$ Shower	$W^\pm W^\pm jj$-EW Scale	−2.1
Jet Flavor Response	$W^\pm Z$ Scale	−2.1
Jet Energy Resolution	Bkg Stat. SR, e^+e^+ Chan, Bin 1	−2.1
$W^\pm W^\pm jj$-EW Scale	μ_{WZ}	2.1
Jet Flavor Composition	$W^\pm Z$ Shower	2.1
$W^\pm Z$ Shower	Bkg Stat. Low-m_{jj} CR, e^+e^+ Chan, Bin 1	2.1
Bkg Stat. SR, $e^+\mu^+/\mu^+e^+$ Chan, Bin 1	μ	−2.1
Bkg Stat. SR, $e^+\mu^+/\mu^+e^+$ Chan, Bin 3	μ_{WZ}	2.1
$W^\pm Z$ Shower	Bkg Stat. SR, e^+e^+ Chan, Bin 2	−2.0
$W^\pm W^\pm jj$-EW EW Corr.	Bkg Stat. SR, $e^+\mu^+/\mu^+e^+$ Chan, Bin 4	2.0
Charge Mis-ID Energy Corr.	Non Prompt e Stat.	2.0
Non Prompt e Sys.	$W^\pm W^\pm jj$-EW Scale	2.0
$W^\pm\gamma$ x-sec.	μ_{WZ}	−2.0
$W^\pm Z$ Shower	Bkg Stat. Low-m_{jj} CR, $\mu^+\mu^+$ Chan, Bin 1	2.0

Table C.15: Pair-wise correlation factors between two nuisance parameters after the fit to observed data. Parameter pairs are sorted by descending absolute correlation value. Only correlations larger than 2 % are given.

C.6 Pre-and Post-Fit Uncertainties on the Precision of Simulated Backgrounds

Lower Bin Boundary [GeV]		Background Precision Uncertainty [%] e^-e^-	e^+e^+	$e^-\mu^-/\mu^-e^-$	$e^+\mu^+/\mu^+e^+$	$\mu^-\mu^-$	$\mu^+\mu^+$
Pre-Fit							
500		±22.81	±33.47	±18.02	±13.97	±8.44	±5.73
700		±42.52	±40.38	±27.02	±16.17	±10.29	±8.22
1000		±59.94	±11.40	±21.38	±18.41	±18.43	±8.16
1500		±52.63	±24.20	±34.45	±30.15	±14.63	±8.06
Post-Fit to Asimov Data							
500	up	5.05	13.99	7.50	4.62	3.22	2.11
	down	−4.38	−11.51	−6.86	−4.28	−3.06	−2.03
700	up	23.74	15.71	6.89	5.15	3.08	2.15
	down	−18.53	−12.57	−5.97	−4.70	−2.90	−2.04
1000	up	10.42	1.18	2.97	3.89	2.87	1.59
	down	−7.39	−1.09	−2.58	−3.42	−2.56	−1.50
1500	up	2.43	1.52	4.52	3.38	1.54	0.99
	down	−1.73	−1.29	−3.65	−2.82	−1.41	−0.94
Post-Fit to Observed Data							
500	up	6.83	15.54	7.53	5.11	3.26	2.02
	down	−5.90	−12.54	−6.80	−4.70	−3.09	−1.95
700	up	22.33	15.32	6.50	4.74	2.92	2.29
	down	−16.51	−11.81	−5.56	−4.26	−2.75	−2.18
1000	up	13.64	1.64	3.08	4.16	3.24	1.57
	down	−9.59	−1.52	−2.69	−3.71	−2.90	−1.50
1500	up	3.60	1.98	5.23	3.45	1.40	0.97
	down	−2.61	−1.71	−4.28	−2.88	−1.28	−0.93

Table C.16: Overview of pre- and post-fit relative systematic uncertainties on the simulated background precision in the signal region.

Lower Bin Boundary		Background Precision Uncertainty [%]					
[GeV]		e^-e^-	e^+e^+	$e^-\mu^-/\mu^-e^-$	$e^+\mu^+/\mu^+e^+$	$\mu^-\mu^-$	$\mu^+\mu^+$
Pre-Fit							
200		±21.98	±13.77	±9.30	±8.87	±4.65	±8.08
Post-Fit to Asimov Data							
200	up	22.48	14.60	9.22	8.38	4.77	7.78
	down	−19.49	−13.22	−8.62	−8.00	−4.62	−7.42
Post-Fit to Observed Data							
200	up	26.05	14.63	8.90	8.38	4.77	7.80
	down	−22.04	−13.34	−8.39	−7.93	−4.63	−7.42

Table C.17: Overview of pre- and post-fit relative systematic uncertainties on the simulated background precision in the low-m_{jj} control region.

Lower Bin Boundary		Background Precision Uncertainty [%]		
[GeV]		Pre-Fit	Post-Fit to Asimov Data	Post-Fit to Observed Data
200	up	+1.15	+1.04	+1.04
	down	−1.15	−1.03	−1.03

Table C.18: Overview of pre- and post-fit relative systematic uncertainties on the simulated background precision in the $W^{\pm}Z$ control region.

C.7 Ranking of Nuisance Parameters

Rank	Nuisance Parameter	$\hat{\theta}$	$\Delta_{\text{post}}\theta$		$\Delta_{\text{post}}\mu_{\text{obs}}$		$\Delta_{\text{pre}}\mu_{\text{obs}}$	
			up	down	up	down	up	down
1	$W^{\pm}W^{\pm}$ EW Shower	-0.0095	0.9809	-0.9843	0.0844	-0.0793	0.0861	-0.0805
2	Non-Prompt e Sys.	-0.7291	0.7807	-0.6154	-0.0573	0.0525	-0.0631	0.0777
3	$W^{\pm}W^{\pm}$ QCD Scale	-0.0339	0.9799	-0.9877	-0.0513	0.0328	-0.0523	0.0332
4	Non-Prompt μ Sys.	-0.1292	0.5642	-0.8599	-0.0398	0.0072	-0.0786	0.0091
5	Jet Flavor Composition	0.5217	0.8764	-1.2215	-0.0288	0.0361	-0.0325	0.0308
6	Luminosity	1.0001	0.0210	-0.0210	-0.0331	0.0347	-0.0331	0.0347
7	Flavor Tag Eff. Eigen Light 0	-0.0602	0.9995	-0.9998	-0.0277	0.0284	-0.0277	0.0284
8	Conversion Model Vgamm	0.1481	0.9985	-0.9897	-0.0220	0.0233	-0.0220	0.0235
9	Pile-up Reweight. data SF	-0.0949	0.9835	-0.9901	0.0225	-0.0227	0.0229	-0.0229
10	WZ Shower	-0.0567	0.9809	-0.9421	0.0146	-0.0222	0.0148	-0.0239
11	Jet EtaIntercalibration Modelling	0.0704	1.0039	-1.0044	-0.0177	0.0187	-0.0176	0.0186
12	$W^{\pm}W^{\pm}$ EW Scale	0.2051	0.9946	-1.0111	-0.0186	0.0162	-0.0187	0.0161
13	$W^{\pm}W^{\pm}$ EW EW Corr.	-0.3367	0.9745	-0.9757	0.0152	-0.0180	0.0155	-0.0184
14	Muon Eff. Sys.	0.0369	0.9986	-0.9986	-0.0168	0.0171	-0.0168	0.0171
15	$W^{\pm}W^{\pm}$ QCD Shower	-0.0148	0.9561	-0.9602	-0.0124	0.0156	-0.0129	0.0163
16	Interference	-0.1665	1.0040	-0.9930	0.0121	-0.0151	0.0121	-0.0152
17	Jet Pile-up p_{T} Term	0.0824	1.0046	-1.0067	-0.0092	0.0136	-0.0091	0.0135
18	FakeMuSt	0.0104	0.9920	-0.9922	-0.0130	0.0103	-0.0131	0.0104
19	Wgamma x-sec.	0.0560	0.9981	-0.9980	-0.0114	0.0112	-0.0114	0.0113
20	Jet Energy Resolution	-0.6344	0.9594	-0.7811	0.0107	-0.0092	0.0111	-0.0104
21	FakeElSt	0.0698	0.9540	-0.9560	-0.0106	0.0086	-0.0112	0.0089
22	Jet EtaIntercalibration Non-Closure	0.0300	1.0094	-1.0191	0.0097	-0.0070	0.0096	-0.0068
23	Jet Flavor Response	0.0299	1.0065	-1.0103	0.0093	-0.0092	0.0093	-0.0091
24	Jet Pile-up OffsetNPV	0.0812	0.9944	-1.0892	-0.0076	0.0005	-0.0076	0.0007
25	Flavor Tag Eff. Eigen C 0	-0.0049	0.9997	-0.9997	-0.0065	0.0066	-0.0065	0.0066
26	Flavor Tag Eff. Eigen Light 1	0.0178	1.0000	-1.0000	0.0064	-0.0063	0.0064	-0.0063
27	Jet EffectiveNP 2	0.0821	1.0147	-1.0245	-0.0044	0.0054	-0.0044	0.0053
28	Charge Mis-ID Energy Corr.	-0.1612	0.9961	-0.9961	0.0050	-0.0050	0.0050	-0.0050
29	$W^{\pm}W^{\pm}$ QCD PDF	0.0017	1.0008	-1.0009	-0.0047	0.0040	-0.0047	0.0040

Rank	Nuisance Parameter	$\hat{\theta}$	$\Delta_{\text{post}}\theta$		$\Delta_{\text{post}}\mu_{\text{obs}}$		$\Delta_{\text{pre}}\mu_{\text{obs}}$	
			up	down	up	down	up	down
30	WZ Scale	-0.0415	1.0084	-1.0103	0.0038	-0.0047	0.0038	-0.0047
31	Muon ID	-0.0061	1.0853	-1.0826	0.0047	0.0043	0.0043	0.0039
32	ZZ x-sec.	0.0019	0.9998	-0.9999	0.0047	-0.0046	0.0047	-0.0046
33	Electron Eff. Iso TOTAL 1NPCOR PLUS UNCOR	-0.0237	0.9997	-0.9997	-0.0046	0.0046	-0.0046	0.0046
34	Charge Mis-ID Scale Fac.	-0.1447	1.0541	-1.0221	-0.0045	0.0001	-0.0043	0.0001
35	Electron Eff. ID CorrUncertaintyNP14	-0.0195	0.9997	-0.9997	-0.0045	0.0045	-0.0045	0.0045
36	Muon Scale	0.0042	1.1005	-1.1032	0.0044	0.0034	0.0040	0.0031
37	Muon Iso Sys.	0.0091	0.9999	-0.9999	-0.0042	0.0042	-0.0042	0.0042
38	Muon MS	-0.0034	1.0968	-1.0941	0.0034	0.0041	0.0031	0.0038
39	Jet Pile-up RhoTopology	-0.0936	1.0211	-1.0083	-0.0035	0.0040	-0.0034	0.0039
40	MET Soft Trk. ResoPer	0.0441	0.9992	-0.9992	-0.0035	0.0039	-0.0035	0.0039
41	Muon Eff. Stat.	0.0090	0.9999	-0.9999	-0.0037	0.0037	-0.0037	0.0037
42	Electron Eff. ID SIMPLIFIED UncorrUncertaintyNP8	-0.0264	0.9998	-0.9998	-0.0035	0.0035	-0.0035	0.0035
43	Jet EtaIntercalibration Total Stat.	-0.0055	0.9831	-0.9836	-0.0032	0.0004	-0.0033	0.0004
44	Flavor Tag Eff. Eigen C 1	-0.0058	1.0000	-1.0000	-0.0030	0.0030	-0.0030	0.0030
45	Muon Eff. TrigSystUncertainty	0.0079	0.9999	-0.9999	-0.0030	0.0030	-0.0030	0.0030
46	Jet EffectiveNP 3	-0.0310	1.0129	-1.0108	0.0025	-0.0028	0.0024	-0.0027
47	$W^{\pm}W^{\pm}$ EW PDF	0.0345	0.9732	-0.9670	-0.0008	0.0028	-0.0008	0.0029
48	Flavor Tag Eff. Eigen Light 2	0.0102	1.0000	-1.0000	0.0027	-0.0027	0.0027	-0.0027
49	Flavor Tag Eff. Eigen Light 3	0.0102	1.0000	-1.0000	0.0027	-0.0027	0.0027	-0.0027
50	$W^{\pm}W^{\pm}$ QCD α_s	-0.0015	0.9999	-0.9999	-0.0026	0.0027	-0.0026	0.0027
51	Flavor Tag Eff. extrapolation from charm	-0.0019	0.9999	-0.9999	0.0018	-0.0018	0.0018	-0.0018
52	Electron Eff. Reco TOTAL 1NPCOR PLUS UNCOR	-0.0072	1.0000	-1.0000	-0.0018	0.0018	-0.0018	0.0018
53	Muon Eff. TrigStatUncertainty	0.0038	0.9999	-0.9999	-0.0017	0.0017	-0.0017	0.0017
54	Jet EffectiveNP 1	-0.0634	1.0033	-1.0020	-0.0017	0.0008	-0.0017	0.0008
55	Flavor Tag Eff. Eigen C 2	-0.0068	1.0000	-1.0000	-0.0016	0.0016	-0.0016	0.0016
56	Jet Pile-up OffsetMu	0.0121	1.0254	-1.0274	0.0016	-0.0004	0.0015	-0.0004
57	Muon TTVA Stat.	0.0036	1.0000	-1.0000	-0.0015	0.0015	-0.0015	0.0015
58	Jet EffectiveNP 4	-0.0034	0.9906	-0.9908	-0.0015	0.0006	-0.0015	0.0006
59	Jet EffectiveNP 8restTerm	0.0054	0.9887	-0.9884	-0.0014	0.0005	-0.0015	0.0006
60	$W^{\pm}W^{\pm}$ EW α_s	-0.0266	0.9971	-0.9975	0.0010	-0.0014	0.0010	-0.0014

Rank	Nuisance Parameter	$\hat{\theta}$	$\Delta_{\text{post}}\theta$		$\Delta_{\text{post}}\mu_{\text{obs}}$		$\Delta_{\text{pre}}\mu_{\text{obs}}$	
			up	down	up	down	up	down
61	e/γ RESOLUTION ALL	-0.0091	1.0057	-1.0054	0.0002	-0.0013	0.0002	-0.0013
62	MET Soft Trk. Scale	0.0003	0.9891	-0.9890	0.0010	0.0012	0.0010	0.0013
63	Muon TTVA Sys.	0.0029	1.0000	-1.0000	-0.0012	0.0012	-0.0012	0.0012
64	WZ α_{s}	0.0199	1.0015	-1.0017	0.0007	-0.0011	0.0007	-0.0011
65	Electron Eff. ID CorrUncertaintyNP11	0.0047	1.0000	-1.0000	0.0011	-0.0011	0.0011	-0.0011
66	Electron Eff. ID CorrUncertaintyNP10	0.0047	1.0000	-1.0000	0.0011	-0.0011	0.0011	-0.0011
67	Flavor Tag Eff. Eigen Light 4	-0.0122	1.0000	-1.0000	-0.0011	0.0011	-0.0011	0.0011
68	Flavor Tag Eff. extrapolation	0.0030	1.0000	-1.0000	0.0010	-0.0010	0.0010	-0.0010
69	WZ PDF	-0.0015	1.0027	-1.0028	-0.0007	0.0009	-0.0007	0.0009
70	Jet EffectiveNP 6	0.0174	0.9892	-0.9881	0.0002	-0.0009	0.0002	-0.0009
71	MET Soft Trk. ResoPar	-0.0895	0.9995	-0.9994	-0.0008	0.0008	-0.0008	0.0008
72	Flavor Tag Eff. Eigen B 0	-0.0100	0.9997	-0.9997	-0.0008	0.0008	-0.0008	0.0008
73	triboson x-sec.	0.0028	1.0000	-1.0001	-0.0007	0.0007	-0.0007	0.0007
74	Electron Eff. ID SIMPLIFIED UncorrUncertaintyNP6	-0.0052	1.0000	-1.0000	-0.0007	0.0007	-0.0007	0.0007
75	Jet EffectiveNP 7	0.0050	0.9929	-0.9928	-0.0001	-0.0007	-0.0001	-0.0007
76	e/γ Scale ALLCORR	-0.0041	1.0037	-1.0036	0.0000	0.0006	0.0000	0.0006
77	Muon Iso Stat.	0.0008	1.0000	-1.0000	-0.0005	0.0005	-0.0005	0.0005
78	Jet EffectiveNP 5	0.0185	0.9876	-0.9863	-0.0004	-0.0001	-0.0004	-0.0001
79	Electron Eff. ID SIMPLIFIED UncorrUncertaintyNP7	-0.0043	1.0000	-1.0000	-0.0004	0.0004	-0.0004	0.0004
80	Electron Eff. Trigger TOTAL 1NPCOR PLUS UNCOR	-0.0001	1.0000	-1.0000	-0.0004	0.0004	-0.0004	0.0004
81	Zgamma x-sec.	0.0185	1.0001	-1.0001	0.0003	-0.0003	0.0003	-0.0003
82	top x-sec.	-0.0336	1.0007	-0.9989	0.0003	-0.0003	0.0003	-0.0003
83	Electron Eff. ID CorrUncertaintyNP9	-0.0029	1.0000	-1.0000	-0.0003	0.0003	-0.0003	0.0003
84	e/γ Scale LARCALIB EXTRA2015PRE	0.0019	1.0085	-1.0086	-0.0003	-0.0001	-0.0003	-0.0001
85	e/γ Scale E4SCINTILLATOR	0.0005	1.0025	-1.0025	-0.0001	-0.0003	-0.0001	-0.0003
86	Electron Eff. ID CorrUncertaintyNP13	0.0017	1.0000	-1.0000	0.0002	-0.0002	0.0002	-0.0002
87	Jet BJES Response	-0.0025	0.9948	-0.9948	0.0002	0.0001	0.0002	0.0001
88	Jet JVT Efficiency	0.0006	1.0001	-1.0001	-0.0001	0.0002	-0.0001	0.0002
89	Electron Eff. ID SIMPLIFIED UncorrUncertaintyNP15	0.0013	1.0000	-1.0000	-0.0002	0.0002	-0.0002	0.0002
90	Flavor Tag Eff. Eigen B 2	0.0011	1.0000	-1.0000	-0.0002	0.0002	-0.0002	0.0002
91	Jet PunchThrough MC15	-0.0004	0.9991	-0.9991	0.0000	-0.0002	0.0000	-0.0002

Rank	Nuisance Parameter	$\hat{\theta}$	$\Delta_{\text{post}}\theta$		$\Delta_{\text{post}}\mu_{\text{obs}}$		$\Delta_{\text{pre}}\mu_{\text{obs}}$	
			up	down	up	down	up	down
92	Electron Eff. ID SIMPLIFIED UncorrUncertaintyNP5	-0.0007	1.0000	-1.0000	-0.0002	0.0002	-0.0002	0.0002
93	e/γ Scale LARTEMPERATURE EXTRA2015PRE	-0.0000	1.0036	-1.0036	-0.0001	-0.0001	-0.0001	-0.0001
94	e/γ Scale LARTEMPERATURE EXTRA2016PRE	-0.0000	1.0036	-1.0036	-0.0001	-0.0001	-0.0001	-0.0001
95	Flavor Tag Eff. Eigen B 1	-0.0038	1.0000	-1.0000	-0.0001	0.0001	-0.0001	0.0001
96	Electron Eff. ID CorrUncertaintyNP7	-0.0002	1.0000	-1.0000	-0.0001	0.0001	-0.0001	0.0001
97	Electron Eff. ID CorrUncertaintyNP8	0.0002	1.0000	-1.0000	-0.0001	0.0001	-0.0001	0.0001
98	Electron Eff. ID CorrUncertaintyNP12	-0.0002	1.0000	-1.0000	0.0000	-0.0000	0.0000	-0.0000
99	Electron Eff. ID SIMPLIFIED UncorrUncertaintyNP14	0.0003	1.0000	-1.0000	-0.0000	0.0000	-0.0000	0.0000
100	Electron Eff. ID CorrUncertaintyNP6	0.0004	1.0000	-1.0000	0.0000	-0.0000	0.0000	-0.0000
101	Electron Eff. ID CorrUncertaintyNP1	0.0000	1.0000	-1.0000	0.0000	0.0000	0.0000	0.0000
102	Electron Eff. ID CorrUncertaintyNP0	0.0000	1.0000	-1.0000	0.0000	0.0000	0.0000	0.0000
103	Electron Eff. ID CorrUncertaintyNP2	0.0000	1.0000	-1.0000	0.0000	0.0000	0.0000	0.0000
104	Electron Eff. ID CorrUncertaintyNP3	0.0000	1.0000	-1.0000	0.0000	0.0000	0.0000	0.0000
105	Electron Eff. ID CorrUncertaintyNP4	0.0000	1.0000	-1.0000	0.0000	0.0000	0.0000	0.0000
106	Electron Eff. ID CorrUncertaintyNP5	0.0000	1.0000	-1.0000	0.0000	0.0000	0.0000	0.0000
107	Electron Eff. ID SIMPLIFIED UncorrUncertaintyNP0	0.0000	1.0000	-1.0000	0.0000	0.0000	0.0000	0.0000
108	Muon Eff. Sys. low p_{T}	0.0000	1.0000	-1.0000	0.0000	0.0000	0.0000	0.0000
109	Electron Eff. ID SIMPLIFIED UncorrUncertaintyNP1	0.0000	1.0000	-1.0000	0.0000	0.0000	0.0000	0.0000
110	Electron Eff. ID SIMPLIFIED UncorrUncertaintyNP10	0.0000	1.0000	-1.0000	0.0000	0.0000	0.0000	0.0000
111	Muon Eff. Stat. low p_{T}	0.0000	1.0000	-1.0000	0.0000	0.0000	0.0000	0.0000
112	Electron Eff. ID SIMPLIFIED UncorrUncertaintyNP11	0.0000	1.0000	-1.0000	0.0000	0.0000	0.0000	0.0000
113	Electron Eff. ID SIMPLIFIED UncorrUncertaintyNP12	0.0000	1.0000	-1.0000	0.0000	0.0000	0.0000	0.0000
114	Electron Eff. ID SIMPLIFIED UncorrUncertaintyNP13	0.0000	1.0000	-1.0000	0.0000	0.0000	0.0000	0.0000
115	Jet SingleParticle HighPt	-0.0000	1.0000	-1.0000	0.0000	0.0000	0.0000	0.0000
116	Jet RelativeNonClosure MC15	0.0000	1.0000	-1.0000	0.0000	0.0000	0.0000	0.0000
117	Electron Eff. ID SIMPLIFIED UncorrUncertaintyNP2	0.0000	1.0000	-1.0000	0.0000	0.0000	0.0000	0.0000
118	Electron Eff. ID SIMPLIFIED UncorrUncertaintyNP3	0.0000	1.0000	-1.0000	0.0000	0.0000	0.0000	0.0000
119	Electron Eff. ID SIMPLIFIED UncorrUncertaintyNP4	0.0000	1.0000	-1.0000	0.0000	0.0000	0.0000	0.0000
120	Electron Eff. ID SIMPLIFIED UncorrUncertaintyNP9	0.0000	1.0000	-1.0000	0.0000	0.0000	0.0000	0.0000

Rank	Nuisance Parameter	$\hat{\theta}$	$\Delta_{\text{post}}\theta$		$\Delta_{\text{post}}\mu_{\text{obs}}$		$\Delta_{\text{pre}}\mu_{\text{obs}}$	
			up	down	up	down	up	down

Table C.19: Ranking of nuisance parameters according to their pre-fit impact on the signal strength. Nuisance parameters accounting for background precision uncertainties are not included. For each nuisance parameters, the pre- and post-fit impact on the signal strength as well as the post-fit parameter pull and uncertainty, $\Delta_{\text{post}}\theta$, are given along with their best estimate, $\hat{\theta}$, after the fit to observed data. The pre-fit uncertainties on the nuisance parameter pulls are ± 1 for all parameters

List of Figures

List of Tables

Acknowledgments

I would like to takes this opportunity to thank the people I have worked with and who have supported me over the last three and a half years. This time was one of the most intense of my life so far, during which I learned a lot, about physics as well as my self; and it lead me to meet many great and remarkable persons.

First of all, I would like to thank my advisor, Michael Kobel, who got me hooked on particle physics in the first place. Your support and encouragement was crucial to my work, and finally motivated me to write up this thesis.
Additionally my thanks is due to Moncia Dunford, who was extremely helpful during her time in Dresden, and kindly agreed to be my second referee.

I would also like to express my gratitude to the Dresden VBS group, especially Joany Manjarrés Ramos, Stefanie Todt, Carsten Bittrich, Tim Herrmann, and Felix Socher. It was great to have colleagues like you, who made coming to work and even night shifts at the office fun. Thank you for all the open discussions (physics-related or not), your advice, encouragement, and proof-reading my thesis even if all of you have many other things on your mind right now. Additionally I would like to thank Heberth Torres Dávila for his continuous support in all fitting-related matters.

Of course analyses in ATLAS are rarely the work of just one institute, and so I would also like to thank all members of the $W^{\pm}W^{\pm}$ analysis group, especially Rustem Ospanov, Philip Sommer, Giulia Gonella, Karolos Potamianos, Chilufya Mwewa, and Will DiClemente. I very much appreciated the open mindset and spirit of collaboration you spread.

I started a job outside of physics at LogMeIn Inc. in July 2018, and would probably not have found the time to actually write up this thesis, if my managers, Eldad Louw and Steffen Wittmann would not have proposed to make it my feature on non-feature Friday. Please know that I sincerely appreciate this generous offer.

I am also deeply grateful to my friends Karla Roszeitis, and Laura Geisler, I admire you for your compassion, patience, and occasional deep insights, and cannot list everything you have done for me. Suffice to say that I am very glad we met!

I would like to thank my family including my parents-in-law, who have supported me, not only during the last years, in any possible way. Finally I would like to thank my husband, Marc. You have been incredibly patient and took care of almost everything else why I spent many late nights working first on the $W^{\pm}W^{\pm}$ paper and later on this thesis. I promise to return the favor!

Erklärung zum Antrag auf Eröffnung des Promotionsverfahrens

Hiermit erkenne ich die Promotionsordnung des Bereichs Mathematik und Naturwissenschaften der Technischen Universität Dresden vom 23.02.2011 an.

Diese Arbeit wurde am Institut für Kern- und Teilchenphysik der Technischen Universität Dresden unter der wissenschaftlichen Betreuung von Prof. Dr. Michael Kobel angefertigt.

Es haben keine früheren erfolglosen Promotionsverfahren stattgefunden.

Weiterhin versichere ich, dass ich die vorliegende Arbeit mit dem Titel „Observation of Electroweak Same-Charge $W^{\pm}W^{\pm}jj$ Production at $\sqrt{s} = 13$ TeV with the ATLAS Detector at the LHC“ ohne unzulässige Hilfe Dritter und ohne Benutzung anderer als der angegebenen Hilfsmittel angefertigt habe; die aus fremden Quellen direkt oder indirekt übernommenen Gedanken sind als solche kenntlich gemacht. Hilfe Dritter wurde nur in wissenschaftlich vertretbarem und prüfungsrechtlich zulässigem Ausmaß in Anspruch genommen. Es sind keine unzulässigen geldwerten Leistungen, weder unmittelbar noch mittelbar, im Zusammenhang mit dem Inhalt der vorliegenden Dissertation an Dritte erfolgt.

Die Arbeit wurde bisher weder im Inland noch im Ausland in gleicher oder ähnlicher Form einer anderen Prüfungsbehörde vorgelegt.

Mir ist bekannt, dass die Nichteinhaltung dieser Erklärung oder unrichtige Angaben zum Verfahrensabbruch oder zum nachträglichen Entzug des Doktortitels führen können.

Franziska Iltzsche
Dresden, 7. Mai 2019